



HAL
open science

Lipid membrane interaction with self-assembling cell-penetrating peptides

Vivien Walter

► **To cite this version:**

Vivien Walter. Lipid membrane interaction with self-assembling cell-penetrating peptides. Biophysique [physics.bio-ph]. Université de Strasbourg, 2017. Français. NNT : 2017STRAE032 . tel-01783559

HAL Id: tel-01783559

<https://theses.hal.science/tel-01783559>

Submitted on 2 May 2018

HAL is a multi-disciplinary open access archive for the deposit and dissemination of scientific research documents, whether they are published or not. The documents may come from teaching and research institutions in France or abroad, or from public or private research centers.

L'archive ouverte pluridisciplinaire **HAL**, est destinée au dépôt et à la diffusion de documents scientifiques de niveau recherche, publiés ou non, émanant des établissements d'enseignement et de recherche français ou étrangers, des laboratoires publics ou privés.

ÉCOLE DOCTORALE PHYSIQUE ET CHIMIE-PHYSIQUE

INSTITUT CHARLES SADRON

THÈSE présentée par :

Vivien WALTER

soutenue le : **12 septembre 2017**

pour obtenir le grade de : **Docteur de l'université de Strasbourg**

Discipline/ Spécialité : Physique

**LIPID MEMBRANE INTERACTIONS WITH
SELF-ASSEMBLING CELL-PENETRATING PEPTIDES**

THÈSE dirigée par :

Dr. MARQUES Carlos

Directeur de recherche, Université de Strasbourg

RAPPORTEURS :

Pr. CLAESSENS Mireille

Professeur des Universités, Université de Twente

Dr. SANDRE Olivier

Directeur de recherche, Institut Polytechnique de Bordeaux

AUTRES MEMBRES DU JURY :

Pr. BECHINGER Burkhard

Professeur des Universités, Université de Strasbourg

Dr. BASSEREAU Patricia

Directeur de recherche, Institut Curie, Paris

Acknowledgments

IL serait inacceptable de ma part d'écrire ce manuscrit sans remercier toutes les personnes qui ont rendu ce travail possible, que ce soit par leurs contributions scientifiques ou humaines. Je ne serai jamais capable de les remercier autant que je le devrais.

Je souhaite remercier en premier les membres de mon jury, Patricia Bassereau, Mireille Claessens, Burkhard Bechinger et Olivier Sandre, pour avoir accepté d'évaluer mes travaux de thèse, et en particulier mes deux rapporteurs qui ont accepté de corriger mon manuscrit durement ces chauds mois d'été.

Je remercie ensuite précieuse Céline, qui se tient à mes côtés depuis ma licence et qui m'a soutenu et supporté ces trois dernières années. Par d'amusants concours de circonstances, je me retrouve à écrire ces lignes quelques jours avant que nous nous unissions à l'église, et tu ne seras plus ma copine mais ma femme quand les gens liront ces mêmes lignes.

Bien entendu, je ne serais jamais là où je suis sans ma famille, et plus spécialement mes parents, Corinne et Didier, ma soeur Marion, et mes grand-parents, Monique, Marlène, et mes deux *papis* Robert. Sans leur immense soutien sur tous les aspects possibles de ma vie, je n'aurais jamais eu l'opportunité d'effectuer une licence, deux masters, et le concours du CAPES avant de partir en doctorat, et enfin de me marier. C'est avec tristesse que j'ai achevé mon second master, obtenu le concours et le contrat doctoral juste après que l'un de mes chers *papi* Robert ne décède, et je regrette beaucoup qu'il n'ait pu me voir au moins réussir ces choses-là.

Je remercie également mes amis les plus proches que sont Hervé, Mickaël et Thibaut. Hervé, mon *frère de lunettes*, qui a toujours été d'un immense secours lorsque je me suis trouvé dépourvu devant des problèmes de chimie organique. Ce fut un réel plaisir de commencer et de finir ma thèse en même temps que toi. Mickaël, cet ami improbable et ubuesque qui, en m'ayant trouvé introverti dans ma jeunesse, s'est démené parfois sans le vouloir pour me faire aimer sortir, profiter de ce qui m'entoure et rencontrer

de nouvelles personnes. Jamais je n'atteindrai ta folie, mais ne plus autant faire l'idiot à tes côtés me manquera toujours. Thibaut, que je connais depuis le premier jour de la maternelle, que j'ai fréquenté toute ma scolarité et avec qui je partage les grandes passions que sont les blagues nulles, la musique et les jeux vidéos. Nos boutades quotidiennes m'ont permis de garder la pêche tout au long de mon doctorat. Mais que Franck, Jordan, Jérémy (le(s)quel(s)?), Florian, et les autres se rassurent : je ne les oublie pas, et toutes mes pensées et remerciements vont vers eux.

Mon doctorat fut également le moment de rencontrer de nouvelles personnes que j'ai l'honneur de compter parmi mes plus proches amis maintenant : Céline, Pierre et Othmène. Céline, ma copine de surveillance de TP, de simulation et de voyage en Allemagne. Où en serions-nous sans nos discussions et délires quotidiens. J'ai toujours été un peu triste ces matins où tu n'étais pas à l'ICS et où je ne pouvais pas prendre mon café en ta compagnie. Pierre, avec qui j'ai aussi partagé de nombreux jeux de mots catastrophiques et qui m'a fait découvrir tant de super jeux de société. J'en ai tant à acheter maintenant pour te rattraper. Cela m'a fait un choc quand tu as décidé d'abandonner ton doctorat, car sans ton génie jamais je n'aurais pu avoir un contrôle en température aussi performant. Othmène, que je ne pourrai jamais appeler autrement que le "stagiaire", alors même que tu es devenu un doctorant très motivé, curieux et débrouillard. La faute à t'avoir suivi et aidé pendant toute l'année que tu as passé en stage de Master dans l'équipe. Je continuerai encore longtemps à t'embêter, et à chaque fois que je reviendrai vous voir, je modifierai ton fichier *bash_profile* pour te faire comprendre que tu dois verrouiller ton ordinateur quand tu vas aux toilettes.

L'Institut Charles Sadron, ce fut aussi plein d'autres amis que je ne peux oublier : Georges, Andreas, Martin, Laure, Loriane, Johan, Fabien, Tony, Alexandre, Guillaume, Morgane, Charchit, Tristan... Et sûrement d'autres que j'oublie, malgré ce que j'ai pu dire. Cet institut, ce fut également des personnalités fortes et attachantes, et dont bon nombre d'entre eux m'ont apporté une précieuse aide : Marc, Olivier, Jean, Hendrik, Alexandre, Philippe, Michel, Patrick, Jean, Jean-Marc, Serge, Katia, Magali, etc. Je ne pourrais citer tout le monde, mais jamais je ne vous oublierai.

Et les autres, tous les autres, qu'ils soient de la famille, des amis plus ou moins proches, ou des collègues. Oui, tous ces autres, jamais je n'aurai la place de tous vous remercier ici. Mais vous avez tous beaucoup compté pour moi, et je vous en suis infiniment reconnaissant.

Les remerciements pour les membranes permanents de l'équipe Mcube méritaient d'avoir une place spéciale, tout comme ces personnes ont eu une place spéciale dans ma vie au cours de ces trois années. J'adresse à chacun un message personnel, accompagné d'une esquisse réalisée pour le dessin de la page d'après.



Carlos, un directeur de thèse incroyable, avec une perspicacité et une imagination hors norme. Il m'a appris à toujours persévérer et toujours croire en moi et, grâce à la confiance qu'il m'a accordé, j'ai pu garder confiance en moi jusqu'au bout.

Tatiana, qui a fait preuve d'une immense patience pour combler toutes les lacunes que j'avais en biophysique et en biologie quand je suis arrivé. J'ai appris énormément à ses côtés, et elle m'a aidé à conserver ma bonne humeur en tout temps.



Pierre, qui s'est assuré que je maîtrise chaque équation et concept avec lesquels j'ai du travailler. Une véritable figure paternelle scientifique, qui a, pendant trois années, partagé sa pause de midi avec moi autour d'une énigme mathématique.

André, mon mentor en microscopie et une source intarissable d'idées et d'inventions. L'enseignement le plus personnel qu'il m'a apporté, peut-être sans le vouloir, est l'importance des sentiments et du côté humain dans la science.



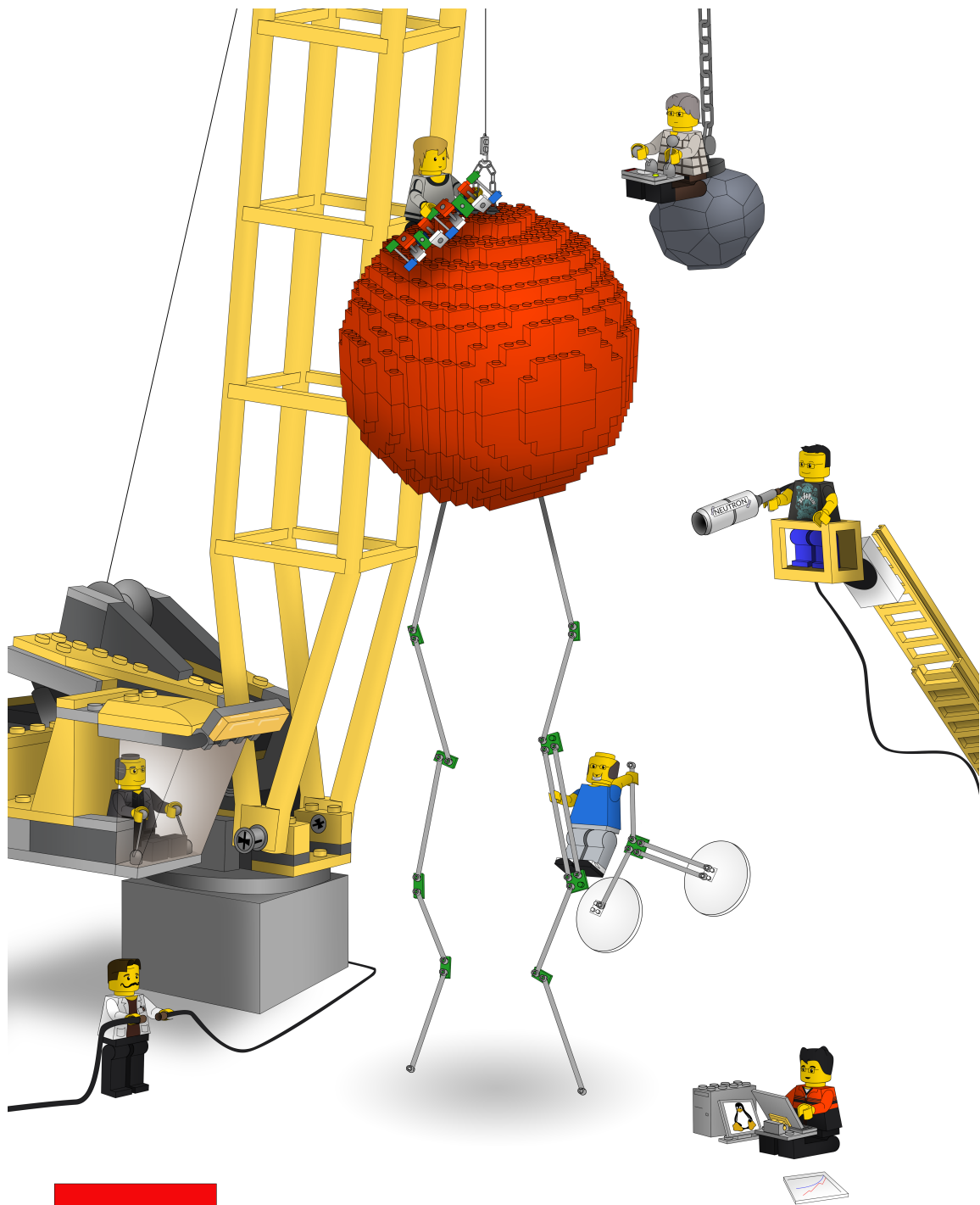
Marc, derrière son incontournable moustache digne de Dali, était le bricoleur de génie, capable de rendre réelle n'importe quelle idée vague que je pouvais avoir. Sans lui et son talent, je ne pense pas que j'aurais pu triompher de tous les problèmes techniques.

Fabrice, ce fut surtout des discussions aussi interminables qu'intéressantes sur des aspects toujours plus variés. Sans lui, jamais je n'aurais pu autant apprendre et comprendre les statistiques, et sans lui je ne saurais pas faire de simulations.



Thierry, peut-être le membre le plus discret au cours de ma thèse, mais sans lequel je n'aurais pas pu entrer à l'Institut Charles Sadron. Bien souvent, les aides les plus précieuses sont les plus silencieuses.

Ce fut un réel bonheur de travailler avec vous tous, et je n'aurais pu espérer meilleure équipe pour m'accompagner durant la préparation de mon doctorat.



Membranes & MicroPores

[Signature]
ART BY MANTER/AMM - 08-2015

Table of Contents

List of Figures	XII
List of Tables	XVIII
List of Abbreviations	XXI
List of Symbols	XXIII
Preface	1
1 Introduction on biomembranes and cell-penetrating peptides	5
A Biomembranes	6
A-1 Cell and membranes	6
A-2 Self-assembling amphipatic molecules	7
A-3 Discussion on lipids	9
A-3.a Definition and general aspects	9
A-3.b Chemical description of phospholipids	11
B Physical properties of the membranes	15
B-1 Fluid lipid bilayer	15
B-2 Phase transitions in lipid bilayers	16
B-2.a Gel, liquid, and other phases	16
B-2.b Role of the lipid structure in the transition temperature	19
B-2.c Lipid mixture and phase separation	20
B-3 Elasticity of a bilayer	23
B-3.a Surface tension	23
B-3.b Bending modulus	25
B-3.c Curvature of a lipid membrane	26
B-4 Membrane permeation	28
B-4.a Permeability	28
B-4.b Osmotic pressure	30

TABLE OF CONTENTS

	B-4.c	Formation of pores	34
C		Interactions of macromolecules with the membrane	35
	C-1	Polymers and cell membrane	35
	C-2	Configurations of lipid-polymer interactions	36
		C-2.a The different configurations	36
		C-2.b Mechanisms of adsorption	38
		C-2.c Adsorption isotherms	39
D		Model systems to mimic the cell membrane	42
	D-1	The concept of a model membrane	42
	D-2	Vesicles	42
		D-2.a Presentation of the liposomes	42
		D-2.b Giant vesicles	43
		D-2.c Sub-microscopic vesicles	46
	D-3	Planar bilayer	48
E		Drug delivery	49
	E-1	Systems for drug delivery	50
		E-1.a Liposomal systems	50
		E-1.b Micelles	52
		E-1.c Nanoparticles	54
	E-2	Cell-Penetrating Peptides	55
		E-2.a The different types of cell-penetrating peptides	56
		E-2.b Arginine-rich peptides	59
2		Systèmes et analyses	63
	A	Molécules fonctionnalisées avec des CPPs	63
		A-1 CPPs courts	64
		A-2 Polypeptides auto-assemblants	64
		A-2.a Polypeptides semblables à de l'élastine diblocs	65
		A-2.b ELP _{BC} fonctionnalisé avec des CPPs	66
		A-2.c Préparation des échantillons	70
	B	Préparation des liposomes	70
		B-1 Phospholipides	70
		B-2 Préparation des GUV	71
		B-2.a Electroformation	71
		B-2.b Formation assistée par gel de PVA	73
		B-2.c Formation de liposomes réalisée avec des lipides saturés	74

B-3	Préparation de SUV et de LUV	74
B-3.a	Solution de MLV	74
B-3.b	Extrusion	75
B-3.c	Sonication	75
C	Analyse de la membrane	75
C-1	Microscopie optique	76
C-1.a	Résolution d'un microscope	76
C-1.b	Microscopie de contraste	77
C-1.c	Microscopie interférométrique	79
C-2	Microscopie de fluorescence	81
C-2.a	Bases	81
C-2.b	Sondes fluorescentes	83
C-2.c	Quantification de la fluorescence	85
C-2.d	Microscopie confocale	87
C-3	Systèmes expérimentaux	89
D	Produits chimiques	92
3	Experimental and analytical development	95
A	Electroformation caps	95
A-1	Vesicle growth	96
A-1.a	Comparison between the electroformation methods at 10 Hz and 1 V	96
A-1.b	Conditions leading to lipid degradation	98
A-2	Formation procedure	99
B	PVA gel-assisted formation in saline solution	100
B-1	Context	100
B-2	PTFE plate for vesicle growth	101
B-3	Growth of zwitterionic GUVs	102
B-3.a	Preparation of the gel	102
B-3.b	Effect of the salt on the growth	102
B-4	Conclusion on the PVA gel-assisted formation	104
C	Surface treatment	105
C-1	Silanization reaction	106
C-2	PEGylation reaction	107
C-2.a	Full coverage of a glass slide	108
C-2.b	Brush coverage of a glass slide	110

TABLE OF CONTENTS

C-3	Results	111
D	Temperature controlled experiments	112
D-1	Experimental set-up	112
D-2	Calibration	112
E	Analysis of interferometric microscopy data	115
E-1	Membrane fluctuations analysis with RICM	115
E-2	Definition of the Autocorrelation Function	117
E-3	Autocorrelation Function computation	118
E-3.a	Time ACF	119
E-3.b	Spatial ACF	121
E-4	Experimental overview	122
4	Interactions between lipid membranes and CPP-ELP_{BC}	127
A	Effect of the micellization of the CPP-ELP _{BC}	128
A-1	Experimental observations	128
A-2	Adsorption is the key for the penetration of the CPP	131
B	Fluorescence quantification of molecules adsorbed on a lipid membrane	132
B-1	Quantification of the intensity	132
B-2	Experimental requirements for the quantification	134
B-3	In vitro measurements of the N_{PTL}	135
C	Does adsorption break the CPP-ELP _{BC} micelles into unimers?	136
C-1	Measurement by dequenching effect	136
C-2	Surface coverage	138
D	Calibration of the confocal microscope	139
D-1	The settings of the confocal microscope	139
D-2	Calibration	142
D-2.a	Reference	142
D-2.b	Fluorescent sample containing a GUV	143
D-3	Calibrated values and analytical procedure	143
D-4	Checking the calibration	144
5	Quantification of the adsorption on model membrane	147
A	Physiological membrane charges	148
A-1	Adsorption isotherms	148
A-1.a	Theoretical background	148
A-1.b	Effect of the membrane charge	150

	A-1.c	Determination of K and N_{PTL}^{Max}	151
	A-2	Thermodynamic analysis	154
	A-2.a	Theoretical background	154
	A-2.b	Adsorption of CPP-ELP _{BC} as a function of the temperature	155
	A-2.c	Calculation of the enthalpy and entropy of adsorption .	157
B		High charge density regime	158
	B-1	Charge effects at a high charge densities: a qualitative description	158
	B-1.a	Unimers adsorption as a function of membrane charge	159
	B-1.b	Micelles adsorption as a function of membrane charge .	160
	B-2	Langmuir adsorption model: structure of the adsorbed layer .	161
	B-2.a	Construction of an unimers monolayer	161
	B-2.b	Construction of a micelles monolayer	164
	B-3	Thermodynamic analysis	165
	B-3.a	Effect of the temperature	165
	B-3.b	Estimation of the enthalpy and entropy of adsorption .	167
6		Adsorption and penetration of short cell-penetrating peptides	171
	A	Adsorption, penetration and folding	172
	A-1	Adsorption of the short CPP	172
	A-2	Membrane folding	173
	A-3	Dealing with multiplicity	175
	A-3.a	Theoretical background	176
	A-3.b	Extraction of the means of concatenated distributions .	178
	A-4	Determination of N_{PTL}	180
	B	Influence of the fluorophore on the adsorption	182
	B-1	Theoretical background	184
	B-2	Evaluation of the affinity of the short TAT	186
		Conclusions	189
		Appendices	193
	Apx-1	Fluorescent probes	194
	Apx-2	Fluorescence spectra	195
	Apx-3	Graphic experimental protocols	196
	Apx-4	PTFE electroformation cap	199
	Apx-5	Interactions between charged lipids and DNA	200

TABLE OF CONTENTS

Apx-5-1	Growth of electrically charged GUVs	200
Apx-5-2	Interaction with DNA	201
Apx-5-3	DNA encapsulation	204
Apx-6	Heating stage	206
Apx-7	Computation procedure for the measurement of the N_{PTL}	207
References		209

List of Figures

1.1	Artist's rendering of an eukaryotic cell.	6
1.2	Representation of the cell membrane and its different types of biomolecule.	7
1.3	Schematic representations of different sort of amphipatic molecules	8
1.4	Representation of different self-assembled systems.	9
1.5	Skeletal formula of the phospholipid backbone and headgroups.	11
1.6	Skeletal formula of three different phospholipids.	14
1.7	Representation of the different lipid diffusions in a bilayer.	15
1.8	Representation of the phases of a lipid bilayer.	17
1.9	Order parameter of a lipid in a membrane.	18
1.10	Influence of the chain length and insaturation position on lipid phase transition temperature.	21
1.11	Phase diagram of a binary mixture of lipids.	22
1.12	Phase diagram of a binary mixture of phospholipid and cholesterol.	22
1.13	Phase diagram of the ternary mixture of three lipids.	23
1.14	Confocal pictures of phase separated vesicles.	24
1.15	Representations of the different possible deformations of a membrane.	25
1.16	Illustration of the membrane curvature.	26
1.17	Confocal pictures of lipid tubes connected to a GUV.	27
1.18	Illustration of the permeability of the lipid membrane.	29
1.19	Permeability of the lipid membrane.	29
1.20	Illustration of the U-shaped tube experiment to highlight osmotic pressure.	31
1.21	Effect of the osmotic pressure on a bilayer.	32
1.22	Effects of the osmotic pressure on a vesicle.	33
1.23	Illustration of pores in a lipid membrane.	34
1.24	Illustration of the pore formation in the case of an osmotic choc.	35
1.25	Representation of the different configurations for the membrane-polymer interactions.	37

1.26	Representation of the monolayer and multilayer coverages.	39
1.27	Comparison of the Langmuir and BET isotherms.	41
1.28	Representation of the different types of vesicles.	43
1.29	Representation of the different methods of GUV formation.	45
1.30	Representation of different methods of SUV and LUV formation.	47
1.31	Representation of the different types of planar bilayers.	48
1.32	Representation of polymer and antigen-decorated liposomes for drug delivery.	51
1.33	Representation of the different shapes of a mixed micelle.	53
1.34	Representation of a lipid-coated nanoparticle translocating through a membrane.	55
1.35	Fluorescence microscopy pictures of the cellular uptake by cell-penetrating peptides.	56
1.36	Illustration of the different mechanism of cellular uptake of the CPPs.	59
1.37	Skeletal formulae of arginine and lysine.	60
1.38	Comparison of the cellular uptake between CPP and CPP grafted onto a molecular cargo.	61
2.1	Representation of a temperature-controlled self-assembling cargo-grafted CPP	65
2.2	Transition temperature of an ELP _{BC}	67
2.3	Description of the structure of the CPP-ELP _{BC}	68
2.4	Temperature-triggered selectivity of the CPP-ELP _{BC} for tumorous cells.	69
2.5	Skeletal formula of the phospholipids of this work.	72
2.6	Picture of the extruder used for LUV preparations.	75
2.7	Illustration of the numerical aperture.	77
2.8	Illustration of the phase difference between two media.	78
2.9	Pictures of GUVs in contrast enhanced microscopy.	79
2.10	Description of the reflection interference contrast microscopy.	80
2.11	Molecular structure and fluorescence properties of fluorescein.	82
2.12	Concept of the reflective microscopy.	83
2.13	Concept of the FRAP technique.	86
2.14	Fluorescence intensity as a function of the dye concentration, highlighting the quenching effect.	87
2.15	Confocal microscopy.	88

2.16	Nikon TE-200 microscope used for this work.	90
2.17	Nikon TE-2000 microscope used for this work.	90
3.1	Home-made PTFE electroformation caps.	96
3.2	Distributions of the vesicles radii obtained using the ITO electrodes or the electroformation caps.	97
3.3	PTFE electroformation caps with thin and wide gaps.	98
3.4	Chromatography of a sample of lipids after degradation by extended electroformation.	99
3.5	Effect of the salt on the growth of DOPC GUVs.	101
3.6	Home-made PTFE plate for gel-assisted formation.	102
3.7	Effect of the PVA gel prepared in a NaCl solution on the growth of GUVs.	103
3.8	Adhesion of the GUV on a glass surface.	105
3.9	Reaction between MPTS and a glass surface.	106
3.10	Measurement of the thickness of the silane layer on a silicon wafer.	107
3.11	Reaction between a MeO-PEG _n -Mal and a MPTS.	108
3.12	Representation of the mushroom-like and brush-like polymer-grafted surface.	109
3.13	Experimental set-up for temperature controlled experiments.	113
3.14	Set-up for the temperature calibration.	114
3.15	Representation of the bijectivity between the measured gray-level of intensity and the distance between the reference surface and the membrane.	116
3.16	Screenshot of the AutoCorrelation Function plug-in function for Im- ageJ.	118
3.17	Pictures used to test the <i>tACF</i> plug-in function.	120
3.18	<i>tACF</i> of the black and white reference pictures.	120
3.19	The two pictures used to test the <i>sACF</i> plug-in function.	121
3.20	Spatial evolution of the thermal fluctuations of GUVs in the presence of nanoparticles.	123
3.21	Temporal evolution of the thermal fluctuations of GUVs in the pres- ence of nanoparticles.	124
4.1	Confocal pictures of GUVs made of pure DOPC interacting with TAT-ELP _{BC} above and below the CMT of the polypeptide.	129

4.2	Confocal picture of a GUV with a lipid composition comparable to the typical phospholipid head composition of mammalian cells interacting with AF488-labelled TAT-ELP _{BC}	130
4.3	Illustration of the two steps process of the cellular uptake by CPPs suggested by our observations.	131
4.4	Radial profiles of intensity of a GUV with and without adsorbed molecules on its surface.	133
4.5	Fluorescence calibration curve for a solution of a control ELP _{BC} labelled with AF488.	135
4.6	Distribution of N_{PTL} values for samples of (a) GUVs of pure DOPC and (b) GUVs made of DOPC, DOPE and DOPG at molar fractions of 65/25/10, exposed to TAT-ELP _{BC}	136
4.7	Illustration of two possible scenarii for the adsorption of CPP-ELP _{BC} on the phospholipid bilayer, either as micelles or in the unimer state.	137
4.8	Emission spectra of a 50% BODIPY-labelled Arg8-ELP _{BC} solution in unimer state and as micelles.	137
4.9	Distribution of N_{PTL} values for samples of GUVs of pure DOPC exposed to BODIPY-labelled TAT-ELP _{BC}	138
4.10	N_{PTL} measured from the raw intensity radial profile of the same vesicle, taken with different photomultiplier gains.	140
4.11	Simplified representation of the elements of the confocal microscope.	141
4.12	Calibration of a non-fluorescent sample.	142
4.13	Calibration of a fluorescent sample.	143
4.14	Verification of the calibration of the confocal microscope.	144
4.15	Verification of the calibration of the confocal microscope on the value of the N_{PTL}	145
5.1	Adsorption isotherms obtained from the experimental measurement of the N_{PTL} for the adsorption of TAT-ELP _{BC} on GUVs.	149
5.2	Effect of the membrane charge on the adsorption of TAT-ELP _{BC} on a lipid membrane.	150
5.3	Fit result of the Langmuir isotherm for the adsorption of TAT-ELP _{BC} on zwitterionic membranes and membranes with a low membrane charge.	152
5.4	Sketch of the two hypothesis used to describe the adsorption of micelles on the surface.	153

5.5	Effect of the temperature on the adsorption of CPP-ELP _{BC} on a zwitterionic membrane.	156
5.6	$R \ln(K)$ as a function of $1/T$	157
5.7	Effect of the membrane charge on the adsorption of unimers of TAT-ELP _{BC} on lipid membranes with low and high proportions of negatively charged lipids	159
5.8	Phase separation observed in a GUV of DOPC/DOPG in presence of TAT-ELP _{BC}	160
5.9	Effect of the membrane charge on the adsorption of micelles of TAT-ELP _{BC} on lipid membranes with low and high proportions of negatively charged lipids	161
5.10	Adsorption isotherms obtained from the experimental measurement of the N_{PTL} for the adsorption of unimers of TAT-ELP _{BC} on GUVs with high membrane charge.	162
5.11	Illustration of the two hypotheses used to describe the adsorption of unimers of polypeptides on the surface.	163
5.12	Adsorption isotherms obtained for the adsorption of micelles of TAT-ELP _{BC} on GUVs with high membrane charge.	164
5.13	Effect of the temperature on the adsorption of CPP-ELP _{BC} on a negatively charged membrane.	166
5.14	Adsorption of unimers and micelles of TAT-ELP _{BC} on a membrane with a high proportion of charges.	167
6.1	Confocal pictures of GUVs taken from the same sample showing penetration of sTAT or not.	172
6.2	Histogram of the distribution of N_{PTL} values measured for a sample of GUVs of DOPC/DOPG immersed in a solution of sTAT.	173
6.3	Confocal picture of a MLV of DOPC immersed in a solution of sTAT.	174
6.4	Illustration of the peptide-induced membrane folding which can occur on a GUV.	174
6.5	Confocal picture of a GUV of DOPC in a solution of sTAT display dense regions of fluorescence, indicating the presence of membrane folding.	175
6.6	Illustration of the effect of the penetration on the measurement of the N_{PTL} value for the adsorption of molecules on a GUV and on a MLV.	176

6.7	Illustration of the effect of the membrane folding on the measurement of the N_{PTL} value for the adsorption of molecules on a GUV with and without penetration.	177
6.8	Representation of the effect of the binning of experimental data on the apparent shape of the distribution.	178
6.9	Representation of the data as their cumulative count for extracting the mean value(s) of the distribution.	179
6.10	Representation of the N_{PTL} values obtained in figure 6.2 as the cumulative count of the values.	180
6.11	Distribution of all the N_{PTL} values multiplicity obtained for the extraction of the mean N_{PTL} value.	181
6.12	Langmuir isotherm for the adsorption of sTAT on the surface of GUVs.	182
6.13	Representation of the difference of proportions between the molecular weight of the fluorescent dye and the molecular weight of the labelled molecule.	183
6.14	Evolution of the N_{PTL} value as a function of the proportion of HL488-labelled sTAT.	183
6.15	Typical curves one could obtain for different ratio between K_{fluor} and K_{pep}	185
6.16	Evolution of the N_{PTL} as a function of the proportion of HL488-labelled sTAT	186
Apx-5.1	Confocal pictures of the growth of DOPG and DOTAP GUVs. . . .	200
Apx-5.2	Confocal pictures of the interaction between DNA and GUVs. . . .	201
Apx-5.3	Confocal pictures of the interaction between YOYO-1 and negatively charged GUVs.	203
Apx-5.4	Results on the yield of DNA encapsulation in DOPC GUVs.	205
Apx-7.5	Graphical interface to measure the adsorbed amount from the microscope intensity profile.	207

List of Tables

1.1	Lipid categories as given by the LIPID MAPS database.	10
1.2	Cell membrane lipid composition of red blood cells.	10
1.3	Cell membrane phospholipid head group composition of red blood cells.	12
1.4	Examples of phospholipid tails.	13
1.5	List of the gel-liquid phase transition temperature of different phospholipids.	19
1.6	List of the gel-liquid phase transition temperature for different monoenoic unsaturated phospholipids.	20
1.7	List of the constants of permeability of different molecules.	30
1.8	List of different methods of formation of giant unilamellar vesicles.	44
1.9	List of different methods of formation of small and large unilamellar vesicles.	47
1.10	List of the different types of CPPs	57
2.1	List of the characteristics of the different CPP-ELP _{BCS} used in this work.	69
2.2	List of the fluorescent probes used in this work.	85
2.3	List of the resolutions of the microscopes.	91
2.4	Fournisseurs des différents produits chimiques utilisés dans ce travail.	92
2.5	Abréviations des produits chimiques utilisés dans ce travail.	93
3.1	List of the different results obtained for the growth of GUVs on a PVA gel.	104
4.1	List of the different qualitative results observed for the interactions between CPP-fonctionnalized and non fonctionnalized ELP _{BC} with GUVs of pure DOPC.	129
4.2	List of the experimental measurements of the adsorption for different types of CPP-ELP _{BC} and lipid membranes.	138

4.3	List of the different values resulting from the calibration of our Nikon TE-2000 C1 Eclipse.	144
5.1	Fitted values of N_{PTL}^{Max} and K measured through fitting.	153
5.2	Values of the Gibbs free energy of adsorption ΔG for the CPP-ELP _{BC} micelles.	154
5.3	List of all the values of constant of adsorption at equilibrium (K), enthalpy (ΔH) and entropy (ΔS) of adsorption of TAT-ELP _{BC} on GUVs.	168

List of Abbreviations

CLSM	Confocal Laser Scanning Microscopy
CPP	Cell-Penetrating Peptide
CPP-ELP _{BC}	Cell-Penetrating Peptide grafted onto a diblock Elastin-Like Polypeptide
DNA	Deoxyribonucleic Acid
DOPC	1,2-dioleoyl- <i>sn</i> -glycero-3-phosphatidylcholine
DOPE	1,2-dioleoyl- <i>sn</i> -glycero-3-phosphatidylethanolamine
DOPG	1,2-dioleoyl- <i>sn</i> -glycero-3-phosphatidylglycerol
DOTAP	1,2-dioleoyl-trimethylammonium-propane
DPPC	1,2-palmitoyl- <i>sn</i> -glycero-3-phosphatidylcholine
ELP	Elastin-Like Polypeptide
ELP _{BC}	diblock Elastin-Like Polypeptide
GUV	Giant Unilamellar Vesicle
ITO	Indium-Tin Oxide
LUV	Large Unilamellar Vesicle
MLV	Multi-Lamellar Vesicle
MVV	Multi-Vesicular Vesicle
PEG	Polyethylene Glycol
PVA	Polyvinyl Alcohol
RICM	Reflection Interference Contrast Microscopy
SUV	Small Unilamellar Vesicle
TAT	HIV Transactivator of Transcription

List of Symbols

a	Monomer length of a polymer
ACF	Autocorrelation function
C	Concentration
C^*	Crossover concentration between dilute and semi-dilute regimes
d_{tot}	Depth of field of a confocal microscope
ΔG	Gibbs free energy of adsorption on the lipid membrane
ΔH	Enthalpy of adsorption on the lipid membrane
ΔS	Entropy of adsorption on the lipid membrane
E	Light energy
ϵ	Molar extinction coefficient
I	Light intensity
K	Constant of adsorption on the lipid membrane at equilibrium
k_B	Boltzmann constant, taken at $1.38 \times 10^{-23} \text{ J.K}^{-1}$
λ	Wavelength
λ_{EM}	Emission wavelength of a fluorescent dye
λ_{EX}	Excitation wavelength of a fluorescent dye
m	Mass
M	Magnification of the objective
M_W	Molecular weight
N	Average number of monomers in a polymer chain
N_a	Avogadro number, taken at $6.02 \times 10^{23} \text{ mol}^{-1}$
NA	Numerical aperture
N_{PTL}	Number of peptides per thousand lipids
N_{PTL}^{Max}	Maximal number of peptides per thousand lipids
PV	Pixel value
Φ	Quantum yield of fluorescence
R	Ideal gas constant, taken at $8.31 \text{ J.K}^{-1}.\text{mol}^{-1}$

R_g	Polymer radius of gyration
r_{max}	Maximal resolution of an optical microscope
S	Surface
θ	Surface coverage
V	Volume

"La science, mon garçon, est faite d'erreurs, mais d'erreurs qu'il est bon de commettre, car elles mènent peu à peu à la vérité."

- Jules Verne, *Voyage au centre de la Terre*

PREFACE

FROM the small bacteria to the largest white whale, the notion of living beings is indissociable from the cell. First described by Robert Hooke in the late 17th century, the cells have been rapidly identified as the unit components of life.

Medicine hit a turning point once scientists began to consider the purpose and importance of the cell in the human body, as compared to the medical principles from Antiquity. Infections and other diseases were no longer attributed to the so-called *humours*, but to microbes found under the microscope of the researchers. It became then clear that science should focus on how the cell behaves once suffering from a disease. Focusing on cell behaviour lead scientists to succeed at creating efficient ways to treat most terrible illnesses, such as Poliomyelitis or Tuberculosis to only name a few.

Nowadays, the development of new treatments is required. Science is facing illnesses of increasing complexity in situations where simple antidotes or vaccines are no longer effective, cancer being arguably the most notorious example one can think about. Obviously, when considering a disease which specifically targets and infects the cells, the different treatments one can think of have to target and treat the cells as well. And given the ubiquitous presence of lipid membranes in cells, promoting the interaction of a chemical or a physical stimulus with the cell for treating it, cannot be achieved without understanding the interaction of chemical or stimulus with the lipid membrane.

The work presented in this thesis has been made while I was a member of Membranes and Microforces, Carlos Marques' team at the Charles Sadron Institute in Strasbourg. As its name suggests, the team studies the overall behavior and the physical

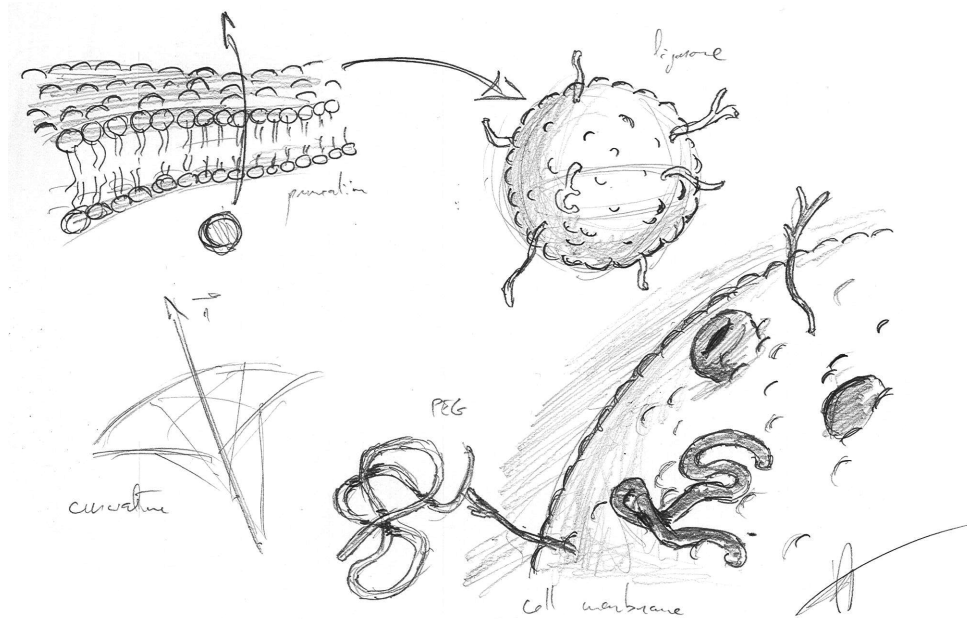
properties of the cell membrane. These three years were for sure some of the most intense years of my life, but I feel satisfied about all the things I had the opportunity to study during this time, and I also feel satisfied from having the chance to give a try to all the idea I could have on my subject.

My PhD work dealt with physical phenomena of the lipid membranes relevant drug delivery applications. As briefly described above, the purpose of the drug delivery is to interact directly with the infected cells. The principle is to bring the drug, also named molecular cargo, inside the target cell to treat it or to kill it. Nonetheless, the molecular cargo can only penetrate the cell if it translocates through the membrane, which hereby reinforce the need to understand how the cell membrane behave.

Using giant unilamellar vesicles, an artificial model system designed to reproduce the physical features of the cell membrane with a controlled composition, we attempt to demonstrate how biomolecules designed for drug delivery interact with the membrane and penetrate through it.

Perhaps the most important difficulty that I faced was to be responsible to push further work that had already achieved some degree of success. This has pushed up the level of the gauge by which I needed to measure my own achievements; it also pointed to directions that I do not always agreed with, and conclusions that I did not always validated. It did take thus a significant effort to build my own vision of the project, correcting experimental bias, finding new ways of better extracting results by developing new protocols or performing very careful calibrations. In the end all this effort paid off very well. It lead to new ways of preparing giant unilamellar vesicles or to new analytical methods, which are all now used by the team and elsewhere. For example, the use of the electroformation cap for the formation of giant unilamellar vesicles became rapidly the standard protocol used by the whole team, due to its efficiency and simple handling. I also had the chance during my thesis to meet different people, such as professor Rongjun Chen, professor Nicolas Vitale, doctor Jean-Baptiste Fleury, and many more, with whom I had the opportunity to develop further the different experimental and analytical methods described in this work. Despite not having had the time to pursue further these collaborations, I am certain that such interactions were of mutual benefit and had a very positive impact on the content of my work as described at different places of this manucrypt.

I first discuss in this manuscript the current knowledge about cell membrane and the physics describing it, and list the different materials and methods which I used during my PhD. In the third chapter, I describe the modifications I brought to existing methods along various experimental and analytical developments I have made to be able to work on complex systems containing CPP or CPP-ELP_{BC}. The three last chapters of this thesis summarize all the experiments I have performed, first on the CPP-ELP_{BC}s and then on the CPPs. Chapter four contains the results obtained on the study of the interaction of the CPP-ELP_{BC} with GUVs and introduce the new quantification method of fluorescence we have developed in the team to measure the adsorption of a molecule on a lipid membrane. In chapter five, we extend this method to measure the equilibrium constant of adsorption of CPP-ELP_{BC} and to extract the thermodynamic quantities of this adsorption. Finally, the sixth and last chapter describes the measurements performed on the bare CPP sequences. It explains how data should be analysed to discriminate permeation and membrane folding-induced multiplicity, and how to quantify the impact of the presence of the fluorescent dye on the adsorption of the peptide. A small summary of the main results is given at the end of the chapters three to six.



CHAPTER 1 Introduction on biomembranes and cell-penetrating peptides

TWO parts have to be developed in order to create an effective system for drug delivery: the molecular cargo and the carrier. The former simply corresponds to the drug one wishes to transfer inside the target cell, while the latter ought to recognize the target cell inside the organism and translocate the cargo within the cell. In this work, we discuss a family of biomolecules currently investigated as potential carriers in drug delivery applications, the cell-penetrating peptides.

This first chapter introduces the concepts of the model systems used by biophysicists to mimic the cell membranes, and the cell-penetrating peptides which are brought in contact with such systems. We also discuss about the different methods for analysing the interactions between biomolecules and lipid membranes, and the experimental methods and protocols investigated in this work.

A Biomembranes

To investigate the internalisation of the molecular cargo in the context of a drug delivery application, one has to understand how the cell membrane behaves and interacts with the carrier. And to do so, we first have to introduce the cell membrane.

A-1 Cell and membranes

The cell is the smallest unit which can describe a living being. It is a small organism housing several components, or organelles, acting as the organs of the cell and each having a specific role for the life of the cell (*cf.* figure 1.1). Two types of cells have to be distinguished: prokaryotic cells from bacteria, and eukaryotic cells from animal, plants and fungi. The latter is characterized by a membrane-bound nucleus, which the former lacks.

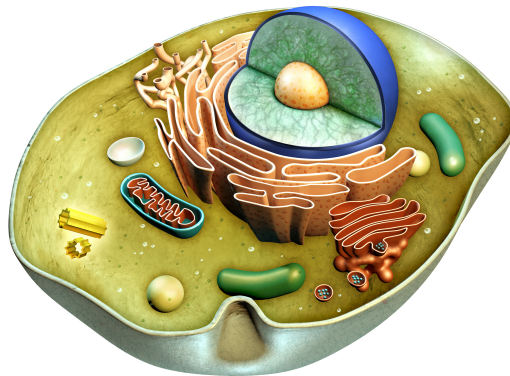


Figure 1.1: Artist's rendering of an eukaryotic cell and its different components. Image taken from [1].

In 1847, Theodore N. Gobley isolated the phospholipids from the egg yolk [2], naming them lecithin (*lekithos*, egg yolk), and attributed them to the cell membrane. Gorter and Grendel pointed out in 1925 [3] that this lipid membrane is a bilayer. While lipids, and specifically phospholipids, are the primary molecules found in the lipid bilayer, other molecules can be found inside it, as illustrated in figure 1.2.

Among the various non-lipid biomolecules located in the cell membrane, one can find the multiple types of membrane proteins. Some of these proteins are used by the cells as channels or pores for specific molecules, and some others act as probes, reacting with target biomolecules to activate the internalisation processes of the cell.

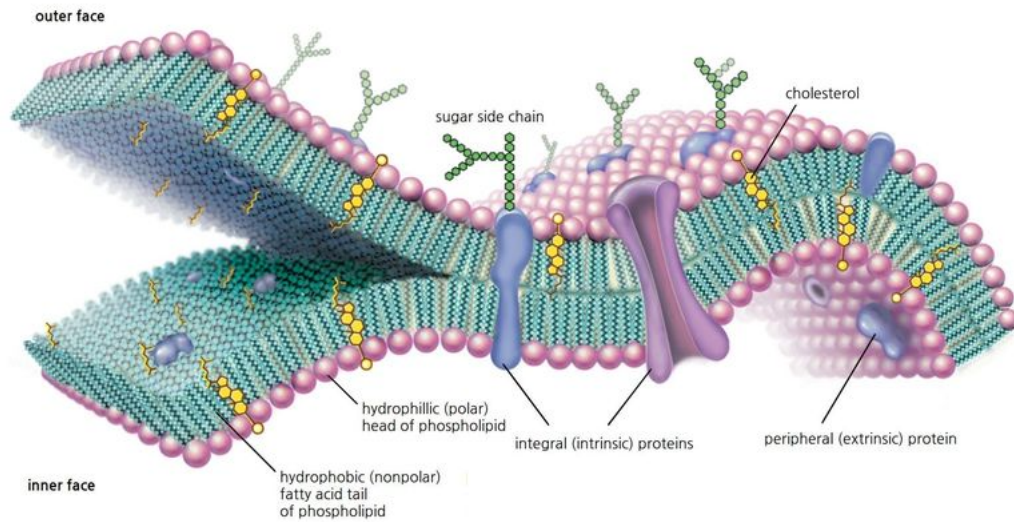


Figure 1.2: Representation of the cell membrane, with a non-exhaustive list of the different biomolecules one can find inside it. Image taken from [4]

A-2 Self-assembling amphipatic molecules

The existence of the lipid bilayer is possible due to their amphipatic nature. Amphiphilic molecules, or lyotropic liquid crystals, are a combination of two types of molecules groups bond together: hydrophilic and hydrophobic groups. Hydrophilic groups are polar molecules that are soluble in aqueous solvents, while hydrophobic groups are commonly long carbon chains, or oils, which can not mix with aqueous solvents. The coexistence of these groups in the same molecules generate a molecular stress, where one group tends to escape from water while the other one seeks for it.

As examples of amphipatic biomolecules, one can find fatty acids, phospholipids and cardiolipins, which are respectively made of one hydrophilic 'head' group and one, two and four hydrophobic alkyl chains, or 'tails' (see figure 1.3).

When brought in contact with an aqueous solution, amphipatic compounds self-assemble into supramolecular structures. If an interface between the solvent and another medium exists, for low concentration the amphipatic molecules will self-assemble as a monolayer at the interface. Langmuir described such configuration for lipids in 1917 [5]. As the concentration increases, interface will be saturated with surfactants and the molecules, which can no longer fit at the interface, will turn into a suspension in the solvant. A threshold is then reached, called the Critical Micellisation Concen-

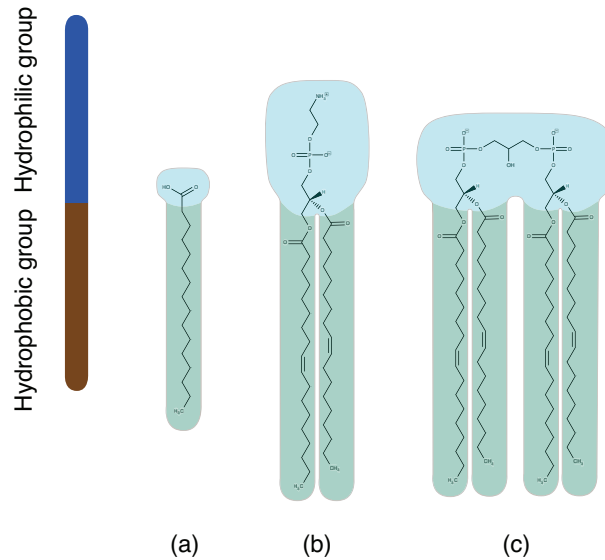


Figure 1.3: Amphipatic molecules are generally represented as multi-blocks systems, where hydrophilic group(s) are chemically bonded to hydrophobic group(s). Three common examples of such representation are given here: (a) a fatty acid, with one hydrophilic polar 'head' group and one hydrophobic alkyl chain or 'tail', (b) a phospholipid with one head and two tails, and (c) a cardiolipin with one head and four tails.

tration (CMC), above which the amphiphilic molecules self-assemble as micelles in the aqueous solution (*cf.* figure 1.4).

In the case of phospholipids, micelles are less likely to occur. While fatty acids can be seen as conic molecules, phospholipids have a cylindrical shape. Large curvatures can not be easily achieved with such shape, and phospholipids will therefore self-assemble as flat or weakly curved bilayers. While micelles are spherical monolayers of amphiphilic compounds, vesicles are spherical bilayers. These structures are only given as examples here, as these molecules can form self-assemblies of many different shapes. More information on the other configurations can be found in the Handbook of biological physics by Lipowsky and Sackmann [6].

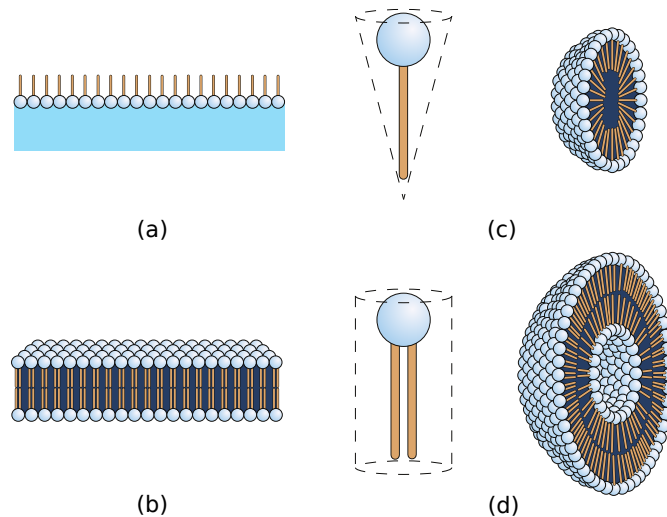


Figure 1.4: Representations of different structures obtained by self-assembling amphiphilic molecules. (a) a monolayer at an interface, (b) a bilayer such as the one forming cell membranes, (c) a micelle obtained by self-assembled cone-shaped molecules, and (d) a vesicle constructed by self-assembled cylinder-shaped molecules.

A-3 Discussion on lipids

A-3.a Definition and general aspects

As stated in the two previous sections, lipids are the key elements of the cell membrane. Indeed, the latter exists thanks to the amphiphilic properties of the lipids. Lipid (*lipos*, fat) is a generic name referring to several categories of chemicals. Indeed, the lipid composition of a simple red blood cell membrane features about 250 different lipid species [7]. The current list of lipid categories, updated by the LIPID MAPS consortium and the IUPAC in 2008 [8], is given in table 1.1.

For the purpose of the classification, the lipids are defined by the LIPID MAPS consortium as hydrophobic or amphipatic molecules which originates from the condensation of two molecular building blocks: thioesters and isoprenes.

The exact lipid composition of the cell membrane can largely differ from one organelle to another, and also from one sort of living being to another. Exact compositions of the membrane of organelles is complicated to obtain, but several articles describes that heterogeneity. Van Meer [10] cites the example that proportion of sphingolipids and sterol lipids is ten times lower in the Golgi apparatus and the endocytotic organelles than in the rest of the cell. An example of the variation of lipid composition between the membranes of red blood cells is given in table 1.2, where the compositions of the red blood cell membrane are compared for different animals.

Category	Referenced	Example
Fatty acyls	7010	Palmitic acid
Glycerolipids	7542	Tristearin
Phospholipids	9620	1-2-dioleoyl-3-glycero-phosphatidic acid
Sphingolipids	4352	Sphingomyelin
Sterol lipids	2835	Cholesterol
Prenol lipids	1256	Vitamin E
Saccharolipids	1316	Acyltrehalose
Polyketides	6742	Ansamycin

Table 1.1: Lipid categories of the comprehensive classification system and the number of structures in the LIPID MAPS database [8], along with the number of referenced lipids of each categories [9] and an example of these molecules.

Lipid	Species					
	Pig	Human	Cat	Rabbit	Horse	Rat
Phospholipids	44.0	47.0	45.3	53.3	45.0	58.4
Sphingolipids	15.8	16.0	16.0	12.5	7.0	8.6
Sterol lipids	26.8	26.0	26.8	28.9	24.5	24.7
Saccharolipids	13.4	11.0	11.9	5.3	23.5	8.3

Table 1.2: Cell membrane lipid composition by weight percent of mammalian red blood cells [11].

A-3.b Chemical description of phospholipids

The glycerophospholipids, or phospholipids for short, are a specific category of lipids. As shown in table 1.2, the phospholipids are the main lipids of the cell membrane, about 50% in weight of the overall lipids. The backbone of a phospholipid is a glycerol linked to a phosphate group (*cf.* figure 1.5(a)). A polar headgroup is grafted onto the phosphate and two fatty acid tails are linked to the remaining hydroxyl group of the glycerol by an ester bond.

The LIPID MAPS nomenclature uses abbreviations to name every phospholipids. These abbreviations consist on four capital letters: the two first letters refer to the tails of the lipid, and the two last ones to the lipid headgroup.

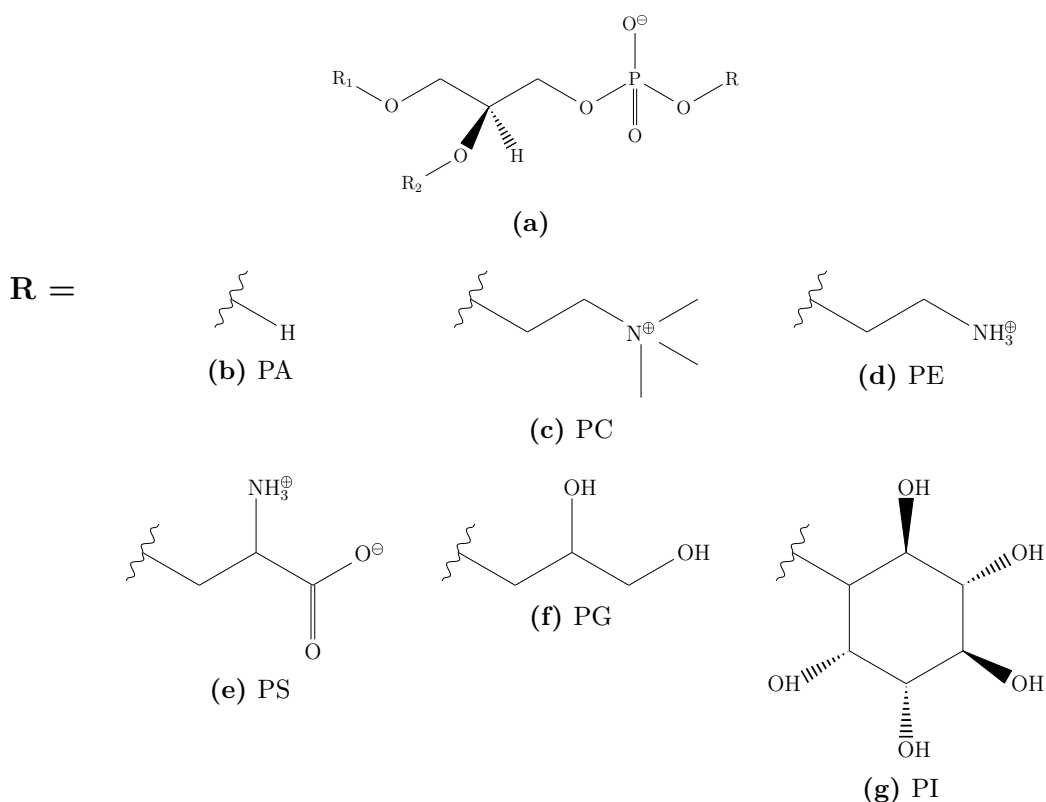


Figure 1.5: Skeletal formula of the phospho-glycerol backbone (a) and the common phospholipid headgroups. Substituents R_1 and R_2 correspond to the alkyl chains 'tails' of the lipids. The common headgroups are listed here with their LIPID MAPS abbreviation: (b) Phosphatidic Acid (PA), (c) Phosphatidylcholine (PC), (d) Phosphatidylethanolamine (PE), (e) Phosphatidylserine (PS), (f) Phosphatidylglycerol (PG), and (g) Phosphatidylinositol (PI).

The most common headgroups for phospholipids are given in figure 1.5(b)-(g). The

Phospholipid Head	Species					
	Pig	Human	Cat	Rabbit	Horse	Rat
PC	31.6	39.2	41.0	41.7	48.6	54.4
PE	40.2	37.1	29.8	39.2	27.8	24.6
PS	24.1	17.7	17.8	14.9	20.8	12.3
PI	2.5	2.7	9.9	1.9	0.4	3.9
PA	1.6	3.3	1.5	2.3	2.4	4.8

Table 1.3: Cell membrane phospholipid head group composition by weight percent of total phospholipid mass of mammalian red blood cells, sorted by headgroups [11].

two main headgroups one can find in a cell membrane are the phosphatidylcholine (PC) and phosphatidylethanolamine (PE) headgroups. Both PC and PE are zwitterionic, while the rest of the common headgroups are negatively charged. Like the types of lipids, the proportion of every headgroups in a cell membrane differs between cells and species. Table 1.3 shows the different proportions of PC, PE, and other phospholipids headgroups between the red blood cell membranes of different mammalian. This table highlights that, in average, around 25% of the phospholipids of a membrane are negatively charged (circa 12% of the total lipids according to table 1.2).

The alkyl tails of the phospholipids are named after the corresponding fatty acids. The natural fatty acids were historically named after the source where they were extracted from [12]. These names - and therefore abbreviations - are still in use for the LIPID MAPS nomenclature of physics, but it unfortunately poorly applies to the synthetic phospholipids. To overcome this problem, the nomenclature is slowly evolving to use a name corresponding to the chemical structure of the fatty acid. Examples of both nomenclatures and description of the tails are given in table 1.4.

The tail groups of the phospholipids can be sorted by chain lengths and number of insaturations. To do so, the structure of the tail is given as n:m, where n corresponds to the number of carbon atoms in the alkyl chain - or chain length - and m indicates the number of insaturations in the tail. For example, a myristoyl tail which is a saturated chain of fourteen carbons is described as 14:0, while a palmitoleoyl tail made of sixteen carbons with one insaturation is described as 16:1.

Figure 1.6 gives the example of three phospholipids with their abbreviated name using LIPID MAPS nomenclature. POPC refers to the 1-palmitoyl-2-oleoyl-glycero-3-phosphatidylcholine, a phospholipid with a phosphatidylcholine (PC) headgroup, one

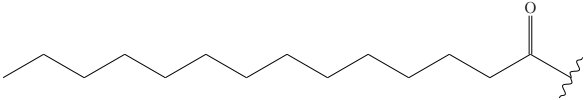
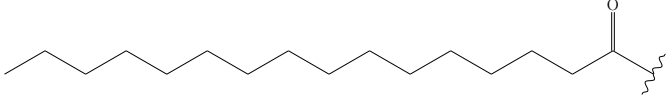
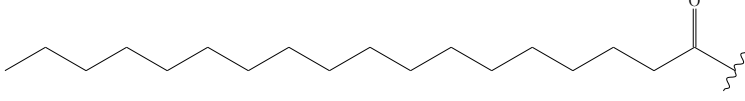
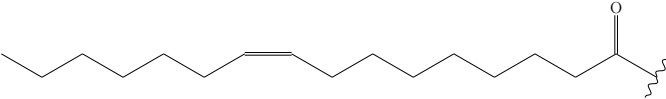
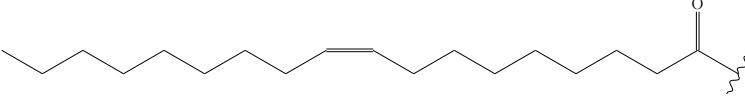
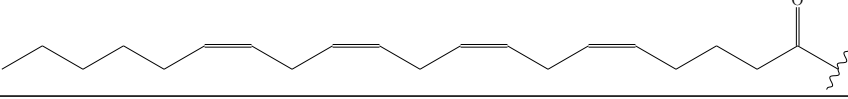
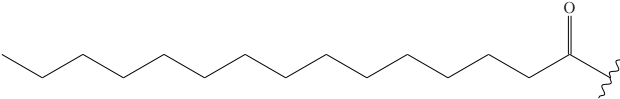
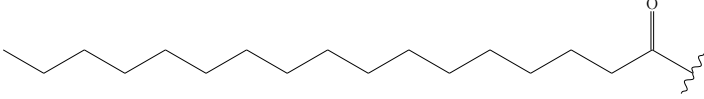
Structure	Old name	Abbr.	New name
Natural fatty acids			
Saturated chains			
14:0	Myristoyl	M	Tetradecanoyl
			
16:0	Palmitoyl	P	Hexadecanoyl
			
18:0	Stearoyl	S	Octadecanoyl
			
Unsaturated chains			
16:1	Palmitoleyl	-	9Z-hexadecanoyl
			
18:1	Oleoyl	O	9Z-octadecanoyl
			
20:4	Arachidonoyl	A	(5-8-11-14)Z-eicosatetraenoyl
			
Synthetic fatty acids			
15:0			Pentadecanoyl
			
17:0			Heptadecanoyl
			

Table 1.4: Examples of several alkyl chain tails one can find linked to the glycerophosphate backbone of a phospholipid. The tails are sorted by the natural/synthetic fatty acids they are derived from, and their saturated or unsaturated structure. For each tail, the structure is given as n:m, where n corresponds to the carbon chain length and m to the number of insaturations in the chain. The old traditional and new names are also given, along with the LIPID MAPS abbreviation.

palmitoyl (P) and one oleoyl tail (O). In the case of DMPS, 1,2-dimyristoyl-glycero-3-phosphatidylserine, the D for "di" and refers to the fact that both tails are identical. If the phospholipid has only one tail, it will be named a lysophospholipid and the prefix lyso- (*lúsis*, loosening) should be added as the first letter of the abbreviated name. Using this notation, lysoSPA (or 18:0 lysoPA) is the abbreviated name of the 1-stearoyl-2-hydroxy-glycero-3-phosphatidic acid.

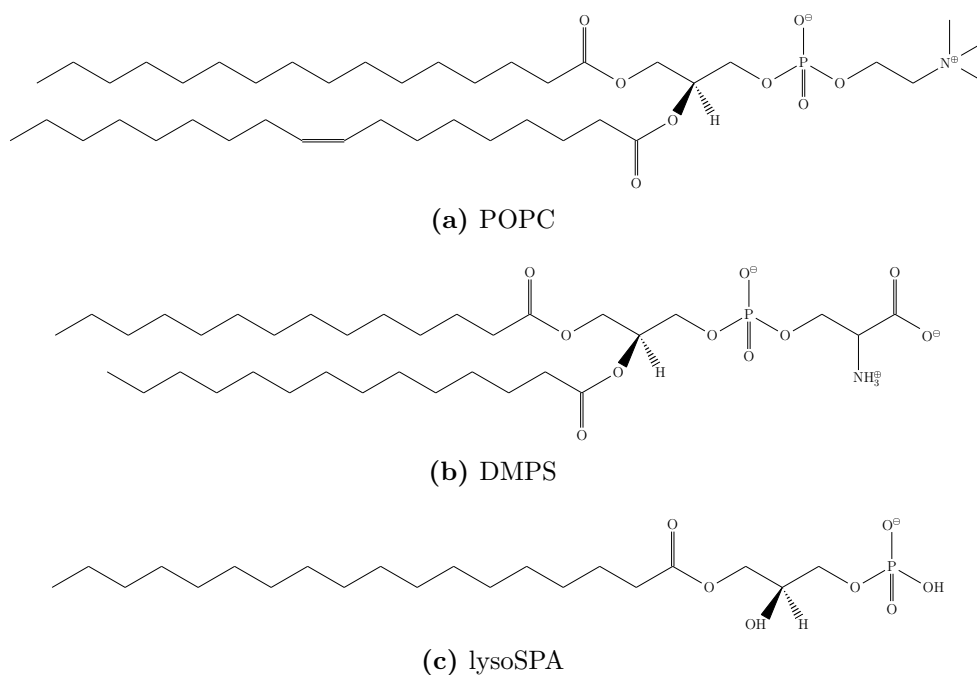


Figure 1.6: Skeletal formula of three different phospholipids with their LIPID MAPS nomenclature: (a) POPC: 1-palmitoyl-2-oleoyl-glycero-3-phosphatidylcholine, (b) DMPS: 1,2-dimyristoyl-glycero-3-phosphatidylserine, and (c) lysoSPA: 1-stearoyl-2-hydroxy-glycero-3-phosphatidic acid.

B Physical properties of the membranes

Due to their amphiphilic properties, lipids self-assemble in aqueous solution into vesicles. In the case of vesicles as large as a cell (radius larger than $1\ \mu\text{m}$), the bilayer forming the envelope of the vesicle can locally be assimilated to a planar bilayer. We will focus here on the different physical aspects describing the lipid bilayer.

B-1 Fluid lipid bilayer

Singer and Nicolson described in 1972 the cell membrane as a fluid mosaic of lipids and proteins, where all molecules are free to move in the bilayer [13]. In the same way, the basic lipid bilayer is also a fluid self-assembled construction, and the lipids which are part of this supramolecular structure have the ability to move inside the leaflets, and also from one layer to the other. These two movements are respectively called lateral diffusion and transverse diffusion, the latter commonly named *flip-flop* for short (*cf.* figure 1.8).

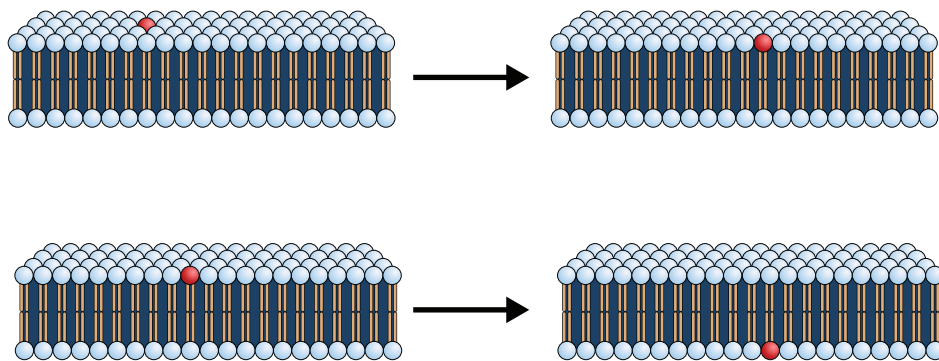


Figure 1.7: Illustrations of the two different types of lipid diffusions which can happen in a lipid bilayer. (Top) Lateral diffusion, where a lipid moves freely in the leaflet of the bilayer. (Bottom) Transverse diffusion, or *flip-flop*, where a lipid can move from one monolayer to the other.

- The transverse diffusion, or *flip-flop*, is the transfer of one lipid from a leaflet of the bilayer to the other. The rate of the flip-flop is really small, around $10^{-5}\ \text{s}^{-1}$ [14][15], hence a lipid undergoes a transverse diffusion every $10^5\ \text{s}$, which corresponds to *circa* 1 day. In a vesicle with a $10\ \mu\text{m}$ radius made of 3.6 billion lipids, 360,000 lipids switch to the other leaflet of the bilayer.

- The lateral diffusion is the ability of the lipid to move freely in the monolayer which it is part of. The coefficient diffusion of phospholipids in the bilayer has an order of magnitude of $10^{-12} \text{ m}^2 \cdot \text{s}^{-1}$ [16]. In one second, a lipid will cover a surface of $1 \mu\text{m}^2$. A lipid in a vesicle with a $10 \mu\text{m}$ radius will cover entire surface of the vesicle in about 20 minutes.

As a consequence, the lipid bilayer is constantly rearranging and both diffusions promote the homogeneity of the lipid bilayer in model systems. In the case of the cell membranes, these diffusions are guided by the organism and might lead in some case to a controlled heterogeneity, even between the two leaflets of the bilayer. Lipid diffusions are temperature dependent phenomena, and rate of diffusions will increase with the temperature.

B-2 Phase transitions in lipid bilayers

B-2.a Gel, liquid, and other phases

Due to their amphipatic nature, phospholipids display lyotropic phase behaviour. In such case, one has to consider more phases for phospholipids than the usual solid, liquid and gas phase [17]. The molecular stress induced by the chemical bonds between hydrophilic and hydrophobic groups allow the different groups to switch from an ordered phase to a more chaotic one at different temperatures (*cf.* figure 1.8).

The phospholipids commonly used in biophysical studies display three distinct phases which are characterised by their degrees of order. Going from low to high temperatures, one will find:

- The crystal phase (L_c). In this weakly hydrated phase, both head and tail groups are well ordered. The lipid tails are packed together, and the headgroups arrange along an hexagonal lattice. Lipid diffusions in crystal phase is very low and less likely to occur than in any other phase.
- The gel phase (L_β). In this phase, the degree of order of the headgroups is drastically reduced, while the order of the tails remains comparable to the one of the crystal phase. Headgroups and lipid molecules are able to freely rotate.
- The liquid phase (L_α). The degrees of order of both tails and headgroups are small in this phase, leading to thousands of possible conformational isomers [17].

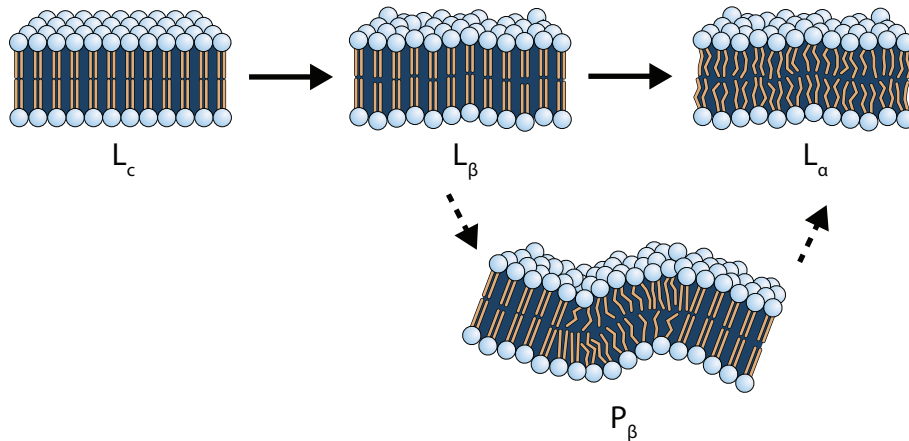


Figure 1.8: Representation of the different phases of a lipid bilayer. All transitions are reversible albeit with different degrees of hysteresis. Arrows show the path for increasing temperatures. All lipid bilayers can be found in three main phases: the crystal phase (L_c) where both tails and head groups are ordered, the gel phase (L_β) where head groups are disordered while tails remain ordered, and the disordered liquid phase (L_α) where neither tails nor head groups are no longer ordered. Certain types of phospholipids, in particular certain lipids with a phosphatidylcholine head group, can encounter an extra phase between the gel and liquid phase, called the ripple phase (P_β).

The difference in degrees of order between L_β and L_α phases can be highlighted through the measurement of the order parameters by NMR [18], as illustrated in figure 1.9. The order parameter of a lipid in a bilayer is defined, for each carbons n of the lipid tails, as the angle θ between the normal direction to the bilayer and the direction between the carbons n and $n + 2$, such as

$$S = \left\langle \frac{3 \cos^2 \theta - 1}{2} \right\rangle. \quad (1.1)$$

Measurement of the order parameters is also commonly used in molecular dynamics simulations to distinguish between the two phases. In the liquid phase, the order parameter of the carbon atoms in the chain is decreasing as the position of the atom in the tail increases (the chains can freely rotate), while it remains constant in the gel phase as all the tails of the lipids are aligned in the same direction in this phase.

Some lipids, and in particular phospholipids with a phosphatidylcholine headgroup, have an additional phase in between the gel and the liquid phase, called the ripple phase (P_β). The ripple phase can be macroscopically described as corrugations of the membrane surface with well-defined periodicity with an axis parallel to the mean

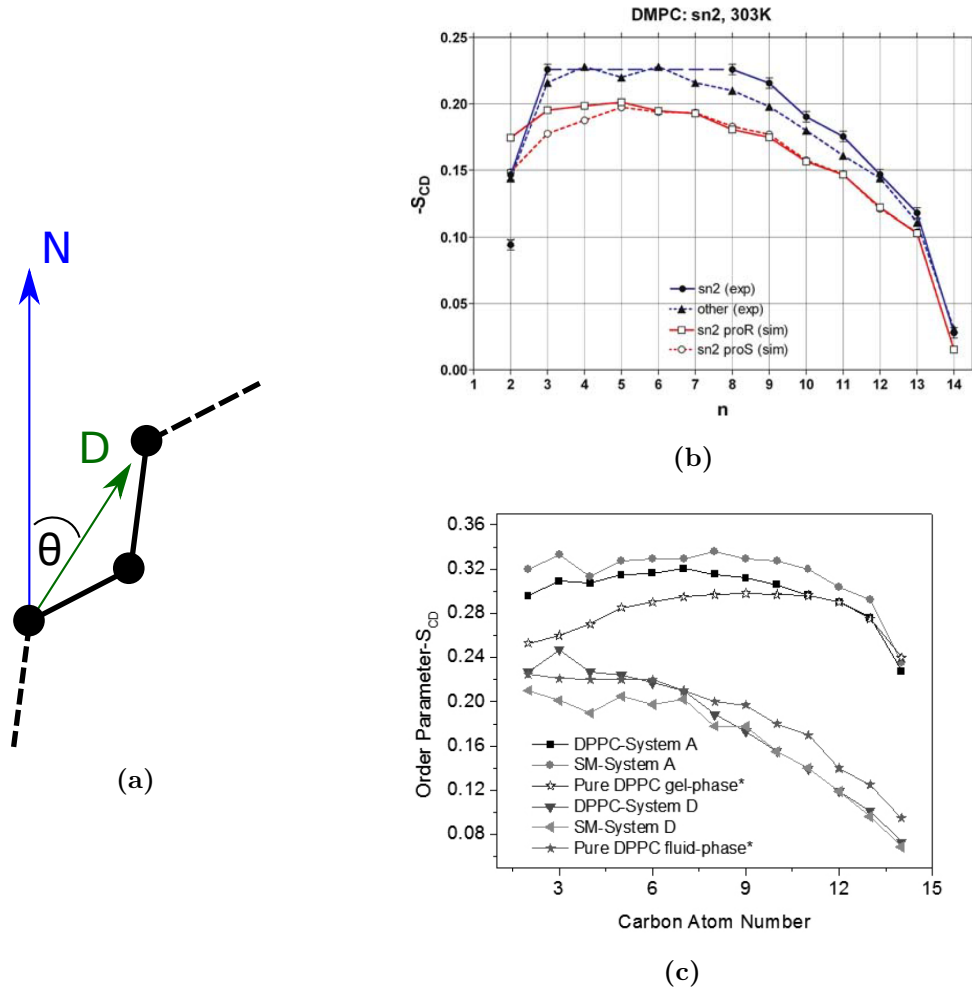


Figure 1.9: Definition and illustration of the order parameters of a lipid in a bilayer. (a) The order parameter of the n carbon in a lipid tail is given by the mean angle between the normal direction to the bilayer and the direction between the carbons n and $n + 2$. (b) Representation of the order parameter of the sn2 tail of the DMPC in a bilayer as a function of the position of the carbon in the tail n . Values are taken from NMR experiments and molecular dynamics simulations performed by Vermeer *et al.* [18], and shows the good agreement between the results of both methods. (c) Results of molecular dynamics simulations of bilayers made of different proportions of DPPC and sphingomyelin (SM). DPPC is in the gel phase, while the SM is in the fluid phase. In the fluid phase, the order parameter decreases along the chain, while it would remain constant in the gel phase. Data from Montecinos and Neira-Jimenez [19].

bilayer plane. Heimburg suggested in 2000 [20] that the ripple phase originates from the creation of liquid defects in the lipid gel phase [21].

Lipid	Structure	T_m (°C)
DMPC	14:0-14:0 PC	23.9
DPPC	16:0-16:0 PC	41.4
PSPC	16:0-18:0 PC	48.8
DSPC	18:0-18:0 PC	55.3
SOPC	18:0-18:1 PC	5.6
DOPC	18:1-18:1 PC	-17.3
DOPE	18:1-18:1 PE	-8
DOPG	18:1-18:1 PG	-21.5
	18:2-18:2 PC	-57.0

Table 1.5: List of different phospholipids, sorted by tail chainlength, headgroup and number of insaturations, and their corresponding gel-liquid transition temperature (T_m). The transition temperature increases with the chainlength of the tail and decreases with the number of insaturations. The nature of the headgroup has little effect on T_m compared to tail composition. Transition temperatures are taken from the Handbook of lipid bilayers [22] and unsaturated lipids are given as *cis*- only, as they are the most common ones.

B-2.b Role of the lipid structure in the transition temperature

The phase transition temperatures depend on the molecular composition of the bilayer. The nature of the tails of the phospholipid has the strongest effect on the transition temperature, while the headgroup has a comparatively smaller impact. Examples of the gel-liquid transition temperature (T_m) for different phospholipids are given in table 1.5 to highlight these effects.

The longer the alkyl chain of the tail the higher the transition temperature is. DMPC (14:0-14:0) has a T_m of 23.9°C while the T_m of DSPC (18:0-18:0) is of 55.3°C. The presence of insaturations in the carbon chain drastically decreases the transition temperature. DOPC (18:1-18:1) has a T_m of -17.3°C and the 18:2-18:2 PC has a T_m of -57.0°C, were all insaturations are *cis*. The position and the *cis*-*trans* nature of the insaturation also has an important effect on the transition temperature (*cf.* table 1.6).

To distinguish between the different types of unsaturated phospholipids, the nomenclature commonly used is to write the lipid tail as $n:m \times \Delta p$, where n is the number of carbons in the chain, m the number of insaturations, x the type of isomer (*c* for *cis*

Structure	Type	T_m (°C)
18:1-18:1 PC	<i>c</i> Δ3	35
	<i>c</i> Δ9	-17.3
	<i>t</i> Δ9	12.0
	<i>c</i> Δ15	24
24:1-24:1 PC	<i>c</i> Δ5	59.0
	<i>c</i> Δ9	34.0
	<i>c</i> Δ15	26.7

Table 1.6: List of different monoenoic unsaturated phospholipids, sorted by chain-length, insaturation position and cis/trans type. In the case of the 18:1-18:1 PC, the *c*Δ9 is the most common lipid used for the assembly of lipid model systems. Transition temperatures are taken from the Handbook of lipid bilayers [22].

and t for trans), and p the position of the insaturation(s), starting from the carboxylic carbon. As an example, the most common commercial DOPC used to prepare lipid bilayer is the 18:1 *c*Δ9 - 18:1 *c*Δ9 PC, with the transition temperature of -17.3°C already cited above. Its trans isomer 18:1 *t*Δ9 - 18:1 *t*Δ9 PC, and its position isomers 18:1 *c*Δ3 - 18:1 *c*Δ3 PC and 18:1 *c*Δ15 - 18:1 *c*Δ15 PC all have a higher T_m of respectively 35, 12.0 and 24°C.

Meanwhile, the nature of the headgroup has a smaller effect on T_m, in comparison to the effects of the chainlength and the presence, type and location of insaturations. DOPE and DOPG have a transition temperature of respectively -8 and -21.5°C. All these observations are illustrated in figure 1.10.

B-2.c Lipid mixture and phase separation

Membranes made of mixtures of lipids display complex behaviours. Lipids are affected by their interactions with other types of lipids. As a consequence, the phase transition temperatures of a mixture of lipids will define domains in which different phases coexist in the membrane. For a two components mixture, the phase transition temperatures depend on the ratio between the two lipids. For example, while pure DPPC has a gel-phase transition temperature of 41.4°C, a mixture of DPPC/DOPC at a molar ratio of 4:6 will display a coexistence between liquid and gel phases at room temperature. These domains of coexistence are illustrated in phase diagrams, such as the one given in figure 1.11.

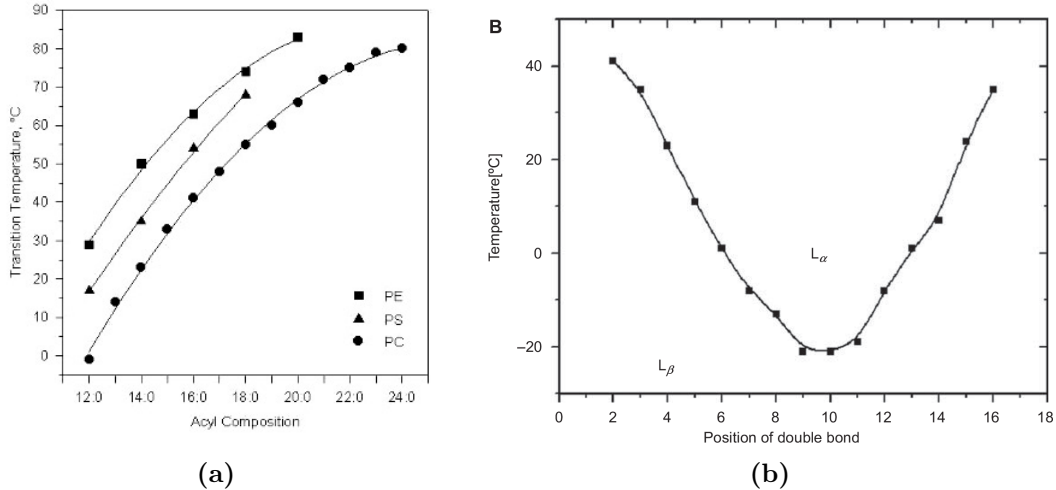


Figure 1.10: (a) Influence of the chain length and head group on the gel-liquid phase transition temperature. Values are taken from Avanti Polar Lipids' website [23]. (b) Influence of the position of the insaturation in the lipid tail on the gel-liquid phase transition temperature. The data are taken from the review by Koynova and Tenchov [24].

Cholesterol, a well-known lipid from the sterol lipid category shown in figure 1.12 a, is known to fluidify the lipid mixture to which it is added. As a result, a new phase can be observed, called the ordered liquid phase (L_o) in opposition to the disordered liquid phase L_α found with phospholipids (*cf.* figure 1.12 b). In domains of coexistence, the ordered and the disordered liquid phase are immiscible, but gain their name of liquid phase as their large lateral diffusion coefficients have the order of magnitude of a liquid phase [26]. The difference of orders between the two phases come historically from the observation that alkyl chains in the L_o phase are all-trans conformally ordered, while the chains of the L_α phase remains conformationally disordered [27].

Of course, it is also possible to form ternary mixture of phospholipids, either with phospholipids only or by adding cholesterol as well. Analyzing such systems is not trivial, and the phase diagrams of these mixtures will mostly be realised for a given temperature (*cf.* figure 1.13 a). The evolution with temperature of ternary mixtures can be predicted through thermodynamic models. For this purpose, a 3D representation of the phase diagrams have been suggested by Wolff *et al.* [29], as given in figure 1.13 b.

The phase coexistence discussed above can be observed macroscopically with a great accuracy, using optical microscopy. In the case of coexistence, the different types of lipids will tend to separate from each others and will accumulate in areas where only

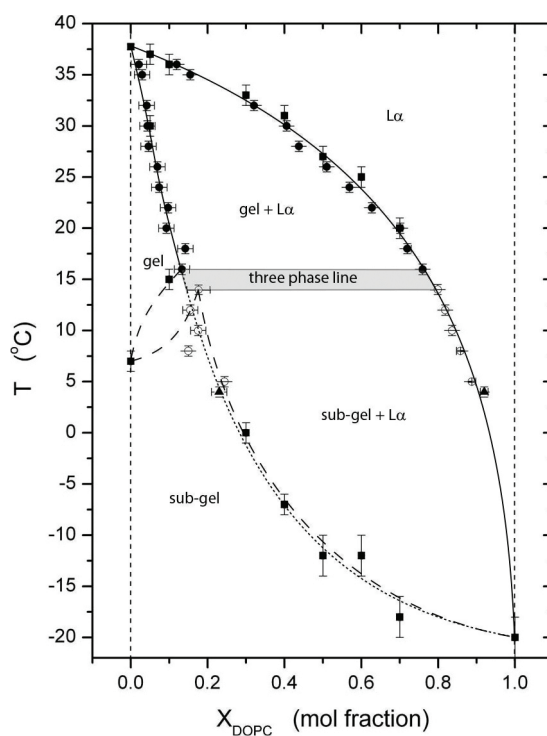


Figure 1.11: Phase diagram of a binary mixture of DOPC/DPPE, highlighting the different phases in which a mixture of lipid can undergo. The subgel phase presented here is a transitional phase between the crystal and gel phase, in which the lipids are extremely ordered but does not arrange in a crystal lattice. The figure is taken from the publication by Schmidt *et al.* [25].

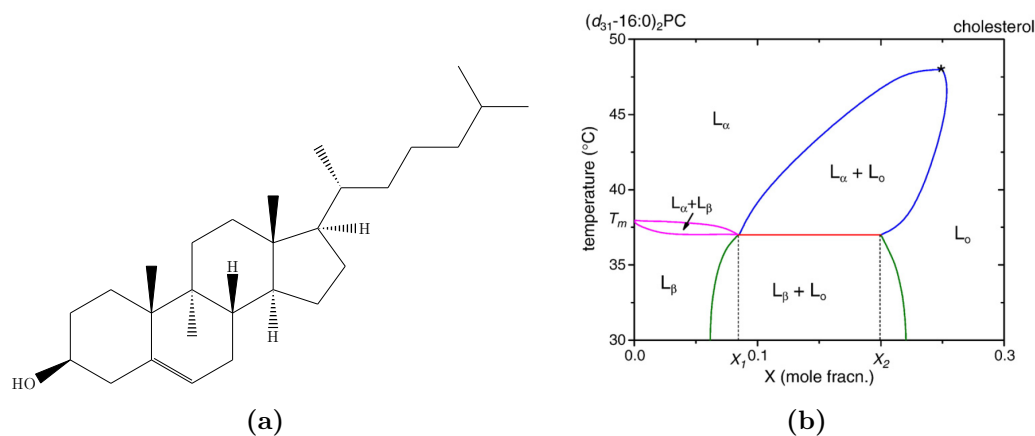


Figure 1.12: (a) Skeletal formula of the cholesterol. (b) Phase diagram of the binary mixture DPPC/Cholesterol as a function of the temperature of the system. The diagram is taken from Marsh [28].

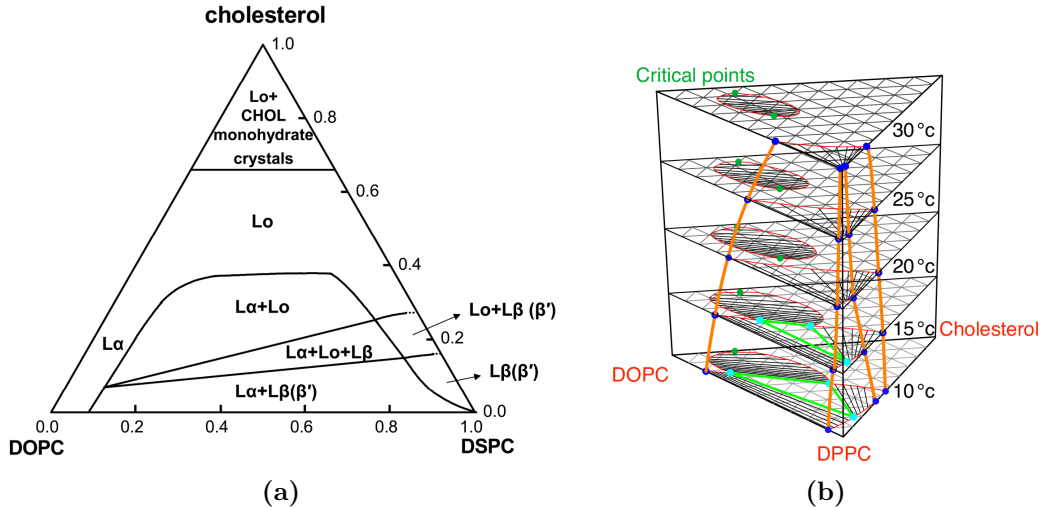


Figure 1.13: (a) Phase diagram of the ternary mixture of DOPC/DSPC/Cholesterol at 23°C, taken from the publication by Zhao *et al.* [30]. (b) 3D representation of a thermodynamic calculation for a temperature dependent phase diagram for a ternary mixture of DOPC/DPPC/Cholesterol, as suggested by Wolff *et al.* [29].

one type of phase exists, hence producing a phase separation (*cf.* figure 1.14).

B-3 Elasticity of a bilayer

Section B-1 described the different kinds of motion of a lipid in a bilayer. As the membrane is a supramolecular construction in a fluid state, the collective displacement of groups of lipids also has to be considered.

Three types of collective lipid rearrangements can be considered in a lipid bilayer (*cf.* figure 1.15): the parallel displacements of two adjacent groups of lipids in opposite directions (shear), the drifting of molecules away from each other (stretch), and the movement of a group of lipid out of the plane of the bilayer (bend).

In a fluid lipid bilayer, the contribution of the shear stress can be neglected. Therefore, this section only discusses bending and stretching stresses.

B-3.a Surface tension

A cohesion exists between the lipids of a bilayer. As a result, if the membrane is stretched by a surface difference dA , the bilayer can be considered as a spring with a force that will try to bring the bilayer membrane back to its relaxed configuration. This force is proportional to the surface tension of the bilayer γ . The energy required to deform the bilayer by stretching it by a surface element dA is

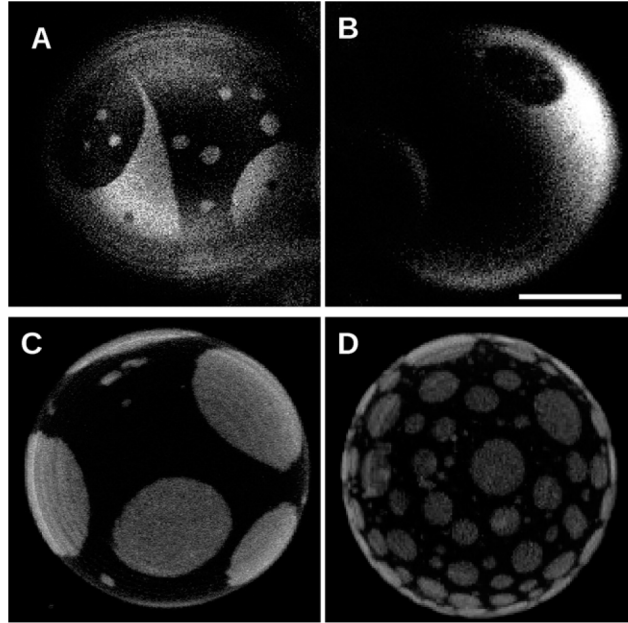


Figure 1.14: Confocal microscope images of vesicles made with different lipid mixtures: (a) Sphingomyelin/DOPC/Cholesterol at a molar fraction of 1:1:1, (b) lipids extracted from brush border membranes from rat kidney cells, (c) DOPC/DPPC/Cholesterol at a molar fraction of 1:1:1, and (d) native porcine pulmonary surfactant. The pictures illustrate different geometries of phase separations, where only one type of lipid is fluorescently labeled. The scale bar corresponds to 15 μm . Adapted from Bagatolli *et al.* [31].

$$dE_e = \gamma dA. \quad (1.2)$$

If the bilayer is stretched too much, interactions between the phospholipids will no longer be strong enough to maintain the cohesion of the membrane. The strength required to destroy the membrane under these conditions corresponds to a surface tension of a few mN/m [32], called the lysis tension, and a deformation of the surface of a few percent only. The surface tension of a DSPC bilayer, for instance is about 1 mN/m [33].

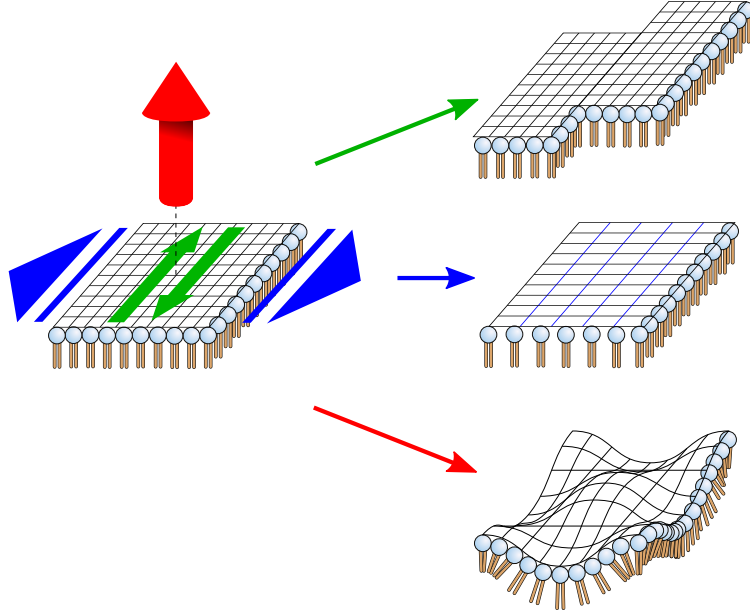


Figure 1.15: Representations of the different possible deformations of a membrane. From top to bottom, the displacement of two adjacent groups of lipids (shearing), the expansion of the bilayer in its own plane (stretching), and the fluctuations of the membrane out of its plane (bending).

B-3.b Bending modulus

Due to thermal fluctuations, the lipid membrane can not be considered as a flat construction. The fluid membrane will rather be found as an oscillating surface, as illustrated in figure 1.15.

To describe these fluctuations, Helfrich suggested a model defining the curvature energy of the membrane [34]. The model, given in equation 1.3, links the energy dE_c required to deform the membrane per surface unit dA to the main curvature radii R_1 and R_2 , to the spontaneous radius of curvature R_0 and to κ and $\bar{\kappa}$, which correspond respectively to the bending moduli of the mean curvature and of the Gaussian curvature:

$$dE_c = \left(\frac{1}{2} \kappa \left(H - \frac{2}{R_0} \right)^2 + \bar{\kappa} G \right) dA. \quad (1.3)$$

In this equation, H corresponds to the mean curvature such as $H = \frac{1}{R_1} + \frac{1}{R_2}$, and G corresponds to the Gaussian curvature $G = \frac{1}{R_1 R_2}$.

In the case of symmetric lipid bilayer, the spontaneous curvatures of each leaflets compensate each other. Therefore, there is no spontaneous curvature R_0 of the bilayer, and equation 1.3 can be rewritten as

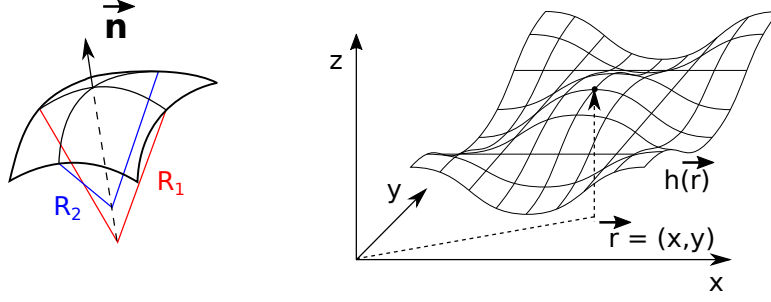


Figure 1.16: Illustration of the membrane curvature. (Left) Representation of the local curvature radii R_1 and R_2 of the membrane, and (Right) the Monge representation of an oscillating membrane.

$$dE_c = \left(\frac{1}{2} \kappa H^2 + \bar{\kappa} G \right) dA. \quad (1.4)$$

The bending moduli κ and $\bar{\kappa}$ in equation 1.4 can be seen as the bending moduli of the thermal fluctuations and of the bilayer topology respectively, as the Gauss-Bonnet theorem states that the integrals of GdS over the whole vesicle is a constant depending on the topology of the closed shape. κ is strongly correlated to the phase of the lipid membrane. A bilayer in the gel phase will have a κ of *circa* 200-400 $k_B T$, while a fluid phase bilayer has a κ of about 10 $k_B T$ [6].

B-3.c Curvature of a lipid membrane

Adding a small quantity of a liquid in a solvent in which it is immiscible with will form a droplet. The difference of pressure δP between the inner liquid of the droplet and the outer one is given by the Laplace law as a function of the radius of the droplet, such as:

$$\delta P = \frac{2\gamma}{R}. \quad (1.5)$$

In the case of a vesicle, the mean radius depends also on the bending modulus of the lipid membrane. Zhong-can *et al.* suggested in 1989 a correction of the Laplace law to describe the shape of the vesicle as a function of the difference of pressure [35], giving

$$\delta P = \gamma H - 2\kappa H \left(\frac{1}{4} H^2 - G \right) - \kappa \nabla^2 H. \quad (1.6)$$

This corrected equation is of importance in order to describe the budding effects one can see on vesicles displaying a phase separation, as illustrated in figure 1.14 (c).

Indeed, in the case of a coexistence of a gel and a liquid phase in the bilayer of a vesicle, the bending moduli of the two regions will have a ten fold difference. As the difference of pressure δP does not differ from one region to the other, the curvatures H and G will be different for the two regions as well, hence the buddings on the surface of the vesicle.

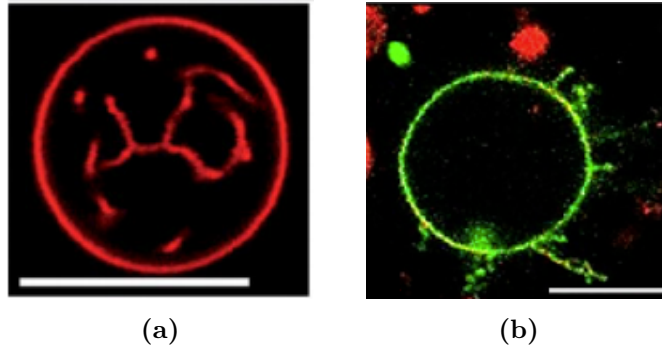


Figure 1.17: Confocal pictures of lipid tubes connected to a GUV. (a) Pictures of inner tubes, located inside the vesicle. Scale bar corresponds to $15 \mu\text{m}$; picture is adapted from [36]. (b) Pictures of outer tubes formed from a GUV, decorating the surface of the vesicle. Scale bar is $10 \mu\text{m}$; picture adapted from [37]

Equation 1.6 describes also the formation of lipid tubes in vesicles, as one can observe experimentally (*cf.* figure 1.17). When δP is too high, the vesicle will extract lipids from its membrane and form tubes of lipids. These tubes are still connected to the vesicles and work as reservoirs of materials. Stability of tubes can be explained by the compensation of the negative bending term and the positive surface tension. Under this condition, the difference of pressure is equal to 0. The tubes, which are hollow cylinders, only have one curvature $1/R_1$, hence $H = 1/R_1$ and $G = 0$. One can therefore rewrite equation 1.6 as

$$\gamma - \frac{2}{4}\kappa H^2 = 0, \quad (1.7)$$

which leads to the expression of the radius of the tube R_1

$$R_1 = \sqrt{\frac{\kappa}{2\gamma}}. \quad (1.8)$$

A more comprehensive discussion on the structural properties of the lipid tubes can be found in [38].

B-4 Membrane permeation

The cell membrane creates a separation between the cell and the external medium. But this separation does not prevent all translocation of material through it. As a matter of fact, it controls and regulates the molecules penetrating or leaving the cell through a wide range of biosensors and protein channels, but also through physical processes.

This section describes briefly the different physical properties of the membrane which enable and control the translocation of molecules.

B-4.a Permeability

Some molecules are able to pass through the membrane without any active process of internalisation. This passive diffusion is the result of the permeability of the membrane.

We consider a lipid membrane with two bulk concentrations of solute on each side of the membrane C_1 and C_2 . If the membrane is not permeable to the solute, the concentrations of solute on the membrane on both sides $C_{m,1}$ and $C_{m,2}$ are equal to their respective bulk concentrations. The convection of the solute from the bulk to the membrane is given by the coefficients of diffusion of the solute in the solvents D_1 and D_2 , as illustrated in figure 1.18.

In the case where the membrane is permeable to the solute, one will find a gradient of concentration $\frac{\partial C}{\partial x}$ in between each side of the membrane [39]. In the steady state case of permeation across the membrane, the gradient can be considered as linear, and so the flux is constant through the membrane, which allows one to express the permeability of the membrane to the solute P_m as

$$J = P_m(C_{m,1} - C_{m,2}). \quad (1.9)$$

The permeability coefficient P_m is characterized by the coefficient of diffusion of the molecule in the membrane D , by the thickness of the bilayer l_{memb} , and by a partition coefficient B , a dimensionless quantity defining the number of solute molecules dissolved in the membrane. P_m is therefore given by

$$P_m = \frac{BD}{l_{\text{memb}}}. \quad (1.10)$$

In the same way as with the coefficient of diffusion, the permeability of the membrane to the solute depends on the nature of the solute. In the case of lipid membranes,

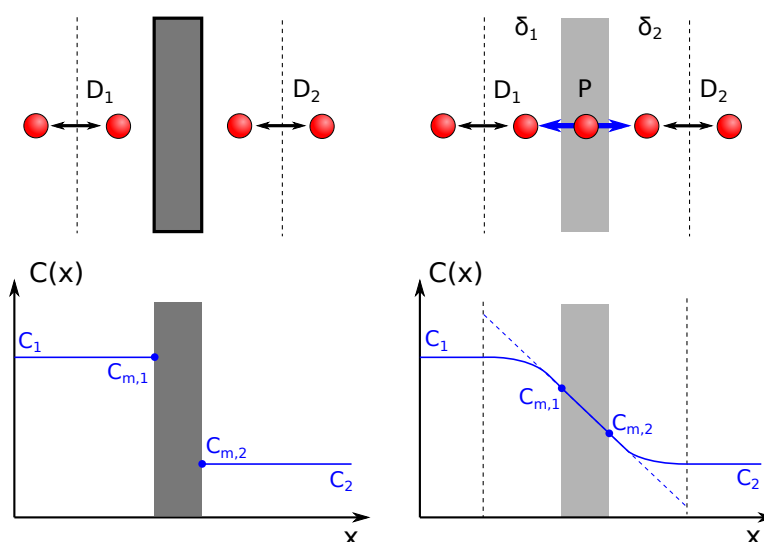


Figure 1.18: Representation of the evolution of the concentration along the axis perpendicular to the membrane, in the case of a non permeable membrane (left), and in the case of a permeable membrane. In the case of permeation, one can see a gradient of concentration of solute in the vicinity of the membrane. This gradient is only significant at a distance inferior to a distance δ linked to the coefficient of diffusion of the solute in the solvent D .

the order of magnitude of the constant of permeability is strongly related to the nature of the molecule (*cf.* figure 1.19). For example, hydrophobic molecules such as dissolved gases are diffusing much faster through the membrane than polar molecules or ions.

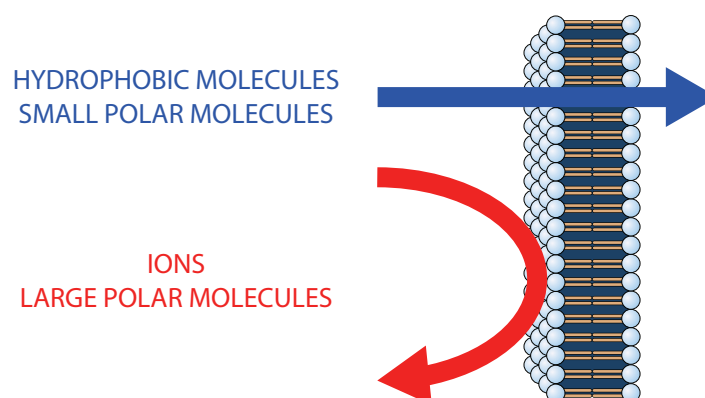


Figure 1.19: Representation of the different levels of permeability of the membrane. Hydrophobic molecules (O_2 , steroids, *etc.*) and small uncharged polar molecules (water, glycerol, *etc.*) are able to pass through the membrane by passive diffusion, while ions and large uncharged polar molecules (saccharides, *etc.*) are not able to.

Molecules with small permeability are said to be unable to go through the bilayer.

For example, ions have an order of magnitude of constant of permeation at about 10^{-16} m/s, which corresponds to the diffusion of one ion every 10^9 seconds in a phospholipid vesicle of $10\ \mu\text{m}$ of radius [40]. The permeability of different molecules is given in table 1.7.

Molecule	P_m (m/s)	Ref.
Hydrophobic molecules		
O ₂	2.3×10^{-1}	[41]
CO ₂	3.5×10^{-3}	[42]
Steroids	10^{-5} to 10^{-6}	[43]
Polar molecules		
H ₂ O	3.4×10^{-5}	[44]
Glycerol	5.4×10^{-8}	[45]
Sucrose	1×10^{-12}	[46]
Ions		
Na ⁺	5.0×10^{-16}	[40]
K ⁺	4.7×10^{-16}	[40]

Table 1.7: List of the constants of permeability P_m of different molecules through artificial membranes. Ions are unlikely to diffuse through the membrane as compared to the other types of molecules, hence the fact that the lipid membrane is considered as non permeable to ions. Values are taken from the review on permeation by Yang *et al.* [47]

B-4.b Osmotic pressure

The previous section stated that the lipid membrane is permeable to the water molecules surrounding it, but not to the solute. As a consequence, the membrane is sensitive to the osmotic pressure.

The osmotic pressure is an effect of the osmosis: if two solutions with a solute of different concentrations are separated by a semi-permeable membrane (such as the one from a cell), the solvent will move through the membrane and equalize the concentrations (*cf.* figure 1.20).

Osmosis (*ósmós*, push) was described first in the 18th century and the name was suggested by Graham in 1854 [48]. To explain the migration of the solvent from one

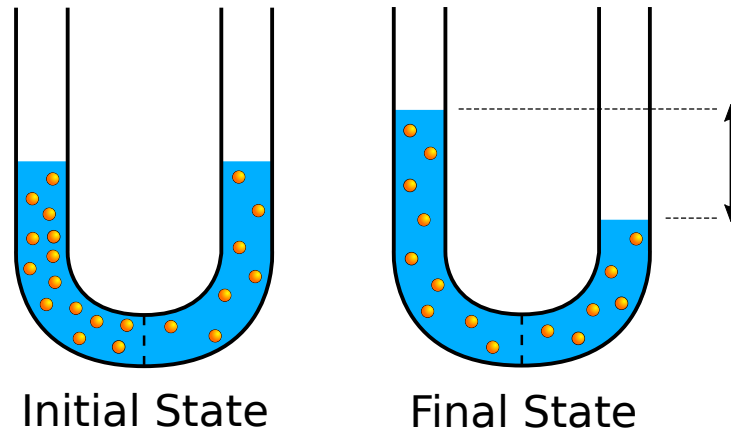


Figure 1.20: Illustration of the U-shaped tube experiment to highlight the existence of osmotic pressure. A U-shaped tube, separated in two halves by a semi-permeable membrane, is filled with water. Due to the atmospheric pressure, the level of the water will be the same in both sides of the tube. A solute is added in each part of the tube, but at different concentrations. The osmosis phenomenon will force water to move to the more concentrated side of the tube, hence highering the water level despite the atmospheric pressure. The pressure compensating the atmospheric pressure is called the osmotic pressure.

side of the membrane to the other, the concept of osmotic pressure was suggested. The first derivation of a relation on the osmotic pressure was made by J. H. van't Hoff in 1887 [49]. Van't Hoff saw the similarities between the osmosis and the pressure from a gas, and adapted the laws from Boyle and from Gay-Lussac for gases to apply them in the case of the osmotic pressure,

$$\Pi = cRT, \quad (1.11)$$

where c is the molar concentration of solute in the solution, R the gas constant, and T the temperature. A correction of this equation was proposed by Morse and Frazer [50]. Morse and Frazer suggested that the molality of the solute should be used instead of the molar concentration. When working with ionic solutions, molarity and molality are no longer relevant, as the ions dissociate in the solvent and therefore increase the number of particles of the solute as compared to the non-dissolved state. The molar concentration of equation 1.11 is therefore replaced by the osmolarity of the solute ω , such as

$$\Pi = \omega RT. \quad (1.12)$$

Following this equation, if two solutions of osmolarities ω_1 and ω_2 are separated by a lipid bilayer such as $\omega_1 < \omega_2$, then equation 1.12 states that $\Pi_1 < \Pi_2$.

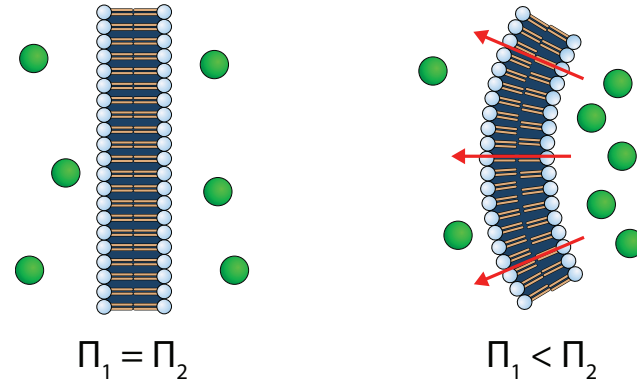


Figure 1.21: Representation of the effects of the osmotic pressure on a lipid bilayer. If the concentrations on both side of the membrane are equal, no pressure forces will be applied on the bilayer. If the concentration rises on one side of the bilayer as compared to the other, pressure forces will be applied on the membrane and water will move to decrease the concentration.

In the case of a vesicle filled with a solution of osmolarity ω_{in} and immersed in a solution of osmolarity ω_{ex} , the difference of pressure between the two sides of the membrane $\delta\Pi = \Pi_{in} - \Pi_{ex}$ will have a direct influence on the shape of the vesicle, as described by equation 1.6 (*cf.* figure 1.22). If both concentrations are the same, $\delta\Pi = 0$ and all the description of the membrane fluctuations given in section B-3.b are relevant. If $\delta\Pi > 0$, the vesicle will be stretched and the membrane will be tight. If the membrane is much stretched, its fluctuations will be reduced significantly. In the case where $\delta\Pi < 0$, the forces applied on the vesicle will tend to make it shrink. An excess surface will result enhancing its fluctuations. If the vesicle shrinks too much, tubes of lipids can form and fill the vesicle, in order to reduce its volume.

The overall shape of the vesicle is driven by the reduced volume of the vesicle ΔV , corresponding to the ratio between the volume of the vesicle and the volume of a vesicle with the same area A , and by the reduced area of the membrane ΔA , which is given by the difference in surface between the inner and outer leaflet of the bilayer [51]. Equations of ΔV and ΔA are

$$\Delta V = \frac{V}{\frac{4}{3}\pi R^3}, \quad (1.13)$$

and

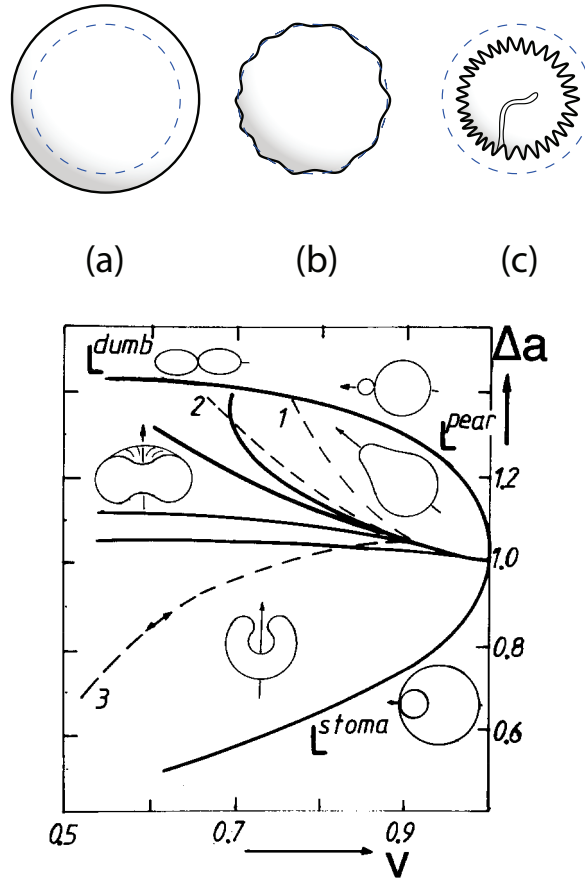


Figure 1.22: Representation of the different vesicle shapes. (Top) Deformations induced by the difference of osmotic pressure inside and outside of the vesicle, for a reduced area $\Delta A = 1$. If both pressures are equal (b), the bilayer will undulate slightly, due to the thermal fluctuations described in section B-3.b. If the osmotic pressure is higher inside the vesicle (a), the membrane will be stretched and fluctuations will be significantly reduced. If the pressure inside is lower than outside, the vesicle will be compressed, and an excess surface will result, as the volume is conserved. Tubes of lipids can form in this configuration, in order to reduce the vesicle membrane excess area. (Bottom) Diagram of the different possible shapes for vesicles, given as the reduced volume ΔV as function of ΔA . The diagram is taken from Sackmann [51].

$$\Delta A = \frac{A_{ex} - A_{in}}{8\pi R d_m}, \quad (1.14)$$

where d_m is the thickness of the membrane. The shapes (a), (b) and (c) of the vesicles as a function of the osmotic pressure in figure 1.22 are given for $\Delta A = 1$ in the shape diagram (*cf.* figure 1.22).

B-4.c Formation of pores

In certain conditions, pores can form in the lipid membrane. Aside from the channels formed by the proteins of the cell membrane, which are specific to a certain range of molecules, an open pore in a lipid membrane will let pass any molecules big enough to fit through it, as illustrated in figure 1.23. Many ways exist to force the creation of pores in the lipid membrane. Only some of these ways will be briefly discussed here.

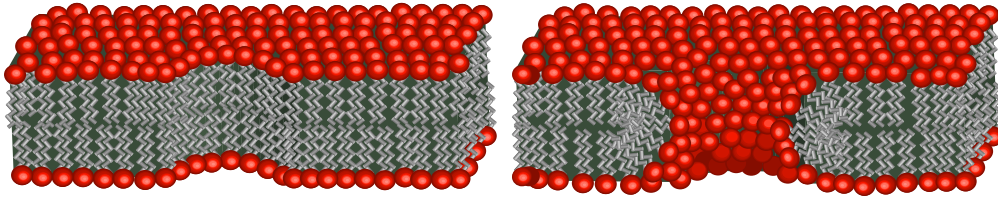


Figure 1.23: Illustration of pores in a lipid membrane. The illustrations represent two geometries of pores: (left) a hydrophobic pore, where the hydrophobic tails of the lipids are in contact with the solvent from the pore, and (right) a hydrophilic pore, where the lipid membrane bends to cover the tails with the hydrophilic heads in the pore. *Illustration source: Wikipedia.*

The osmotic pressure introduced in the previous section can generate a stress on the membrane important enough to force the formation of a pore. When the difference of osmotic pressures between each side of the membrane of a vesicle $\delta\Pi$ is different from 0, osmosis will generate a flux of water through the membrane to regulate the pressure. As a matter of fact, a vesicle is only capable of a small amount of swelling. If $\delta\Pi \gg 0$, the stress applied on the membrane of the vesicle might be significant enough to burst the vesicle. To prevent this, pores will form in the membrane to relieve the tension, as illustrated in figure 1.24. The solutes escape through the pores and lower $\delta\Pi$ until both concentration are balanced enough [52]. In certain conditions, such as when the pore is too big compared to the size of the vesicle, the pore will not be able to close back, and the GUV will burst.

Neumann and Rosenheck demonstrated in 1972 that it was possible to induce pore formation on a cell membrane by applying an electric field on the cell [53]. This method to generate pores, called electroporation, has been widely used to translocate materials through the membrane of the cell, in gene therapy or for the treatment of cancers [54]. Also, Bernard *et al.* have shown that the forced adhesion of vesicles on a decorated surface can generate transient macroscopic pores in the lipid membrane [55].

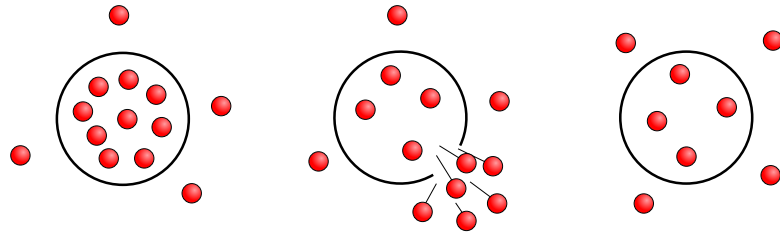


Figure 1.24: Illustration of pores in a lipid membrane. The tension induced by the high osmotic pressure inside the vesicle (left) forces the vesicle to open a pore through which the solute escapes (middle). The osmotic pressure inside and outside the vesicle are then equilibrated (right).

C Interactions of macromolecules with the membrane

As described previously, the cell membranes are the boundary of the living cells and of their different organelles. Many interactions occur at this boundary, either on the external leaflet, which is decorated with various macromolecules, or on the inner leaflet which interacts with the cytoskeleton, a dynamic macromolecular network. All the different interactions between macromolecules and the lipids from the bilayer drastically change the properties of the membrane, either structurally or mechanically.

C-1 Polymers and cell membrane

Many types of macromolecules can interact with the cell membranes. In particular, polymers (from the Greek *polus* many, and *meros* parts) are repetitions of monomeric units, either linear, branched or dendritic, connected by covalent bonds. Polymers can be homopolymers, which are repetitions of a single monomer, or copolymers made of two or more monomeric units. If the different monomeric units are only located in different sequences of the polymer chains, the macromolecule is named a block copolymer.

We describe in this section the different interactions between macromolecules and the membrane and their configurations through the interactions of the polymers with the lipid membrane.

The interactions between polymers and membranes depend on both polymer and lipid bilayer chemical structures and charge properties. As a matter of facts, all the interactions can be sorted into four categories of interactions [56]

- In the case where the polymer presents hydrophobic moieties, one can observe hydrophobic interactions [57]. The hydrophobic parts of the polymer are able to penetrate the membrane and interact with the lipid tails by forming stable anchoring.
- Multivalent ions or complexing agents can mediate the interactions between the polymers and the lipid membrane [58]. In these cases, the polymer will be crosslinked to the membrane.
- As shown in the previous sections, a lipid membrane can be made of zwitterionic lipids (PC, PE) and negatively charged lipids (PS, PG, *etc.*). Coulombic interactions can therefore occur between the lipids from the membrane and charged polymers, also called polyelectrolytes [59].
- Hydrogen bonding interactions can occur between the bilayer and the polymer, but these interactions display a weak strength as compared to the other types of interactions [60].

C-2 Configurations of lipid-polymer interactions

C-2.a The different configurations

The interactions of a polymer or any macromolecule with the lipid membrane, as the two are attracted to each other, can happen in three different configurations listed below. All of these configurations are illustrated in figure 1.25.

- The molecule can adsorb on the membrane, either on the inner or outer leaflet. In the case of a polymer chain, one can observe various possible conformations for the adsorption: the whole chain can be adsorbed on the surface, the polymer remaining flat. One can also observe cases where only certain portions of the polymer will be adsorbed on the surface, while the rest of the macromolecule will form loops out of the surface. In the last case, only limited sections of the chain will be adsorbed, while the rest will be freely moving in the aqueous solution.
- The molecule can be embedded inside the membrane, inside its hydrophobic part. This can happen if the polymer, or only some part or functions of it, are hydrophobic and will join the membrane to hide from the aqueous solution. If the whole macromolecule is hydrophobic it might be fully embedded in the membrane. But if only parts of it are hydrophobic, then one will rather find

an anchored polymer, where only the hydrophobic parts are embedded in the membrane while the rest of the molecule remains in the aqueous solvent.

- The molecule can attach chemically to the membrane. In this case, the polymer can be grafted covalently to a molecule from the membrane, such as a lipid, or via a spacer. In this last case, the polymer does not affect so much the mechanical properties of the membrane (spontaneous curvature, bending rigidity, *etc.*) compared to the adsorbed or embedded molecules.

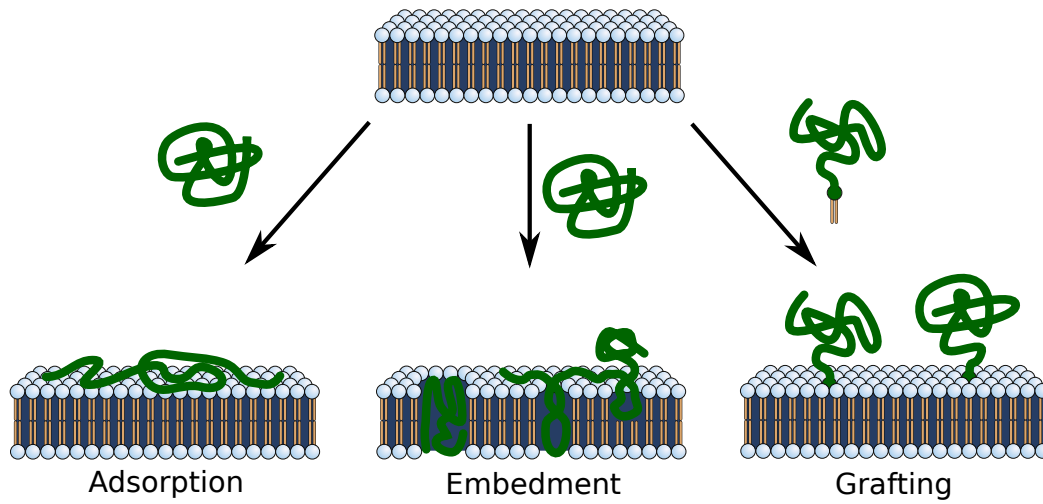


Figure 1.25: Representation of the different configurations for the membrane-polymer interactions. A macromolecule can adsorb on the surface, or can be embedded into it. The embedding can be either full, or just partial with only small fractions of the polymer inside the membrane. For the latter, one can also talk about anchoring of the macromolecule. If the molecule is chemically bonded onto a amphiphilic molecule, the macromolecule will form a grafted polymer layer.

The interactions between the membrane and a macromolecule might lead to several changes in the membrane behaviour. Mechanical properties might be affected, but one can also observe changes in the dynamical behaviour of the membrane. Indeed, the macromolecules interacting with the membrane can induce the formation of lipid patterns [61], or change the lateral and transverse diffusions of the lipids in the membrane [62][63].

C-2.b Mechanisms of adsorption

In the system of interest for our work, the adsorption of the polymer on the membrane of the cell is the only configuration relevant. Therefore we will only describe this aspect of the lipid-polymer interactions further.

As described above, the adsorption is the attachment of a particle (adsorbate) to a surface (adsorbent, substrate). When the particle detach from it, the phenomenon is called desorption. Most of the historical investigations on the adsorption have been conducted on the adsorption of gas molecules on solid structures, such as the zeolites [64]. While our work only focus of the adsorption of suspended molecules in an aqueous solution on a fluid lipid membrane, all the descriptions and concepts used to describe the adsorption of gas are relevant for our model.

The adsorption and desorption of particles on a surface are processes driven by the thermodynamics [65]. Therefore, there is an equilibrium between the number of particles adsorbed on the surface of a membrane and the number of free particles in the vicinity of the surface, available for adsorption. One can therefore write the relation



The rate constants of these processes are given as k_a for adsorption and k_d for desorption. This define the equilibrium constant of the adsorption K , such as

$$K = \frac{k_a}{k_d}. \quad (1.16)$$

In general one can observe two configurations for the adsorbate on the surface. The adsorption will either be as a coverage of a single monolayer, in the case where the adsorbate cannot adsorb on itself, and the coverage by multilayers of adsorbate, as shown in figure 1.26.

For macromolecules such as polymers or polypeptides, the adsorption will be strongly influenced by the configuration of the chains on the lipid membrane. The configuration of the chains of a polymer on the membrane can be studied by various techniques, such as solide state NMR [66] or methods based on fluorescence [67].

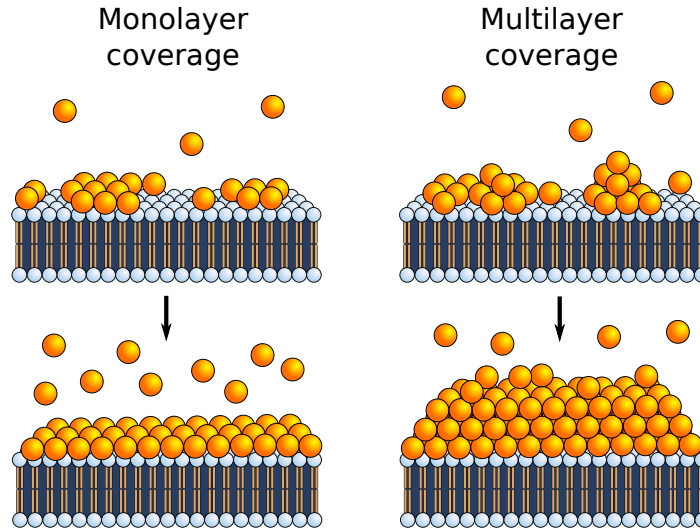


Figure 1.26: Representation of the monolayer and the multilayer coverages of an adsorbate on a lipid membrane. Illustrations on top show the coverage during the growth of the layers, while illustrations on top show a complete monolayer at saturation (left) and a multilayer still growing (right).

C-2.c Adsorption isotherms

The adsorption of molecules on a surface have been mathematically described in various models. We only describe here two models which are relevant in our work: the Langmuir isotherm and the Brunauer-Emmett-Teller isotherm.

The adsorption of molecules on a surface has been described by Langmuir in 1918 [64]. He developed a model to describe the adsorption of a single monolayer of gases molecules on a metal surface, where the adsorption is driven by the partial pressure of the gas p , such as

$$\theta = \frac{Kp}{1 + Kp}. \quad (1.17)$$

In this equation, called the Langmuir isotherm, the surface coverage θ is defined as the fraction of adsorbed molecules σ over the total number of sites which can be occupied by the molecules on the surface σ_m , such as $\theta = \frac{\sigma}{\sigma_m}$. K represents the equilibrium constant of adsorption of the gas on the surface given by equation 1.16.

The Langmuir isotherm can be easily used to express the adsorption of molecules in liquid phase [68]. For this purpose, one has to rewrite equation 1.17 by replacing the partial pressure p by the concentration of the adsorbate C , therefore

$$\theta = \frac{KC}{1 + KC}. \quad (1.18)$$

To perform experimental data fitting with the Langmuir isotherm in the most accurate way, one can rewrite equation 1.18 in a linear form, such as

$$\frac{C}{\sigma} = \frac{C}{\sigma_m} + \frac{1}{K\sigma_m}. \quad (1.19)$$

Here, by expressing experimental data as C/σ , one will obtain a straight line with a slope equals to $1/\sigma_m$ and an intercept equals to $1/K\sigma_m$.

The Langmuir isotherm introduced above only describes the case of the adsorption of one single monolayer of molecules on a substrate. This model implies that the molecules can not interact nor adsorb on themselves.

The Brunauer–Emmett–Teller (BET) theory developed by Brunauer *et al.* in 1938 describes the adsorption of multimolecular layers of gases on a surface [69]. The BET isotherm from their theory is given by

$$\theta = \frac{cz}{(1-z)(1-c+cz)}. \quad (1.20)$$

In this model, the surface coverage θ is given as the ratio between the number of molecules adsorbed on the surface and the maximum number of molecules one can adsorb in one single monolayer. With this definition, one can find $\theta > 1$. In the BET isotherm, the partial pressure p of the adsorbate is not directly used, but instead one will use z , the ratio between the partial pressure p and the partial pressure at saturation p^* , such as $z = p/p^*$.

Moreover, in the BET theory, c is a parameter used to fit the function. It can be physically defined as

$$c = \frac{K}{K_L}, \quad (1.21)$$

with K the equilibrium constant of adsorption of the first layer, as previously defined by the Langmuir isotherm, and the adsorption equilibrium constant of upper layer K_L .

Nonetheless, applying the BET theory to the liquid phase adsorption is less trivial than for the Langmuir isotherm. Indeed, while p can be simply replaced by the concentration of the adsorbate in solution C , p^* can not find any corresponding concept in the liquid phase adsorption situation. A correction of the BET isotherm can be found in the work by Ebadi *et al.* [70]. They suggested that z should be expressed as a function of K_L , such as $z = K_L C$. The correct equation is therefore

$$\theta = \frac{\sigma}{\sigma_m} = \frac{KC}{(1-K_L C)(1-K_L C + KC)}. \quad (1.22)$$

One can observe that this equation is equal to the Langmuir isotherm given in 1.18 for $K_L = 0$. Figure 1.27 shows the differences in the evolution of both models over the concentration of molecules in the solution.

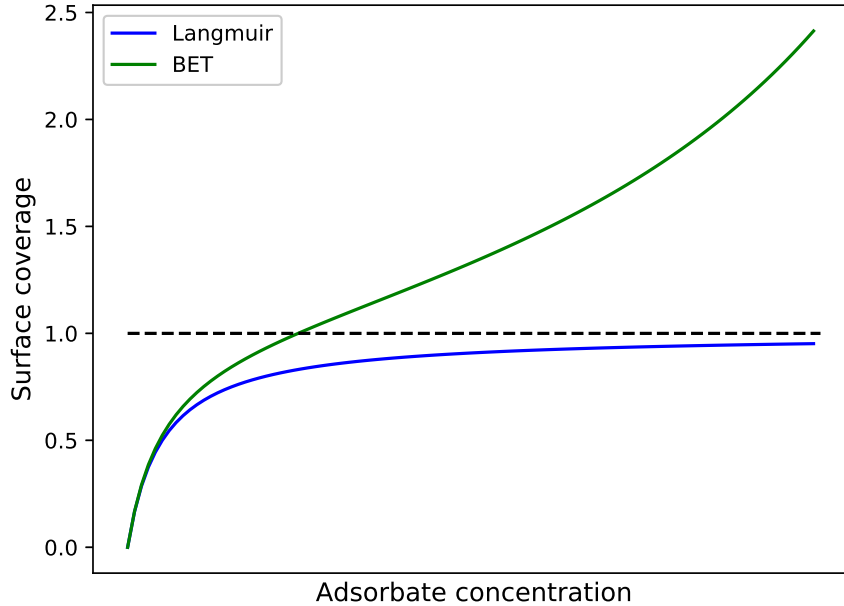


Figure 1.27: Comparison between the Langmuir and the BET isotherms, respectively describing the adsorption of a single monolayer and the adsorption of a multi layer system. While the Langmuir isotherm converges toward 1 (surface covered by one monolayer), the BET can exceed 1 as more molecules adsorb on upper layers. On this graphical representation, K_L is set to 3% of the value of K .

Similarly to the Langmuir isotherm, the BET isotherm can be rewritten as a linear model, such as

$$\frac{K_L C}{\sigma(1 - K_L C)} = \frac{K_L}{\sigma_m K} + \frac{K_L \left(1 - \frac{K_L}{K}\right)}{\sigma_m} C. \quad (1.23)$$

D Model systems to mimic the cell membrane

250 different lipids can be found in a single cell membrane. Understanding the role of each type of lipid in such a complex system is beyond what is presently possible. Model lipid membranes, where only one or a few lipid species are present, are thus the natural systems of choice to mimic cell membranes.

D-1 The concept of a model membrane

A model membrane is an artificial construction which mimics the biological cell membrane. The concept is to produce a simplified lipid bilayer, with a reduced number of parameters to better understand the structure and the properties of the cell membrane. In this case, the composition of the membrane can be controlled in an experiment. Different geometries can be reached with model membranes, such as spheres or flat bilayers, providing an important choice to the scientists. This section presents some of the most common shapes used in the different research fields involved in the study of lipid membranes.

D-2 Vesicles

Following the work by Bangham *et al.* [71], vesicles - or liposomes - are one of the major model systems used to investigate the properties of lipid membranes. By their spherical shape and the existence of an internal compartment able to hold materials, vesicles are the closest artificial model structure to the cell one can get. They are also extensively used because the methods for preparing liposomes are easy to implement and can be readily adapted to different compositions and goals of study.

D-2.a Presentation of the liposomes

Liposome and vesicle are names referring to several types of supramolecular constructions, sorted by their structures and sizes [72][73] (*cf.* figure 1.28).

- Multi-Lamellar Vesicles (MLV) are vesicles made of several bilayers in an onion-like structure.
- Multi-Vesicular Vesicles (MVV) are structures where small vesicles are encapsulated in bigger ones.

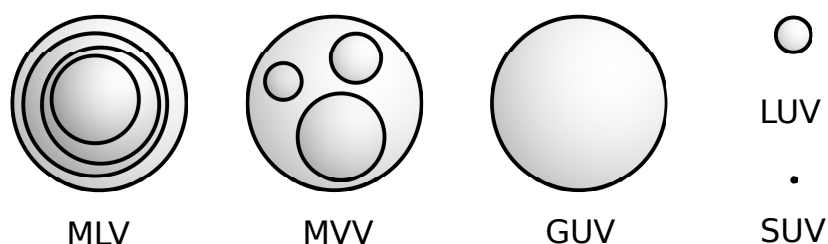


Figure 1.28: Representation of the different types of vesicles used in research on lipid membranes: Multi-Lamellar Vesicles (MLV), Multi-Vesicular Vesicles (MVV), Giant Unilamellar Vesicles (GUV), Large Unilamellar Vesicles (LUV), and Small Unilamellar Vesicles (SUV). As illustrated, MLV, MVV and GUV differ by their structures, while GUV, LUV and SUV differ by their sizes.

- Small Unilamellar Vesicles (SUV) are vesicles with only a single bilayer, with a diameter smaller than 100 nm.
- Large Unilamellar Vesicles (LUV) are vesicles with only a single bilayer, with a diameter greater than 100 nm, but yet too small to be observed with an optical microscope (diameter smaller than 500 nm).
- Giant Unilamellar Vesicles (GUV) are vesicles with only a single bilayer, with a diameter large enough to be observed with an optical microscope (larger than 500 nm).

The differences between the different structures and sizes allow the vesicles to be used in a wide range of experiments, making them desirable model systems for the scientists. Nonetheless, the methods to obtain the different types of liposomes greatly differ for each type. While MLV form spontaneously upon hydration of phospholipids, unilamellar liposomes require a controlled formation process, and often need injection of energy in the system in order to avoid the formation of MLV.

D-2.b Giant vesicles

The Giant Unilamellar Vesicle, or GUV, is certainly one of the favorite model system to reproduce the structure and the behaviour of the cell membrane. Indeed, the size of a GUV is close to the size of a cell ($> 1 \mu\text{m}$), which means that both curvatures are comparable. The size of the GUV also allows observation directly under an optical microscope and to perform similar experiments between GUVs and cells. Modifications of the composition of the bilayer of the GUV and encapsulation of materials bring the

GUV even closer to the biological cell while keeping a control on all the properties of the GUV [74].

The first reported method to prepare GUV was a controlled hydration of a dry film of phospholipid by Reeves and Dowben in 1969 [75]. Since then, a wide range of methods to form GUV have been developed. These methods differ by the applications they are designed for - such as material encapsulation or interactions of molecules with the membrane - and by their advantages and drawbacks. Table 1.8 lists a small number of these methods, which are illustrated in figure 1.29.

Procedure	Ref.
Controlled hydration	[75]
Electroformation	[76]
Gel assisted formation	[77],[78]
Simple or double emulsion	[79],[80]
SUV or LUV fusion	[81],[82]
Jet-blowing	[83]

Table 1.8: List of different methods of formation of giant unilamellar vesicles. For each method, a reference is given.

The main difficulty in the development of a method to prepare GUV is to avoid the formation of MLV [84]. Indeed, unilamellar liposomes are not in a thermodynamic equilibrium, but rather in a kinetically trapped state. Therefore, the transformation of a MLV into GUV is extremely unlikely to happen, as the transformation is not energetically favourable. Nonetheless, the transformation of MLV in SUV and LUV is a rather easy process, as described in the next section.

Most of the methods to obtain GUVs are based on controlled deformations of a lipid film. If the fluctuations are important enough, the growth solution is able to penetrate between the layers of lipid and the substrate. As a result, the osmosis effect swells the lipid membrane and form GUVs [85]. Of course, this means that the yield of formation of GUV is greater if the lipid membrane is fluid enough to fluctuate with ease. For this reason, the formation of GUVs is usually conducted above the gel-fluid phase transition temperature of the phospholipids.

The current section only describes two of these methods. Both are based on the enhancement of the swelling by different processes to facilitate the formation of GUVs and reduce the number of defects in the vesicles. More information about all the

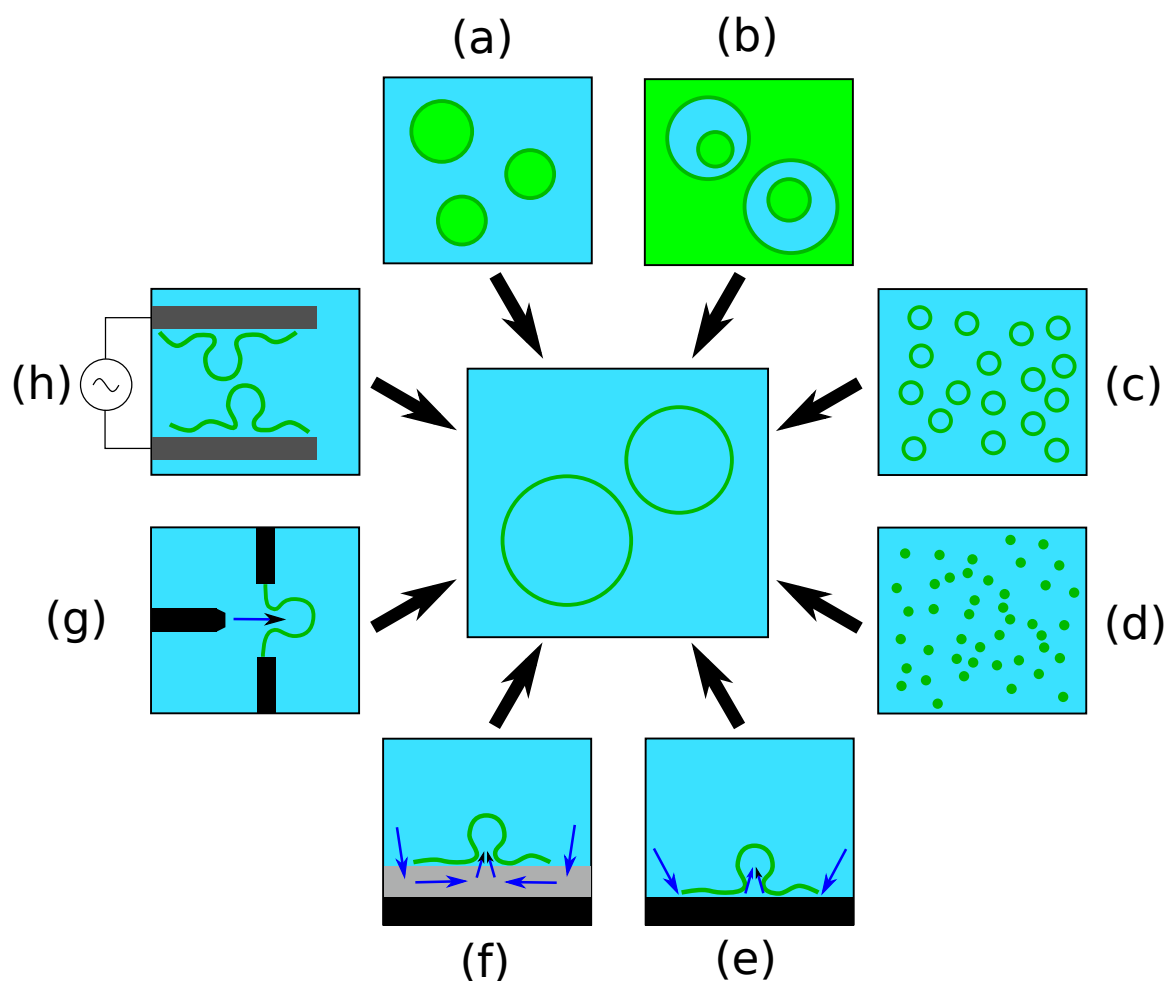


Figure 1.29: Representation of the different methods of GUV formation: (a) water/oil emulsion, (b) water/oil/water double emulsion, (c) LUV fusion, (d) SUV fusion, (e) controlled hydration, (f) gel-assisted formation, (g) jet-blowing, and (h) electroformation.

different methods of GUV formation can be found in the review by Walde *et al.* [73]

Currently, one of the most widely used methods to generate GUVs is electroformation. Developed by Angelova and Dimitrov in 1986 [76], the principle of the electroformation is to apply an alternative electric field to a hydrated lipid film, dried on the electrodes prior to the hydration. Angelova and Dimitrov suggested a mechanism for the electroformation in 1988 [86], and explained the formation of GUV in their model by the electroosmotic effect: the oscillating electric field lead to a fluctuation of the surface charges of the lipid film, which bend away from the surface and facilitate the swelling by osmosis, as described above. The size of the formed GUVs depend on the membrane fluidity [87]. While the electroformation is a method allowing a production of vesicles with a rather precise size distribution in a very quick time and with a large

population free from defects [88], it does not work well in a presence of physiological buffer, *i.e.* a buffer with an important salt concentration. Modifications to the original protocol can be found, which allow the electroformation of GUV in a saline buffer by variation of the electric field during the formation process [89][90].

Another method, developed recently by Horger *et al.* [77], uses a thin layer of agarose gel between the substrate and the lipid film. The layer gel, initially dried, swells while the lipid film is hydrated, enhancing the flow of liquid between the substrate and the lipids. As a result, GUVs are formed in a shorter time than with the gentle hydration method, with a reduced number of defects. Unfortunately, the agarose used in the initial protocol pollutes the GUVs formed. Indeed, during the hydration process, the water flowing in the gel is able to brake small bits of gel, which will end in the GUVs formed. To overcome this problem, our team suggested a modification of the protocol, and replaced the agarose by a gel made with polyvinyl alcohol (PVA) [78]. During the drying process, the PVA gel becomes semi-crystalline. Therefore, water cannot break it upon hydration, and the PVA does not contaminate the GUVs.

D-2.c Sub-microscopic vesicles

SUVs and LUVs are unilamellar vesicles with a size smaller than the limit of resolution of optical microscopy. With diameters ranging from 20 to 500 nm, SUVs and LUVs are perfect systems for observation of spherical unilamellar objects in an electron microscope, which allow a better understanding of the structure of the bilayer at a nanoscopic scale, especially during interactions with molecules [91]. Due to their capacity of material encapsulation, small liposomes are also interesting systems for drug delivery applications.

The two most common methods to prepare SUVs and LUVs are the ultrasonic irradiation and extrusion of a sample of MLV (*cf.* figure 1.30). Indeed, MLV are the easiest type of liposome to obtain.

The ultrasonic irradiation method has been developed by Saunders *et al.* [92] in 1962. As explained above, the formation of unilamellar vesicles requires one to bring energy to the system. Sonication is an efficient way to bring a large amount of energy in a solution of MLV in order to break them in small unilamellar liposomes. Two types of sonication protocols can be found in the litterature: ultrasound irradiation using a probe sonicator [97], and ultrasound generation using a bath sonicator [98]. The latter requires a specific care in the positioning of the tube and in the time of sonication, while the former has the disadvantage of possible contamination of the sample. The

Procedure	Size range	Ref.
SUV		
Ultrasonic irradiation	20 - 50 nm	[92]
Detergent removal	20 - 150 nm	[93]
Extrusion	> 20 nm	[94]
LUV		
Reverse phase evaporation	80 - 240 nm	[95]
Extrusion	> 100 nm	[96]

Table 1.9: List of different methods of formation of small and large unilamellar vesicles. For each method, the typical size range and a reference to the method is given.

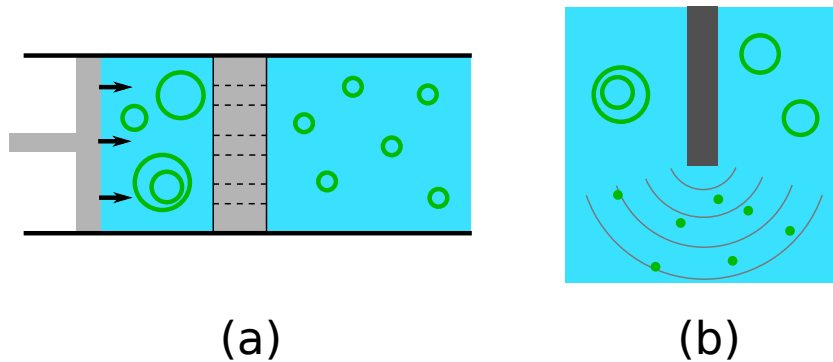


Figure 1.30: Representation of different methods of SUV and LUV formation: (a) Extrusion of a MLV solution through a porous membrane. The MLVs break when forced through the pores into SUVs or LUVs. The size of the resulting vesicles is given by the size of the pores. (b) Sonication of a MLV solution using a probe dipped in the solution. The energy brought by the ultrasonic radiations break the MLVs into SUVs or LUVs. The size of the resulting vesicles depends on the amount of energy brought to the system.

size of the resulting liposomes depends on the lipid composition and on the time of sonication.

Extrusion of MLV into LUV [96] or SUV [94], also called the French press method, is a transformation induced by a mechanical stress. The solution of liposomes is forced through a porous membrane multiple times, where the pores have a precisely defined diameter. Hence, liposomes prepared with this method have a reduced size range. This

method has also a good reproducibility and is non destructive.

More informations on the different methods of SUV and LUV formation can be found in the review by Hauser [99].

D-3 Planar bilayer

Another geometry commonly used in model lipid systems is the planar membrane. The cell membrane can locally be considered as a flat bilayer. As a consequence, a planar bilayer is a sufficient representation of the local cell membrane. This geometry is often preferred to the spherical vesicle for a large variety of experiments and conditions, such as the measurement of the membrane permeability [100], atomic force microscopy [101] or neutron scattering [102].

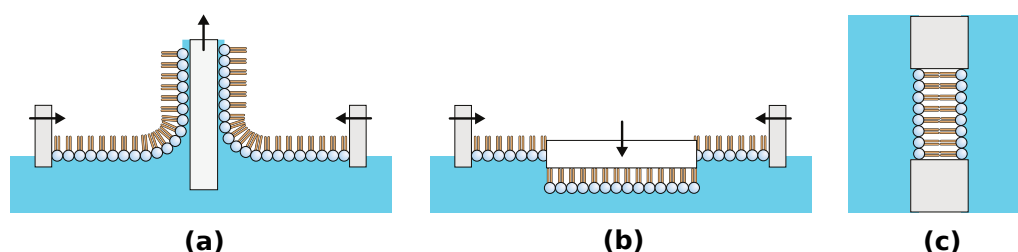


Figure 1.31: Representation of the different types of planar bilayers. Illustrations (a) and (b) shows supported lipid bilayers, constructed respectively by Langmuir-Blodgett and Langmuir-Schaefer method. In both cases, the lipid membranes are deposited on a substrate by vertical or horizontal dipping in a solution or pulling from the solution with a lipid monolayer at the water/air interface. Multiple dipping and choosing between a hydrophobic or hydrophilic substrate allows one to select the number of monolayers to be deposited and their organisation. (c) A black lipid membrane, where a bilayer is painted on a hole of a surface separating two aqueous solutions.

Several methods exist in order to create planar membranes. One of the most common way to achieve such geometry is the creation of a supported lipid bilayer (SLB). The concept of the SLB is to dip a substrate in an aqueous solution, or to pull the substrate out of the solution, with a lipid film at the air-water interface. During the dipping/extracting process, layers of lipid will be deposited on the surface of the substrate, and the process can be repeated several times to increase the number of layers on the substrate. Following the first observation made by Agnes Pockels in her kitchen sink [103], Langmuir and Blodgett developed the trough and method which bear their names [104]. The Langmuir-Blodgett method (LB) consists in the dipping of a vertical substrate in the conditions described above. Nonetheless, the LB protocol is only able

to deposit a maximum of three layer on the surface of the substrate when using the typical lipids for the construction of model membranes. In order to reach four layers with these lipids - a double bilayer - or more, one has to use the variation of the LB method developed by Schaefer in 1938 [105], called the Langmuir-Schaefer method (LS). For the LS method, the substrate has to be held horizontally through the dipping process. As the film of lipid can be changed in between each deposition, LB and LS methods allow one to easily create asymmetrical lipid membranes.

Another common way used to obtain planar membrane is the construction of a black lipid membrane (BLM). First published by Mueller *et al.* in 1962 [106], the concept of the BLM is to paint a film of lipid over a hole separating two reservoirs. In order to make it possible, the substrate in which the hole is drilled should be made of an hydrophobic material, such as the poly(tetrafluoroethylene) (PTFE). The two reservoirs are filled with an aqueous solution, and the lipids are painted on the hole, usually using a micropipette to bring an air bubble with lipids at its interface. Once the BLM has been created, different products can be dissolved in the reservoirs, in order to measure the permeability or to investigate the structure of the lipid and protein channels [107] for example.

E Drug delivery

Following the major breakthrough in medical research of the two last centuries, humans succeeded in enhancing the quality of their life and in increasing their life span. Thanks to the development of the concept of vaccination, the Human kind was able to repel and free an important fraction of the World from a lot of terrible diseases. One of the most impressive success of medical research was the eradication of the smallpox. However, a lot of lethal illnesses, where vaccines are inefficient for example, are still requiring an effective treatment nowadays. From all of these diseases, one can list viruses unable to be healed by the immune system (HIV, *etc.*), the various types of cancers, or the different genetic disorders (cystic fibrosis, sickle-cell disease, *etc.*).

For all these illnesses, one of the key is the cell: HIV and other viruses interact with the individual cells, cancers are degenerative cells, and the cells are storing and expressing the broken genes. It is obvious then that the cures for all these diseases can be found by interacting with these same cells. For example, the treatment of cancers turns often into killing the ill cells, and the genes can be corrected by replacing in the cells the broken DNA with a healthy one. This means that either the genetic materials or the drugs have to be brought directly inside the cells to cure. These protocols are

termed drug delivery applications.

E-1 Systems for drug delivery

The traditional way to administer a drug to an organism is to give periodically a high dose of the drug, every few hours or days. Obviously, this method has two major drawbacks: first of all, it requires an important quantity of the drug to be efficient, way above what is really needed to heal the ill cells. Then, a lot of side effects can arise from being exposed to an important quantity of the drug, side effects which may damage the organism in a critical way [108]. It is therefore essential to develop new methods to heal an organism using only a small amount a drugs with an increased efficiency. The controlled-release technologies are defining new ways to carry the drugs into the organism, such as the uses of nasal and buccal aerosol sprays, oral gels, or drug delivery devices.

Drug delivery systems are molecular designs created to carry the drug in the organism. In these designs, the drug of interest is brought to the tissue or cell concerned by the treatment through the use of a molecular carrier. Different geometries and types of molecular carriers are being investigated: liposomal systems, micelles of lipid or copolymers, emulsions, nanoparticles, *etc.* We will describe here some of these systems.

E-1.a Liposomal systems

Liposomes are considered as excellent candidates for drug delivery applications. Their design mimics the capsid of the viruses, encapsulating the material of interest inside a lipid bilayer. Some liposomal drug delivery systems have already been clinically approved and are currently being produced and sold by pharmaceutical groups for the treatment of different types of diseases: Abelcet[®] for fungal infections, Epaxal[®] for hepatitis A, *etc.* [109]. However, these systems do not have any specificity toward a target, and are developed as controlled released systems to administrate smaller quantities of the drug they are based on.

With the traditional way of administration, the drugs are able to react with all the different cells and tissues it might encounter from the entry point to the target. If the drug is designed to induce apoptosis, it means that all the cells encountered will be killed by the drug, and the whole tissue can die from such treatment. With drug delivery systems, the drug is designed to only interact with a specific type of cells, such as infected or tumorous ones, which reduces the amount of drug required for the

treatment. In this case, drugs made to induce apoptosis will not interact with healthy cells and will not kill them.

Many ways are being investigated for the development of targeted liposomal systems. Most common ways considered to prepare these systems rely on grafting or embedding antibodies in the liposome membrane [110][111], as shown in figure 1.32. These decorated liposomes, called immunoliposomes, are made to obtain the specificity of the antibodies added to their surface toward the receptors decorating the target cells. For example, Moles *et al.* decorated the surface of liposomes with anti-Human Immunoglobulin G antibodies which are specific to the Fc receptors found on the membrane of Plasmodium-infected red blood cells [110].

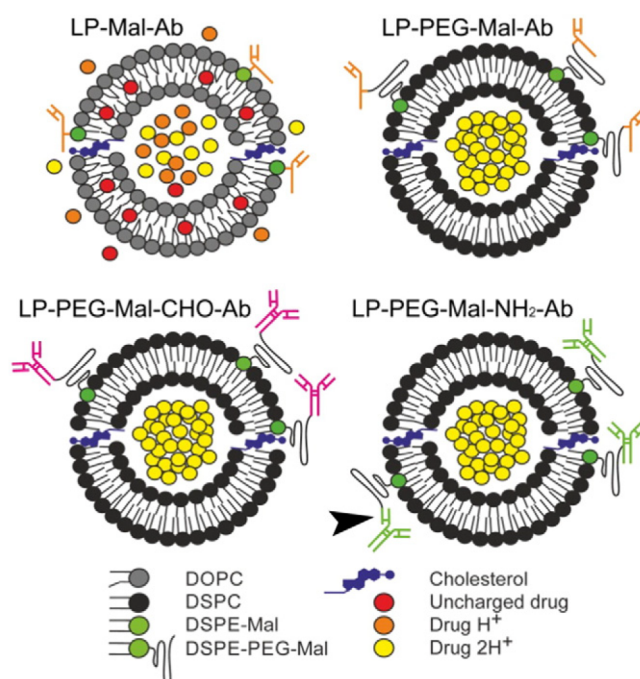


Figure 1.32: Representation of different compositions of polymer and antigen-decorated liposomes for drug delivery, encapsulating an amphiphilic drug. Antigens were grafted on the lipid membrane (top-left) or on one end of a polyethylene glycol (PEG) mediator, using various types of reactive group: maleimide (Mal), carbohydrate (CHO), or amine (NH_2). The figure is taken from the publication by Moles *et al.* [110]

Physical properties are also studied for creating intelligent liposomal systems. One can find thermosensitive liposomal systems [112], pH-sensitive systems [113], light sensitive systems [114], *etc.* For all these types of intelligent liposomal systems, the concept is not to induce a capacity of cell-recognition to the liposome for specific targets, but to create a liposome capable to release its content, either by poration or bursting, in certain conditions which can be induced experimentally.

E-1.b Micelles

Micelles made of lipids or copolymers can also be used to carry the drug inside the organism, either for controlled release or targeted delivery.

Lipid-based micelles are spherical systems with a hydrophobic core, as there is no lipid bilayer to form the shell like in liposomes. And like liposomal systems, drugs carried by lipid micelles are also already being distributed by pharmaceutical groups, such as Valium[®] or Konakion[®].

To form lipid micelles for drug delivery applications, one needs to stabilize the system. This can be either done by functionalizing the lipids with a polymer [115], or by mixing the lipids with a surfactant [116].

- Micelles combining lipids and surfactants are called mixed micelles. One of the most common surfactant used for building mixed micelles are the bile salts, a chemical produced by the liver. In this structure, bile salts stabilize the lipid micelles, while the phospholipids prevent the bile salts from disrupting plasma membranes [117]. By changing the ratio between lipids and bile salts, one can change the structure of the micelle, from a lamellar particle to a spherical one, as shown in figure 1.33. Therefore, a change in the concentration might induce a change in size and shape of the micelle [118].
- Polymer-stabilized lipid micelles are made by grafting polymers like poly(ethylene glycol) on lipids: indeed, lipid-PEG molecules can self-aggregate to form sterically stabilized micelles. The circulating times of these structure can be controlled by the amount of insaturations in the micelles [119]. However, polymer-stabilized lipid micelles have a limited solubilization capability for poorly soluble drugs, solubilization which can be enhanced by variation of the lipid composition [120].

In both cases, in the same way than with liposomal systems, the lipids forming the micelles can be functionalized with a ligand to induce a selectivity of the micelle for a specific target.

The polymers used for the creation of micelle-based drug delivery systems, or polymeric micelles, are amphipatic diblock copolymers. Due to their position in the micelle, the hydrophilic block of the copolymer is called the shell, while the hydrophobic block is the core of the micelle [122].

- Polymers used for the hydrophilic shell of the micelle are for instance poly(ethylene glycol), poly-(N-acryloylmorpholine), poly-(vinylpyrrolidone), poly-(L-

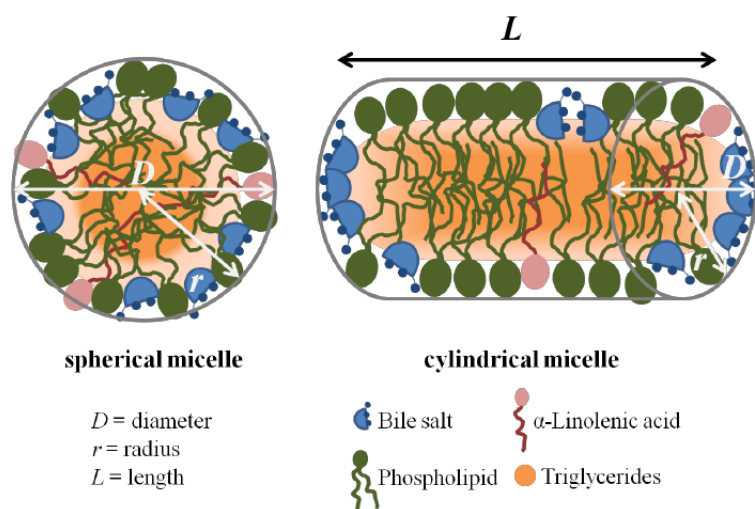


Figure 1.33: Representation of the different shapes a mixed micelle designed for drug delivery can reach, as a function of the ratio between surfactant and lipid. If there is more surfactants than lipids, then the micelle will be spherical. Otherwise, it will appear as cylindrical. Illustration from Courraud *et al.* [121]

glutamate), poly-(L-aspartate), *etc.* These polymers are chosen for giving stealth properties to the micelles.

- Examples of polymers used for the hydrophobic core of the micelle are poly-(L-amino acid) with hydrophobic residues (*e.g.* poly-(benzyl-L-glutamate)), polyesters (poly-(glycol acid), poly-(D,L-lactic-co-glycolic acid), *etc.*), or poloxamers (Pluronic[®]).

Polymeric micelles can be functionalized to improve their performances in drug delivery applications. These functionalizations can be sorted in three categories: first, in the same way than liposomal systems, the surface of the micelles can be functionalized with ligands which will direct the device toward a specific site of interest [123][124].

Polymeric micelles can also be functionalized using crosslinkable groups, either in their shell (shell crosslinked micelles [125]) or in their core (core crosslinked micelles [126]). The crosslinked micelles show greater stability than their non-crosslinked counterparts, and they have the ability to remain as micelles at concentrations lower than the critical micellization concentration of the same non-crosslinked copolymers. These systems have been investigated for controlling the release rate of the drug in the organism as well as for drug targeting purposes [127].

E-1.c Nanoparticles

Nanoparticles are another system of interest for the development of drug delivery systems. Two geometries are investigated for this purpose: nanocapsules and nanospheres.

Nanocapsules consist of a polymer shell surrounding a core in which the drug is located [128]. Nanocapsules have to be distinguished from polymeric micelles: polymeric micelles are made of amphiphilic diblock copolymers, in which the blocks form the shell and the core of the structure, while the shell of the nanocapsule is not chemically bonded to the core. In the latter, the drug inside the nanocapsule is either in a liquid medium [129] or in a polymer matrix [130]. The shell of the nanocapsule is made of polymers like poly-(ϵ -caprolactone) [131], poly-(lactide) [132], and poly-(lactide-co-glycolide) [133]. Nanocapsules are designed for controlled release of the drug, as the polymer capsule will slowly release its content over time.

Nanospheres are amorphous or crystalline constructions which have a size between 10-200 nm in diameter. A drug can be attached or dissolved in the nanosphere [134], unlike nanocapsules inside which the drug is encapsulated. Different materials can be used for the synthesis of nanospheres: polymers, silica, magnetic materials, *etc.*

- The polymers used for nanospheres can be either synthetic ones, such as poly-(caprolactone) [135] or poly-(acrylamide) [136], or natural ones, like chitosan [135]. These types of nanospheres have the advantage to be biodegradable, and the organism can process them after use.
- Mesoporous silica nanoparticles offer biocompatibility and a good capacity to be functionalized [137]. The most famous types of silica nanomaterials are MCM-41 and SBA-15 [138]. Drugs are loaded on the nanoparticles by physical or chemical adsorption [139], and are usually released by diffusion [140].
- Magnetic nanoparticles for drug delivery can be made of pure magnetic metals, alloys and oxides [141]. The drug can be connected to the nanoparticle by covalent bonding, electrostatic interactions or adsorption [142]. Advantages of magnetic nanoparticles are their easy handling with an external magnetic field, the ability of visualization, and the possibility of using passive and active strategies for the cellular uptake [143]. However, these nanoparticles tend to aggregate into larger clusters.

All these different types of nanoparticles can be decorated with ligands, such as peptides or polymers, to induce a selectivity or facilitate the cellular uptake. For ex-

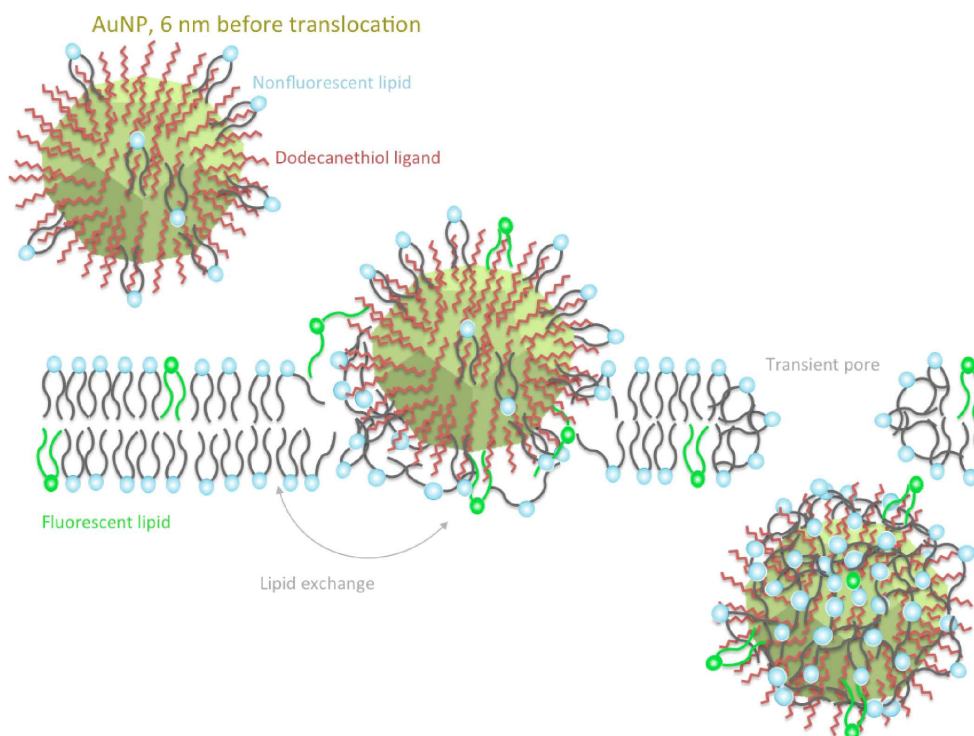


Figure 1.34: Representation of a lipid-coated nanoparticle translocating through a membrane. The nanoparticle is able to interact with the lipid membrane due to its lipid coating, and will penetrate inside the cell afterward. Figure from Guo *et al.* [144]

ample, Guo *et al.* have shown that gold nanoparticles larger than 5 nm could translocate through the membrane once coated with a layer of lipid [144] using only passive processes of internalization.

E-2 Cell-Penetrating Peptides

The specificity of a drug or of its carrier towards a target cell or tissue is one of the crucial aspects in the development of new systems for drug delivery. Often, the specificity is achieved by decorating the system with ligands, such as proteins, specific to the target which will trigger the cellular uptake upon recognition by the corresponding receptor. However, in some cases, the target cell lacks specific receptors to any type of ligands, as the same type of receptors decorating the cell will be found in other cells which are not of interest. Good examples are the tumorous cells, which remains close to the healthy cells from which they are originated from.

New systems need to be developed to induce a selectivity to these types of target, a selectivity often based on the physical properties of the cells of interest. We only focus here in this work on one type of these systems currently being investigated: the

cell-penetrating peptides.

E-2.a The different types of cell-penetrating peptides

Cell-penetrating peptides (CPPs) are oligopeptides, typically with 5–30 amino acids, which facilitates the cellular uptake. The CPPs have the capacity to translocate through any type of membrane, and are able to reach the nucleus of a cell, as shown in figure 1.35.

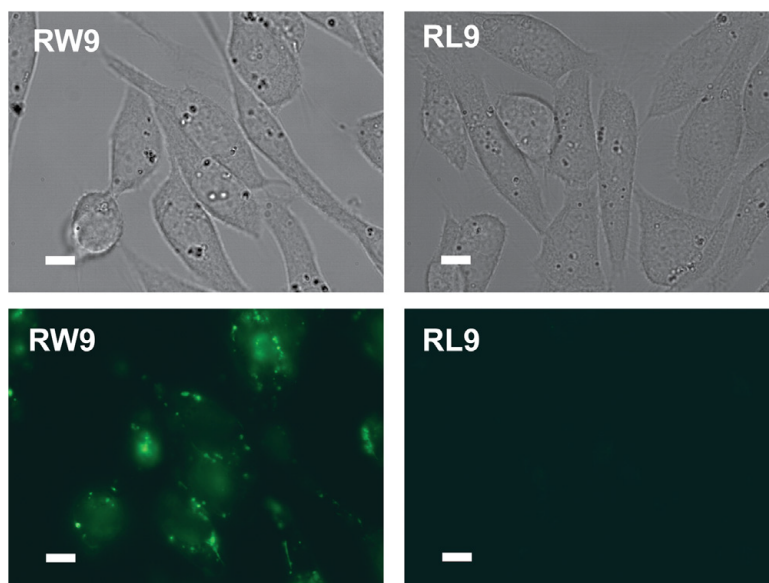


Figure 1.35: Pictures of Chinese hamster ovary cells taken in phase contrast microscopy (top) and fluorescence microscopy (down), to show their interactions with fluorescently green-labeled oligopeptides: RW9, a cell-penetrating peptide, and RL9 which does not show any penetrating capacity. RW9 is able to translocate into the cells and into the nuclei, while RL9 is not internalized. Picture is taken from the paper by Walrant *et al.* [145]

The main interest of CPPs for the current research is their ability to carry materials inside the cells. They are indeed able to induce the cellular uptake of siRNA [146], small molecules, proteins [147], *etc.* For this reason, the CPPs are one of the most investigated ligands for targeted drug delivery applications. CPP-based drugs have not been yet commercialized, but few of them are currently in clinical trials with human subjects, such as the p28 [148].

The first CPP to be characterized was the transactivator or transcription (TAT) of the HIV. The penetrating properties of the TAT was reported by two distinct teams in 1988: Frankel *et al.* [149], and Green and Loewenstein[150]. The transduction domain

of the TAT corresponds to the 47-57 sequences of the protein: Y-G-R-K-K-R-R-Q-R-R-R [150]. The other most commonly used CPP is the Penetratin, a transduction domain found in the Antennapedia gene from the *Drosophila* in 1991 by Joliot *et al.* [151]. The exact sequence of the Penetratin is R-Q-I-K-I-W-F-Q-N-R-R-M-K-W-K-K.

Nowadays, hundreds of CPPs have been identified: the cationic peptides, the amphipatic peptides, and the hydrophobic peptides. A list of examples of CPPs for each of these types is given in table 1.10.

Type	Name	Sequence	Ref.
Cationic	TAT	YGRKKRRQRRR	[149][150]
	Antp	RQIKIWFQNRRMKWKK	[151]
	NLS	CGYGPKKKRKVG	[152]
Amphipatic	MPG	GLAFLGFLGAAGSTM GAWSQPKKKRKV	[153]
	pVEC	LLIILRRRIRKQAHASK	[154]
	VP22	NAATATRGRSAASRPTQR PRAPARSASRPRRPVQ	[155]
	Transportan	GWTLNSAGYLLG KINLKALAALAKKIL	[156]
Hydrophobic	SG3	RLSGMNEVLSFRW	[157]
	FGF	PIEVCMYREP	[158]

Table 1.10: List of the different types of cell-penetrating peptides (CPPs), with few examples for every types, along with their sequences. The references correspond to the initial paper investigating the sequence as a CPP.

- Cationic CPPs are primarily made of positively charged amino acids, and especially of arginine (R, Arg) and lysine (K, Lys) groups. For example, TAT is made of 6 arginine and 2 lysine groups (nominal charge: 8+), and Penetratin is made of 3 arginine and 3 lysine groups (nominal charge: 6+), for respectively a total of 11 and 16 amino acids. As the presence of arginine amino acids seems to be more effective than the presence of lysine, the group of arginine-rich peptides can be found within the group of cationic CPPs. More information on the arginine-rich peptides is given below. The penetrating properties of the cationic CPPs are

expected to come from favourable Coulombic interactions between the peptide and molecules from the cell membrane [159].

- Amphipatic CPPs are divided into two categories: primary and secondary amphipatic CPPs. Primary amphipatic peptides are either chimeric peptides, where a hydrophobic domain for efficient targeting of the cell is covalently bonded to a NLS [153], or natural peptides which includes a K-K-R-P-K-P motif [160]. Secondary amphipatic peptides are based on a α -helix structure, in which hydrophilic and hydrophobic amino acids are grouped in separate faces of the helix. Although most of these CPPs are cationic, evidences suggest that the penetrating properties are a consequence of the amphipaticity, and not of the positive charges [161].
- Hydrophobic CPPs are hydrophobic peptides, or polar peptides with a low net charge. Only a few hydrophobic CPPs have been discovered so far, as compared to cationic and amphipatic ones. Most of these peptides are made of specific pentapeptides: PMLKE, VPALR, VSALK, IPALK, IPMLK, VPTLQ, QLPVM, ELPVM, *etc.* [162] One can also find the stapled hydrophobic CPPs, which are obtained by ring-closing metathesis [163].

The exact mechanism of translocation of the CPPs is still currently debated, as it has not been completely resolved yet [164][165][166]. However, it is assumed that the uptake mechanism of the CPP varies for the different types of CPPs, and that one CPP can have several mechanisms, depending on the experimental conditions. It has been shown that three mechanisms can be used by the CPPs to penetrate the cell: direct penetration [167], endocytosis-mediated translocation [168], and formation of a transitory membrane structure [169]. All mechanisms are illustrated in figure 1.36.

Endocytosis is believed to be the main pathway used by the CPP to penetrate the cell. Moreover, experimental parameters, such as incubation temperature and time have to be considered [171][172].

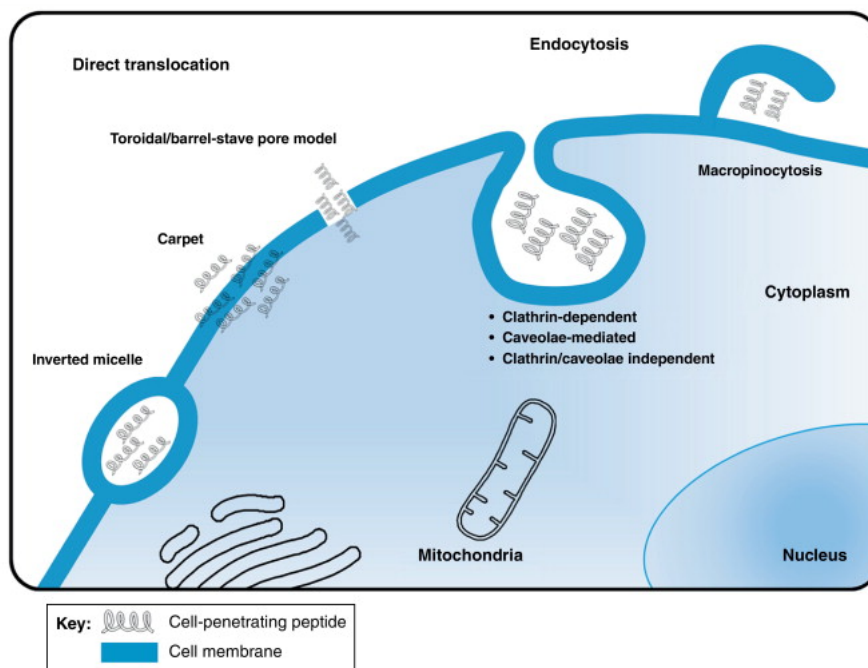


Figure 1.36: Illustration of the different mechanism of cellular uptake of the CPPs: direct translocation, by carpet insertion or poration, endocytosis by the different ways allowed by the cell active mechanisms, and the transitory membrane structure, with the formation of an inverted micelle. Illustration from Koren and Torchilin [170].

E-2.b Arginine-rich peptides

Arginine-rich peptides are cationic CPPs for which the majority of the positively charged amino acids are arginines. They are the most studied types of CPP, in which one will find the TAT and the Penetratin.

Current observations suggests that the CPP should have at least 7 charges to promote the cellular uptake [173], and that increasing the number of charges increases the cellular uptake. It has also been shown that arginine groups are more efficient than lysine ones [174]. Arginine and lysine amino acids are shown in figure 1.37 for reference. Following these statements, artificial arginine-rich peptides have started to be synthesized to create new CPPs. These artificial CPPs, made by simple repetitions of arginine amino acids, are called oligoarginines or polyarginines.

While being promising systems for drug delivery applications, arginine-rich peptides suffer from several drawbacks. First of all, like every types of CPPs, the mechanisms of cellular uptake of the arginine-rich peptides are not completely resolved. It is also known that the arginine-rich peptides lack specificity toward target cells, and might interact with every types of cell encountered in the organism [175]. The last problem

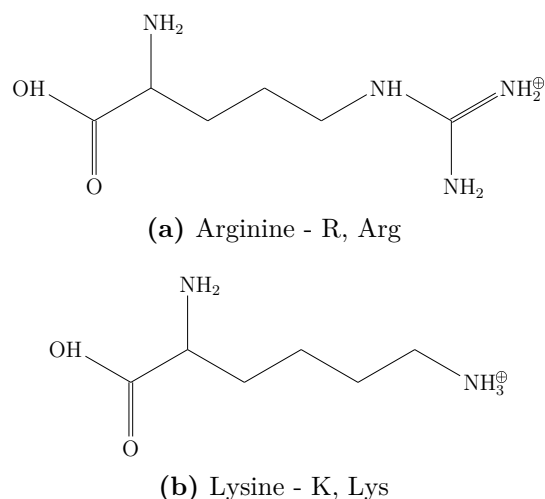


Figure 1.37: Skeletal formulae of the two positively charged amino acids used to design synthetic cell-penetrating polypeptides: arginine (R, Arg) and lysine (K, Lys). The resulting polypeptides are termed polyarginines and polylysines.

with the arginine-rich peptides is that it has been shown that these peptides lose their penetrating properties once a cargo has been attached to them (cf. figure 1.38).

Maiolo *et al.* have shown that the presence of a molecular cargo prevents the arginine-rich CPPs to translocate inside the cells [176]. To demonstrate this, they used only short sequences of amino acids, D-T-R-L and W-V-Q-D, grafted onto polyarginines. However, polyarginines grafted onto a single tryptophan amino acid (W, Trp) was still able to penetrate the cell, which suggests that the length of the molecular cargo has an effect on the ability of the CPP.

While arginine-rich cell-penetrating peptides remain one of the preferred systems for targeted drug delivery, it is critical to investigate and resolve these three drawbacks in order to proceed toward clinical trial of arginine-rich cell-penetrating peptide-based drugs. This was one of the inspiring challenges for the work of my PhD thesis.

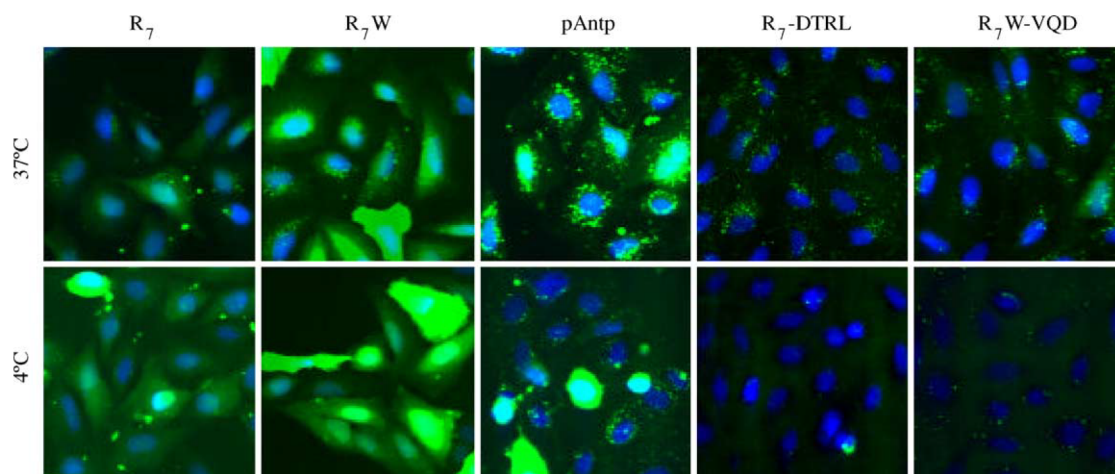
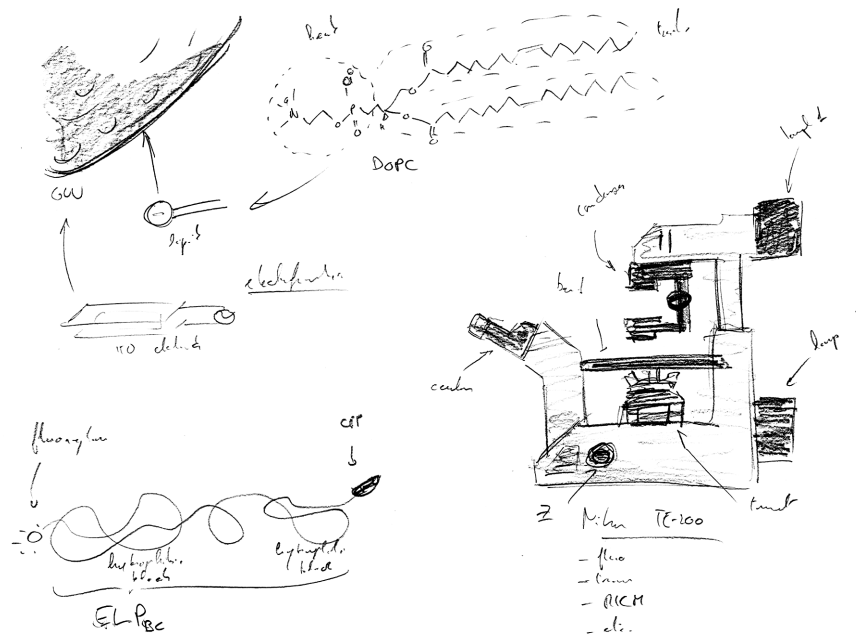


Figure 1.38: Confocal pictures of different CPPs and CPPs grafted onto a molecular cargo, brought in contact with cells (U2OS). R₇ and R₇W corresponds to polyarginines with 7 arginine amino acids and 7 arginine amino acids plus a tryptophan (W). pAntp is the Penetratin from *Drosophila*'s *Antennapedia*'s gene. All these three CPPs display penetration properties, as the green-labeled CPP is able to reach the nuclei of the cells (labeled in blue). When attached to a molecular cargo, R₇ and R₇W, respectively attached to a DTRL and a VQD sequence, are unable to translocate inside the cell. The molecular cargo therefore prevent the penetration of the CPP. Pictures from Maiolo *et al.* [176].



CHAPTER 2 **Systemes et analyses**

LE second chapitre de ce manuscrit est dédié à la description des différents produits chimiques utilisés dans ce travail, ainsi qu'aux techniques de microscopie utilisées pour observer et analyser le comportement de nos échantillons.

A Molécules fonctionnalisées avec des CPPs

Trois CPPs ont été étudiés dans ce travail: le TAT₄₇₋₅₇ déjà décrit dans l'introduction, et deux CPPs cationiques riche en arginine, l'arginine 5 (Arg5) et l'arginine 8 (Arg8), nommés d'après leurs structures. Ces CPPs ont été fonctionnalisés par leur fusion sur un polypeptide semblable à de l'arginine. Les CPPs non-fonctionnalisés ont également été étudiés pour comparaison.

A-1 CPPs courts

Nous nous concentrons ici sur les peptides pénétrateurs de cellules cationiques, et particulièrement sur ceux riches en arginine. Les polyarginines comme l'Arg8 (comme son nom le suggère, sa séquence est R-R-R-R-R-R-R-R) sont capables de pénétrer la cellule, d'une manière similaire à ce que fait le TAT₄₇₋₅₇. Cependant, Mitchell *et al.* ont montré que les résidus de polyarginines avec une charge nominale de 5 charges positives ou moins ne peuvent pas se déplacer à l'intérieur des cellules [177]. Cette observation suggère que la quantité locale de charge est le déclencheur du déplacement, mais Mitchell *et al.* a aussi montré que l'efficacité de la pénétration diminue lorsqu'il y a plus de 15 répétitions d'arginine dans le polyarginine. Tout comme le TAT₄₇₋₅₇, les polyarginines sont incapables de traverser la membrane une fois qu'un cargo moléculaire est attaché sur eux [176].

Les peptides pénétrateurs de cellule courts (sCPP) ont été achetés auprès d'AnaSpec (Fremont, CA, USA). Tous les sCPPs ont été achetés sous forme de poudre. Les mêmes CPPs, marqués avec le fluorophore HiLyte 488 ont également été achetés auprès du même vendeur. À la réception, les peptides ont été dissous dans une solution de tampon phosphate salin (PBS) au pH 7.4 et conservés à -20°C dans un congélateur. Pour les expériences, les solutions mères de peptides ont été préparées à la concentration requise avec 1% de CPPs marqués en fluorescence, aliquotés et conservés au congélateur jusqu'à utilisation. Les peptides ont été décongelés au cours de la nuit précédant les expériences. Dans ce but, les aliquots ont été placés dans un agitateur rotatif dans un réfrigérateur. Les échantillons ont ensuite été centrifugés à 17000 g pendant 1 minute à 4°C.

Les sCPPs ont été utilisés comme système de référence pour comparer leurs propriétés de pénétration de cellule avec ceux des CPP-ELP_{BC} correspondants (voir plus bas).

A-2 Polypeptides auto-assemblants

MacEwan et Chilkoti ont suggéré en 2012 qu'augmenter la densité locale de charge permettrait de retrouver les propriétés pénétrantes des CPPs greffés sur des cargo moléculaires [178]. Pour tester cette hypothèse, des CPPs greffés sur des cargos spécifiques ont été synthétisés avec les propriétés d'un cargo amphiphile. Comme on peut le voir sur la figure 2.1, quand les molécules s'auto-assemblent, les fonctions CPPs décorent la coquille des micelles ainsi formées, ce qui augmente donc la densité locale de charge.

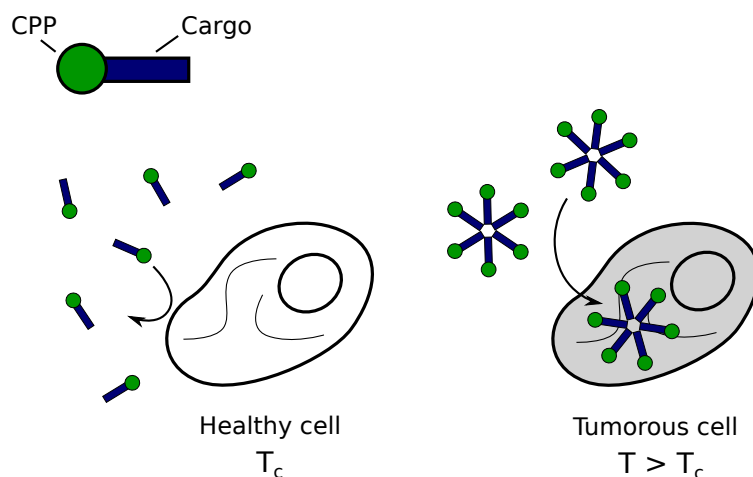


Figure 2.1: Représentation des CPPs greffés sur des cargos auto-assemblants contrôlés par la température et leurs interactions avec des cellules saines et cancéreuses. Le CPP ne s’auto-assemble qu’au-dessus d’une température supérieure à celle d’une cellule saine, et peuvent donc seulement pénétrer les cellules tumorales, qui ont une température supérieure à celle des cellules saines après un cycle de chauffage et de refroidissement.

L’intérêt d’un système auto-assemblant est d’induire une certaine sélectivité, ce qui manque aux CPPs. Par exemple, les cellules cancéreuses sont connues pour avoir de faibles propriétés d’échange thermiques [179][180]. En conséquence, quand un tissu biologique complet est chauffé puis laissé refroidir, les cellules tumorales du tissu nécessiteront un temps plus important que les cellules saines pour retrouver leur température initiale. Ainsi, une molécule fonctionnalisée avec des CPPs qui s’auto-assemble seulement au-dessus d’une température précise ne pourra interagir qu’avec les cellules cancéreuses dans cette situation, et les systèmes non-assemblés ne pourront pas pénétrer les cellules saines plus froides.

A-2.a Polypeptides semblables à de l’élastine diblocs

De tels systèmes auto-assemblant fonctionnalisés avec des CPPs ont été suggérés par MacEwan et Chilkoti en 2012 [178]. Leur molécule, dont l’amphiphilie est contrôlée par la température, est basée sur les polypeptides semblables à de l’élastine (ELP) conçu par Urry *et al.* en 1974 [181] et les copolymères diblocs basés sur de l’ELP (ELP_{BC}) par Lee *et al.* en 2000 [182].

Suivant la démonstration par Gray *et al.* [183] et Foster *et al.* [184] de la présence de séquences peptidiques répétées dans la structure de l’élastine, Urry *et al.* a conçu des polypeptides artificiels faits de la répétition de ces séquences, d’où leur nom de

polypeptides semblables à de l'élastine. Une des propriétés les plus intéressantes des ELP est l'existence d'une température de transition de phase inverse, à laquelle l'ELP peut devenir hydrophile ou hydrophobe [185]. De plus, la température de transition dépend de la séquence de l'ELP, et peut donc être sélectionné au travers de la conception de la séquence de répétition de l'ELP, mais aussi par l'addition d'un groupe supplémentaire à l'une de ses extrémités [186][187].

En 2000, Lee *et al.* a relié de façon covalente deux ELP avec des températures de transition différentes, créant un polypeptide semblable à de l'élastine dibloc (ELP_{BC}) [182]. A basse températures, les deux blocs sont hydrophiles et l'ELP_{BC} restent sous forme d'unimère en solution. Quand l'ELP_{BC} atteint la température de transition du premier bloc, ce dernier devient hydrophobe et la molécule toute entière s'auto-assemble en micelles (*cf.* figure 2.2(a)). Au-dessus de la seconde température de transition du système, l'autre bloc devient également hydrophobe, et les molécules s'agrègent en solution. Ces transitions et ces différents états peuvent être mesurés par diffusion dynamique de lumière, comme montré dans la figure 2.2. Le nombre d'agrégation des micelles résultantes peut être mesurée par diffusion statique de la lumière [188]. Des changements structuraux se produisent toujours entre la micellisation et l'agrégation. Garanger *et al.* ont prouvé que la quantité d'eau contenue dans la micelle d'ELP_{BC} décroît avec la température [189].

A-2.b ELP_{BC} fonctionnalisé avec des CPPs

MacEwan et Chilkoti ont combiné les propriétés d'auto-assemblages des ELPs diblocs avec les capacités pénétrantes des CPPs par la fusion des fonctions CPPs avec l'extrémité hydrophile des ELP_{BC}. De tels polypeptides sont nommés CPP-ELP_{BC}. Cinq différent types d'ELP_{BC} on était créé pour ce travail en utilisant la ligature directionnelle récursive par reconstruction plasmidique dans des cellules d'EB5α *Escherichia Coli*. Trois d'entres eux ont été fonctionnalisés avec une fonction CPP: 60/60 TAT, 60/60 Arg8, et 60/96 Arg5. Les notations 60/60 et 60/96 font référence à la composition des blocs hydrophiles et hydrophobes des polypeptides semblables à de l'élastine, comme décrit dans la figure 2.3. Parmi ces CPP-ELP_{BC}, deux diblocs exempts de fonction CPP, respectivement nommés 60/60 Ctrl et 60/96 Ctrl, ont été préparés.

Les CPP-ELP_{BC} et les ELP_{BC} de contrôle ont été conçus pour avoir une CMT aux alentours de 33°C, comme montré dans la table 2.1. Pour accomplir cela, le bloc hydrophobe a été conçu comme une répétition de 60 séquences V-P-G-V-G. Cependant,

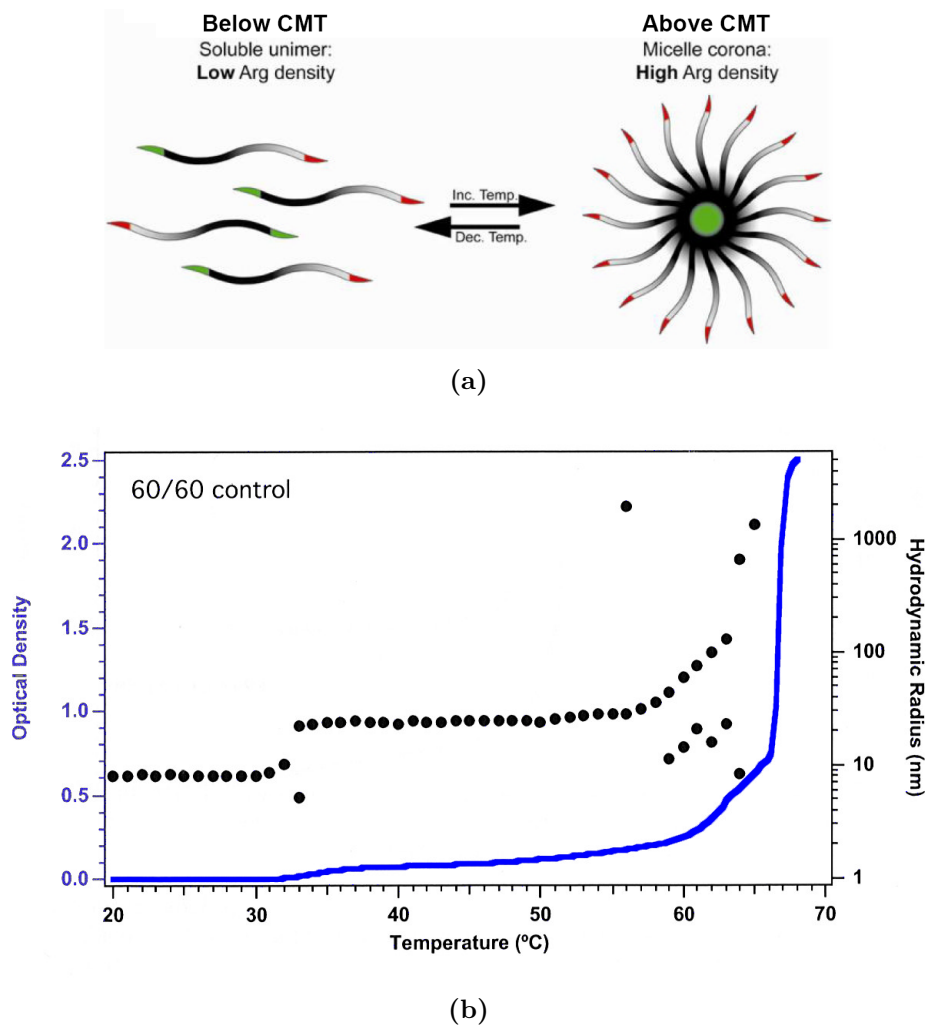


Figure 2.2: (a) Représentation du CPP-ELP_{BC} développé et synthétisé par MacEwan et Chilkoti [178]. Le CPP-ELP_{BC} s’auto-assemble au-dessus d’une température précise, appelée la température de micellisation critique (CMT). Lors de la formation des micelles, les fonctions CPP décoorent la coquille des micelles et augmente donc la densité locale d’arginine. Illustration adaptée du papier de MacEwan et Chilkoti. (b) Rayon hydrodynamique du ELP_{BC} utilisé dans ce travail en fonction de la température, mesuré par diffusion dynamique de la lumière. La densité optique du polypeptide a également été mesurée par spectroscopie UV. Les deux résultats montrent l’existence de deux températures de transition: une première à 32°C et une seconde au-dessus de 50°C. La première température de transition correspond à la température de micellisation de l’ELP_{BC} et la seconde à la transition entre micelles et agrégats.

le bloc hydrophile du CPP-ELP_{BC} Arg5 diffère de celui des autres ELP_{BC} fonctionnalisés avec des CPPs. Ce dernier est une répétition de 96 séquences de V-P-G-X-G,

	60/60	60/96
	CPP TAT ₄₇₋₅₇ , Arg8	Arg5
	Remorque <i>CPP-S-G-G-P-ELP</i>	<i>CPP-S-G-G-P-G-ELP</i>
	Bloc hydrophile	(V-P-G-X-G) _n
	n = 60	n = 96
	X=G:A (1:1)	X =V:G:A (1:7:8)
	Bloc hydrophobe	(V-P-G-V-G) _n
	n = 60	n = 60
	Leader	<i>ELP-G-P-W-G-C-G-M</i>

Figure 2.3: Description de la structure des CPP-ELP_{BC} utilisés dans ce travail. Les CPP-ELP_{BC} de contrôle ont également été synthétisés, sans la fonction CPP sur la remorque. Une sonde fluorescente peut être greffée sur la cystéine de la partie leader du polypeptide.

avec X étant V, G ou A avec un ratio de 1:7:8, tandis que les autres CPP-ELP_{BC} ont un bloc hydrophile composé d'une répétition de 60 séquences de V-P-G-X-G, avec X = G ou A avec un ratio de 1:1. La séquence remorque, séparant le CPP de l'ELP_{BC}, est une séquence S-G-G-P dans le cas des 60/60 CPP-ELP_{BC} et une séquence S-G-G-P-G pour les 60/96 CPP-ELP_{BC}. Pour les contrôles, la sérine de la remorque est laissée vierge. Le bloc hydrophobe des est terminé par une séquence leader de G-P-W-G-C-G-M dans tous les cas. Une sonde fluorescente peut être ajouté en faisant réagir la fonction maléimide d'une sonde avec le thiol de la cystéine.

A cause de ces différentes structures, les CPP-ELP_{BC} diffèrent entre eux par leur masses molaires et par leurs rayons hydrodynamiques, comme montré dans la table 2.1.

Tous les ELP_{BC} utilisés dans ce travail ont été synthétisés par Sarah MacEwan durant son travail post-doctoral au sein du groupe Chilkoti de l'Université de Duke (Durham, NC, USA), et offerts gracieusement à notre groupe. Deux fluorophores ont été utilisés pour marquer les CPP-ELP_{BC} : l'AlexaFluor 488 et le BODIPY.

Dans leurs travaux précédents [178], Chilkoti et MacEwan ont conçu un CPP-ELP_{BC} avec une CMT de 42 °C, et ces CPP-ELP_{BC} marqués en fluorescence ont été mis en contact avec des cellules de type HeLa. Les interactions de ces polypeptides avec ces cellules ont été étudiés (*cf.* figure 2.4). Les ELP_{BC} fonctionnalisés avec des CPPs, une fonction arginine, ont été capable de se déplacer au travers des membranes

Nom	Fonction	M (g/mol)	CMT °C	R_h (nm)	
	CPP			25°C	37°C
60/60 TAT	TAT ₄₇₋₅₇	49560	32	6.0 ± 0.7	25.9 ± 1.4
60/60 Arg8	Arg8	49290	32	7.5 ± 0.2	26.4 ± 0.3
60/60 Ctrl	-	48020	33	5.9 ± 0.8	24.1 ± 1.1
60/96 Arg5	Arg5	62600	32	6.8 ± 0.2	28.6 ± 0.6
60/96 Ctrl	-	61800	32	6.8 ± 0.1	27.1 ± 0.9

Table 2.1: Liste des caractéristiques des différents CPP-ELP_{BC} utilisés dans ce travail. La nomenclature des noms des polypeptides est décrite dans la figure 2.3. La CMT et les rayons hydrodynamiques des unimères et micelles ont été mesurés en diffusion dynamique de lumière. Le nombre d'agrégation des micelles a été mesuré par Sarah MacEwan et trouvé égal à 89.

cellulaire après auto-assemblage en micelle, alors qu'ils en étaient incapable sous leur forme unimère. Ces expériences ont également été réalisées avec un CPP-ELP incapable de s'auto-assembler ainsi que des ELP_{BC} sans fonction CPP. Les deux contrôles ont été incapable de pénétrer ou même d'interagir avec la membrane.

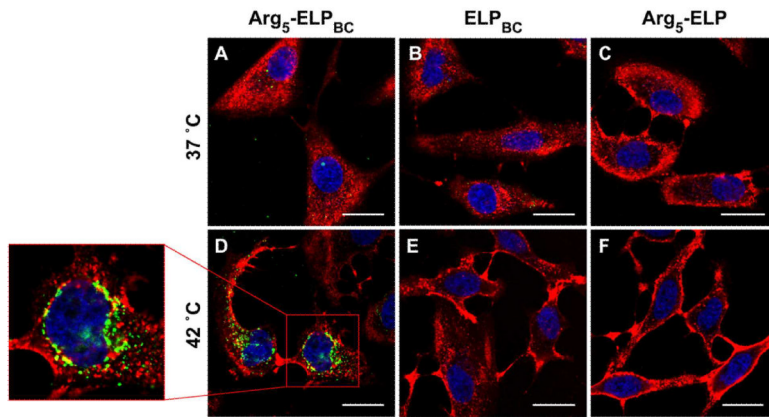


Figure 2.4: Photographies confocales de la sélectivité déclenchée par la température des CPP-ELP_{BC} pour la membrane cellulaire. Trois types de molécules basées sur les ELP_{BC} ont été mis en contact avec des cellules de type HeLa au-dessus et en-dessous de la température de micellisation des CPP-ELP_{BC} : le CPP-ELP_{BC}, une molécule de contrôle sans la fonction CPP (ELP_{BC}), et une molécule de contrôle ne pouvant pas former de micelle (CPP-ELP). Les photographies et résultats sont issus du papier de MacEwan et Chilkoti [178].

Ces expériences suggèrent fortement que l'augmentation de la densité locale de charge au cours de la micellisation est un élément essentiel pour retrouver les propriétés pénétrantes du CPP, et ce malgré la présence d'un imposant cargo moléculaire. Les systèmes étudiés permettent également d'induire une sélectivité des CPPs pour les cellules par la température. Dans le même article, MacEwan et Chilkoti ont étudié le mécanisme d'internalisation de leur CPP-ELP_{BC}. En incubant les cellules et les CPP-ELP_{BC} avec de la génistéine et de l'amiloride, ils ont observé que la pénétration dans la cellule était fortement affectée par la désactivation de l'endocytose à cavéole. Ainsi, ils ont montré que le mécanisme a une importance cruciale dans l'absorption cellulaire du CPP-ELP_{BC}.

A-2.c Préparation des échantillons

Les CPP-ELP_{BC} lyophilisés ont été conservés au congélateur à -20°C dès leur arrivée. Les polypeptides sont ensuite mis en suspension dans une solution de PBS à pH 7.4, centrifugés trois fois à 17000 g pendant 30 secondes et pipetés hors du tube et réinjectés, afin d'améliorer la dissolution du polypeptide. Les CPP-ELP_{BC} marqués et non-marqués en fluorescence sont mixés à la concentration et au ratio voulu, avant d'être aliquotés et conservés au congélateur à -20°C pour réduire de trop congeler et décongeler la solution.

Avant l'expérience, les CPP-ELP_{BC} furent décongelés toute une nuit. Dans ce but, les aliquots ont été placés dans un agitateur rotatif au frigo. L'échantillon était ensuite centrifugé à 17000 g pendant 1 minute à 4°C.

B Préparation des liposomes

Les interactions entre membranes lipidiques modèles et les différentes biomolécules décrites ci-dessus ont été réalisées avec des liposomes. Cette section donne les détails sur les méthodes utilisées pour préparer les vésicules, et les lipides utilisés pour réaliser les membranes.

B-1 Phospholipides

Tous les principaux phospholipides utilisés dans ce travail ont deux queues oleoyl, étant différents entre eux par leurs têtes: DOPC, DOPG et DOPE. Du DPPC, un lipide saturé avec deux queues de seize carbones, a également été utilisé. De plus, du DOTAP, un lipide artificiel chargé positivement, a été utilisé pour les interactions entre

ADN et membrane. Les représentations semi-développées des lipides sont données en figure 2.5.

Les lipides avec une tête PC ont été utilisés comme représentatifs des lipides zwitterionique. Le DOPG a été utilisé en tant que lipide chargé négativement, pour moduler la charge de la membrane. Le DOPE a été ajouté à la bicouche pour sa capacité à induire une courbure négative dans la membrane.

Tous les lipides ont été achetés auprès d'Avanti Polar Lipids (Alabaster, AL, USA) sous forme de poudre. Les solutions mères ont été préparées en dissolvant les lipides dans du chloroforme (qualité HPLC de chez Sigma-Aldrich, St. Louis, MO, USA) à la concentration massique de 10 mg/mL. Les solutions de lipide à 1 mg/mL ont été préparées au ratio molaire voulu à partir des solutions mères avant utilisation. Les solutions diluées et les solutions mères ont été conservées au congélateur à -20°C jusqu'à 6 mois après préparation.

B-2 Préparation des GUV

Les vésicules unilamellaires géantes ont été préparées pour les observations et expériences au microscope. Deux méthodes de formation de GUV ont été utilisées dans ce travail. L'électroformation de liposomes fut la principale méthode choisie pour préparer les échantillons, mais la formation assistée par gel a également été utilisée pour comparer les résultats ou réaliser des tests rapides.

B-2.a Electroformation

La méthode d'électroformation des liposomes d'Angelova et Dimitrov a été la principale méthode pour la préparation de vésicules. Au lieu des électrodes de platine du protocole originel [76], des électrodes en oxyde d'indium-étain (ITO) ont été utilisées, suivant le protocole d'Angelova *et al.* [190]. Nous avons utilisé des lamelles de verre couverte d'ITO achetées auprès de Präzisions Glas & Optik (Iserlohn, Germany). Cet alliage, transparent en couche mince, permettait l'observation de la pousse des vésicules au microscope.

Pour ce protocole, une électrode d'ITO était couverte avec 5 μL de la solution lipidique, et les lipides furent séchés pendant 30 minutes sous vide. Une chambre était alors créée à l'aide de cire scellante (Vitrex, Copenhagen, Denmark), en façonnant à la main un cylindre de cire compressé ensuite entre les deux électrodes d'ITO. La chambre étanche ainsi obtenue est remplie avec une solution de sucrose à la concentration requise.

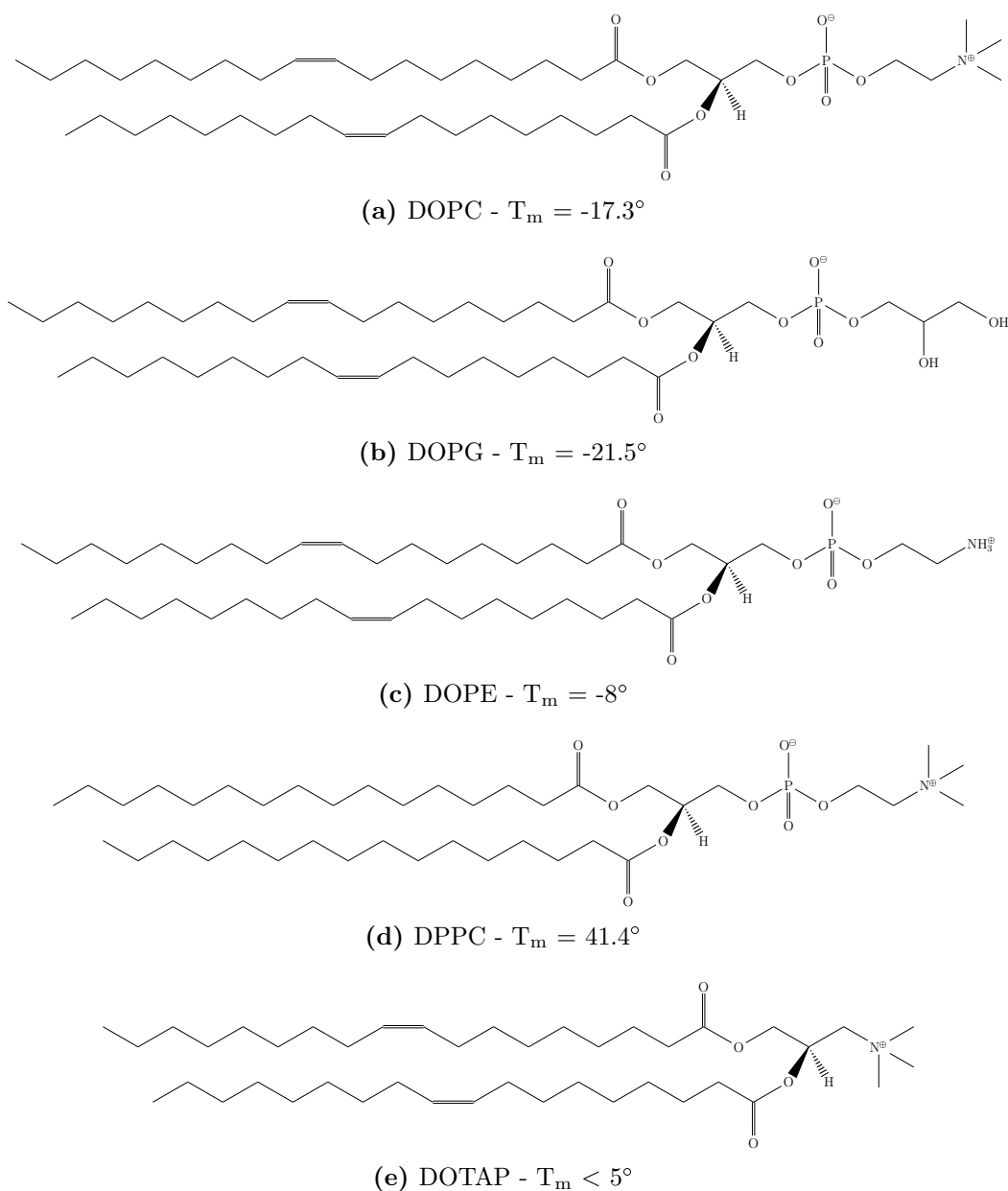


Figure 2.5: Représentations semi-développées des différents phospholipides et lipides artificiels utilisés dans ce travail, ainsi que leur température de transition gel-liquide (T_m). (a) DOPC: 1,2-dioleoyl-glycero-3-phosphatidylcholine, (b) DOPG: 1,2-dioleoyl-glycero-3-phosphatidylglycerol, (c) DOPE: 1,2-dioleoyl-glycero-3-phosphatidylethanolamine, (d) DPPC: 1,2-dipalmitoyl-glycero-3-phosphatidylcholine, and (e) DOTAP: 1,2-dipalmitoyl-trimethylammonium-propane. Toutes les températures de transition des phospholipides sont issues du Marsh's Handbook of lipid bilayers [22].

Les électrodes sont connectées à un générateur électrique, et l'électroformation est réalisée à 1 V_{PP} et 10 Hz pendant 4 à 15 heures. A la fin de l'électroformation, la chambre de pousse est ouverte et les vésicules collectées et transférées dans un microtube de centrifugation (Eppendorf, Hamburg, Germany). La solution est ensuite diluée une fois avec une solution de glucose isotonique et laissée au repos au réfrigérateur pendant 15-30 minutes avant utilisation, permettant la sédimentation des vésicules.

Le choix des solutions de sucrose et de glucose est motivée par deux raisons. Etant donné que le sucrose est plus dense que le glucose, la formation de vésicules avec du sucrose à l'intérieur et du glucose à l'extérieur force la sédimentation des vésicules au fond de la chambre. Cette sédimentation rend les vésicules plus faciles à collecter et plus faciles à observer au microscope. De plus, le sucrose et le glucose ayant deux indices optiques différents, cela crée un contraste de phase quand l'échantillon est observé au microscope optique. Plus d'informations sur ce point sont donnés plus tard dans ce chapitre. Les osmolarités des solutions de sucrose et glucose sont contrôlées grâce à un osmomètre cryoscopique (Gonotec Osmomat 030, Berlin, Germany).

B-2.b Formation assistée par gel de PVA

A cause du temps de pousse important, l'électroformation était parfois délaissée quand la formation rapide de GUV était requise. Dans ce cas, la méthode de formation de vésicule assistée par gel de PVA développée par l'équipe était utilisée [78]. Cette méthode permet d'obtenir un grand nombre de GUV en moins d'une heure, avec un grand nombre de vésicules unilamellaires.

Le gel de PVA a été préparé en dissolvant le polymère (masse molaire approximativement égale à 145000 g/mol) acheté auprès de Merck (Darmstadt, Germany) dans de l'eau ultrapure (Millipore, Billerica, MA, USA) avec un ratio massique de 5 %. La dissolution complète du PVA est assurée par chauffage de la solution à 90 °C tout en agitant. Après refroidissement, le gel de PVA était conservé pour plusieurs mois.

Une couche fine de gel ((70 μ L pour une surface de 76 \times 26 mm) était étalée sur un substrat de verre, initialement activée grâce à un nettoyeur UV-ozone pendant 15 minutes, et recuit à 80 °C pendant 30 minutes jusqu'à ce que le gel fut complètement sec. 5 μ L de la solution de lipide dans le chloroforme est déposé sur la surface et séché sous vide pendant 30 minutes. Le système est ensuite hydraté avec 150 μ L d'une solution de sucrose à la concentration requise pour un temps allant de 10 minutes à 1 heure, un temps suffisant pour permettre à un grand nombre de GUV de pousser. La suspension de vésicules est ensuite collectée et conservée au réfrigérateur dans un

microtube, dilué une fois avec une solution de glucose isotonique, et laissé au repos pendant 15-30 minutes pour laisser aux vésicules le temps de sédimenter.

B-2.c Formation de liposomes réalisée avec des lipides saturés

Les lipides saturés, comme le DPPC, sont le plus souvent en phase gel à température ambiante. Cet état n'est pas favorable à la formation de liposomes, à cause de l'absence de fluctuations de membrane suffisantes. Pour résoudre ce problème, les échantillons contenant les lipides saturés sont amenés dans leur phase fluide en chauffant la chambre de pousse pendant le processus.

Dans les deux méthodes décrites ci-dessus, les chambres sont placées à l'étuve, pré-chauffée à une température supérieure à celle de la température de transition gel-fluide, avant hydratation. La solution de pousse est aussi pré-chauffée dans un bain à eau à la même température. A cause de la chaleur, la cire Vitrex a du être remplacée par un espaceur en PTFE, et la chambre maintenue scellée avec des pinces. Tandis que la chambre d'électroformation est maintenue étanche, la chambre de pousse utilisée pour la formation assistée par gel de PVA doit rester ouverte pendant le processus. Dans ce cas, la chambre devait être hydratée régulièrement afin d'empêcher la dessiccation. Cette procédure peut conduire à des problèmes concernant la concentration finale de sucre.

Après formation, la solution de GUV peut être soit conservée à 4°C, soit à la température requise en immergeant le microtube dans un bain à eau chauffé.

B-3 Préparation de SUV et de LUV

Les expériences de titrations calorimétriques isothermes, de diffusion dynamique de la lumière, et de spectrofluorométrie ont nécessités des liposomes plus petits que les GUV. Pour cette raison, des SUV et LUV de lipides ont également été préparées, suivant les méthodes décrites ci-dessous.

B-3.a Solution de MLV

Les deux méthodes utilisées dans ce travail pour préparer des SUVs et des LUVs nécessitent une suspension initiale de MLV. Pour préparer la suspension de MLV, 1 à 10 μg de lipides dissous dans le chloroforme sont étalés au fond d'un pilulier en verre de 4 mL. Le solution est séché sous flux d'azote, et séché encore plus sous vide pendant 30 minutes au moins, afin que toute trace de chloroforme soit retiré de l'échantillon.

Les lipides sont hydratés avec la solution requises et secoué pendant quelques minutes. La solution résultante apparaît blanche et trouble, similaire à une solution de lait.

B-3.b Extrusion

Dans le but de briser les MLV en LUV de taille contrôlée, nous avons extrudé les liposomes au travers d'une membrane avec des pores de 100 nm de diamètre. L'extrudeur et les membranes ont été achetés auprès d'Avanti Polar lipids. Deux seringues en verre d'1 mL (Hamilton, Reno, NV, USA) sont insérées dans l'extrudeur, l'une contenant la solution de MLV à extruder, tel que montré dans la figure 2.6.



Figure 2.6: Photographie de l'extrudeur utilisé pour la préparation de LUV, acheté auprès d'Avanti Polar Lipids. La partie centrale du système contient une membrane poreuse. Une des seringue est remplie avec la suspension de MLV, et la suspension est poussée au travers de la membrane 21 fois. Les MLV se brisent au passage de la membrane en LUV. La photographie est extraite du site internet d'Avanti Polar Lipids [191].

La solution est poussée au travers de la membrane 21 fois tel que requis par le protocole du fournisseur.

B-3.c Sonication

Une autre façon de briser les MLV en SUV et LUV est la sonication de l'échantillon de MLV. Cette méthode rapide a été utilisée dans ce travail afin de produire des petits liposomes quand le contrôle de leur taille n'était pas essentiel.

Dans ce but, le pilulier de verre était simplement immergé dans un bain à ultrason pour temps allant de 30 minutes à 1 heure.

C Analyse de la membrane

Dans cette section sont décrites les différentes méthodes expérimentales utilisées pour analyser les membranes lipidiques, les biomolécules d'intérêt, les sondes molé-

lares, et leurs différentes interactions.

C-1 Microscopie optique

Développée durant le XVII^{ème} siècle, le microscope, et plus précisément le microscope optique, a toujours été le dispositif expérimental utilisé par les scientifiques de tout domaine pour étudier les membranes. En effet, le microscope optique permet d'observer des objets avec une résolution allant jusqu'à $1 \mu\text{m}$. Tandis qu'une telle résolution est toujours trop faible pour distinguer précisément les différents constituants de la membrane, elle est assez forte pour analyser le comportement général de cette dernière dans une grande gamme de situations.

C-1.a Résolution d'un microscope

La résolution latérale d'un microscope est définie comme la distance minimale au-dessus de laquelle il est possible de distinguer deux objets ponctuels au travers du système optique. La résolution latérale maximale r_{max} d'un microscope dépend de λ , la longueur d'onde de la lumière utilisée pour observer l'échantillon, et de l'ouverture numérique du microscope NA . Plusieurs équations décrivent cette relation, telle que

$$r_{max} = \frac{\lambda}{2NA}. \quad (2.1)$$

L'ouverture numérique du microscope est un nombre sans dimension qui caractérise l'angle maximal i par lequel la lumière peut être collectée ou émise par le système, tel que montré dans la figure 2.7.

L'ouverture numérique est donnée par

$$NA = n \sin(i), \quad (2.2)$$

où n représente l'indice de réfraction du milieu. Pour améliorer la résolution du microscope il est donc possible de diminuer la longueur d'onde de la lumière où d'augmenter l'ouverture numérique du microscope (*cf.* équation 2.1). Par exemple, un objectif Nikon x100 à immersion à huile plan achromat avec une ouverture numérique de 1.40 a une résolution de 196 nm, si l'on considère la longueur d'onde moyenne de 550 nm [192].

La résolution longitudinale du microscope, aussi appelée profondeur de champ d_{tot} , correspond à la distance entre le plan objet net le plus proche et le plan objet net le plus éloigné au même moment. La profondeur de champ est donnée par

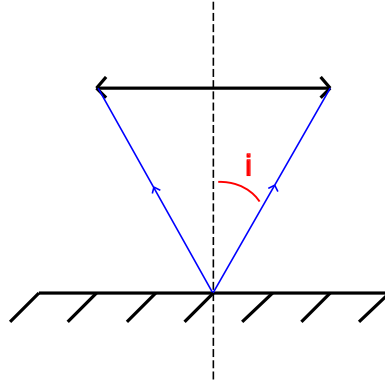


Figure 2.7: Illustration de la définition de l'ouverture numérique NA d'un microscope. NA est donné par i , l'angle maximal à lequel la lumière peut être collectée par le système à partir d'un seul point, et de n l'indice de réfraction du milieu. La distance de travail à laquelle i peut être calculé est une caractéristique du système optique pour l'objectif.

$$d_{tot} = \frac{\lambda \cdot n}{NA^2} + \frac{n}{MNA}e, \quad (2.3)$$

où n est l'indice de réfraction du milieu entre la lamelle de microscope et la lentille de l'objectif de grossissement M (air, eau ou huile d'immersion) et e est la plus petite distance pouvant être résolue avec un détecteur placé dans le plan image de l'objectif. e est donné par la taille des pixels de la caméra (en incluant l'échantillonnage possible). La profondeur de champ et la longueur d'onde doivent être exprimés en unités similaires. Pour le dispositif décrit plus haut, et avec une caméra possédant des pixels carré de $7.4 \mu\text{m}$, la profondeur de champ d_{tot} est égale à 559 nm [193].

C-1.b Microscopie de contraste

L'épaisseur d'une bicouche lipidique est d'approximativement 5 nm [22], ce qui est beaucoup trop petit par rapport à la résolution maximale d'un microscope optique, ainsi qu'il l'a été démontré ci-dessus. Etant donné que les GUVs sont typiquement remplies avec une solution aqueuse transparente, elles apparaîtraient comme des objets presque totalement transparents, leur observation au microscope étant par conséquent loin d'être triviale. Pour résoudre ce problème, il est possible d'utiliser des méthodes pour améliorer les contrastes d'un microscope optique.

Tel que décrit dans la section B-2 du présent chapitre, les GUVs sont couramment préparées dans une solution de sucrose avant dilution dans une solution de glucose isotonique. Les deux milieux ayant des indices optiques n différents, la lumière va voyager plus vite dans un milieu que dans l'autre. Cela crée une différence de phase, ce

qui cause des interférences, telles que présentées dans la figure 2.8, obtenant ainsi un meilleur contraste. En plus du contraste de phase, il est également possible d'obtenir un contraste d'amplitude. Ici les contrastes entre les différentes parties de l'échantillon sont induits par les différentes absorptions de la lumière [194]. Le contraste d'amplitude produit un effet similaire au contraste de phase et rend les objets comme les GUVs distinguable au microscope.

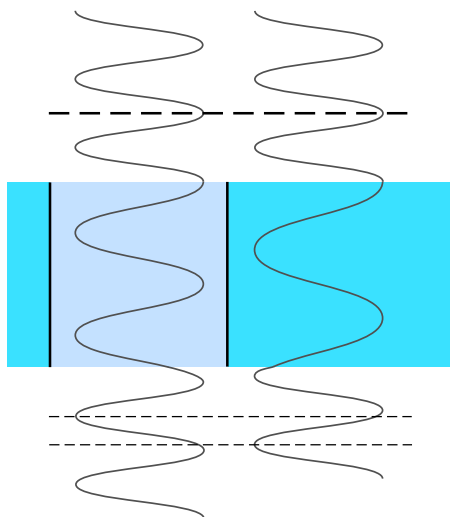


Figure 2.8: Illustration du contraste de phase entre deux milieux, typiquement la solution tampon (bleu sombre) et la solution interne d'une GUV (bleu clair). A cause de la différence d'indice de réfraction, un décalage de phase apparaît après que la lumière ai traversé l'échantillon.

Afin d'utiliser de façon avantageuse ces effets, plusieurs techniques de microscopie ont été développées. Ces techniques peuvent être classifiées en tant que techniques de microscopie améliorant le contraste.

- La microscopie à contraste de phase améliore encore plus le contraste en produisant des interférences destructrices. Dans ce but, deux éléments sont ajoutés sur le chemin optique du microscope: un anneau de phase sur le condenseur, et une plaque de phase sur l'objectif. L'anneau et la plaque ont des formes complémentaires. Le principe a été découvert et développé par Zernike [195]. Cette méthode augmente les contrastes entre les solutions internes et externes des GUVs (*cf.* figure 2.9(a)).
- Microscopie à contraste interférentiel différentiel (DIC) utilise des prismes et des polariseurs au-dessus et en-dessous de l'échantillon pour séparer et recombinaer les rayons. Dans ce système, développé et breveté par Nomarski in 1952 [196], les

interférences sont induites par la variation des longueurs du chemin optique. En conséquence, le DIC augmente plus les contrastes entre la membrane et le milieu aqueux qu'entre les solutions internes et externes, donnant typiquement un relief tridimensionnel à l'image (*cf.* figure 2.9(b)).

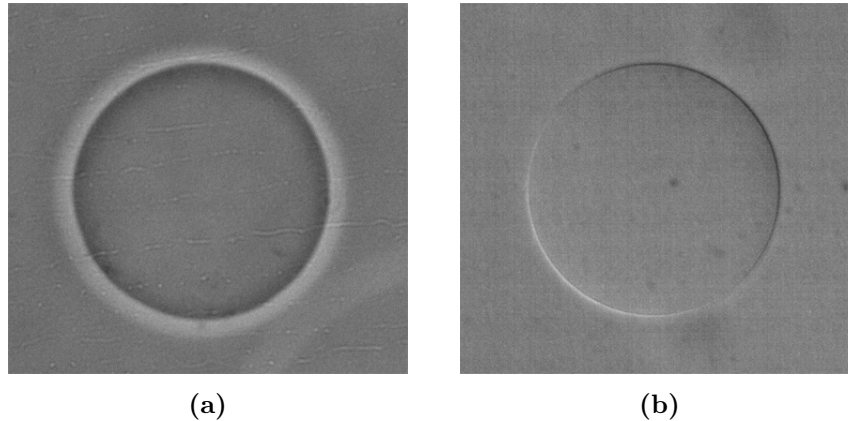


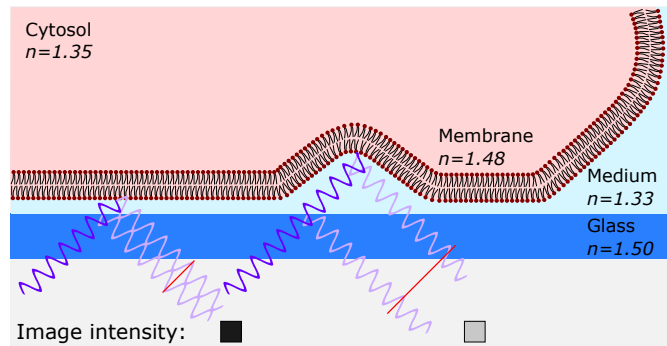
Figure 2.9: Photographies de deux GUVs en microscopie améliorant le contraste: (a) microscopie à contraste de phase, et (b) microscopie à contraste interférentiel différentiel (DIC). La microscopie à contraste de phase optimise le contraste entre l'intérieur et l'extérieur de la membrane, tandis que le DIC augmente les contrastes entre la membrane lipidique et la solution.

C-1.c Microscopie interférométrique

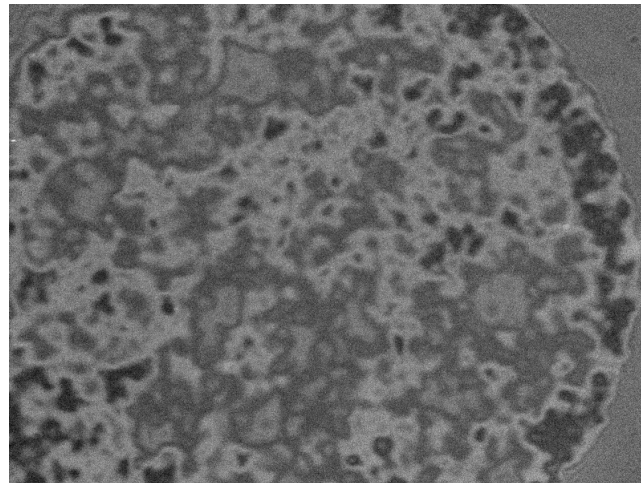
De nouvelles méthodes de microscopie optiques utilisant les interférences sont toujours développées, étant donné que ces méthodes ont des capacités en dehors de celles de la microscopie optique classique, telle que la détection de variations nanométrique dans la position d'objets plus petit que la résolution maximale du microscope. Deux de ces méthodes sont décrites brièvement ici.

En 1962, Curtis a réalisé des expériences sur l'adhésion de cellule sur une surface de verre en utilisant ce qu'il a appelé la microscopie par réflexion d'interférence [197]. Des décennies plus tard, Zilker *et al.* [198] ont appliqué le principe de Curtis à la mesure du module d'élasticité de courbure de la membrane cellulaire dans une méthode nommée microscopie de contraste par réflexion d'interférences (RICM). Contrairement au DIC, qui utilise les interférences pour augmenter les contrastes entre la membrane et la solution, le RICM ne visualise que la portion de la membrane située à proximité de la surface de verre sous elle. En RICM, les contrastes sont produit par les interférences

entre le rayon de référence, réfléchi par la surface de verre, et les rayons réfléchis par la membrane, tel que montré dans la figure 2.10. Avec cette méthode, des fluctuations de la membrane de quelques nanomètres peuvent être visualisés [199].



(a)



(b)

Figure 2.10: (a) Description de la microscopie de contraste par réflexion d'interférence. Les différents retards entre la lumière réfléchi par le verre et la lumière réfléchi par la membrane lipidique à différentes hauteurs génère différents contrastes à cause des interférences. *Illustration source: Wikipedia.* (b) Photographie d'une membrane lipidique reposant sur une surface de verre prise en RICM. Les différentes nuances de gris correspondent à différentes hauteurs de la membrane.

Plus récemment, Lindfors *et al.* ont démontré que les interférences en microscopie pouvaient être utilisées pour détecter et suivre des objets avec une taille aussi petite que 10 nm [200]. La microscopie à diffusion interférométrique (iSCAT) utilise les interférences générées par la lumière diffusée par des nanoparticules d'or avec la lumière réfléchi par la surface de verre lorsque l'échantillon est illuminé avec un laser pour

visualiser la position tridimensionnelle des billes d'or. La position et les mouvements peuvent alors être enregistrés au microscope avec une précision nanométrique.

C-2 Microscopie de fluorescence

Les méthodes de microscopies interférentielles utilisent les interférences produites par la superposition de deux signaux pour détecter et suivre des objets nanométriques dans un échantillon. Mais dans tous les cas, la plupart des objets dans l'échantillon, même ceux n'ayant pas d'intérêt, peuvent être visualisés sur les images obtenues. La microscopie de fluorescence permet de choisir précisément les objets que l'on désire observer sur les images finales. En effet, seuls les objets marqués en fluorescence peuvent être détectés et donc visualisés dans cette méthode.

C-2.a Bases

Lorsqu'elles sont illuminées par une source de lumière, les molécules vont absorber des énergies précises, correspondant aux différences d'énergie entre leurs niveaux électroniques. Cette absorption va faire passer les électrons d'un état fondamental (S_0) à un état excité (S_1). Ces molécules excitées vont chercher les façons les plus rapides de ramener leurs électrons à l'état fondamental. La solution la plus commune pour ces molécules est la conversion en agitation thermique. Cependant, pour certaines molécules, la façon la plus favorable de revenir à l'état fondamental est d'émettre un photon. Ce phénomène est appelé fluorescence. Les molécules qui ont cette capacité sont appelées sondes fluorescentes, ou fluorophores. Un des fluorophore les plus célèbre est la fluorescéine, synthétisé en 1871 par Adolf Baeyer [201], et présenté dans la figure 2.11(a).

A cause des vibrations moléculaires, une petite quantité d'énergie est perdue entre l'absorption et l'émission des photon. En conséquence, les photons émis auront une énergie plus basse que celle des photons absorbés, et donc une longueur d'onde différente. Ce décalage en longueur d'onde est appelé le décalage de Stokes (*cf.* figure 2.11(b)). A cause de ce phénomène, les longueurs d'ondes d'excitation et d'émission peuvent être optiquement séparées par des filtres colorés. En faisant cela, la lumière collectée par le microscope correspond strictement à la lumière émise par la sonde fluorescente.

L'observation optimale de la fluorescence en microscopie requiert l'utilisation d'une géométrie spécifique pour le microscope nommée réflexion (voir *figure 2.12*). Dans ce mode, la lumière n'est pas transmise au travers de l'échantillon, mais émise et collectée du même côté. Un miroir dichroïque est utilisé pour séparer la lumière d'excitation

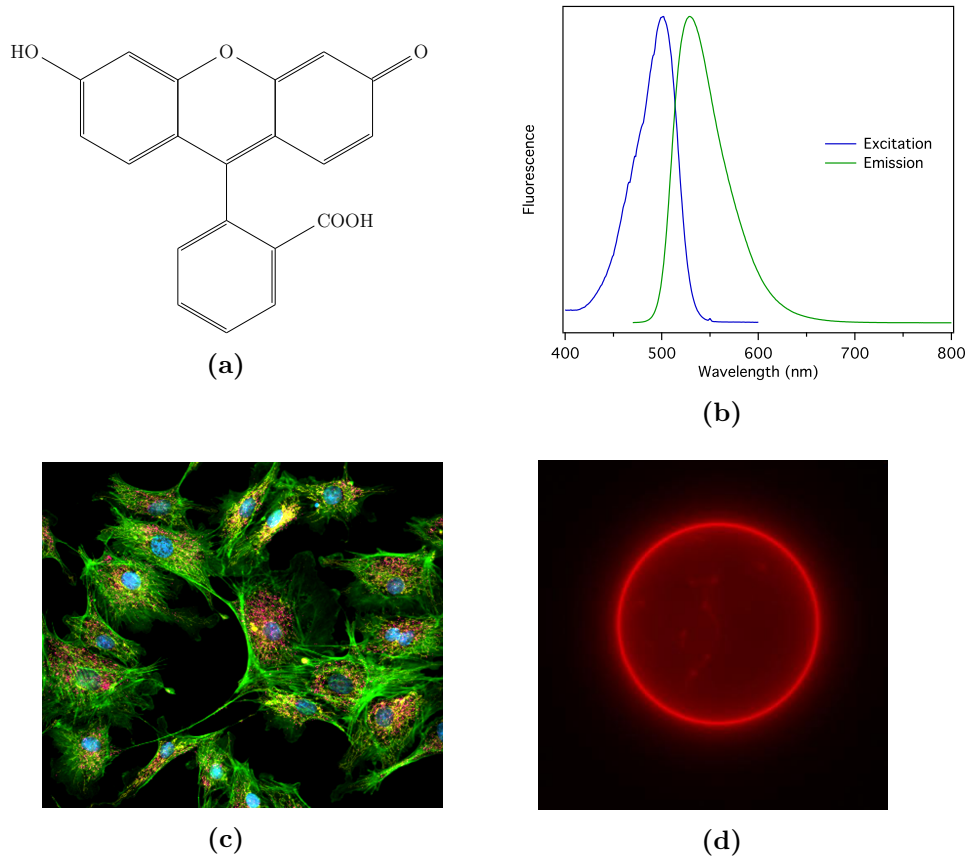


Figure 2.11: (a) Formule semi-développée de la fluorescéine. (b) Illustration du déplacement de Stokes entre les spectres d'émission et d'excitation d'une sonde HiLyte 488, un dérivé de la fluorescéine. (c) Photographie de cellules prises en microscopie de fluorescence. Seulement les parties de la cellule marquées avec une sonde fluorescente peuvent être vues. Ici, les mitochondries sont marquées en orange, l'actine en vert, et les noyaux en bleu. La photographie provient de Probes Online Newsletter [202]. (d) Photographie en microscopie de fluorescence d'une GUV marquée en fluorescence.

de la lumière émise par l'échantillon et collectée par le système, de sorte à éviter les perturbations causées par la lumière d'excitation. Le miroir dichroïque et les filtres d'émission et d'excitation sont choisis en fonction de la nature de la sonde fluorescente étudiée.

La microscopie n'est pas la seule méthode expérimentale basée sur la fluorescence. Par exemple, la fluorescence peut aussi être utilisée en cytométrie de flux, une méthode utilisée pour compter les cellules d'un échantillon donné en forçant un flux de cellules dans un tube équipé d'un détecteur optique [203]. En cytométrie de flux, la fluorescence peut être utilisée pour simplement augmenter la sensibilité du détecteur, mais aussi

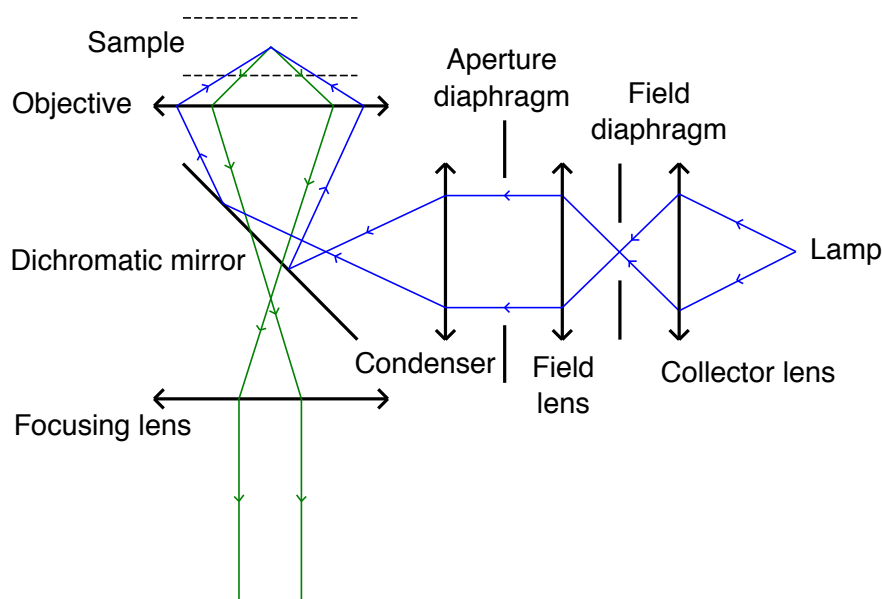


Figure 2.12: Concept de la microscopie de réflexion utilisée en fluorescence. La lumière est émise et collectée du même côté de l'échantillon, diminuant ainsi la collecte de la lumière incidente par le détecteur. Les deux rayons sont séparés par un miroir dichroïque.

pour discriminer différents types de cellules et ainsi obtenir un ratio précis sur une population entière. La fluorescence peut aussi être utilisée pour séparer différentes populations de cellules dans un échantillon, en activant ou désactivant un électroaimant à la détection d'un signal fluorescent quand une cellule traverse le détecteur [204]. Les cellules fluorescentes et non-fluorescentes sont ainsi dirigées vers différents endroits.

C-2.b Sondes fluorescentes

La fluorescéine est loin d'être la seule sonde fluorescente utilisée en microscopie. Une grande gamme de molécules ont été développées et synthétisées par les chimistes, afin de couvrir les longueurs d'ondes de la lumière visible, ultraviolette, et même infrarouge [205]. Les sondes fluorescentes sont des systèmes conjugués, principalement composés de cycles aromatiques, tel qu'on peut l'observer sur la formule semi-développée de la fluorescéine (*cf.* figure 2.11(a)). De plus, on peut également trouver plein de dérivés commerciaux de la fluorescéine, modifiée pour améliorer ses performances, sa stabilité, ou ses longueurs d'ondes caractéristiques.

Il y a cinq paramètres définissant les propriétés d'une sonde fluorescente: les longueurs d'onde d'excitation et d'émission, le coefficient d'extinction, le rendement quantique de fluorescence et la sensibilité au photoblanchiment:

- Les longueurs d'onde d'excitation (λ_{EX}) et d'émission (λ_{EM}) doivent être sélectionnées avec précaution quand deux sondes sont présentes dans l'échantillon afin d'éviter un transfert de fluorescence. En effet, si une sonde fluorescente émet dans une longueur d'onde proche de celle d'une autre sonde présente dans l'échantillon, elles seront impossibles à distinguer. Aussi, si la longueur d'onde d'émission de la sonde correspond à la longueur d'onde d'excitation d'une seconde sonde, la première aura une efficacité de fluorescence drastiquement réduite. Certaines techniques, comme le transfert d'énergie par résonance de type Förster (FRET) [206], sont basées sur cet effet, mais les méthodes traditionnelles pour l'observation et la quantification peuvent en souffrir.
- Le rendement quantique de fluorescence Φ peut être défini comme le ratio entre le nombre de photons émis et le nombre de photons absorbés par la sonde. Plus le rendement quantique est élevé, et plus l'échantillon apparaîtra brillant pour la même énergie d'excitation.
- Durant le processus de fluorescence, la structure des fluorophores peut être modifiée, par coupure de liaisons covalentes ou par réactions avec les molécules environnantes. Habituellement ces transformations ne sont pas réversibles et les sondes perdent leurs capacités de fluorescence. Cet effet est connu sous le nom de photoblanchiment. La plupart du temps on cherche à éviter le photoblanchiment et les sondes sont choisies en conséquence. Cependant certaines techniques de microscopie de fluorescence telle que le recouvrement de fluorescence après photoblanchiment (FRAP) nécessite des sondes sensibles à cet effet [207].
- Le coefficient d'extinction ϵ d'une molécule est le paramètre utilisé principalement dans la mesure de l'absorption de la lumière transmise. Quand la lumière traverse une solution, une partie de la lumière est absorbé par le soluté. Plus la fraction est grande et plus la profondeur de pénétration de la lumière dans l'échantillon sera faible. La fraction de lumière absorbée par l'échantillon par unité de volume est donnée par ϵ . En microscopie de fluorescence, la distance parcourue par la lumière dans l'échantillon est d'environ $10 \mu\text{m}$, ce qui est plus faible que la distance à laquelle l'absorption de la lumière est significative.

Bien entendu, il faut également choisir la sonde fluorescente en fonction du système optique disponible et en fonction de la capacité à la sonde à se lier chimiquement à la molécule que l'on souhaite marquer. Par exemple, le YOYO-1 est utilisé pour marquer l'ADN pour sa capacité à pénétrer la double hélice et à s'y attacher [208]. Les différents

matériaux observés en microscopie de fluorescence dans ce travail ont été marqués avec différentes sondes, listées dans la *table 2.2*.

Nom	λ_{EX} (nm)	λ_{EM} (nm)
AlexaFluor 488	496	518
BODIPY	487	517
HiLyte 488	502	529
NBD	457	528
RhoB	572	593
YOYO-1	491	509

Table 2.2: Liste des sondes fluorescentes utilisées dans ce travail, avec leurs longueurs d’onde d’excitation et d’émission. Les longueurs d’ondes ont été mesurées à partir de leurs spectres de fluorescence respectifs, qui peuvent être trouvés dans les Appendices Apx-1 et Apx-2.

Les lipides ont été marqués avec du nitrobenzoxadiazol (NBD) ou de la rhodamine B (RhoB), tous deux achetés auprès d’Avanti Polar Lipids. La RhoB, qui émet dans le rouge, a été utilisée pour l’observation de l’interaction entre les lipides et les peptides, qui ont été marqués avec de l’AlexaFluor 488, du BODIPY ou du HiLyte 488, toutes trois émettant dans le vert. L’ADN a été marqué avec du YOYO-1. Plus d’informations sur les formules semi-développées et leurs spectres de fluorescence peuvent être trouvées dans les Appendices Apx-1 et Apx-2.

C-2.c Quantification de la fluorescence

Etant donné que la lumière fluorescente émise est seulement produite par les molécules marquées en fluorescence, et étant donné que l’intensité d’émission est liée à la concentration en sondes, plusieurs méthodes ont été développées afin de quantifier un échantillon en utilisant l’imagerie en fluorescence [209].

Dans la plupart des cas simples, la fluorescence peut être utilisée pour compter les objets dans un échantillon. Cela peut permettre de compter tous les objets, ou de faire la distinction entre différentes sortes d’objets en n’en marquant qu’un type [210].

La fluorescence peut aussi être utilisée pour suivre des objets individuels dans un échantillon au cours du temps [211]. Au travers de cette méthode, on peut déterminer les coefficients de diffusion des objets marqués dans un milieu. De telles mesures peuvent être réalisées sur une membrane marquée en utilisant la méthode de FRAP [207].

Dans ce cas, certains lipides sont marqués en fluorescence. L'image apparaît initialement homogène. Une petite fraction de la membrane est alors blanchie en focalisant un puissant rayon lumineux, et le temps nécessaire pour retrouver un état homogène est mesuré. Finalement, le coefficient de diffusion du lipide est calculé à partir du temps caractéristique du recouvrement de fluorescence (cf. figure 2.13).

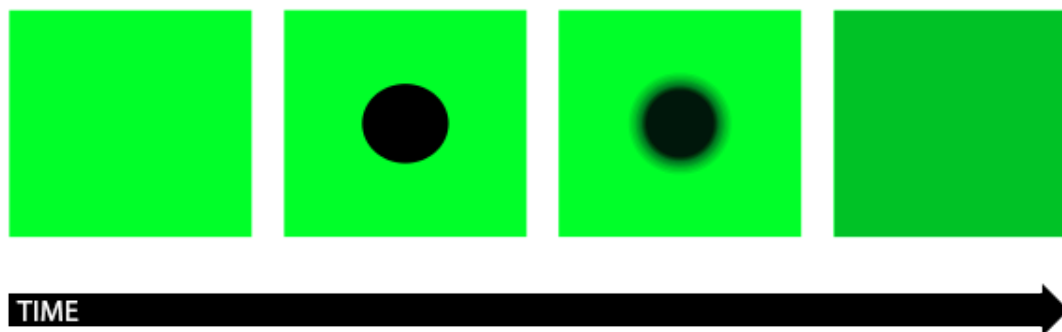


Figure 2.13: Illustration de la technique de FRAP. Une membrane, apparaissant fluorescente de façon homogène initialement, est blanchie dans un domaine restreint. A cause de la diffusion latérale des lipides dans la membrane, cette dernière va retrouver son homogénéité après un certain temps, duquel on peut calculer le coefficient de diffusion du lipide.

L'intensité locale de la fluorescence peut être aussi reliée à la concentration locale de sonde fluorescente ou d'autres paramètres. Tandis que l'intensité de fluorescence émise dépend de la puissance de la lumière excitante, elle dépend également de la concentration en fluorophores. En conséquence, deux zones de la même image avec deux concentrations différentes en sonde auront différentes intensités en fluorescence. En utilisant cette propriété, la microscopie peut être utilisée pour mesurer directement les concentrations locales dans un échantillon [212].

Cependant la proportionnalité entre l'intensité et la concentration n'est valable que dans une certaine gamme de concentrations. Si la concentration est trop importante, les fluorophores peuvent souffrir d'auto-*quenching*. En effet, si la distance entre deux fluorophores est assez faible, l'énergie de la sonde excitée sera transférée à l'autre sonde, au lieu d'être émise sous forme de photon. L'intensité diminuera donc à haute concentration, tel que montré dans la figure 2.14. Pour maintenir la proportionnalité, il vaut mieux travailler dans de gammes de concentrations faibles, et une calibration est donc nécessaire pour s'assurer de travailler dans les bonnes conditions.

Certaines sondes fluorescentes peuvent aussi être sensibles à la température, et leur intensité sera donc une fonction de la température locale dans l'échantillon. Cette

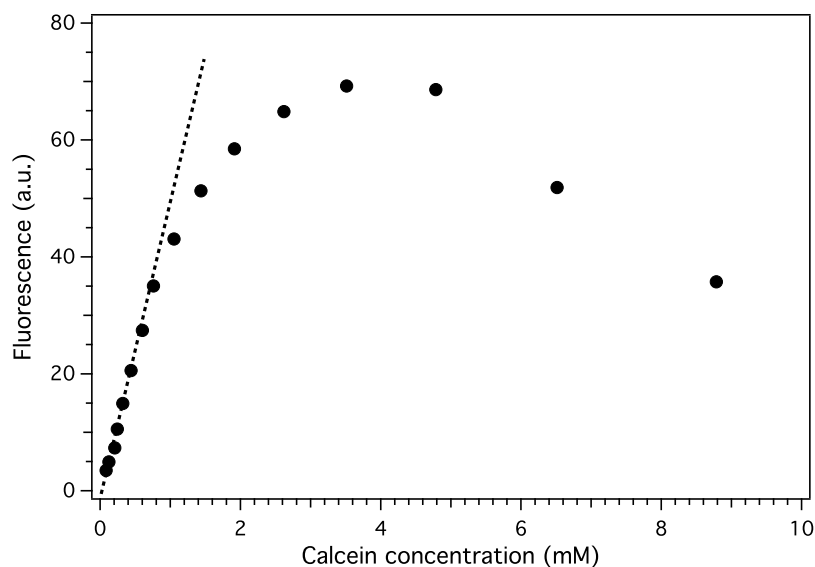


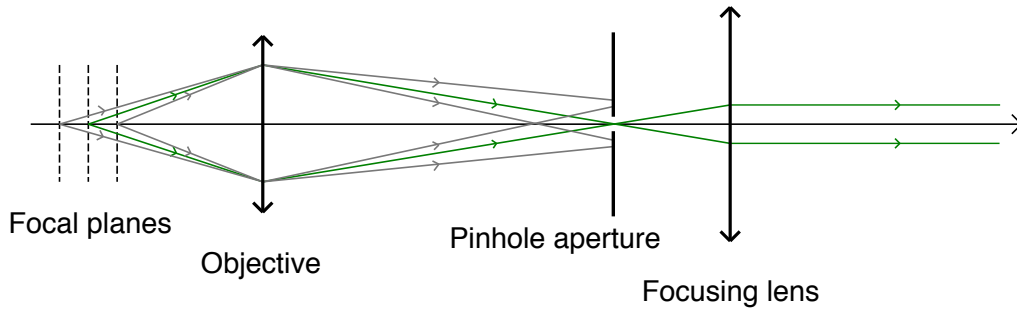
Figure 2.14: Intensité de fluorescence en fonction de la concentration en sonde. Au-dessus d'une concentration de 2 mM, l'intensité de fluorescence n'est plus proportionnelle à la concentration en fluorophore à cause de l'auto-*quenching*, et diminue au-dessus de 4 mM. L'image a été adaptée de l'article de Hamann *et al.* [213]

propriété peut notamment être utilisé afin de réaliser une imagerie des gradients de température en microscopie [214].

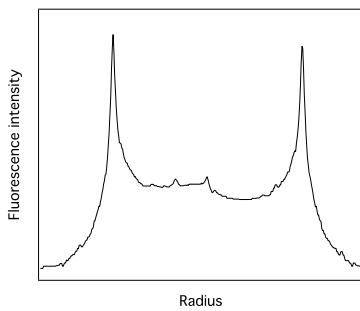
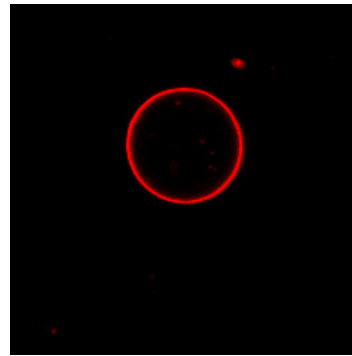
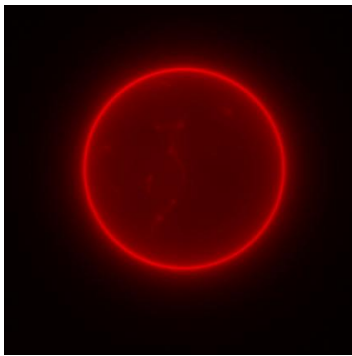
C-2.d Microscopie confocale

La méthode de microscopie confocale est une modification du principe de la microscopie optique, décrite pour la première fois par Marvin Minsky en 1961 [215]. Un petit trou d'épingle - avec un diamètre inférieur ou égal à $100\ \mu\text{m}$ - est placé dans le plan confocal de la lentille de l'objectif, afin d'éliminer les rayons non-focalisés collectés par le système, tel que montré dans la figure 2.15. En conséquence, seule une petite tranche de l'échantillon est imagée, environ 500 nm, et en accumulant les images de l'échantillon à différentes positions il est possible de générer une reconstruction tridimensionnelle de l'échantillon.

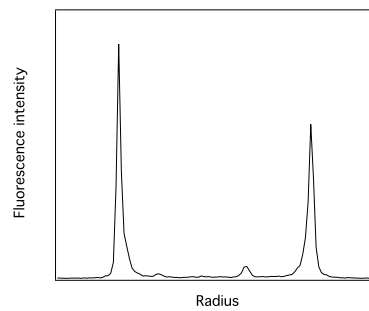
Les microscopes confocaux se basent sur l'utilisation d'une source laser pour imager les échantillons. Le microscope confocal focalise le rayon laser sur le point d'intérêt de l'échantillon, et utilise des miroirs galvanométriques oscillants pour déplacer le point d'intérêt dans l'intégralité de l'échantillon, le scannant ainsi point par point. L'image finale est donc une reconstruction de cette imagerie point par point, ce qui limite la fréquence d'échantillonnage du système. On parle donc de microscopie confocale à



(a)



(b)



(c)

Figure 2.15: (a) Microscopie confocale: une ouverture en trou d'épingle est placée dans le plan confocal de l'objectif, correspondant au plan focal d'intérêt. Toute la lumière provenant d'objets non-focalisés est arrêtée par le trou d'épingle. Plus le trou d'épingle est grand et plus le plan focal observé sera épais. Comparaison de vésicules visualisées en microscopie de fluorescence (b) et en microscopie confocale (c), avec leurs profils d'intensité diamétraux respectifs. En microscopie confocale, seule une fine tranche de la GUV peut être visualisée, qui apparaît alors comme un anneau.

balayage laser (CLSM).

L'épaisseur de la tranche optique enregistrée par le microscope confocal th_{confocal} est fonction du diamètre du trou d'épingle (PH) et dépend des fonctions tridimensionnelles d'étalement des points, tels que

$$th_{\text{confocal}} = \sqrt{\left(\frac{\lambda_{ex}n}{NA^2}\right)^2 + \left(\frac{n\sqrt{2}PH}{NA}\right)^2}. \quad (2.4)$$

Dans l'équation 2.4, le diamètre du trou d'épingle PH doit être exprimé en unité d'Airy, ce qui correspond au ratio entre le diamètre du trou d'épingle et le diamètre du disque d'Airy généré avec le même système optique. Le diamètre du disque d'Airy dans le plan image est donné par

$$d_{\text{Airy}} = \frac{1.22\lambda_{ex}}{NA} M_{\text{tot}}, \quad (2.5)$$

où M_{tot} correspond au grossissement total du système, *i.e.* M_{tot} est le produit du grossissement de l'objectif M avec le grossissement du reste du système M_{sys} . Avec les valeurs utilisées dans la section C-1.a du chapitre présent, en considérant un trou d'épingle avec un diamètre de $30 \mu\text{m}$, et avec M_{sys} égal à 1, les équations 2.5 et 2.4 donnent une épaisseur optique de $1.05 \mu\text{m}$ [216].

C-3 Systèmes expérimentaux

Toutes les observations utilisant la microscopie en transmission standard ou en fluorescence ont été réalisées sur un Nikon TE-200, présenté dans la figure 2.16(a), ou un microscope Nikon Ti Eclipse.

Les objectifs utilisés étaient des Nikon x10 plan fluor avec une ouverture numérique de 0.30 pour les observations en champ large, ou un Nikon x40 plan fluor avec une ouverture numérique de 0.60 pour des observations plus précises. Pour améliorer les contrastes entre solutions internes et externes aux GUV, le diaphragme d'ouverture du microscope était presque entièrement fermé (figure 2.16(b)). Les images et vidéos ont été enregistrées avec une caméra 1.80 monochrome de chez Diagnostic instruments (Sterling Heights, MI, USA), avec une résolution de 800×600 $14.8 \mu\text{m}$ unités CCD carrées (échantillonnage 2 avec $7.4 \mu\text{m}$ unités CCD carrées).

Pour la microscopie confocale, nous avons utilisé un Nikon TE-2000 Eclipse équipé d'une tête confocale Nikon D-Eclipse C1si et d'une source laser argon-ion (Melles-Griot, Bensheim, Germany). Toutes les images ont été enregistrées en utilisant le logiciel Nikon EZ-C1.

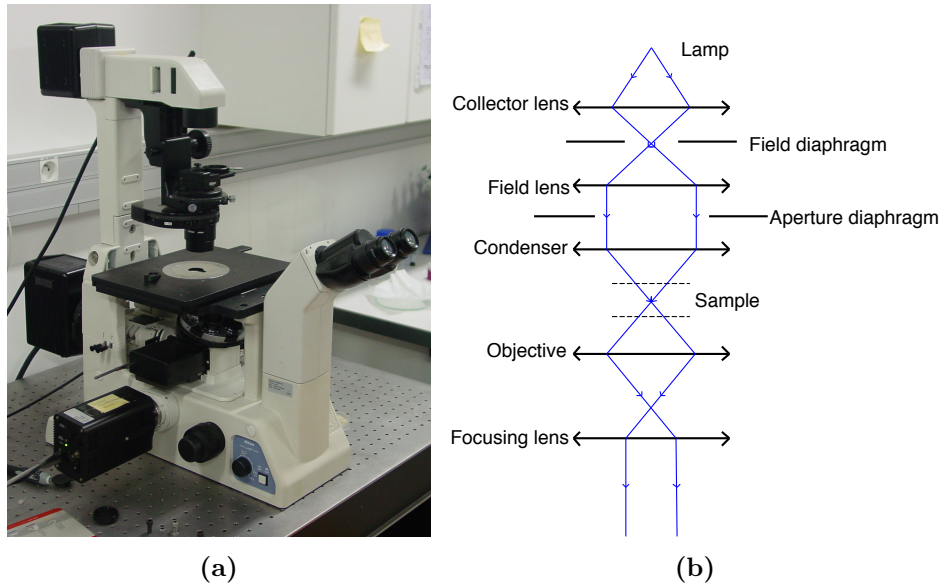


Figure 2.16: (a) microscope inversé Nikon TE-200 utilisé dans ce travail, et (b) représentation schématique du système optique du microscope, avec les différents diaphragmes qui peuvent être utilisés pour mettre au point et améliorer les contrastes.

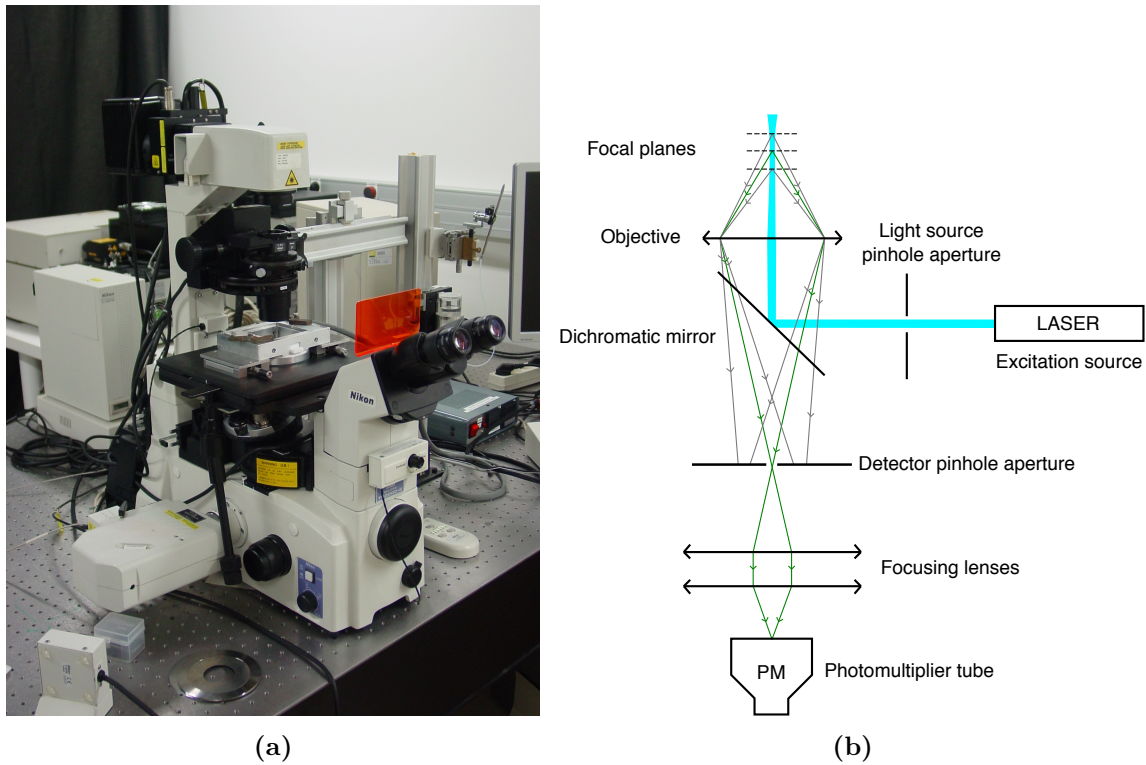


Figure 2.17: (a) Microscope confocal inversé Nikon TE-2000 C1 Eclipse utilisé pour ce travail, et (b) représentation schématique de notre système optique pour le CLSM. La source de lumière est un laser argon-ion.

L'objectif utilisé était un Nikon x60 à immersion à eau plan achromat avec une ouverture numérique de 1.20. Avec une longueur d'onde de travail de 488 nm, l'équation 2.1 prédit une résolution maximale pour notre système de 203 nm. Alors que l'ouverture du trou d'épingle la plus petite du microscope (30 μm de diamètre) obtiendrait la tranche confocale la plus fine, le diamètre du trou d'épingle a été fixé à l'ouverture la plus large (100 μm) pour maximiser l'intensité lumineuse collectée par le système.

Les résolutions latérales et longitudinales de chaque système optique, ainsi que l'épaisseur confocale pour l'objectif x60, obtenues par les équations 2.1, 2.3 et 2.4, sont listées dans la table 2.3.

Objectif	r_{max} (μm)	d_{tot} (μm)	th_{confocal} (μm)	
			S	L
x10	0.92	11.14		
x40	0.46	2.17		
x60	0.20	1.00	1.64	5.28

Table 2.3: Liste des résolutions latérales et longitudinales des microscopes pour les différents objectifs utilisés avec une caméra 1.80 monochrome de chez Diagnostic Instruments. L'épaisseur confocale de l'objectif x60 est également donnée pour les trous d'épingles petits (S) et larges (L). Une longueur d'onde moyenne de 550 nm est utilisée pour calculer les valeurs pour les objectifs x10 et x40, tandis qu'une longueur d'onde d'émission de 488 nm est utilisée pour l'objectif x60.

Toutes les photographies, prises avec un microscope optique standard ou avec le microscope confocal, ont été analysées et traitées en utilisant le logiciel libre ImageJ [217]. Les images prises avec le microscope confocal avec le plug-in Bioformat du site internet Open Microscopy Environment [218].

D Produits chimiques

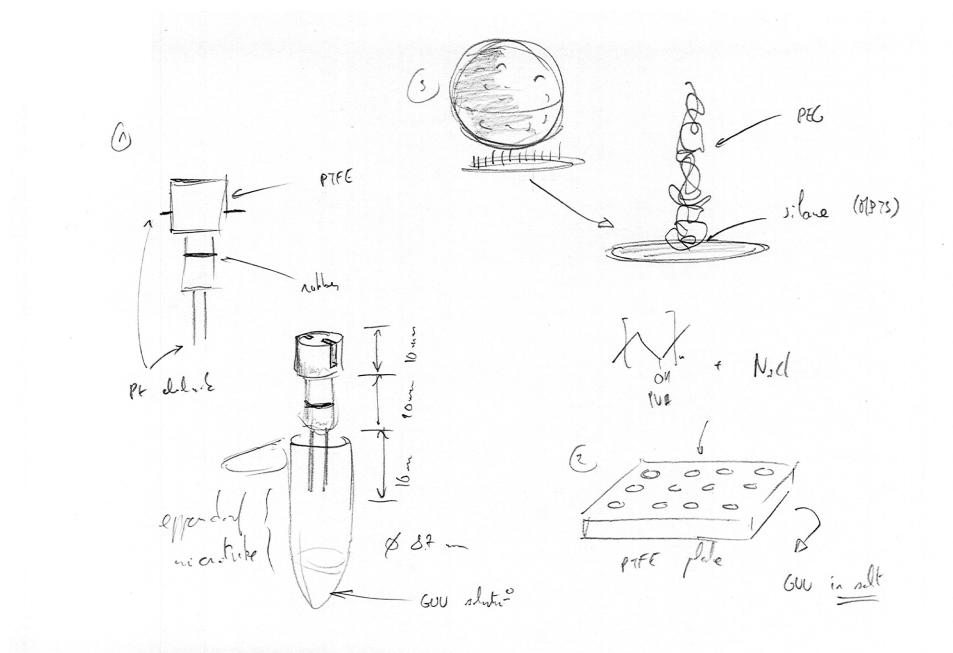
Nous listons ici les produits chimiques synthétisés, achetés, et utilisés dans ce travail. La table 2.4 donne la liste exhaustive de tous les fournisseurs et des produits achetés auprès d'eux, et la table 2.5 énumère les abréviations utilisés pour faire référence à un produit chimique spécifique.

Fournisseur	Provenance	Produits
Sigma-Aldrich	Saint-Quentin Fallavier (FR)	Sucrose, glucose, MPTS CHCl ₃ et EtOH (qualité HPLC) MeO-PEG ₅₀₀₀ -Mal
Avanti Polar Lipids	Alabaster, AL (USA)	DOPC, DOPG, DOPE DPPC, DPPE-NBD, DPPE-RhoB DOTAP
AnaSpec	Fremon, CA (USA)	TAT ₄₇₋₅₇ , Arg8, Arg5
Thermo Scientific	Waltham, MA (USA)	MeO-PEG ₁₂ -Mal
Invitrogen	Carlsbad, CA (USA)	Salmon sperm DNA
Fermentas	Waltham, MA (USA)	Lambda-phage DNA
Molecular Probes	Eugene, OR	YOYO-1
Carlo Erba Reagents	Val de Reuil (FR)	Solvants pour nettoyage: CHCl ₃ , EtOH, Acétone, Toluène

Table 2.4: Fournisseurs des différents produits chimiques utilisés dans ce travail.

Abréviation	Nom complet
Lipides	
DOPC	1,2-dioleoyl- <i>sn</i> -glycero-3-phosphocholine
DOPE	1,2-dioleoyl- <i>sn</i> -glycero-3-phosphoethanolamine
DOPG	1,2-dioleoyl- <i>sn</i> -glycero-3-phospho-(1'-rac-glycerol)
DPPC	1,2-dipalmitoyl- <i>sn</i> -glycero-3-phosphocholine
DOTAP	1,2-dioleoyl-3-trimethylammonium-propane
Cell-Penetrating Peptides	
ArgX	polyarginine avec X résidues
TAT ₄₇₋₅₇	séquence 47-57 du transactivateur de transcription du VIH
CPP	Peptide pénétrateur de cellule court (fonction)
sCPP	Peptide pénétrateur de cellule court
CPP-ELP _{BC}	Peptide pénétrateur de cellule greffé sur un polypeptide dibloc semblable à de l'élastine
Molécules fluorescentes	
AF488	AlexaFluor 488
BODIPY	boron-dipyrrromethene
HL488	HyLite 488
NBD	nitrobenzoxadiazole
RhoB	rhodamine B
YOYO-1	oxazole yellow-oxazole yellow
Polymères	
PEG	polyéthylène glycol
PTFE	polytetrafluoroéthylène
PVA	alcool polyvinylique
Autres	
MPTS	(3-mercaptopropyl)-triméthoxysilane
PBS	tampon phosphate salin

Table 2.5: Abréviations des produits chimiques utilisés dans ce travail.



CHAPTER 3 Experimental and analytical development

THE present chapter describes specific technical developments required for optimizing vesicle growing, for CPP-ELP_{BC} manipulation, and for experimental calibration and analysis.

A Electroformation caps

The traditional method using ITO electrodes described in the introduction suffers from some practical drawbacks. Indeed the growth chamber containing the two electrodes has to be sealed either by using PTFE spacers held to the ITO electrodes with clamps, or by building the growth chamber with Vitrex, a soft wax. In both cases, leakage can occur in case of inattentive manipulation, for example when the chamber is opened in order to collect the vesicles formed there. Since the GUV solution has to be diluted in an isotonic glucose solution prior to the observation and usually stored in an

Eppendorf centrifugation microtube before being collected again, we have developed a new form of GUV electroformation chamber which consist of a PTFE cap shaped to perfectly fit inside a 2 mL microtube, as pictured in figure 3.1. A set of holes were drilled through the PTFE cap and platinum wires with a diameter of 1.2 mm were installed through these holes. The part of the wires inside the Eppendorf tubes were mechanically flattened up to form the electrodes while the other end remained as wires, and could be connected to an electric generator. The blueprints of this PTFE cap can be found in Appendix Apx-4.



Figure 3.1: Picture of the home-made PTFE electroformation cap, with and without the growth chamber consisting of a centrifugation microtube.

These electroformation caps allow anyone to grow vesicles directly and simply inside a microtube, the further was used as the storage vial of the vesicle solution, possibly after a dilution with an isotonic glucose solution. With such a device, the transfer from the growth chamber to the storage chamber is avoided, reducing significantly the material loss and making the vesicles easier to collect. Leakage is of course much less likely in this geometry.

A-1 Vesicle growth

A-1.a Comparison between the electroformation methods at 10 Hz and 1 V

We carefully compared the products, in terms of GUV size, number and quality, of our electroformation caps and that of the traditional ITO-coated slide-based electroformation method.

GUVs were grown at 10 Hz and 1 V from 5 μ L of lipid solution at 1 mg/mL after a formation of 1 hour in 1 mL of sucrose solution at 280 mM then diluted in 1 mL of an

isoosmotic glucose solution. 150 μL of the final solution was collected at the bottom of the storage tube after setting for 15 minutes in the fridge. The measurement of the size, number and quality was performed using a Nikon TE-200 microscope. Results are shown in figure 3.2.

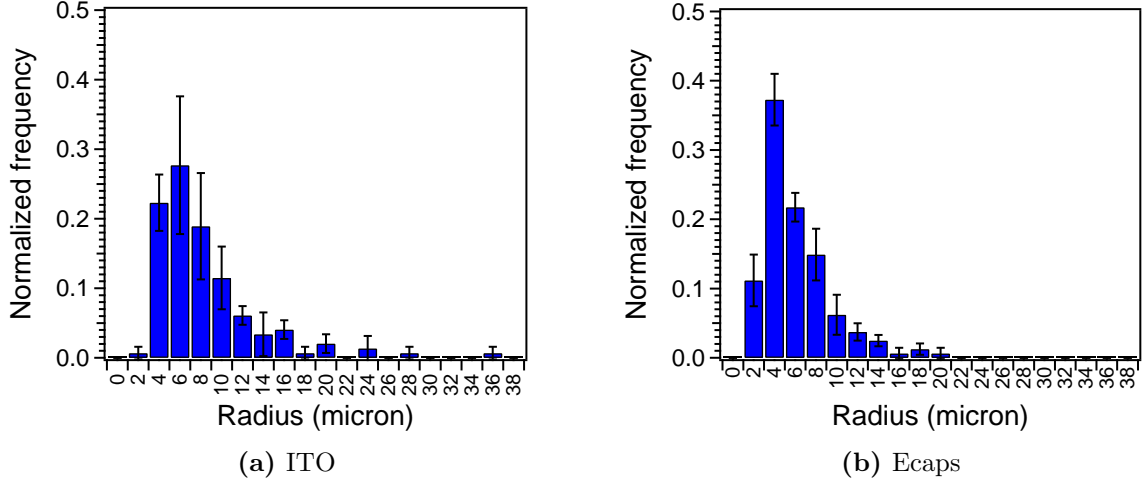


Figure 3.2: Distributions of the vesicles radii obtained using (a) ITO electrodes, with an average radius of $9 \pm 3 \mu\text{m}$, or (b) the electroformation caps (ecaps), with an average radius of $7 \pm 2 \mu\text{m}$. The measurements were performed on three samples and averaged.

We found an equal averaged number of vesicles of 1740 ± 80 for the 150 μL solution prepared with the electroformation caps, and 1600 ± 400 for the sample prepared with the ITO electrodes. The size distribution of the vesicles were also comparable, with an average radius of $7 \pm 2 \mu\text{m}$ for the vesicles prepared with the caps, and $9 \pm 3 \mu\text{m}$ for the ones prepared with ITO electrodes. Moreover, all vesicles appeared as giant unilamellar vesicles in the two cases. This proves that our new type of growth chamber did not suffer from any problems regarding the formation of the vesicles, as compared to the previous protocol using ITO electrodes.

After the first test, we investigated the effects of the different electroformation parameters on the yield of the GUV formation, by analysing the size and number of vesicles as described in section A-1.a. The effects of the frequency of the applied voltage were studied, as the effects of the gap between the two electrodes (see figure 3.3). The effects of the voltage itself were not investigated.

No critical effect of the frequency nor the gap were observed. We therefore decided to keep the electroformation parameters at 1 V_{PP} and 10 Hz. We also decided to keep a thick gap between the electrodes, since the thin one was complicated to use. Indeed,



Figure 3.3: Picture of two home-made PTFE electroformation caps with different gaps between the platinum electrodes, (left) 1 mm and (right) 2.5 mm.

while spreading the lipid solution on the electrodes, the capillary forces were strong enough to bend the electrodes and made them touch each other.

A-1.b Conditions leading to lipid degradation

As reported by Zhou *et al.* [219], the GUV electroformation can damage the lipids, for example by reduction-oxidation reactions. While the traditional ITO-based system for GUV growth was already optimized to avoid such problems, we checked that the new system was degradation-free as well.

Due to the small amounts of lipids used for a GUV electroformation, *i.e.* less than 10 μg per sample, the purity of the so formed GUVs was controlled by thin layer chromatography (TLC), a simple analytical method using only very small quantities of product per analysis. The following analytical procedure for performing TLC analysis was taken from Morris Kates' *Techniques of lipidology* [220]. After electroformation, the lipids were extracted from the GUV solution by a Bligh and Dyer protocol [221]: a given volume of aqueous solution containing the vesicles was diluted with one volume of chloroform and two volumes of methanol. The mixture was vortexed for 30 seconds after each addition of solvent. In such proportions, methanol, chloroform and water form a single phase in which lipids are soluble without aggregation. One volume of water and one volume of chloroform were then consecutively added, the mixture being vortexed after each addition, and centrifugated at 112 g for 5 minutes, leading to phase separation. The organic phase which contained the lipids was finally collected in a glass vial.

Following the extraction, the lipid solution was first dried under nitrogen until no traces of chloroform remained, and then dissolved again in chloroform at a concen-

tration of roughly 0.1-1 mg/mL (calculated from the initial amount of lipid used for the electroformation). This solution was analysed on a silica plate, with a mixture of chloroform/methanol/water (65/25/4) as eluent and revealed using phosphomolybdic acid. This experiment was performed on GUVs made of DOPC, DPPC, and DOPG.

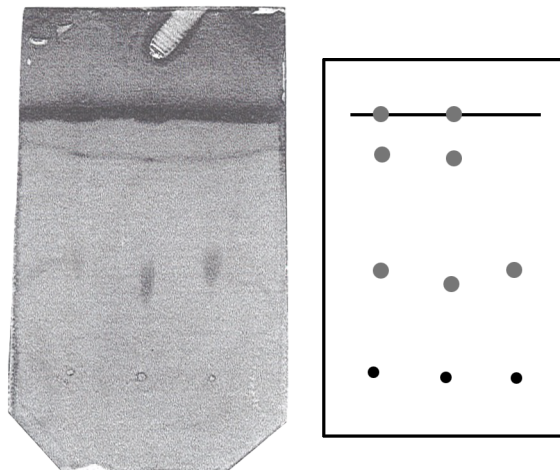


Figure 3.4: Thin layer chromatography of a GUVs sample of DPPC prepared by electroformation for 48 hours (left spots) and compared to the stock solution of pure DPPC (right spot). The middle spots correspond to the co-spots used to calculate the retention factor of each product. In the sample, two extra spots appeared in the sample as compared to the reference, highlighting changes in the composition of the product. The sketch on the right figure shows the position of each spots on the left picture.

The lipids extracted from GUVs formed by electroformation during up to 24 hours were analysed with the procedure described above, but no differences could be seen as compared to lipids from the stock solution or between the two electroformation techniques, no matter the type of lipid used (see figure 3.4). As a conclusion, we have proven here that the new electroformation method is safe for the lipids, and can be used without any fear of biochemical degradation.

A-2 Formation procedure

Considering the different tests described above, the following experimental procedure for GUVs electroformation using the cap was established:

Lipid solution in chloroform is deposited on the inner side of both electrodes and dried for 30 minutes under vacuum. The microtube is filled with 1 mL of a sucrose solution and the chamber is closed with the PTFE cap. Electroformation is set for up

to 15 hours at 1 V_{PP} and 10 Hz. The chamber was then opened by removing the PTFE cap from the microtube. By taking the electrodes off the solution, the vesicles which were still attached to the electrodes detach and remained in the solution. 1 mL of an isotonic solution of glucose was poured inside the microtube, which was then closed and gently shaken to homogenise the solution. The sample was then left undisturbed in the fridge for 15-30 minutes before the microscope observation to let the GUVs settle at the bottom of the tube.

B PVA gel-assisted formation in saline solution

B-1 Context

As described in the introduction, the cell-penetrating peptides used in this work are dissolved in a PBS solution. A molarity of 150 mM has been chosen close to that of biological fluids, and also used in many drug delivery protocols. We thus grew GUVs in the same buffer. However, it has been shown that growing GUVs directly in a saline solution, either with electroformation or gel-assisted method, rises issues. For growth in a saline solution, the vesicles cannot reach a suitable size for microscope observation. Moreover, GUVs will not detach from the substrate they grew onto.

To overcome these problems, solutions have already been proposed, such as the electroformation protocole developed by Pott *et al.* [89]. Indeed, they have shown that the GUVs electroformation in a saline solution is possible, by increasing the frequency up to 500 Hz and by alternatively increasing and decreasing the voltage throughout the electroformation. Nevertheless, the exact voltage ramps depend on the electrodes materials and the overall geometry of the system. For these reasons, we find that this method is not suitable for quick and easy experiments. Furthermore, the electroformation requires several hours of growth in order to obtain a sample containing only a few GUVs. This can be restricting for performing rapid attempts. The gel assisted formation developed in the team with a PVA gel [78] provides an interesting alternative but depending on the growing conditions vesicles might not grow with a convenient size distribution (*cf.* figure 3.5(a)).

The protocol that we developed and describe here to solve the problems caused by the salt was to improve the PVA gel-assisted method to make it work with saline solution. Unlike electroformation, the gel-assisted method allows growing GUVs easily with cheap and easy to find materials. The growth of a large number of vesicles can be performed on several samples in parallel.

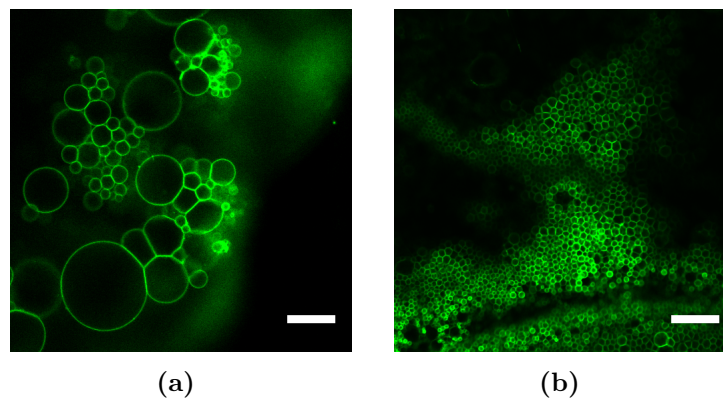


Figure 3.5: Confocal pictures of NBD-labelled vesicles of DOPC growing on a PVA gel in two different conditions: (a) non-saline sucrose solution on standard gel and (b) sucrose solution with 150 mM of NaCl on standard gel. Vesicles growing in saline solution on standard gel remains extremely small, about $7.5 \mu\text{m}$ of diameter. Scale bar represents $45 \mu\text{m}$.

B-2 PTFE plate for vesicle growth

Initially, the substrate used for the gel-assisted formation was a $76 \times 26 \times 1$ mm microscope glass slide (Carl Roth, Karlsruhe, Germany) activated using an UV-ozone cleaner (Novascan PSD Pro Series). A growth chamber was formed by using either Vitrex wax or a thick rubber spacer (Grace BioLabs CoverWell, purchased from Sigma-Aldrich), but both systems suffered from the same leaking problems as described in section A, especially for longer growth time. Indeed, for growth times longer than 2 hours, 50% of the samples were lost. Moreover, this configuration was not suitable for temperature-controlled experiments.

To solve all of these problems, a PTFE plate with a 3×4 grid of formation wells drilled into it was designed, as shown in figure 3.6. Each well is 12 mm wide and 10 mm deep, to hold *circa* 1 mL. As a comparison, the rubber spacers could only hold $150 \mu\text{L}$ at a time.

The choice of the PTFE was mainly motivated by its resistance to chloroform and the simplicity of cleansing between each use.

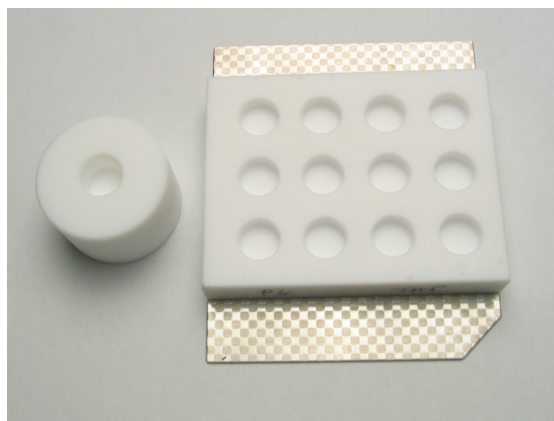


Figure 3.6: Picture of the home-made PTFE plate with a 3x4 grid of formation wells (right), next to its prototype (left).

B-3 Growth of zwitterionic GUVs

B-3.a Preparation of the gel

Gel containing various quantities of NaCl has been used as the growing substrate for GUVs in various aqueous solutions. For these experiments, a stock solution of NaCl at 150 mM was prepared. The osmolarity of this solution was measured at 271 mOsm/kg. The protocol described in section B-2 of chapter 2 for the preparation of the PVA had been used while replacing the ultra-pure water by the solution of NaCl, although the temperature had to be raised to 110°C. The solutions of sucrose and glucose at 280 mM of saccharide were prepared from the same NaCl solution.

B-3.b Effect of the salt on the growth

The effect of the preparation of the PVA gel in a solution with the same saline concentration as in the solution of growth was observed under the microscope during the growth. The size of the vesicles obtained in these conditions is comparable to the size of the vesicles obtained in a non-saline solution on a standard PVA gel, as illustrated in figure 3.7. The vesicles would also easily detach from the growth substrate, unlike the vesicles grown in the saline solution on standard gel.

This experiment was also performed with different combination of buffer solutions, such as phosphate-buffered saline solution (PBS), HEPES and Tris, and with a divalent salt (MgCl_2). Hence, a PVA gel was directly prepared with the buffer solution directly, or with a NaCl solution matching the concentration of NaCl in the buffer. The vesicles were able to grow with results comparable to the one described above in all conditions

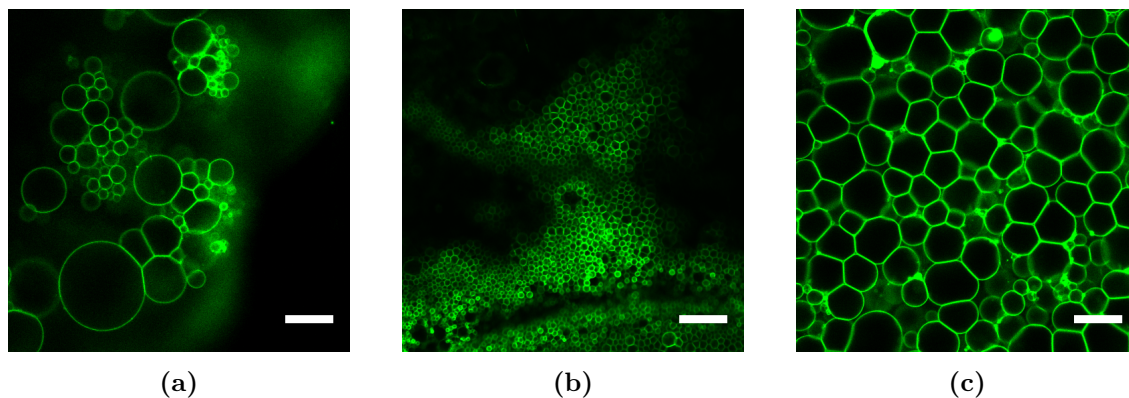


Figure 3.7: Confocal picture of NBD-labelled vesicles of DOPC growing on a PVA gel with 150 mM of NaCl in sucrose solution with 150 mM on NaCl (c), compared to GUV grown in (a) non-saline sucrose solution on standard gel and (b) sucrose solution with 150 mM of NaCl on standard gel. Vesicles growing in this conditions recovers a size distribution comparable to the one of non-saline solution on standard gel, of about $30 \mu\text{m}$ of diameter. Scale bar represents $45 \mu\text{m}$.

(*cf.* table 3.1). From this observation we can deduce that the presence of a similar salt concentration in the PVA gel than in the growth solution is the key to overcome the problems encountered growing GUVs in saline solution.

Other types of lipids, such as DPPC or lecithin (EggPC), were tested. Although the growth was as successful as with DOPC, the formation chambers needed to be brought above the gel transition temperature of the lipids in every case. In order to form the vesicles, the PTFE plate was placed in an oven for the whole duration of the process, and the wells were periodically refilled with pre-heated growth solution to avoid drying. However, this protocol brings important concerns about the final salt concentration in the growth solution, and its possible effect on the vesicles.

To extend the applications of this new method to form GUVs in saline solution, experiments were conducted with negatively and positively charged lipids, namely DOPG and DOTAP. The GUVs formed thereby were mixed with DNA, and their interaction are described in Appendix Apx-5. This work was performed with Nicolas Schalck during his third year of bachelor degree's internship.

Growth	PVA				
	water	NaCl	MgCl ₂	HEPES	Tris
water	o	x	x	x	x
NaCl	x	o	-	-	-
MgCl ₂	x	o	o	-	-
HEPES	x	o	-	o	-
Tris	x	o	-	-	o

Table 3.1: List of the different results obtained for the growth of GUVs on a PVA gel, with different solutions of PVA (columns) and different growth solution (rows). A circle (o) corresponds to a condition of formation where the vesicles have a size comparable to the one of the reference (growth solution made of water on a gel of PVA prepared in water), while a cross (x) corresponds to a condition where no vesicle could be observed under the microscope after extraction of the growth solution.

B-4 Conclusion on the PVA gel-assisted formation

We have proven here that the PVA gel-assisted GUVs formation was perfectly suitable for producing vesicles in saline solutions, with a salt concentration as high as 150 mM, if PVA is dissolved in a solution with the same concentration of salt. The formation can be used with buffer solution, while only salt is required within the PVA gel.

This protocol can be used with charged lipids, such as DOPG or DOTAP, and would produce a large number of vesicles of large size even when 100% of the charged lipids were used for the formation. All these vesicles appeared to be perfectly suitable for interactions with biomolecules such as DNA.

We have also shown that this protocol could be used in order to encapsulate DNA inside DOPC vesicles, where all vesicles observed in the microscope were filled, as long as the DNA chain is not too long (encapsulation impossible with ≥ 48000 bp).

C Surface treatment

The main characteristic of the CPPs used in this work is their high amount of nominal charges, from 5 to 8 positive charges. This cationic molecule unfortunately tends to stick to the glass surface of the microscope slides. In the case of the CPP-ELP_{BCS}, the chemical group will bind both on the glass surface and on the lipid membrane. As a result, the CPP-ELP_{BC} will bridge the membrane and the glass surface, so the vesicles will appear hemispherical (*cf.* Figure 3.8).

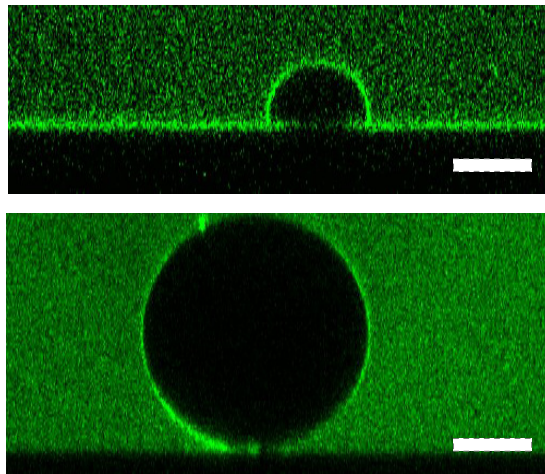


Figure 3.8: Confocal pictures taken in the XZ plane of two GUVs of DOPC immersed in a solution of CPP-ELP_{BC}. (Top) CPP-ELP_{BC} bridge the GUV to the glass surface, making it hemispherical. (Bottom) CPP-ELP_{BC} are not able to bridge the GUV to the glass surface, and the GUV appears spherical. Scale bars correspond to 20 μm .

To accurately investigate the adsorption of fluorescent molecules on a GUVs, one should scan the vesicles at their equator. This is unfortunately impossible in the case of strong adhesion of the GUV on the glass surface, as shown in figure 3.8. Moreover, even a slight adhesion can avoid performing correct measurements, as the presence of surface-adsorbed peptide might increase locally the fluorescence.

To prevent the adhesion of the GUV on the glass surface, we had to perform a surface treatment on the slides. The concept is to graft a polymer, namely poly(ethylene glycol), on the glass surface. The initial experimental protocole was taken from Perret *et al.* [222] and adapted for our experiments. The different steps of the reaction and optimization are described in the following section.

C-1 Silanization reaction

The first stage of the surface treatment is a silanization of the glass slides (see figure 3.9). Freshly distilled (3-Mercaptopropyl)trimethoxysilane (MPTS) is diluted in a solution of ethanol with 0.25% of ultra-pure water, at a concentration of 5.4×10^{-3} mol/L. Glass slides, activated with UV-ozone cleaner 45 minutes, are dipped in the silane solution and stored in a desiccator previously filled with argon for the whole reaction time. The silanized slides are then washed two times with pure ethanol, dried with nitrogen and annealed in the oven at 110°C . They are then rinsed again under sonication to detach ungrafted molecules. The yield and quality of the silanization as a function of the dipping time is controlled by ellipsometry, using silicon wafers as a template.

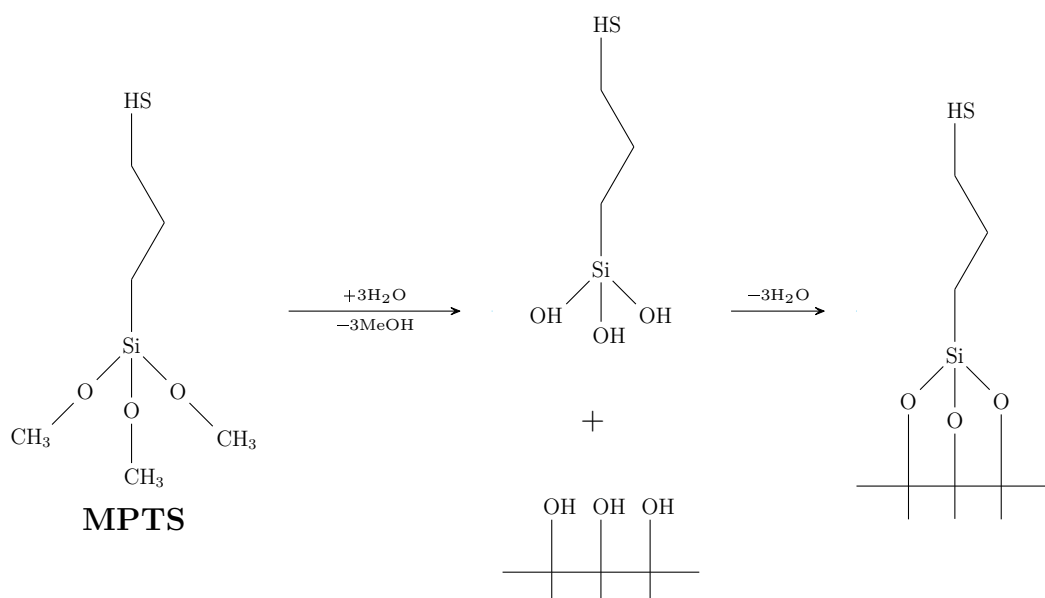


Figure 3.9: Schematic representation of the reaction between (3-Mercaptopropyl)trimethoxysilane (MPTS) and a glass surface.

The thickness of the silane layer is found proportional to the dipping time, as shown in figure 3.10(a). The theoretical length of the silane was calculated and found equal to 6.34 \AA (*cf.* figure 3.10(b)), which corresponds to a dipping time of roughly 35 min. For all the following silanization, the dipping was set to 1 hour, to be sure that the whole slide was covered with one layer of silane.

The silanized glass slides were annealed for 5 and 10 min. The resulting thicknesses are comparable, with an average difference of $0.7 \pm 0.7 \text{ \AA}$. In order to ensure a better stability of the system, the slides were then always annealed for 10 minutes. The reproducibility of the new protocol was tested, and an average thickness of $5.7 \pm 1.4 \text{ \AA}$ is

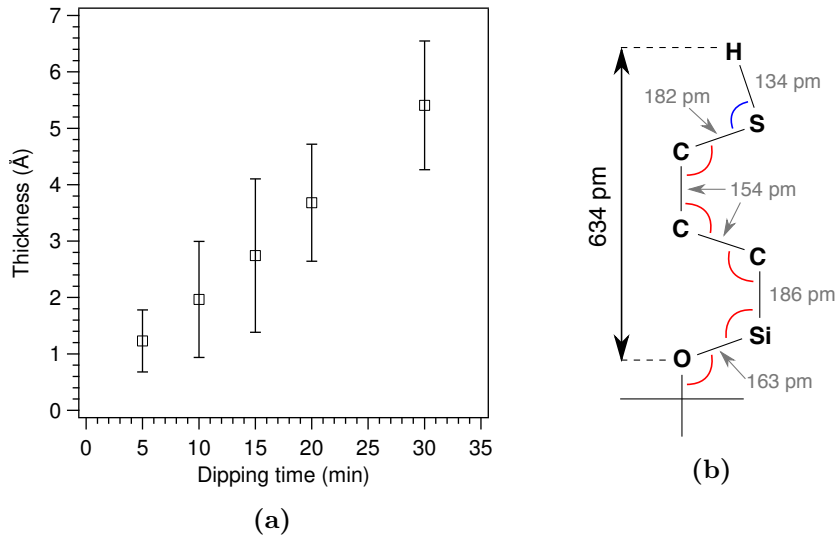


Figure 3.10: (a) Thickness of the layer of silane on top of a silicium wafer, measured by ellipsometry, as a function of the dipping time of the glass surface in the silane solution. (b) Theoretical calculation of the total length of a molecule of silane attached to a glass surface. Angles in red are equal to 109.5° and the angle in blue is equal to 92.1° . Bond lengths and angles are taken from tables.

obtained on silicon wafers.

C-2 PEGylation reaction

The second step of the surface modification is the reaction of the thiol-terminated silane grafted on the glass surface with a polyethylene glycol (PEG) functionalized with a maleimide group (see figure 3.11), called Methoxy-PolyEthylene Glycol Maleimide (MeO-PEG_n-Mal). The reaction between the maleimide and the thiol group is performed right after the annealing part of the silanization process. $50 \mu\text{L}$ of the MeO-PEG_n-Mal solution in PBS at pH 6.4 is deposited on the silane-grafted glass slide, and a second functionalized slide is used to cover the first slide in a sandwich-like fashion. The pair of glass slides is stored for 24 hours in a watertight crystallizer. Ultra-pure water is used to separate the two tightly packed glass slides and to rinse them. Additionally, to remove the excess of MeO-PEG_n-Mal which were only physically adsorbed on the glass slides, the glass surface were immersed in ultra-pure water and sonicated for 10 seconds.

Two MeO-PEG_n-Mal with different molecular weight were used : the first one with a molecular weight of 5000 g/mol which correspond to an average chain length of 110

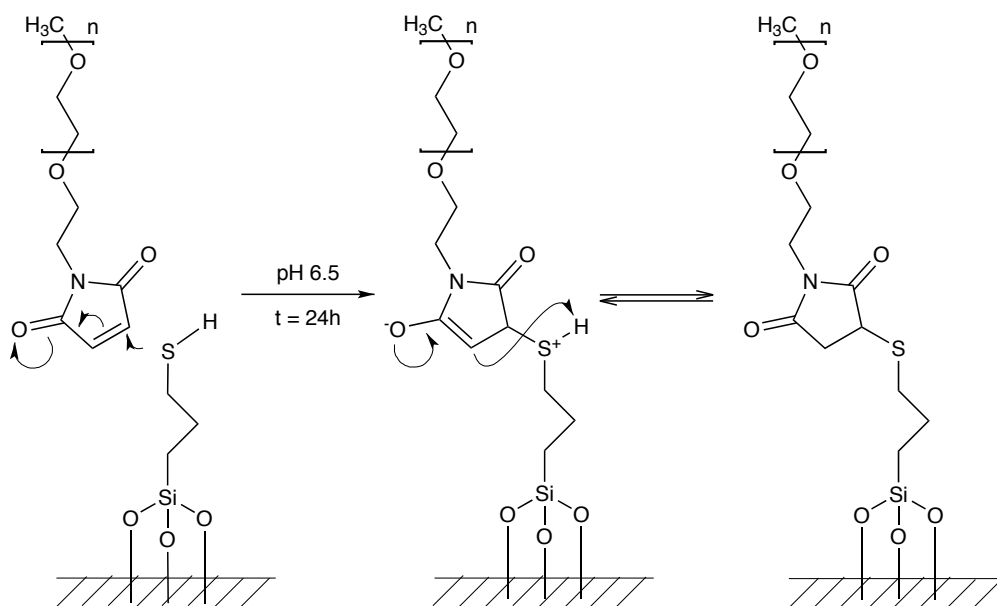


Figure 3.11: Mechanism of the PEGylation reaction. The lone pair of the sulfur atom from the grafted silane reacts with the double bond from the maleimide group of the PEG.

monomers, and the second one with a molecular weight of 683 g/mol with an average chain length of 12. The polymers are therefore respectively called MeO-PEG₅₀₀₀-Mal and MeO-PEG₁₂-Mal.

C-2.a Full coverage of a glass slide

The PEG concentration used was first calculated in order to be in excess to get a full polymer coverage in the mushroom regime on a glass slide with a $R_{glass} = 15$ mm radius (*cf.* figure 3.12).

In water, which is a good solvent for the PEG, the MeO-PEG_n-Mal is expected to swell to form a soft sphere with a radius of gyration R_g , which is approximated using Flory's mean field approach

$$R_g = aN^{\frac{3}{5}} \quad (3.1)$$

$$\begin{aligned} S_{PEG} &= \pi R_g^2 \\ &= \pi \left(aN^{\frac{3}{5}} \right)^2, \end{aligned} \quad (3.2)$$

with a the monomer length and N the number of monomers in one chain. The ratio between $S_{glass} = 2\pi R_{glass}^2$ and S_{PEG} is equal to N_{PEG} the number of polymers required

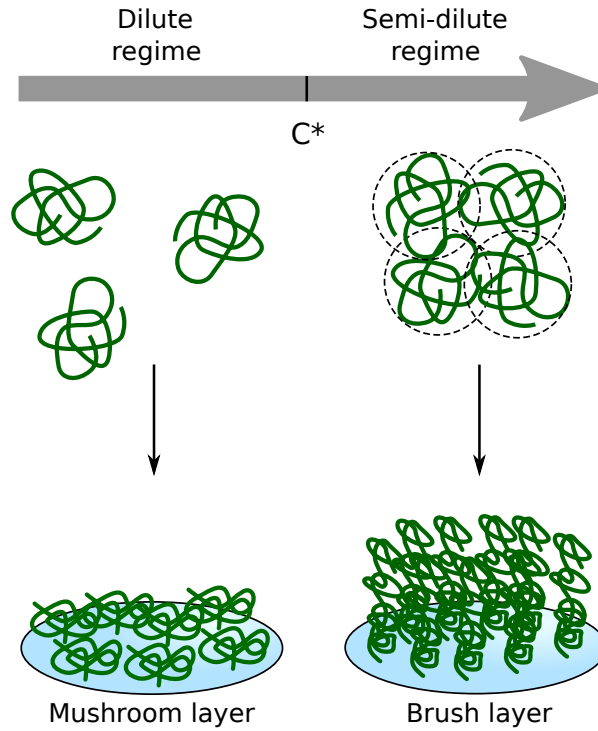


Figure 3.12: Representation of the mushroom-like and brush-like polymer-grafted surface. Mushroom-like surface coverage is obtained for polymers in the dilute regime (below C^*). The area occupied by each polymer is given by the square of its radius of gyration R_g . In the brush-like regime, obtained for polymers in the semi-dilute regime, the area occupied by each polymer is given by its average cylindrical section.

to cover the surface of the two glass slides of the sandwich in a triangular carpet, such as

$$\begin{aligned}
 N_{PEG} &= 0.9 \frac{S_{\text{glass}}}{S_{PEG}} \\
 &= \frac{2\pi R_{\text{glass}}^2}{\pi R_g^2} \\
 &= \frac{2R_{\text{glass}}^2}{a^2 N^{\frac{6}{5}}}.
 \end{aligned} \tag{3.3}$$

Using equation 3.3, we can calculate the mass concentration C_m corresponding to a full coverage

$$\begin{aligned}
 C_{\text{coverage}} &= \frac{n_{PEG}}{V} \\
 &= \frac{N_{PEG}}{N_a V} \\
 &= \frac{2R_{\text{glass}}^2}{N_a V a^2 N^{\frac{6}{5}}} \\
 C_{m,\text{coverage}} &= \frac{2R_{\text{glass}}^2}{N_a V a^2 N^{\frac{6}{5}}} \times 5000. \tag{3.4}
 \end{aligned}$$

With a volume $V = 50 \mu\text{L}$ required to cover a glass slide, equation 3.4 returns a concentration of $2.95 \times 10^{-3} \text{ mg/mL}$ for MeO-PEG₅₀₀₀-Mal and $42.1 \times 10^{-3} \text{ mg/mL}$ for MeO-PEG₁₂-Mal. In both cases, the concentration was 5 mg/mL.

C-2.b Brush coverage of a glass slide

We also performed glass treatment at a higher polymer concentration, *i.e.* above the semi-dilute concentration C^* . Indeed, above this concentration, the MeO-PEG_n-Mal is expected to cover the glass slide in a brush-like pattern (*cf.* figure 3.12) [223]. C^* can be calculated using the mass of a soft sphere of MeO-PEG_n-Mal m_{PEG} with a volume V_{PEG} , such as

$$C^* = \frac{m_{PEG}}{V_{PEG}}. \tag{3.5}$$

V_{PEG} is calculated from the radius of gyration R_g already used in equation 3.2, and m_{PEG} is given by the molecular weight of the MeO-PEG_n-Mal M_W divided by Avogadro,

$$\begin{aligned}
 C^* &= \frac{M_W}{\frac{4}{3}\pi R_g^3 N_a} \\
 &= \frac{3M_W}{4\pi a^3 N^{\frac{9}{5}} N_a}. \tag{3.6}
 \end{aligned}$$

Equation 3.6 returns a concentration of 9.3 mg/mL for MeO-PEG₅₀₀₀-Mal. This calculation cannot be achieved for MeO-PEG₁₂-Mal. Indeed, this polymer is too short for this model to be accurate. Concentration for MeO-PEG₅₀₀₀-Mal experimentally used is set to 140 mg/mL.

C-3 Results

The optimal experimental procedure was defined by looking at the adhesion of GUVs in the usual conditions for the study of adsorption of fluorescent molecules. Adhesion was controlled by performing 3D rendering of the GUVs using the confocal microscope, as previously pictured in figure 3.8.

With MeO-PEG₁₂-Mal all the GUVs appeared strongly adhered, with hemispherical shape. In the case of full coverage of MeO-PEG₅₀₀₀-Mal, a large amount of GUV did not adhere on the glass surface, but both CPP-ELP_{BC} and CPP formed aggregates in the solution, due to the presence of the PEG.

The brush-like coverage of MeO-PEG₅₀₀₀-Mal was thus the only procedure which completely prevented both the adhesion of GUVs and the CPP-ELP_{BC} or the CPP aggregation in the solution.

D Temperature controlled experiments

Working in a temperature-controlled environment is critical in biophysics. Indeed, the behaviour of biological systems can depend strongly on temperature, and it is often required to work above room temperature, usually 37°C.

The Nikon TE-2000 optical microscope used for this work was not initially designed to perform temperature-controlled experiments. While a first system had been already developed prior to this work, it was crucial to optimize and calibrate it to work with system as sensitive as the CPP-ELP_{BC}.

D-1 Experimental set-up

The initial experimental set-up for the temperature control designed in the team was made of two elements: a heating metal stage, created by Pierre Chapuis during his master degree internship in the team, and a water-tight metal observation chamber closed by two microscope glass slides. Pierre Chapuis' blueprints can be seen in Appendix Apx-6.

The first experiments performed with the CPP-ELP_{BC} pointed out that this initial system did not enable a precise control of the temperature in the sample. In particular, a difference in temperature as high as 10°C existed between the set temperature and the very bottom of the sample, *i.e.* just above the glass slide that was in contact with the microscope objective. Moreover, the system appeared to be significantly dependent of the room temperature. We thus developed a new experimental set-up, illustrated in Figure 3.13.

We introduced an objective mantle purchased from ALA Scientific Instruments (Farmingdale, NY, USA), modified to be coupled with the heating stage temperature controller, and an insulator ring tightly adapted to the objective. The new system was successfully tested. A calibration over the temperature range of 25 to 42°C has shown that the gap between the set temperature and the sample temperature was significantly reduced, and that this new system was independent on the room temperature.

D-2 Calibration

As shown in the introduction, CPP-ELP_{BC}s are characterised by a structural transition dependant of the temperature, with a sharp transition region. For example, the temperature at which the adsorption of the CPP-ELP_{BC} takes place runs over *circa*

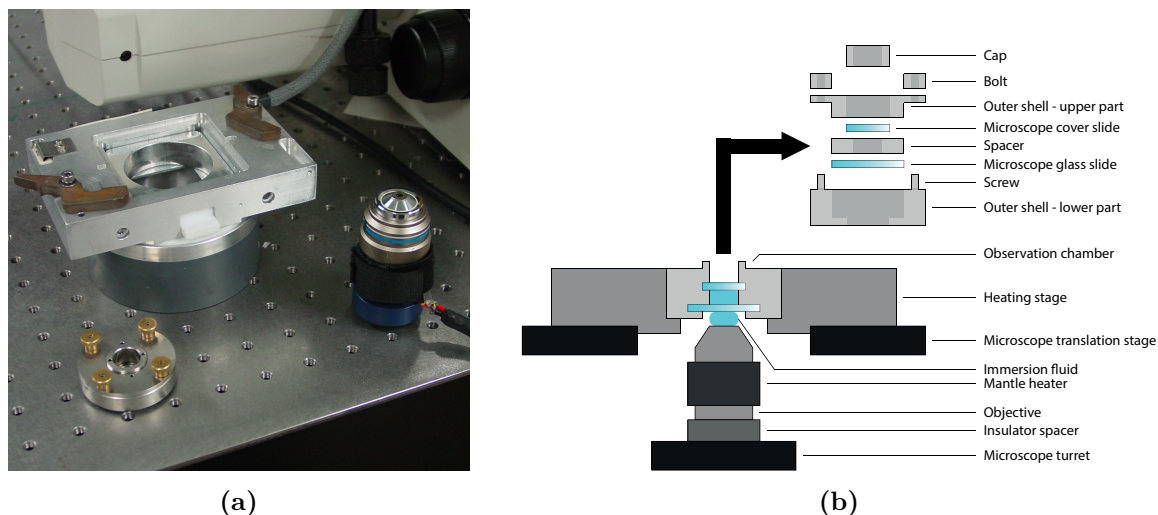


Figure 3.13: Illustration of the temperature control system used for this work. The system is made of four parts: the water-tight observation chamber, the heating stage, the heating mantle for the objective, and the insulator spacer installed between the objective and the microscope. Top-right illustration represents the different parts of the observation chamber.

1°C. It was therefore crucial that our heating system could be driven with a similar, 1 °C, precision.

Four probes have been disposed as shown in figure 3.14.

- One temperature probe was immersed inside the sample (PBS solution in the case of the calibration), and forced against the microscope glass slide (S). This probe gave us a precise estimation of the sample temperature for each setting of the heating device.
- A probe was plugged in a cavity drilled on the side of the metal heating stage (M). This probe allowed us to verify the temperature recorded by the inner probe of the heating stage.
- One probe was attached to the side of the objective, below the heating mantle and above the insulator spacer (O). This probe allowed us to estimate the temperature loss due to the contact between the microscope and the objective, despite the insulator.
- Another probe was located in the immersion fluid of the objective, against the bottom side of the microscope glass slide (W). This probe allowed us first to

confirm the temperature recorded by the probe S and to check for any kind of temperature loss through the microscope glass slide. Moreover, performing a first calibration with S and W on allowed us to repeat the calibration with W only, in order to verify the temperature with a complete water-tight observation chamber.

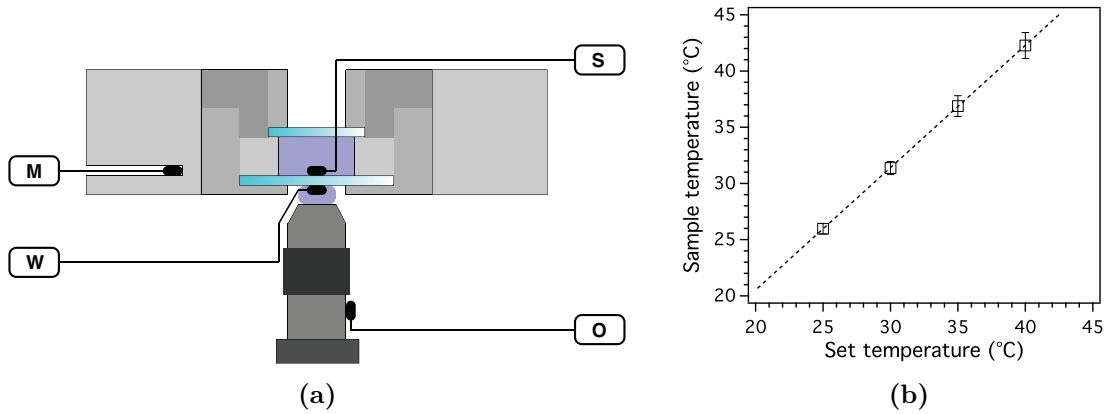


Figure 3.14: (a) Illustration of the experimental set-up for the calibration of the temperature control system. The temperature probes could be installed in four positions in this configuration: inside the water sample against the microscope glass slide (S), inside the immersion medium for the objective (W), against the objective below the heating mantle (O), and inside the heating metal plate (M). (b) Calibration curve of the sample temperature as a function of the temperature set for the sample, obtained using the experimental set-up described here.

As seen in the figure 3.14(b), the new temperature control system has therefore been proved to be precise up to 0.5°C . Also, the temperature of the sample is stabilised after 15 minutes.

E Analysis of interferometric microscopy data

We present in this part a programming-only project, in which an ImageJ plug-in function has been developed. This plug-in function was developed within the framework of an internal collaboration with two second year master degree interns of the team: Marta Salvador Castell and Yannis Arcorio. Both students investigated the impact of nano-objects on the fluctuations of a lipid membrane using RICM. In this context, the purpose of the ImageJ plug-in was to analyse the results of their RICM measurements.

Possible applications of the plug-in function concern some of the subjects of the internships listed and described below. After final revisions, the plug-in software is planned to be published on-line.

E-1 Membrane fluctuations analysis with RICM

RICM is a method of optical microscopy which is sensitive to the distance between the reference glass surface and the membrane. However, the relation between the intensity of the signal I and the distance between the membrane and the glass surface h is not bijective, being mainly characterized by a sinusoidal function [224], such as

$$I = I_1 + I_2 + 2\sqrt{I_1 I_2} \cos(2kh + \phi), \quad (3.7)$$

where I_1 and I_2 are the interfering rays, ϕ the phase shift usually equals to π , and $k = 2n\pi/d$ depending on the refractive index of the medium between the glass and the membrane n and λ the light wavelength. $I = f(h)$ is shown in figure 3.15 [225].

Nonetheless, equation 3.7 allows one to obtain a precise measurement of the relative distance, only if the location in a given branch is proven, which is of interest to evaluate the topology of the membrane, or to measure the thermal fluctuations of the membrane. The latter case was the primary motivation for the development of the plug-in software for ImageJ.

We chose to investigate both spatial and temporal evolutions of the thermal fluctuations through this software. In order to do so, the software calculates a spatial and temporal autocorrelation function from the picture of a movie, to extract from them the average size of the membrane patches fluctuating on the surface, and the frequency of these fluctuations.

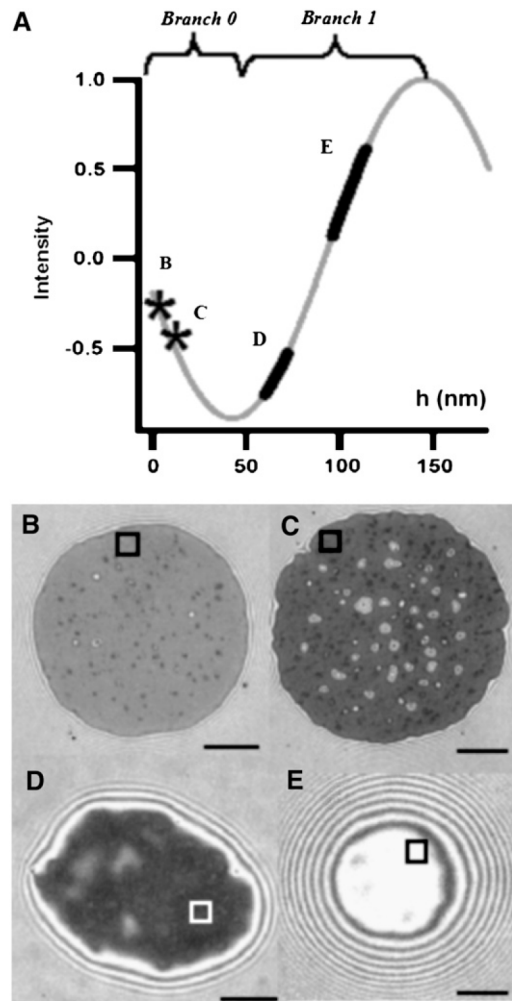


Figure 3.15: Representation of the bijectivity between the measured gray-level of intensity and the distance between the reference surface and the membrane. (A) The theoretically expected intensity as a function of membrane-substrate distance. Branch 0 and branch 1 of the sinusoid are marked. (B-E) RIC micrographs of vesicles resting at different heights and as a consequence exhibiting different contrasts: (B) On avidin and (C) on a hyaluronan cushion the vesicles adheres strongly. Height is calculated on branch 0. For (D) and (E), the heights are calculated on branch 1. Scale bars correspond to $5 \mu\text{m}$. Pictures and graph are taken from Limozin and Sengupta [225].

E-2 Definition of the Autocorrelation Function

The Autocorrelation Function (ACF) of a signal $Y = f(X)$ is the correlation of Y with itself along X . It can be defined as the mathematical expectation E of the product of the $X(t)$ values by the values $X(t + \tau)$ for a given time separation τ [226]

$$ACF(\tau) = E [Y(X) \times Y(X + \tau)]. \quad (3.8)$$

In the case of a finite function with a discrete range of values, this equation can be rewritten as

$$ACF(\tau) = \frac{1}{N - \tau} \sum_i^{N-\tau} (Y(X_i) \times Y(X_i + \tau)), \quad (3.9)$$

where N is the number of values and τ the step between two X values.

Another way to calculate the ACF use the Fourier Transform. This is demonstrated by the Wiener-Khinchin theorem,

$$ACF(\tau) = F_V[|Y|^2](\tau). \quad (3.10)$$

The Wiener-Khinchin theorem states that the ACF of a signal has a spectral decomposition given by the power spectrum of that signal. By multiplying the Fourier transform of one function by the complex conjugate of that same Fourier transform, one can obtain the Fourier transform of the autocorrelation of this function. As a matter of fact, for image processing, the Fast Hartley Transform (FHT) is preferred to the FFT in the algorithms [227]. While the Fourier transform converts real-valued functions into complex-valued functions, the Hartley transform converts these real-valued functions into a new set of real-valued functions. The Hartley transform is defined as

$$H(\omega) = \frac{1}{\sqrt{2\pi}} \int_{-\infty}^{+\infty} f(t) [\cos(\omega t) + \sin(\omega t)]. \quad (3.11)$$

As a consequence, the software relies on the algorithms using the FHT for calculating the autocorrelation functions, but we decided to keep the term "FFT" in the software, as the results are analogous, and to avoid confusion by the users.

E-3 Autocorrelation Function computation

The plug-in function we wrote for ImageJ computes temporal or spatial ACF of a set of pictures (screenshot in Figure 3.16). The programming language used is Java, and the graphic user interface is based on the Radial Profile Extended plug-in from Philippe Carl [228]. The plug-in function is used to investigate possible existence of characteristic times distributions in a movie and/or spatial distribution in the pictures of membrane fluctuations.

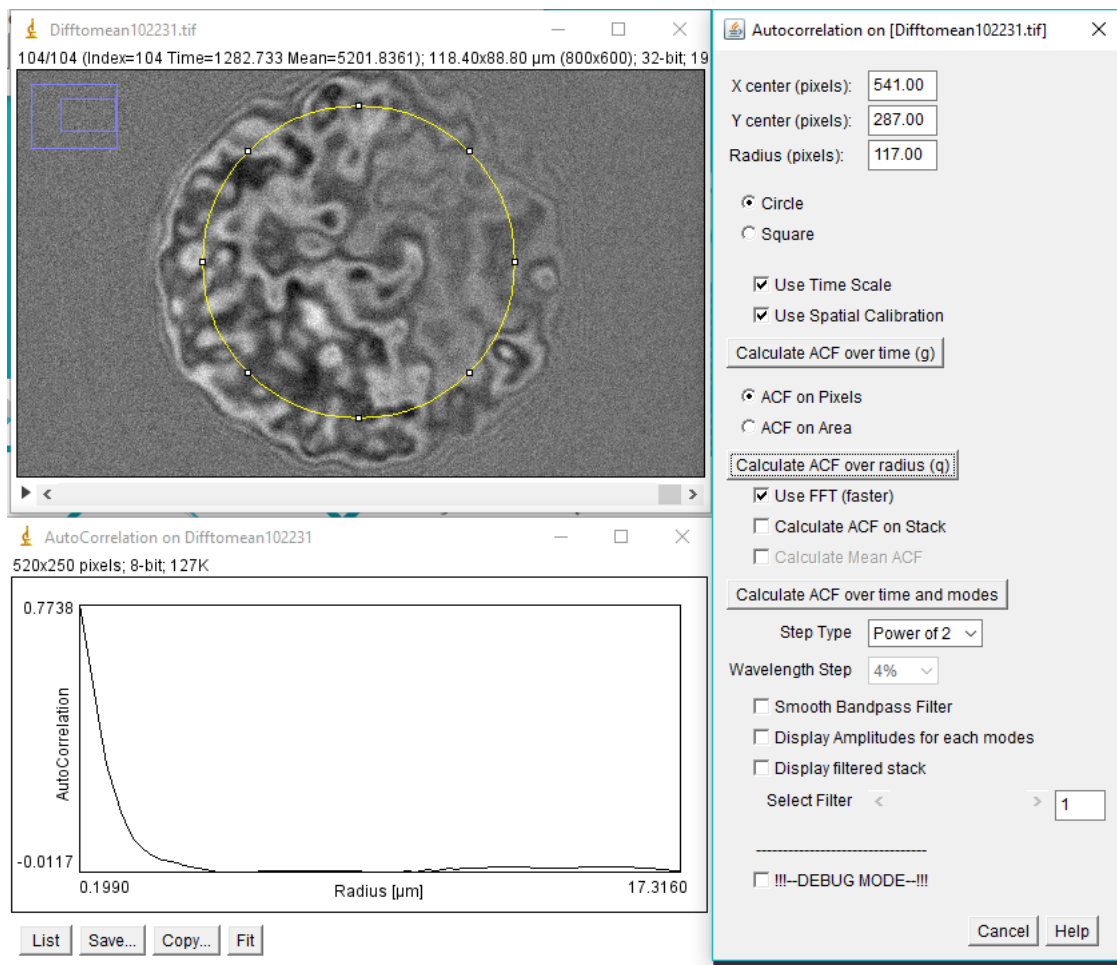


Figure 3.16: Screenshot of the AutoCorrelation Function plug-in function for ImageJ. The plug-in was used here to measure the spatial ACF (bottom-left) of a pictures of a GUV taken in RICM (top-left). Pixel taken into account for the $tACF$ are those enclosed in the yellow circle.

E-3.a Time ACF

The time ACF ($tACF$) of the intensity of a pixel will return the characteristic times range of oscillations of the signal. $tACF$ can only be applied to a movie made of regularly time spaced images. Given equation 3.9, the $tACF$ of a pixel j can be expressed by

$$tACF_j(\tau) = \frac{1}{t_{max} - \tau} \sum_{i=0}^{t_{max}-\tau} (I_j(t_i) \times I_j(t_i + \tau)). \quad (3.12)$$

For $\tau > t_{max}/2$, the number of intensities $I(t) \times I(t + \tau)$ used for the calculation is less than half of whole numbers of intensities in the signal. In order to sustain good precision on the measurement, τ_{max} is set to $t_{max}/2$.

The $tACF$ is calculated for $\tau \leq t_{max}/2$, since the characteristic times are negligible as compared to $t_{max}/2$. The overall $tACF$ of the stack of pictures is the average of the $tACF_j$ over the N pixels considered for the measurement:

$$tACF(\tau) = \frac{1}{N} \sum_j^N tACF_j(\tau). \quad (3.13)$$

The $tACF$ of the plug-in function was tested using a series of black and white pictures (see Figure 3.17). Each pictures is made of 8 black or white squares, arranged in a predefined pattern. Each square switches from black to white or white to black every three frames. The expected correlated values returned by the $tACF$ are therefore harmonics of the signal fundamental frequency $f_0 = \frac{1}{6}$.

The $tACF$ is measured using the plug-in function and, in order to compare, the $tACF$ is also measured from the binary signal $(-1, -1, -1, 1, 1, 1, -1, -1, \dots)$ with a data analysis software. The two resulting $tACF$ are displayed in Figure 3.18. The two $tACF$ of the signal return maxima at 6, 12, 18, ... frames, and minima at 3, 9, 15, ... frames, corresponding to the correlation and anti-correlation of the intensities. While the $tACF$ from the data analysis software is decaying over time, the $tACF$ measured by ImageJ remains stable.

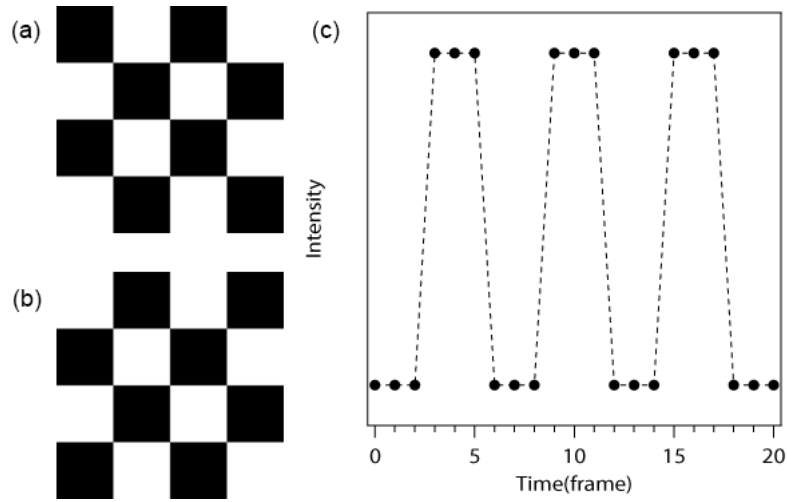


Figure 3.17: (a & b) The two pictures used to test the $tACF$ plug-in function. (a) and (b) alternate every three frames. (c) The resulting evolution in time of the intensity of one pixel of the picture.

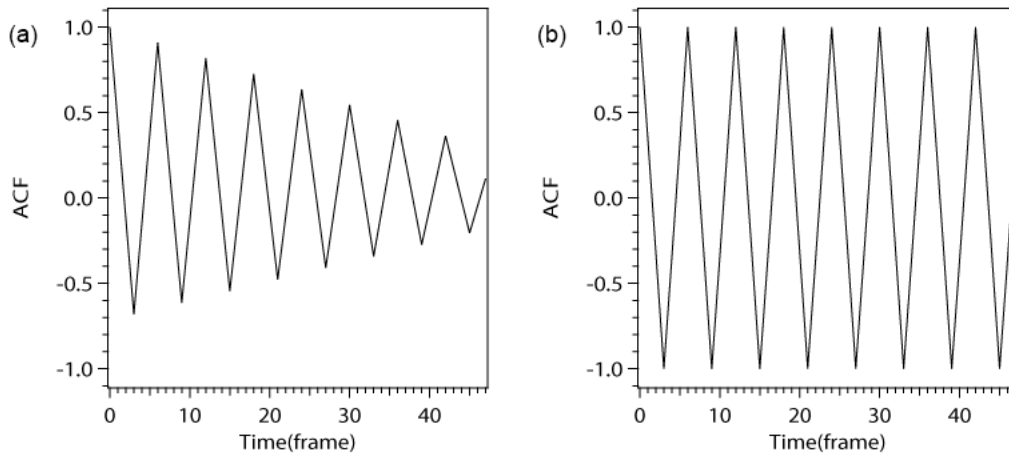


Figure 3.18: $tACF$ of the black and white pictures (Figure 3.17), calculated with (a) a data analysis software and (b) the plug-in function from ImageJ. The frequencies returned by the $tACF$ are the same, but the $tACF$ measured by the data analysis software is found decaying over time while the $tACF$ from ImageJ is constant.

E-3.b Spatial ACF

We also developed a spatial ACF (*sACF*) plug-in. *sACF* should enable to determine some characteristic sizes in the sample. It is a 2D ACF that can be expressed by

$$sACF(\gamma) = \frac{1}{N(\gamma)} \sum_X \sum_Y I(x, y) \times I(x', y') \quad (3.14)$$

where $\gamma = \sqrt{(x' - x)^2 + (y' - y)^2}$

The *sACF* can also be calculated using the Fast Fourier Transform (FFT). In both case, the *sACF* can be averaged over time in a stack. We compared both methods on two model 2D images, as seen in figure 3.19.

The two pictures are filled with 32 black dots with a 25 pixels diameter. Only the position of the dots change from one picture to another. Each method gives the same result when applied to the two pictures. We conclude that only the size of the domains influence the *sACF* calculation, and not their position. An average characteristic size in the sample can be taken as the value for which *sACF* reaches half of its maximal value. Clearly, the two methods give very close results.

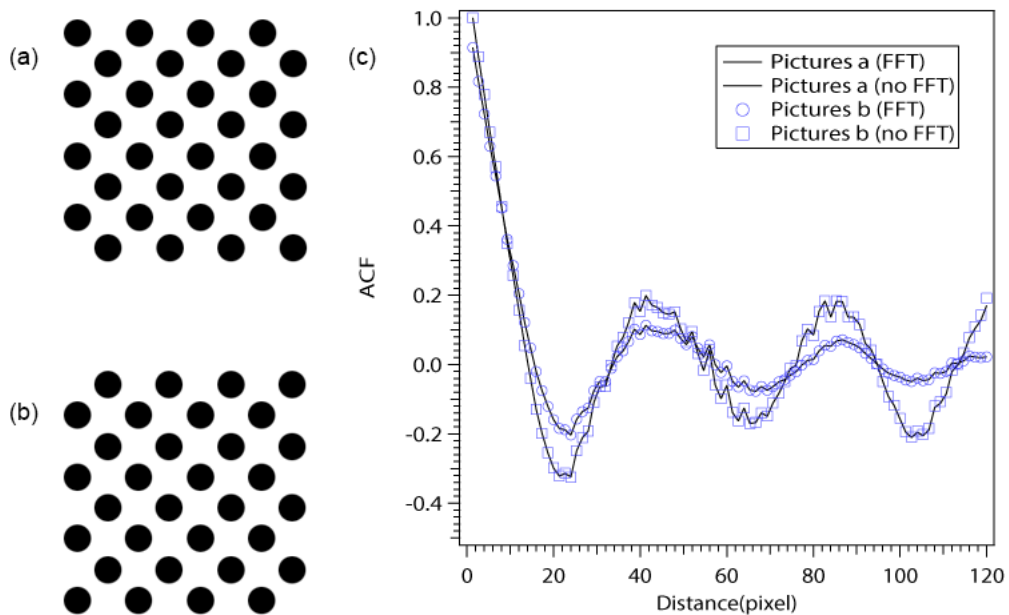


Figure 3.19: (a & b) The two pictures used to test the *sACF* plug-in function. The dots in (a) and (b) all have a 25 pixel diameter. (c) The resulting *sACF* measured for (a) and (b) with and without the FFT method. Both returns a value close to 25 pixels. The FFT method decays with the time, unlike the calculation made without FFT.

E-4 Experimental overview

As explained above, the ImageJ plug-in function for the computation of the auto-correlation functions has been developed for the analysis of experimental data obtained during two internships in the group. We show here some of the results obtained during the internship of Marta Salvador Castell.

We studied the interaction between gold nanoparticles (AuNPs) and GUVs made of POPC and DOPS, a negatively charged lipid: 0% (pure DOPC), 20 or 40% of DOPS. Using RICM and the ACF plug-in, we investigated the effect of the presence of the AuNPs on the thermal fluctuations of the lipid membrane, in order to see if the AuNPs would interact or not with the membrane. Indeed, we expect that adsorption of AuNPs on the surface of the GUVs would result in a modification of the bending modulus of the membrane κ , and therefore would change the thermal fluctuations.

Two phenomena have been highlighted through these experiments. First of all, the characteristic size of the blisters depends on the presence of DOPS in the membrane, and therefore in the presence of negative charges, but does not change above 20% of charges. Secondly, we have proved that the AuNPs were able to interact with the membrane, as the characteristic size of the blisters increases in the presence of the nanoparticles. Moreover, the difference of size depends on the membrane charge.

For the measurement of the $tACF$, we used a Miro LC 320S camera (Vision Research Phantom, Wayne, NJ, USA) which can reach acquisition frame rates as high as 10.000 fps. Indeed, the acquisition frame rate has to be higher than the characteristic time of the oscillations of the sample, hence the choice of the camera used here. We measured the characteristic time of a vesicle for different frame rates, but we were not able to reach a frame rate above which the characteristic time does not depend on the frame rate (*cf.* figure 3.21(a)). Nonetheless, we compared the relative characteristic time, with a strong dependence of the frame rate, at 500 fps and 1000 fps, and compared the effect of the membrane charge and the presence of AuNPs, as shown in figure 3.21(b).

The characteristic times found range between 10 and 25 ms, which is above the acquisition time (one picture every 1 or 2 ms). Without nanoparticles, the characteristic times are decreasing for 500 fps but constant for 1000 fps. With AuNPs, no differences were seen unless for 40% of membrane charge, where the characteristic time increases for both frame rates. Knowing the previous results on the characteristic sizes of the blisters, we can conclude here that our experimental set-up is not precise enough to measure small variations of the characteristic time.

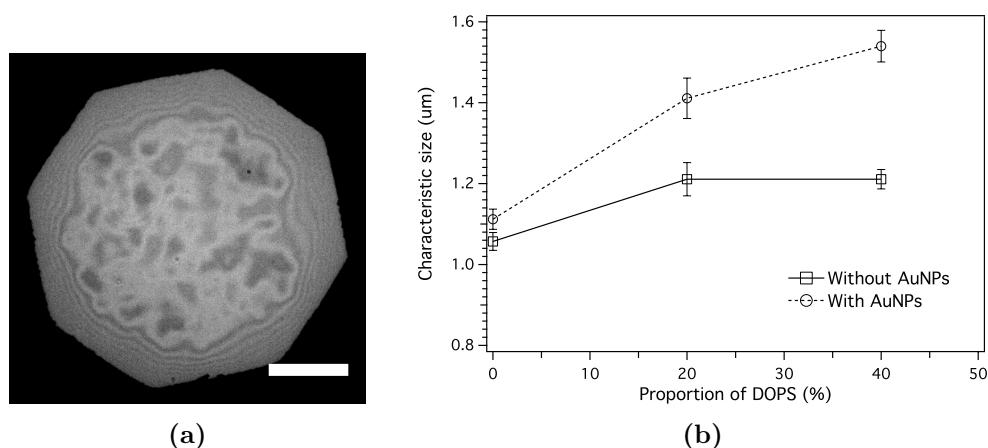


Figure 3.20: (a) Typical RICM picture obtained from a GUV resting on a glass surface. The thermal fluctuations can be visualized, as different distances between the membrane and the surface correspond to different intensities on the pictures. (b) Measurements of the characteristic sizes of the blisters on the GUV, performed on RICM pictures using the plug-in software. Different types of GUVs (POPC with 0, 20 and 40% of DOPS) are brought in contact with a suspension of gold nanoparticles (AuNPs). The experiments prove that the characteristic size of the blisters depend on the proportion of DOPS, and this size increases when AuNPs are in the solution. Scale bar correspond to $10 \mu\text{m}$.

As a conclusion, we have proven here that the ACF plug-in software that we have developed for ImageJ is very efficient and allows measuring precisely the spatial and temporal correlations of the fluctuations of the lipid membrane. The plug-in function also pointed out the limit of our high-speed camera in our experimental conditions.

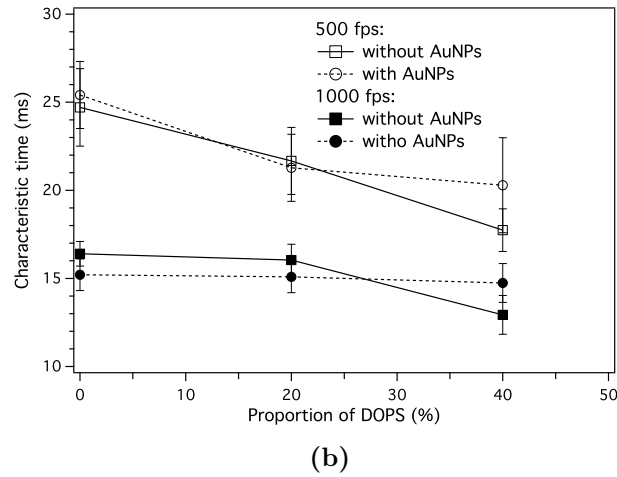
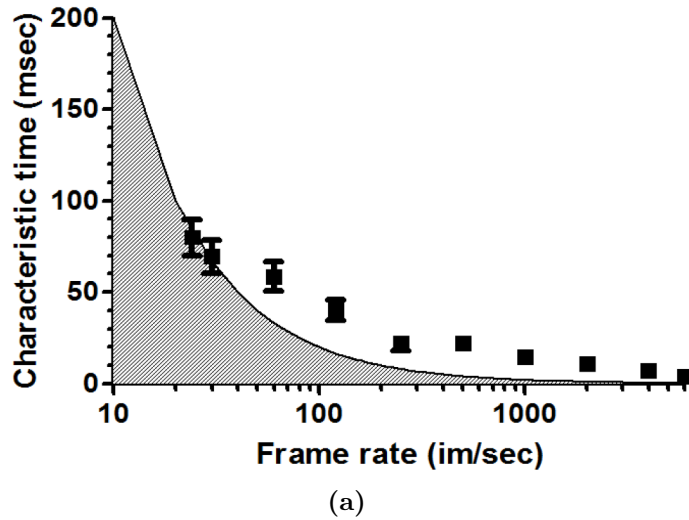
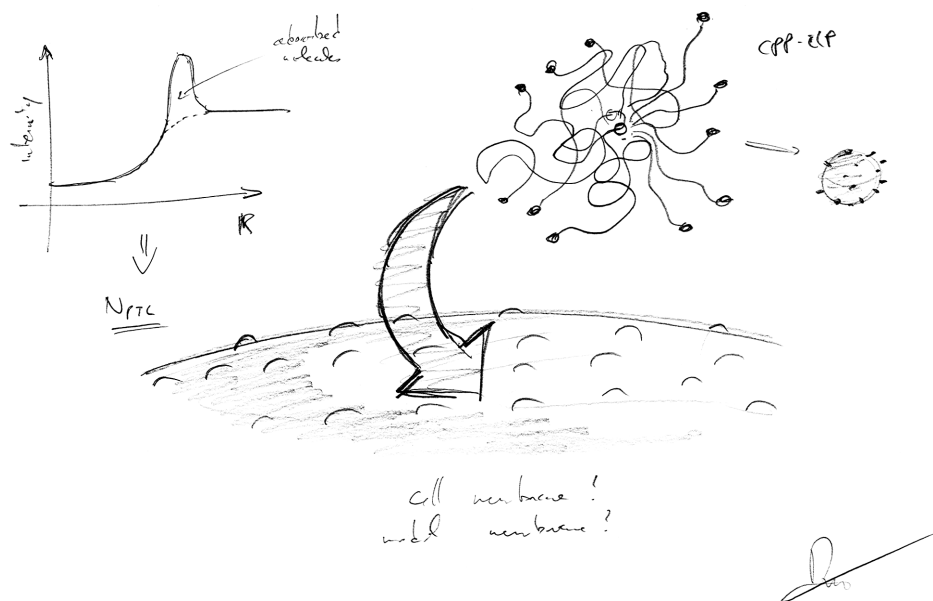


Figure 3.21: (a) Characteristic time of the oscillations of a vesicle, measured for different frame rate of the camera. The characteristic time corresponding to the frame rate is represented as a plain line. While the characteristic times of the oscillations are always over the corresponding frame rate, the value did not converge before we reached the limits of our camera. (b) Measurements of the characteristic times of the thermal fluctuation of the membrane of GUVs, performed on RICM movies using the plug-in software. Different type of GUVs (POPC with 0, 20 and 40% of DOPS) are brought in contact with a suspension of gold nanoparticles (AuNPs). The characteristic times were measured at 500 and 1000 fps. The evolution of the characteristic times over the membrane charge is strongly dependent on the frame rate. AuNPs only have an effect for 40% of membrane charge, where it increases the characteristic time.

KEY-POINTS OF THE CHAPTER

- We developed an alternative design for the chamber of GUV electroformation, by making a PTFE cap which can fit a standard Eppendorf tube. This design significantly simplifies the GUV electroformation procedure, and its simple handling has since appealed to many scientists.
- We developed PVA based protocols for GUV growth in saline buffer, by modification of the PVA gel-assisted method. Zwitterionic as well as negatively and positively charged lipids can easily form GUVs under the conditions that we defined.
- DNA fragments can be encapsulated inside GUVs of DOPC by embedding the DNA molecules in the PVA gel used for the growth of vesicles. The concentration of DNA encapsulated is proportional to the quantity of DNA mixed in the PVA
- We developed a plug-in function for ImageJ for the analysis of RICM pictures and movies. The plug-in can compute spatial and time correlation functions of the RICM images.
- A surface treatment of the glass slides, using silane and PEG, was adapted to our measurements requirements to avoid strong adhesion between the GUVs and the substrates in the presence of peptides.



CHAPTER 4 Interactions between lipid membranes and CPP-ELP_{BC}

THIS chapter summarizes the work initiated with Andreas Weinberger during his PhD at the Charles Sadron Institute and completed during my PhD. We investigate here the interactions between model lipid membranes and the CPP-ELP_{BC} - see Chapter 2 for a description of the elastin-like polypeptides functionalized with CPPs used in this work - designed by the Chilkoti group. After highlighting the importance of the adsorption of the polypeptide on the cell membrane for the mechanism of cellular uptake, we develop a new analytical method to quantify the number of adsorbed molecules on the surface of a GUV. These results were published in Scientific Reports in 2017 [229].

A Effect of the micellization of the CPP-ELP_{BC}

In their previous paper [178], MacEwan and Chilkoti have shown that the self-assembly of CPP-ELP_{BC} recover their penetrating properties towards cells, such as HeLa wild type. Their observations suggested that the interactions are triggered by the local density of charges, as even short oligoarginines like Arg5, which are known to be unable to penetrate the cells by themselves, translocate through the membrane upon self-assembly. First investigations on the mechanism of translocation pointed out that some endocytosis pathways have an important role for the penetration of the CPP-ELP_{BC}.

A-1 Experimental observations

In our work, we investigated the interactions of different CPP-ELP_{BC} with model lipid membranes: TAT-ELP_{BC}, Arg8-ELP_{BC} and Arg5-ELP_{BC}, and also the interaction of their non CPP-functionnalized counterparts. For this purpose, a solution of CPP-ELP_{BC} at a concentration of 20 μ M with 1% of AF488-labelled polypeptides was brought in contact with a suspension of GUVs of DOPC, a zwitterionic lipid, and incubated under the microscope for half an hour before being imaged in confocal microscopy. These experiments were performed below and above the CMT of the CPP-ELP_{BC}, at 25°C and 35°C. The samples were observed for several hours, to ensure that they have reached the equilibrium. All the results are summarized in table 4.1.

Below the CMT, the CPP-ELP_{BC} were not able to interact with the lipid membrane, as shown in figure 4.1(a). This is consistent with the observations made on the HeLa cells by MacEwan and Chilkoti, who have observed that the non self-assembled ELP_{BC} prevent the CPPs from translocating inside the cell, just as a standard molecular cargo does, as described by Maiolo *et al.* [176].

The control ELP_{BC}s without CPP functions did not interact at all with the GUVs, both below and above their CMT. Above the CMT, none of the CPP-ELP_{BC} were able to translocate inside the cells, whereas even the Arg5-ELP_{BC} was internalized by HeLa cells (*cf.* figure 4.1(b)). Similarly, Mishra *et al.* have demonstrated that TAT grafted onto poly(lactide) nanoparticles could not penetrate inside vesicles [230]. These observations are consistent with the results from Ciobanasu *et al.* [231], who have proved that simple CPP sequences could not penetrate vesicles unless they either had a certain proportion of negatively charged lipid or phosphoethanolamine (PE) head groups in the membrane. Nevertheless, we observed that the TAT-ELP_{BC} and

Peptide	Unimer	Micelle
	25° C	35° C
TAT	No interaction	Adsorption
Arg8	No interaction	Adsorption
Arg5	No interaction	No interaction
Ctrl 60/60	No interaction	No interaction
Ctrl 60/96	No interaction	No interaction

Table 4.1: List of the different qualitative results observed for the interactions between CPP-functionnalized and non functionnalized ELP_{BC} with GUVs of pure DOPC, below and above the CMT of these polypeptides. None of the CPP-ELP_{BC} was able to penetrate inside the GUVs. Nonetheless, CPP-ELP_{BC} with a nominal charge amount of 8 (TAT and Arg8) adsorbed on the surface of the vesicles. Arg5, with a nominal charge amount of 5, was not able to adsorb. The control ELP_{BC} without CPP function did not adsorb as well.

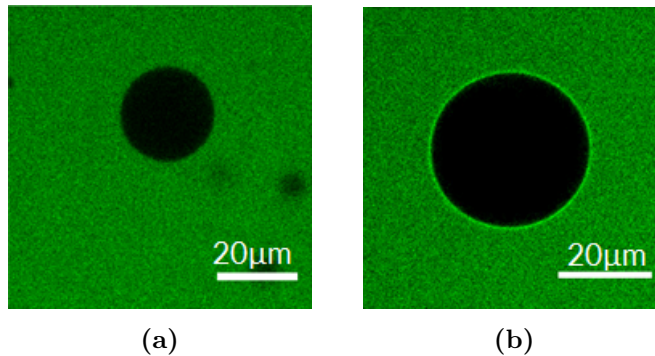


Figure 4.1: Confocal pictures of GUVs made of pure DOPC brought in contact with a suspension of AF488-labelled TAT-ELP_{BC} at different temperatures, (a) below and (b) above the CMT of the polypeptide. In both cases, the CPP-ELP_{BC} are unable to penetrate the vesicles. However, the CPP-ELP_{BC} adsorb on the lipid membrane after undergoing micellization. These observations are consistent with results from MacEwan and Chilkoti [178], Mishra *et al.* [230] and of Ciobanasu *et al.* [231], who observed respectively the temperature-triggered interactions of the CPP-ELP_{BC} with the cell membrane, the lack of penetration from PLA-TAT and short sequences of TAT into GUVs made of pure DOPC.

the Arg8-ELP_{BC} could adsorb on the surface of the GUVs of DOPC, in a similar way than observed by Mishra *et al.* and by Ciobanasu *et al.* with respectively TAT grafted

onto nanoparticles and short sequences of TAT. Arg5-ELP_{BC} could not adsorb on the GUV, as it does not have a sufficient number of charges in its structure, as described by Mitchell *et al.* in their work with short CPPs [177].

Several reasons can be invoked to explain such an increase in affinity for TAT-ELP_{BC} and Arg8-ELP_{BC}. Most notably, the micellar aggregate of p diblock copolymers has a much lower translational entropy than the corresponding p unimers. Therefore, attachment of one micelle implies losing the entropy corresponding to one degree of freedom, while attachment of p unimers would imply losing a much larger entropy corresponding to p degrees of freedom. This is similar to adsorption phenomena of high molecular weight polymers than can adsorb strongly at interfaces even with the modest energy of interaction per monomer [232].

Also, the self-assembly of diblock copolymers into a single micelle induces conformational changes in the hydrophilic block of the ELP_{BC}, leading to a distribution of the end-functional groups that is more favourable for interactions with a wall [233].

The experiment was then performed with GUVs prepared from a mixture of DOPC, DOPE and DOPG at molar fractions of 65/25/10, comparable to the typical phospholipid head composition of mammalian cells, and TAT-ELP_{BC}. Similarly to the results obtained with vesicles made of pure DOPC, the CPP-ELP_{BC} was not able to translocate in the GUVs, but would adsorb on its surface, even for a temperature of 35°C, above the CMT (*cf.* figure 4.2). This results shows a clear difference with the results obtained with small sequences of the same CPP.

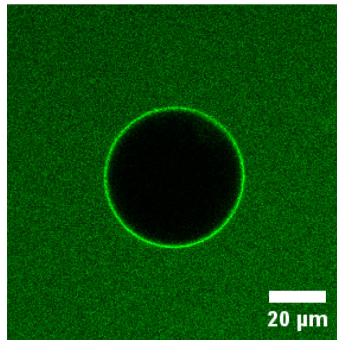


Figure 4.2: Confocal picture of a GUV made of a mixture of DOPC, DOPE and DOPG at molar fractions of 65/25/10, comparable to the typical phospholipid head composition of mammalian cells, immersed in a suspension of micellised TAT-ELP_{BC} ($T = 35^\circ\text{C} > \text{CMT}$). The vesicle is decorated by CPP-ELP_{BC} adsorbed on its membrane, but no translocation of the peptide occurred. By comparison with the results from Ciobanasu *et al.* [231], this observation suggests that the presence of a molecular cargo prevents the internalization of CPPs by passive processes.

A-2 Adsorption is the key for the penetration of the CPP

The comparison of the behaviour of CPP-ELP_{BC} and of short sequences of CPPs towards both biological cells and model lipid vesicles lead us to a better understanding of the mechanisms of cellular uptake by the CPP. The translocation of arginine-rich CPP, fonctionnalized or not with a molecular cargo, through the membrane is a two steps process, as highlighted by our work and by the previous works of MacEwan and Chilkoti [178], of Mitchell *et al.* [177] and of Ciobanasu *et al.* [231]. The overall suggested process is illustrated in figure 4.3.

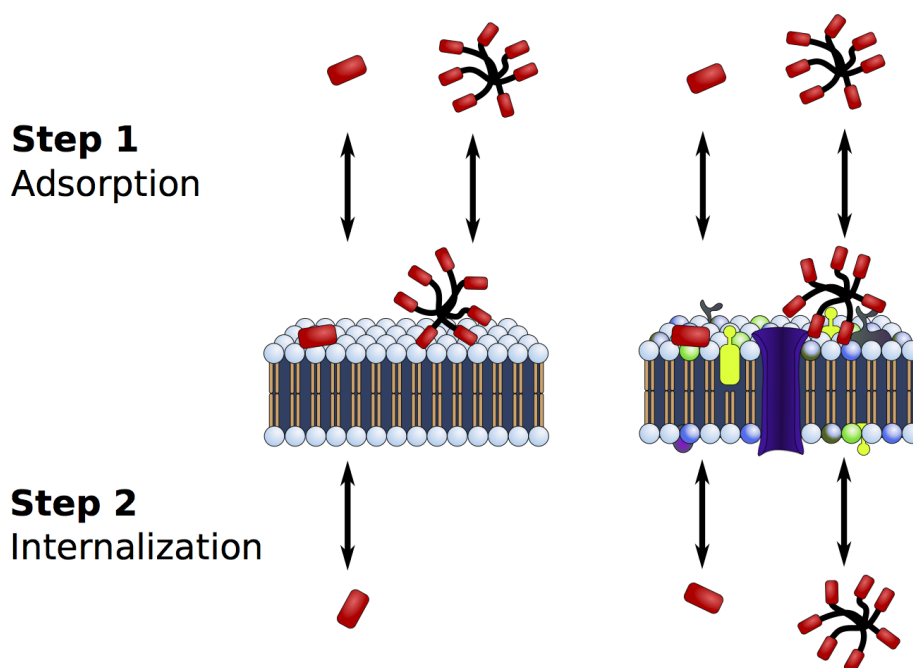


Figure 4.3: Illustration of the two steps process of the cellular uptake by fonctionnalized and non-fonctionnalized CPPs suggested by our observations. The peptides first interact with the surface and adsorb on the membrane, a step triggered by entropy and by the local density of charges in the case of arginine-rich peptides. Once adsorbed on the surface, the peptides are internalized either by passive or by active processes. However, CPPs fonctionnalized with a molecular cargo are unable to translocate by using passive diffusion, as highlighted by our experiments on GUVs.

1. The free molecules from the suspension of CPPs approach the surface of the cell and interact with the lipids from the membrane, adsorbing onto it. To trigger the adsorption, the local density of charge of the CPP should be above a certain threshold [177]. Above this threshold, the adsorption is enhanced by the charge density. Grafting a molecular cargo onto the CPP drastically reduces its affinity

to the lipid membrane and prevents the adsorption. However, increasing the local density of charge, by a process such as the self-assembly of CPP-decorated micelles, will recover the ability of the complex to adsorb on the surface.

2. The CPPs adsorbed on the membrane are internalized by the cell. This can happen either by passive processes of internalization, or by active processes, such as caveolae-mediated endocytosis [178]. Passive diffusion of CPP does not happen for pure phosphatidylcholine (PC) lipid membranes, and either negatively charged lipids or PE head groups are required in the membrane to enable the translocation. Using CPP-ELP_{BC}, we have shown that CPPs functionalized with a molecular cargo are not able to translocate using passive diffusion, and therefore require active processes of internalization.

The mechanism that we describe here implies that adsorption is the crucial step of cellular uptake. As a cell will naturally internalize the CPP and its cargo if it is attached to its surface, a selective adsorption of material will result in a selective translocation.

B Fluorescence quantification of molecules adsorbed on a lipid membrane

B-1 Quantification of the intensity

As described in the previous section, while we have not seen any case of penetration of the GUVs by the CPP-ELP_{BC}, we have observed that the molecules were able to interact with the lipid membrane and adsorb onto it. Adsorption of fluorescent molecules on a GUVs is detected by the formation of a bright corona around the vesicle, as compared to a vesicle without adsorbed molecules onto it. This phenomenon has been observed for different types of molecules, such as α -synuclein [234]. The presence of these coronae on the vesicles corresponds to the presence of a peak in the radial profile of intensity of the vesicle, as shown in figure 4.4.

The area under the additional peak of the profile is proportional to the number of fluorescent molecules adsorbed on the surface. An important number of molecules on the surface will produce a bright corona, hence an important additional peak on the sigmoid signal. The surface concentration of molecules on the lipid membrane can be therefore extracted from the integrated peak of intensity, after subtracting the sigmoid

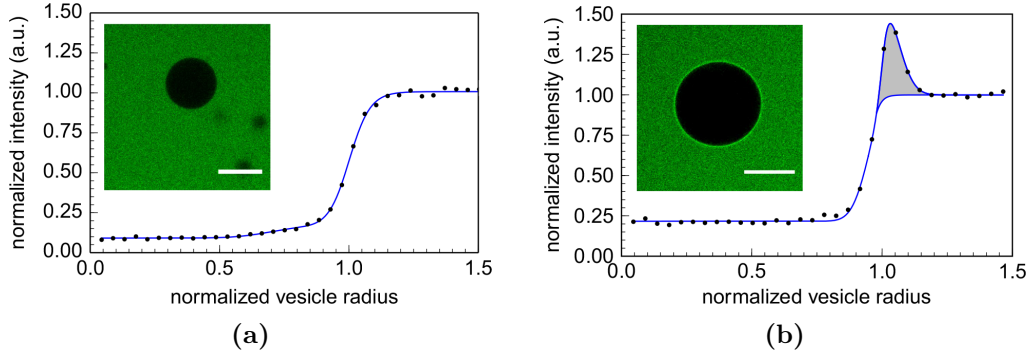


Figure 4.4: Radial profiles of intensity of a GUV (a) without adsorbed molecules on its surface, and (b) with adsorbed molecules on its surface. The corona formed on the surface of the GUV by the presence of adsorbed fluorescent molecules correspond to a Gaussian peak added to the sigmoid signal of a non-decorated GUV. The pictures from which the intensity radial profiles have been extracted are inserted in the top left corner of the corresponding profiles. Scale bars correspond to $20 \mu\text{m}$.

profile corresponding to a similar GUV without adsorbed molecule on it, using a standard calibration of the intensity. This type of method of fluorescence quantification of the adsorption has been already developed and used in the literature [235].

We suggest that the calibration of the intensity can be avoided by comparing the integrated area under the peak to the intensity of the bulk $I_{b,\infty}$, for which the concentration C_b is known. Therefore, only a single picture is required to measure the number of molecules on the surface of the GUV. The equation used to calculate the number of peptides per surface unit Γ is given by

$$\Gamma = \frac{C_b}{R I_{b,\infty}} \int_0^{2\pi} d\theta \int_0^{\infty} r (I_r - I_s) dr. \quad (4.1)$$

where R is the radius of the vesicle, measured at the inflexion point of the sigmoid, and $I_r - I_s$ corresponds to the peak created by the adsorbed molecules, as I_r is the intensity recorded, and I_s the intensity of the corresponding sigmoid without adsorption.

In this work, we decided to not express the adsorption of the CPP-ELP_{BC} as a number of peptides adsorbed per unit surface Γ , but rather as a number of peptides adsorbed per thousand lipids, which we call N_{PTL} :

$$\begin{aligned} N_{PTL} &= 1000 A_H \Gamma \\ &= 1000 A_H \frac{C_b}{R I_{b,\infty}} \int_0^{2\pi} d\theta \int_0^{\infty} r (I_r - I_s) dr. \end{aligned} \quad (4.2)$$

In this equation, A_H is the area per lipid, usually taken at 0.7 nm^2 . The fit function and the fit procedure are given in Appendix Apx-7.

B-2 Experimental requirements for the quantification

The calculation of N_{PTL} using equation 4.2 can only be achieved experimentally if several conditions are met:

- Because of the adsorption of peptides on the surface of the GUVs, one can expect the concentration of peptides in the bulk to decrease, which means that the calculation of the N_{PTL} will be biased. To prevent this, it has to be ensured that the adsorbed material is negligible as compared to the total material available. We do this by calculating the total surface of lipid membrane available.

We used typically $5 \mu\text{g}$ of lipids to prepare our sample of GUVs, and we have shown in section A of chapter 3 that a sample can be used at least 10 times with a sufficient number of GUVs at each observations. Which means that one observation contains up to $0.5 \mu\text{g}$ of phospholipids, so about 0.6 nmol of lipids. These lipids were brought in contact with a typical suspension of CPP-ELP_{BC} of 5 nmol . However, we measured N_{PTL} up to 100. This means that 0.6 nmol of lipids can be covered by up to 0.06 nmol of CPP-ELP_{BC}. This amount represents about 1% of the total material available in the solution. We can therefore conclude that the adsorption of the CPP-ELP_{BC} on the GUVs does not affect the concentration of the bulk in a significant way in our set-up.

- The intensity emitted by the fluorescent dye should be strictly proportional to the concentration of the dye in the solution. As a consequence, all quenching effects described in section C-2.c of chapter 2 need to be avoided in the whole range of concentration. We have controlled the proportionality between both parameters by recording the mean intensity of a sample of AF488-labelled CPP-ELP_{BC} under the confocal microscope for different concentrations of CPP-ELP_{BC}. The results, given in figure 4.5, confirms that the proportionality between intensity and concentration of the dye is respected in the range of bulk concentration of CPP-ELP_{BC} in which we are working.
- The intensity displayed in the confocal picture should be strictly proportional to the light emitted by the sample. In particular, this means that the photomultiplier of the microscope should only modify the energy collected by a pre-factor

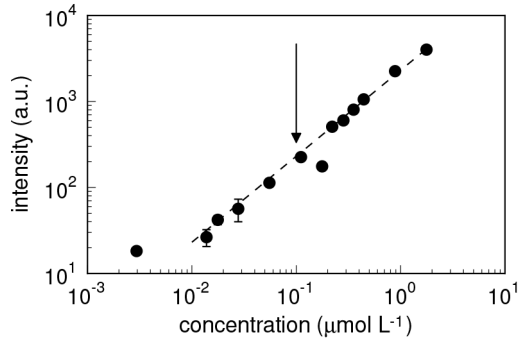


Figure 4.5: Fluorescence calibration curve for a solution of a control ELP_{BC} with 1% of AF488-labelled polypeptides at room temperature, with the intensity given as a function of the dye concentration, obtained with the confocal microscope. The arrow represents the typical working conditions.

and not by any type of offset. This requires the microscope to be perfectly calibrated in intensity. We developed a complete protocol for the calibration of the microscope, which is given in the last section of this chapter.

B-3 In vitro measurements of the N_{PTL}

We first used the measurement of the N_{PTL} to compare the adsorption of the different CPP-ELP_{BC} onto GUVs made of DOPC, and then to compare the effect of the composition of the membrane on the adsorption of TAT-ELP_{BC}.

At 35°C, we measured a N_{PTL} of 13 ± 3 for TAT-ELP_{BC} (*cf.* figure 4.6(a)) and of 7 ± 2 for Arg8-ELP_{BC}, where the values were computed from about 30 vesicle profiles. Such values correspond respectively to surface mass coverages of $1.5 \pm 0.4 \text{ mg.m}^{-2}$ and $0.7 \pm 0.2 \text{ mg.m}^{-2}$, comparable to the values obtained for moderate strength adsorption of polymers on surfaces [232]. The measurement of the N_{PTL} therefore allows us to detect and quantify a difference between the affinity of adsorption of the different CPPs.

When exposed to GUVs made of DOPC, DOPE and DOPG at molar fractions of 65/25/10, the TAT-ELP_{BC} adsorbs with a measured N_{PTL} of 22 ± 3 , as shown in figure 4.6(b), which corresponds to a mass coverage of $2.6 \pm 0.4 \text{ mg.m}^{-2}$. This value is twice as large as the one measured for a membrane made of pure DOPC, proving that the composition of the membrane has a strong impact on the adsorption of CPP-ELP_{BC}. We suggest that this increase is due to the presence of negatively charged lipids in the membrane (DOPG), rather than the presence of DOPE. Indeed, the arginine-rich CPPs used here are cationic peptides which have both a nominal amount of charges of 8. One can therefore expect strong electrostatic interactions between the negatively

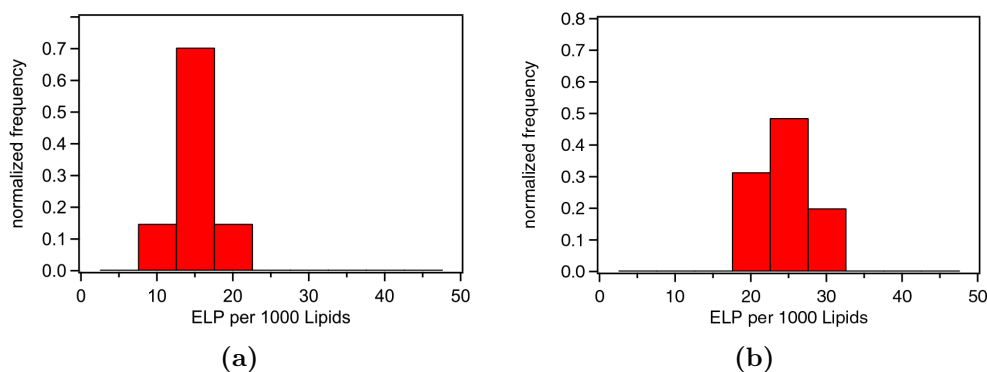


Figure 4.6: Distribution of N_{PTL} values for samples of (a) GUVs of pure DOPC and (b) GUVs made of DOPC, DOPE and DOPG at molar fractions of 65/25/10, exposed to TAT-ELP_{BC}. Histograms of normalized frequency were computed from respectively 27 and 35 GUVs. Experiments were performed at 35°C.

charged membrane and the CPP-ELP_{BC}. This hypothesis is investigated further in the next chapter.

C Does adsorption break the CPP-ELP_{BC} micelles into unimers?

C-1 Measurement by dequenching effect

The adsorption of the CPP-ELP_{BC} can be rationalized equally by the attachment of micelles or unimer polypeptides to the membrane, as displayed in figure 4.7.

In order to discriminate between these two possible scenarios, we suggest here a method based on the measurement of the N_{PTL} . We incorporated a fluorescent dye that self-quenches significantly at high local concentration, the BODIPY, into the CPP-ELP_{BC}. Indeed, a significant reduction of fluorescence intensity is observed in solution upon assembly into micelles for samples containing 54% of BODIPY-labelled polypeptides, as shown in figure 4.8. No quenching is observed for samples with fractions of BODIPY-labelled molecules below 10%.

We performed experiments in similar conditions to those described in section A with two different types of TAT-ELP_{BC}: TAT-ELP_{BC} with 1% of BODIPY-labelled polypeptides, and TAT-ELP_{BC} with 54% of BODIPY-labelled peptides. However, due to the capacity of BODIPY-labelled molecules to bind to the PEG-decorated glass surface, the sample of CPP-ELP_{BC} and GUVs were incubated separately at 35°C prior

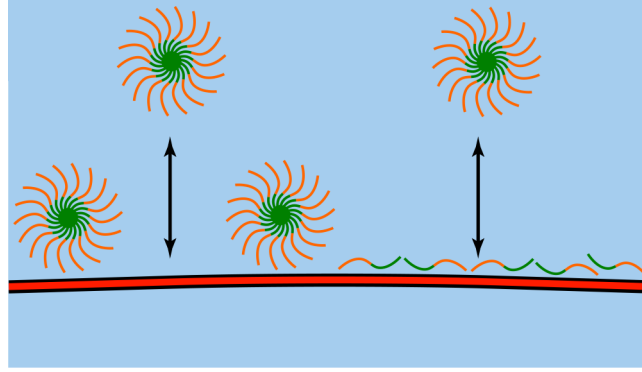


Figure 4.7: Illustration of two possible scenarii for the adsorption of CPP-ELP_{BC} on the phospholipid bilayer, either as micelles or in the unimer state. The arrows emphasize that the attachment process is ruled by the chemical equilibrium between the surface and the bulk.

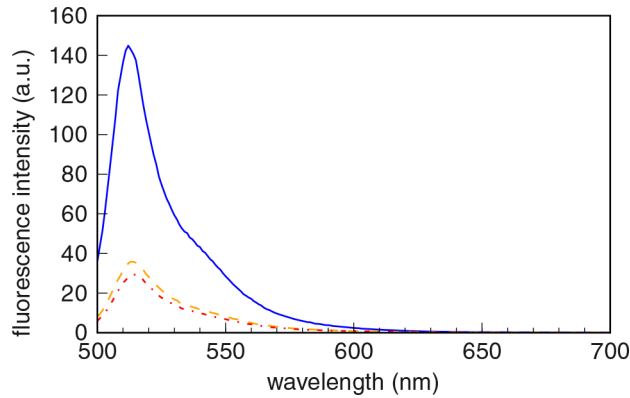


Figure 4.8: Spectrum of a 50% BODIPY-labelled Arg8-ELP_{BC} solution in the unimer state at 25°C (blue solid line) recorded on a spectrofluorimeter. A reduction by self-quenching of around 75% is observed at 40°C (orange dashed line) and 42°C (red dashed line).

to the observation under microscope. With this protocol, the polypeptides injected in the observation chamber were already under their micellar state, thus preventing the BODIPY grafted on the hydrophobic block to interact with the surface. The average N_{PTL} values obtained for these samples does not display any significative difference with the measurement previously performed on AF488-labelled TAT-ELP_{BC}, with an average close to 13 ± 6 corresponding to a mass coverage of $1.5 \pm 0.7 \text{ mg.m}^{-2}$. The detailed results are given in figure 4.9.

Comparison between the two histograms of the BODIPY-labelled TAT-ELP_{BC} shows that the polypeptides adsorb in their micellar form. Indeed, if breakage of the micelles occurred, samples with 54% BODIPY-labelled TAT-ELP_{BC} (9 ± 3) should

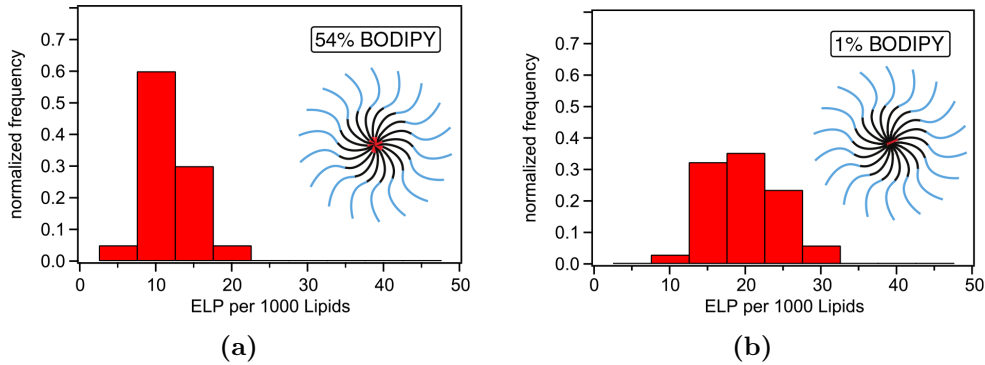


Figure 4.9: Histograms of normalized frequency for the N_{PTL} values distribution for sample of GUVs of DOPC in contact with (a) 54% BODIPY-labelled TAT-ELP_{BC} and (b) 1% BODIPY-labelled TAT-ELP_{BC}. The histograms were computed from respectively 34 and 40 vesicle profiles.

display significantly larger apparent values for N_{PTL} than the sample with 1% of BODIPY-labelled polypeptides (17 ± 5) due to dequenching at the membrane surface. One can note that the results with the AF488-labelled peptides (13 ± 3) give comparable values, showing that the method is independent of the fluorophore.

C-2 Surface coverage

Since we know that the polypeptides adsorb in their micellar form, we can calculate the relative surface coverage for the different CPP-ELP_{BC} and the different surfaces, if one consider the micelles as hard spheres. All the results are summarized in table 4.2.

CPP-ELP _{BC}	TAT-ELP _{BC}	Arg8-ELP _{BC}	TAT-ELP _{BC}
GUV	DOPC	DOPC	Mixed ^a
N_{PTL}	13 ± 3	7 ± 2	22 ± 3
Mass coverage (mg.m ⁻²)	1.5 ± 0.4	0.7 ± 0.2	2.6 ± 0.4
Surface coverage (%)	44 ± 10	23 ± 7	74 ± 10

Table 4.2: List of the experimental measurements of the adsorption for different types of CPP-ELP_{BC} and lipid membranes. The N_{PTL} values are converted here into mass coverage and relative surface coverage.

^aMixed vesicle: mixture of DOPC/DOPE/DOPG at molar fractions of 65/25/10.

At the polypeptide bulk concentrations ($20 \mu\text{M}$) at which our experiments were performed the surface is not completely saturated with micelles. The largest N_{PTL} mea-

sured, for TAT-ELP_{BC} interacting with GUVs made of a mixture of DOPC, DOPE and DOPG at molar fractions of 65/25/10, corresponds to an almost full coverage of 74% \pm 10% of the membrane by micelles, as calculated from an aggregation number of 89 and a radius of 25.9 nm. For comparison, if one would cover the surface with a triangular network of a dense packing of monodisperse hard spheres, a coverage of *circa* 90% would be reached. The surface coverage of the vesicles by the CPP-ELP_{BC} is explored further in the next chapter.

D Calibration of the confocal microscope

The proportionality between the local sample concentration of fluorophores and the intensity displayed in the confocal image is a key requirement to extract the adsorbed fluorophore amount per unit surface of the membrane, a quantity in our work better expressed as the number of polypeptides adsorbed per thousand lipids (N_{PTL}), as described by equation 4.2. It is easy to realise however that analysis of images collected from the same vesicle for different acquisition parameters, such as the photomultiplier gain or the laser power might not yield the same N_{PTL} values, despite the correction by division by the bulk intensity, as shown in figure 4.10.

We therefore ought to develop a way to calibrate our TE-2000 confocal microscope. We present here the method we found to easily account for all variations and assure the proper extraction of N_{PTL} values from the images.

D-1 The settings of the confocal microscope

In order to perform a calibration of the confocal microscope, it is crucial to know perfectly how the fluorescence intensity is produced, modified and collected. The different parameters impacting the measurement are described here, and shown in the figure 4.11).

In fluorescence microscopy, the intensity emitted by a sample at location (x,y,z) $I_{em}(x, y, z)$ depends on two major points : the intensity of the excitation beam on that point $I_{ex}(x, y, z)$, which depends on the laser power (LP) and focalization, and the nature of the sample on that point, which is described by the concentration of dye on that point $C_{dye}(x, y, z)$, and its molar attenuation coefficient ϵ , and the quantum yield of the dye Φ . Due to the low concentration of the dye and the small optical path crossed in the sample, we neglect the exponential decrease of the intensity of the excitation beam while reaching the location, hence

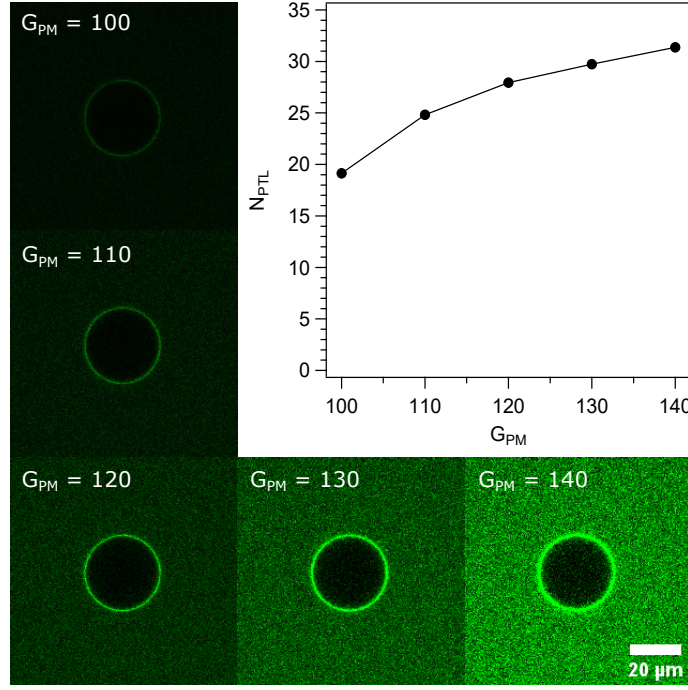


Figure 4.10: N_{PTL} measured from the raw intensity radial profile of the same vesicle, taken with different photomultiplier gains. Pictures display the PM gain G_{PM} used for acquisition, ranging from 100 to 140. The objective of the calibration procedure is to eliminate bias introduced by specific settings.

$$I_{em}(x, y, z) = I_{ex}(x, y, z)C_{dye}(x, y, z)\epsilon\Phi. \quad (4.3)$$

In confocal microscopy, the intensity emitted by the sample is only partially collected by the photomultiplier (PMT). As a pinhole of a controlled size is placed on the confocal plane of the objective lens, only the light located around the object point (x,y,z) can cross the pinhole and reach the PMT. As a consequence, the measured energy $E_s(x, y)$ is proportional to the confocal volume $V_{confocal}$, which depends on objective magnification and on the pinhole diameter.

$$\begin{aligned} E_s(x, y) &= \iiint I_{em}(x', y', z') dx' dy' dz' \\ E_s(x, y) &\propto I_{em}(x, y) \cdot V_{confocal} \end{aligned} \quad (4.4)$$

As described previously, the pixel value PV is not found strictly proportional to the collected energy. We make the arbitrary hypothesis that the measured pixel value of point (x,y) is a linear function of the collected energy, where the pre-factor and the offset depend on the software parameters applied to the PMT, such as the pixel dwell

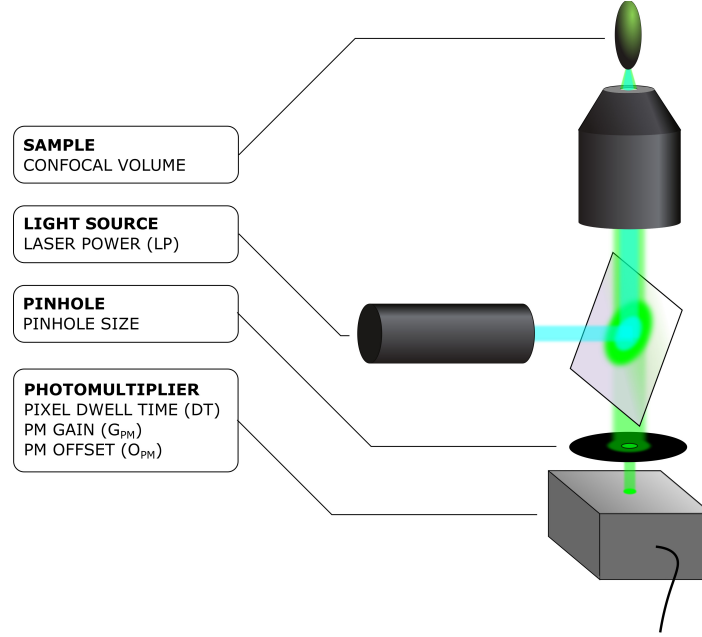


Figure 4.11: Simplified representation of the elements of the confocal microscope, highlighting the different parameters and settings which have an impact on the measured fluorescence intensity. All experiments are performed with the same objective at a fixed pinhole size.

time DT , the PMT Gain G_{PMT} and the PMT Offset O_{PMT} .

$$PV(x, y) = AE_s(x, y) + B \quad (4.5)$$

Adding B is the simplest generalization. Recalling the initial statement, one can deduce that the problem in the computation of the N_{PTL} is the B part of the pixel value function. To make a proper processing of our data, we ought to calibrate the intercept of the function and subtract it from the measured pixel values. As a consequence, it is critical to determine on which acquisition parameters the B depends. We immediately suspected the O_{PMT} to be the most influential parameter, but we nevertheless investigated the effect of all parameters.

D-2 Calibration

The calibration procedure amounts to determine the factors A and B of Equation 4.5. The calibration is performed in two steps: first with a non-fluorescent sample, and then with a sample containing GUVs decorated with fluorescent material.

D-2.a Reference

First part of the calibration was done with a reference non-fluorescent sample (a standard PBS solution without fluorophores), so that in Equation 4.5 one has $PV(x, y) = B$. Measuring pixel values PV while changing the settings of the microscope allows not only to extract the function B (cf. Figure 4.12) but also to confirm that the background value does not depend on laser power, PM gain or even on pinhole size.

The TE-2000 was programmed to record pictures with all combinations for the different parameters of the microscope. The pictures were then sorted and analysed, as pictured in figure 4.12.

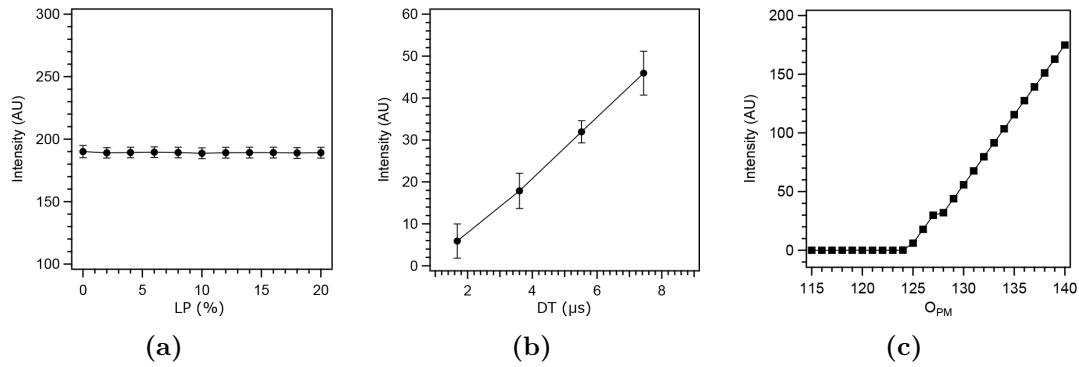


Figure 4.12: Calibration with a reference non-fluorescent sample, to determine the factor B of Equation 4.5. (a) The measured pixel values PV is independent of the laser power LP. Intensity acquired with $O_{PM} = 150$ and $DT = 3.6 \mu s$. (b) Variation of PV with the pixel dwell time DT . Here $O_{PM} = 128$. (c) The importance of the PM offset parameter O_{PM} . Here $DT = 5.52 \mu s$.

All the results confirmed the first impressions, and proved that B only depends on the pixel dwell time DT and the PM offset O_{PM} .

D-2.b Fluorescent sample containing a GUV

The previous observation was confirmed in the second part of the calibration by analyzing the pixel values of four spots of images from a fluorescent solution containing non-fluorescent GUVs while changing the value of the different acquisition parameters (*cf.* figure 4.13(a)).

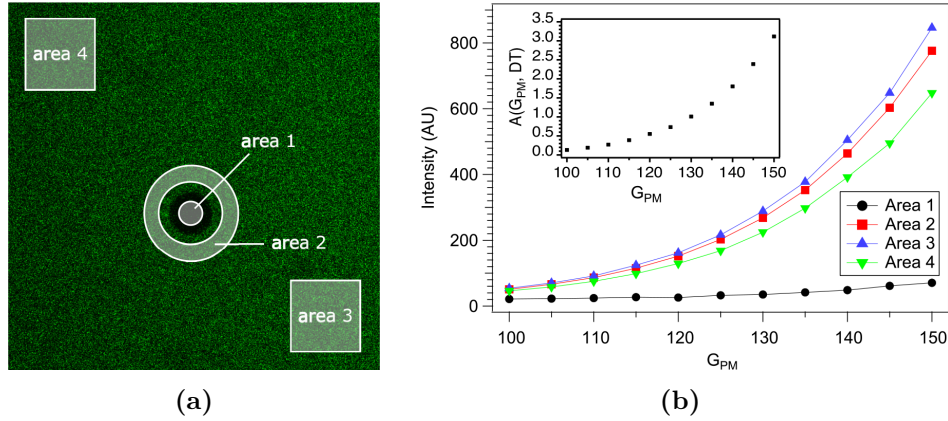


Figure 4.13: Calibration with a fluorescent sample containing non-fluorescent GUVs, to determine the factor $A(G_{PM}, DT)$ of equation 4.5. (a) The four zones of an image under analysis. (b) Intensities of the four zones for different photomultiplier gains G_{PM} at constant $DT = 5.52 \mu s$ and $O_{PM} = 128$. The factor $A(G_{PM}, DT)$ obtained from the calibration is shown in the inset.

We extracted from these measurements the factor A , as shown in figure 4.13(b). Images from this system, where intensities vary due both to inhomogeneous light and fluorophore distributions, conveniently provides for images with a range of intensities and thus allows for acquiring different intensity values with the same image. The calibration consists of using equation 4.5 to find the function $A(G_{PM}, DT)$ that best gives identical true E_S values at the four points from the sample.

D-3 Calibrated values and analytical procedure

The calibration on our Nikon TE-2000 with a C1s confocal head was performed for different values of O_{PM} at a precise value of DT , $5.52 \mu s$ in our case, as shown in table 4.3. The three values of O_{PM} selected were 127, 128 and 130, as 127 and 128 correspond to the values obtained when the auto-offset mode of the microscope was selected. The O_{PM} value of 130 was picked for all post-calibration measurements to avoid peak clipping of the low values of intensity.

O_{PM}	$B(O_{PM}, DT)$
127	16.85
128	19.38
130	52.55

Table 4.3: List of the different values resulting from the calibration of our Nikon TE-2000 C1 Eclipse for a pixel dwell time of $5.52 \mu s$ and different PMT offset.

The computation procedure of the N_{PTL} given in Appendix REF was modified to take account of the calibration. The value of $B(O_{PM}, DT)$ is systematically subtracted from the intensity profile prior to the computation of the N_{PTL} .

D-4 Checking the calibration

After calibration, equation 4.5 can be routinely used to extract the relevant values of collected energy E_s . Also, one can check that derived quantities such as the intensity radial profiles normalized by the intensity of the bulk are independent of the acquisition parameters. An example of such a check is displayed in Figure 4.14 for two different PM gains.

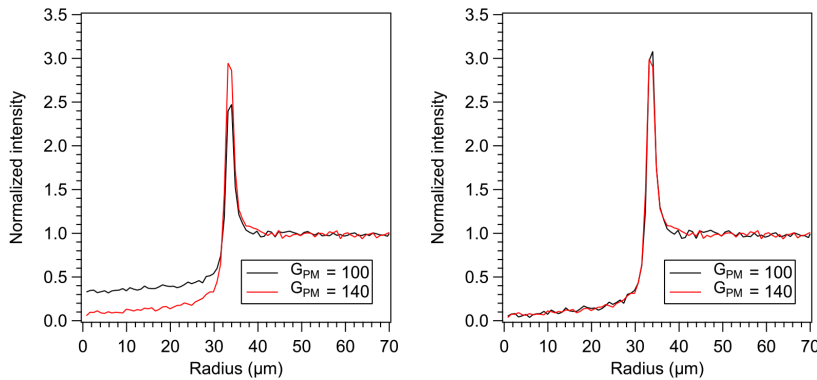


Figure 4.14: Intensity radial profiles acquired for two different PM gains and normalised with respect to the intensity of the bulk. (a) Raw values of the intensities. (b) Intensities after correction by the Equation 4.5.

Most importantly, the derived quantity N_{PTL} which is of relevance for our study, can now be computed independently of the acquisition parameters. As an example, we compare in Figure 4.15 the values corresponding to the Figure 4.10 before and after correction by the calibration procedure.

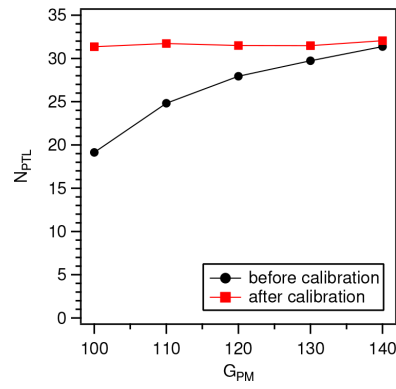
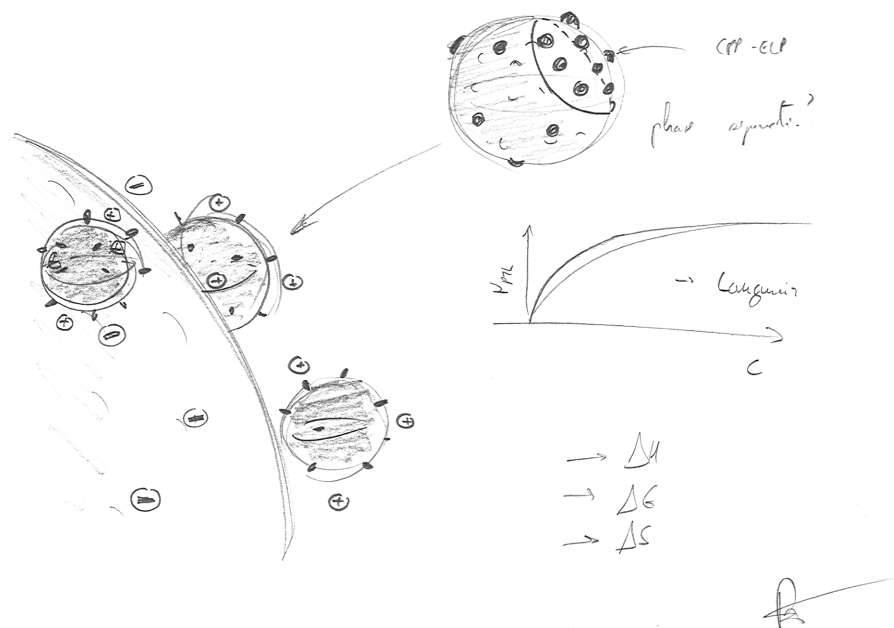


Figure 4.15: Comparison of the N_{PTL} values corresponding to images in Figure 4.10, before and after the calibration procedure. After calibration, the N_{PTL} is found independent of the PMT gain.

KEY-POINTS OF THE CHAPTER

- CPP-ELP_{BC} are not able to translocate through model lipid membranes, even with membrane made of negatively charged lipid or made of PE head groups.
- CPP-ELP_{BC} adsorb on model membranes for CPP-ELP_{BC} with a CPP function having more than 5 nominal positive charges.
- Measurements by a new quantitative method that we developed revealed that the adsorption of TAT-ELP_{BC} is stronger than the one of the Arg8-ELP_{BC}, and that the adsorption on membranes made of PC/PG/PE (65/10/25) is stronger than on zwitterionic ones.
- CPP-ELP_{BC} remain in their micellar state upon adsorption on the lipid membrane.
- We developed a new method to quantify from the confocal images the adsorption of fluorophores on the membrane, and express it as a number of peptides adsorbed per thousand lipids.
- To measure the N_{PTL} , several conditions need to be fulfilled:
 - ▶ The concentration of adsorbate should be large enough for the quantity of adsorbed molecules to be negligible.
 - ▶ The fluorescent-labelled adsorbate concentration should be in the range where the intensity is proportional to the concentration.
 - ▶ The intensity measured by the confocal microscope should be proportional to the energy emitted by the sample.



CHAPTER 5 Quantification of the adsorption on model membrane

WE have shown in the previous chapter that, while the micellisation of the CPP-ELP_{BC} recovers the affinity of the cell-penetrating peptide for the model membrane despite the presence of a molecular cargo, it does not enhance the penetration capacities of the molecule. As we suggested, the key role of the CPP here is to carry the molecular cargo to the target membrane and to adsorb onto it. We expect that in the cell the active internalisation process would give rise to peptide translocation.

Therefore, we thought it was critical to study the mechanism of adsorption of the CPP on the lipid membrane. We demonstrate in this chapter that the quantitative measurement of the N_{PTL} introduced previously can be used to accurately calculate the different thermodynamic quantities of adsorption, namely the constant of affinity K , the Gibbs free energy ΔG , the enthalpy of adsorption ΔH , and the entropy ΔS . These measurements have been performed for different lipid membrane charges.

A Physiological membrane charges

A-1 Adsorption isotherms

As stated in the introduction of this work, the adsorption of molecules on a surface depends on the affinity of the molecule for the surface, represented by the equilibrium constant of adsorption K , and the concentration of the molecule in the solution C .

We measure in this section the N_{PTL} as a function of the concentration of TAT-ELP_{BC} in the solution C_b . The results are depicted in the so-called adsorption isotherms, which can be used to extract K . We have performed these experiments for a range of membrane charge densities below 20% comparable to those of physiological membranes.

A-1.a Theoretical background

The adsorption isotherms were measured for different proportions of negatively charged lipid in the membranes (0, 10 and 20%) at 35°C, for concentrations of polypeptides ranging from 5 to 150 μM . The measurement on higher concentrations could not be achieved, as the presence of too many CPP-ELP_{BC} in the solution caused the GUVs to burst.

In all experiments, the suspension of TAT-ELP_{BC} and GUVs was always preincubated at room temperature, heated at 29°C for 30 minutes stabilization, checked to control the absence of adsorption of the polypeptide in its unimer form, and then heated a second time up to 35°C for final observation and measurement.

We did not reach the plateau predicted by the Langmuir isotherm for any of the three different proportions of negative lipids in the membrane. Thus, we were not able to measure experimentally if the adsorption of the CPP-ELP_{BC} was following an adsorption model of a single monolayer or the BET model for the formation of multilayers. Nonetheless, we know that the self-assembled CPP-ELP_{BC} can be considered as spheres with a positively charged shell. It is therefore unlikely that such electrically charged spheres could adsorb on top of each others, and we can consider that the surface coverage will follow the construction of a single sphere monolayer. This statement is comforted by the work of Decher and Hong [236] performed on the construction of layer-by-layer films of polyelectrolytes, where the adsorption of a new layer of polyelectrolyte can only occur if a layer of polyelectrolyte with the opposite charge is already adsorbed on the surface.

In the case of a single monolayer adsorption, the Langmuir isotherm model given in equation 1.18 is used to describe the adsorption of polypeptides. Since we assume

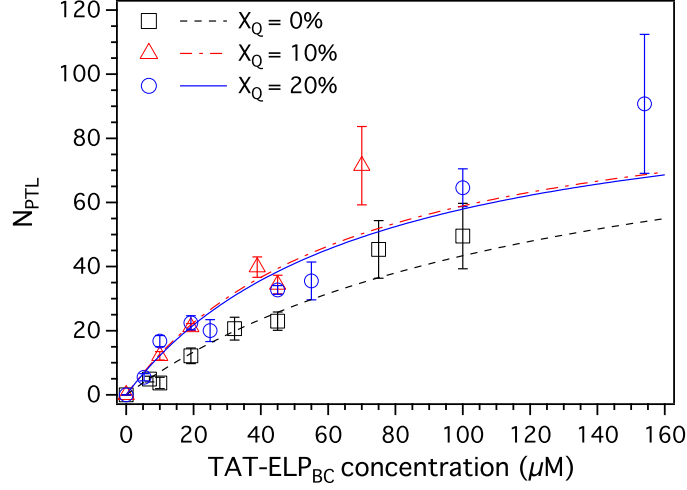


Figure 5.1: Adsorption isotherms obtained from the experimental measurement of the N_{PTL} for the adsorption of TAT-ELP_{BC} on GUVs with different membrane charges (0, 10 and 20% of negatively charged lipids in the membrane) at different concentrations of polypeptides in the solution. The measured values are close to a linear increase at relatively low concentrations, and the presence of the plateau predicted by the Langmuir model could not be observed. The plain and dashed lines are the fits of the data points, fitted with the Langmuir’s equation.

that the adsorption of the CPP-ELP_{BC} could only occur with the formation of a single monolayer, we shall predict the existence of a maximal amount of peptides which can adsorb on a membrane, N_{PTL}^{Max} . We will therefore define the surface coverage as

$$\theta = \frac{N_{PTL}}{N_{PTL}^{Max}}. \quad (5.1)$$

The Langmuir model can now be rewritten for the adsorption of micelles of peptides, such as

$$N_{PTL} = N_{PTL}^{Max} \frac{K \frac{C_b}{p}}{1 + K \frac{C_b}{p}}, \quad (5.2)$$

where p is the aggregation number of the CPP-ELP_{BC} micelles and C_b/p corresponds to the concentration of micelles in the bulk $C_{m,b}$. To perform a more accurate fit of our experimental data, the linear form of the Langmuir isotherm can be also rewritten for the measurement of the N_{PTL} , based on equation 1.19,

$$\frac{C_{m,b}}{N_{PTL}} = \frac{C_{m,b}}{N_{PTL}^{Max}} + \frac{1}{KN_{PTL}^{Max}}. \quad (5.3)$$

In this case, plotting the experimental values rewritten in $C_{m,b}/N_{PTL}$ versus $C_{m,b}$ should give a straight line with a slope equal to $1/N_{PTL}^{Max}$ and an intercept equal to $1/KN_{PTL}^{Max}$.

A first attempt of fitting the experimental data, shown in figure 5.1, indicated that the adsorption of CPP-ELP_{BC} on the membrane charges of 10 and 20% have a similar evolution, with an average N_{PTL} greater than the one of a zwitterionic membrane. Electrostatic interactions between the negative charges of the membrane and the positive charges of the polypeptide micelles can easily explain the differences of adsorption between the zwitterionic and the charged membranes, but the absence of differences between 10 and 20% of charges is surprising.

A-1.b Effect of the membrane charge

To understand better the effect of the membrane charge on the adsorption of the CPP-ELP_{BC}, N_{PTL} values were measured for different amount of negative lipids in the membrane and at three different bulk CPP-ELP_{BC} concentrations. Results are shown in figure 5.2.

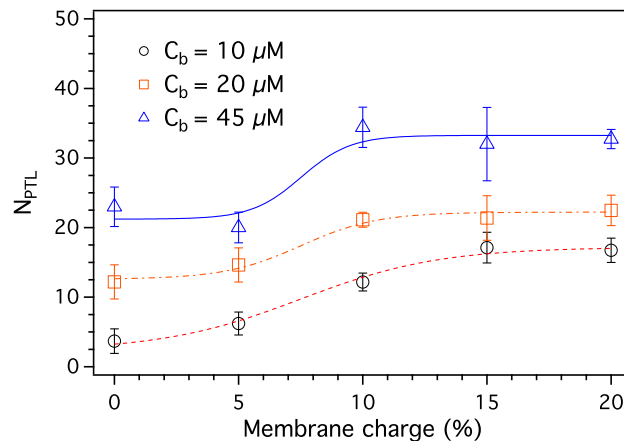


Figure 5.2: Effect of the membrane charge on the adsorption of TAT-ELP_{BC} on a lipid membrane. N_{PTL} were measured for different proportions of negatively charged lipid in the membrane, from 0 to 20%, for three concentrations of polypeptides in the bulk, at 35 °C. This range of membrane charges corresponds to the physiological one.

The N_{PTL} does not seem to increase proportionally to the charge in the membrane. A threshold value around $7.5\% \pm 1.0\%$ separate two regimes of adsorptions: "low" adsorptions and "high" adsorptions. In both regimes, N_{PTL} values are roughly constant over the proportion of negative lipids in the membrane. However, the sharpness of the transition between the two states depends on the concentration of polypeptides in the

bulk. This result confirms the observation made with the adsorption isotherms, and proves that adsorptions of CPP-ELP_{BC} on membrane with 10 and 20% are equivalent.

The value of $7.5\% \pm 1.0\%$ of negatively charged lipids in the membrane correspond to a surface density of -0.11 ± 0.01 elementary charges per square nanometres ($e.nm^{-2}$). It is interesting to note that, within our error limits, this surface density is equal to the one of the TAT-ELP_{BC} micelles. Indeed, if we consider the micelles as hard spheres with an aggregation number of 89, 8 positive charges per polypeptide and a hydrodynamic radius of 25.9 nm, the corresponding surface density is equal to $0.08 e.nm^{-2}$. We can deduce from this observation that, in the physiological range of membrane charges, the threshold between the low and high adsorption regimes roughly matches the charge density of both adsorbate and substrate. Above this limit the micelle of CPP-ELP_{BC} is not influenced by the presence of additional charges.

A-1.c Determination of K and N_{PTL}^{Max}

The isotherms measured in section A-1.a were fitted using equation 5.3. For a better accuracy in the fit, and because of the previous results, the data at 10 and 20% of negatively charged lipids in the membrane were considered all together with the data at 15% previously collected.

We assumed as well that the N_{PTL}^{Max} value is independent from the membrane charge. Indeed, the N_{PTL}^{Max} represents the steric hindrance of the micelles adsorbed at the surface. This takes into account the repulsive forces between the micelles, while the membrane charge affects the affinity of the micelle for the membrane and therefore the surface coverage. Following this hypothesis, we ran global fits on the data, with a unique value for N_{PTL}^{Max} .

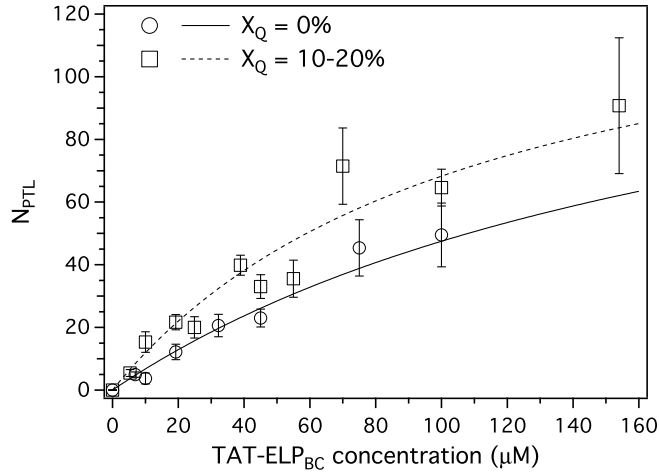


Figure 5.3: Fit result of the Langmuir isotherm for the adsorption of TAT-ELP_{BC} on zwitterionic membranes and membranes with a low membrane charge (10-20% of negatively charged lipids). The data points of the measurements for 10, 15 and 20% of charges were averaged to increase the accuracy of the fit.

We obtained from the fit an equilibrium constant of adsorption K for the micelles almost 2 times higher for a negatively charged membrane than for a zwitterionic one, with K respectively equal to $800000 \pm 300000 \text{ M}^{-1}$ and $450000 \pm 90000 \text{ M}^{-1}$. A comparable increase with the charge has been reported for the interaction between the short TAT 47-57 sequence and model membranes made of different proportions of PC and PG lipids by Rao *et al.* [237], who reported a K equals to $34000 \pm 5000 \text{ M}^{-1}$ for a zwitterionic membrane and $130000 \pm 30000 \text{ M}^{-1}$ for a membrane made of pure PG. For comparison, the constant of adsorption at equilibrium of a polylysine (4-15 kDa, 146 Da per monomer) on a carboxyl-decorated glass surface is about 200000 M^{-1} . For a similar amount of charged monomers per macromolecule than for the short TAT 47-57 sequence, this corresponds to a constant of 23000 M^{-1} [238].

The fit also returns a N_{PTL}^{Max} of 140 ± 30 . This corresponds to a mass coverage of $16 \pm 4 \text{ mg.m}^{-2}$ and a corresponding surface coverage of $500\% \pm 100\%$. This number is calculated with the hypothesis that the micelles can be seen as impenetrable hard spheres on a surface, which turns out to be inappropriate to our case. Moreover, we have shown in the previous chapter that CPP-ELP_{BC} adsorb on the lipid membrane as micelles. With both informations, we suggest that, while they remain as micelles, CPP-ELP_{BC} interpenetrate when being adsorbed on the surface, as illustrated in figure 5.4. Such a configuration is allowed by the chemical structure of the polypeptides. Indeed, only the CPP grafted at the end of the ELP_{BC} is electrically charged, which means

that the ELP_{BC} themselves does not electrostatically repel each other.

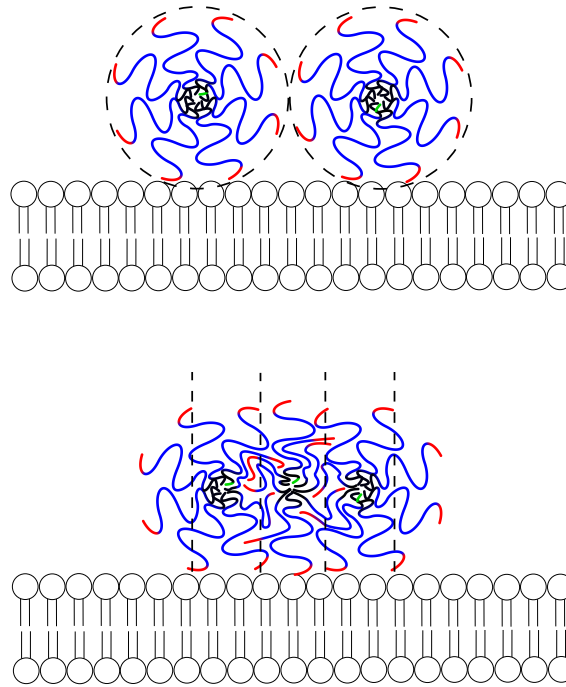


Figure 5.4: Sketch of the two hypothesis used to describe the adsorption of micelles on the surface. (Top) Packing of hard non-interpenetrating spheres on the surface. The maximal surface coverage one can expect (N_{PTL} of 30) is calculated from the hydrodynamic radius of the spheres. (Bottom) Polypeptides micelles entanglement on the lipid membranes, a configuration allowing a surface coverage up to 5 times higher than the one with the packing of hard spheres (N_{PTL} of 140 here).

The results obtained from the analysis of the different systems are summarized in table 5.1.

X_Q (%)	N_{PTL}^{Max}	K (M^{-1})
0	140 ± 30	450000 ± 90000
10-20	"	800000 ± 300000

Table 5.1: Fitted values of N_{PTL}^{Max} and K using the Langmuir isotherm and equation 5.3 to adjust to our experimental data. The maximum surface coverage is identical for membrane charge of 0 and 10-20%.

A-2 Thermodynamic analysis

Knowing the value of K and N_{PTL}^{Max} , we investigated further how the measurement of N_{PTL} can be used, specifically for the determination of thermodynamic quantities, such as the enthalpy and entropy of adsorption.

A-2.a Theoretical background

Gibbs free energy of adsorption ΔG can be calculated directly from the equilibrium constant K through the relation

$$K = \exp\left(\frac{-\Delta G}{RT}\right), \quad (5.4)$$

which can be rewritten as

$$\Delta G = -RT \ln K. \quad (5.5)$$

Through this equation, the results of the fit performed in section A-1.c can be used to calculate the value of the Gibbs free energy of adsorption of TAT-ELP_{BC} on membranes with different proportions of negatively charged lipids. Results are given in table 5.2.

X_Q (%)	ΔG (kJ.mol ⁻¹)	ΔG ($k_B T$)
0	-33.3 ± 0.5	-13.0 ± 0.2
10-20	-34.8 ± 0.9	-13.6 ± 0.4

Table 5.2: Values of the Gibbs free energy of adsorption ΔG for the CPP-ELP_{BC} micelles, for different membrane charges, calculated from the fit performed on the adsorption isotherms.

The Gibbs free energy of adsorption ΔG on both membranes is about -35 kJ.mol⁻¹ for the micelles. If one assumes that all the unimers in the micelles interact with the membrane, the Gibbs free energy of adsorption of unimers are found equal to -374 ± 5 J.mol⁻¹ for the neutral membrane and -390 ± 10 J.mol⁻¹ for the charged one. However, since the micelles are expected to remain as spheres upon adsorption, this hypothesis is very unlikely to happen. Moreover, these expected values for unimers are very small. For comparison, Ziegler *et al.* found a Gibbs free energy of adsorption for the bare TAT sequence on a 25% charged membrane of -4.81 kJ.mol⁻¹ [239]. This value is similar to the one found for the adsorption of poly(L-lysine) on glass spheres

by Latour *et al.* [240], where ΔG was equal to -3.5 kJ.mol^{-1} , with a similar amount of nominal charges than with the TAT sequence ($\Delta G = -60 \text{ kJ.mol}^{-1}$ for a 15-30 kDa poly(L-lysine)). If we assume that the Gibbs free energy of adsorption for the micelles is n times the energy found for the short sequence of TAT by Ziegler *et al.* (n being the number of TAT-ELP_{BCS} in the micelle interacting with the surface), we found that $8.1\% \pm 0.2\%$ within the polypeptides of the micelles are interacting with the membrane.

The enthalpy and entropy of adsorption ΔH and ΔS can be calculated from the relation

$$\Delta G = \Delta H - T\Delta S. \quad (5.6)$$

Nevertheless, it requires measuring ΔG at different temperatures to calculate the values of ΔH and ΔS . Performing the measurement of the N_{PTL} for different concentrations and for different temperatures is time consuming. To be able to measure the enthalpy and entropy of adsorption anyway, we made here the assumption that N_{PTL}^{Max} the maximal number of peptides which can be adsorbed per thousand lipids does not depend on the temperature, as it is mostly a steric value. Following this hypothesis, the value of K can be directly extracted from the N_{PTL} in equation 5.2, as followed

$$K = \frac{N_{PTL}}{\frac{C_b}{p} (N_{PTL}^{Max} - N_{PTL})}. \quad (5.7)$$

Using equations 5.6 and 5.5, we can write a relation between ΔH , ΔS and K , such as

$$R \ln K = -\frac{\Delta H}{T} + \Delta S. \quad (5.8)$$

Therefore, a plot of a $R \ln K$ versus 1 over T should give a straight line with a slope equals to $-\Delta H$ and an intercept equals to ΔS . If all the conditions listed above are fulfilled, a simple measurement of the N_{PTL} as a function of the temperature is enough to measure ΔH and ΔS .

A-2.b Adsorption of CPP-ELP_{BC} as a function of the temperature

The measurement of the adsorption of TAT-ELP_{BC} as a function of the temperature is performed by first incubating the polypeptides with the GUVs made either of zwitterionic lipids or with 20% of negatively charged lipid in the membrane at room temperature. The temperature of the sample under the microscope is then increased to 25°C and left undisturbed for 30 minutes until it stabilizes. After making sure that the

sample is non aggregated or that adsorption has not occurred, the temperature is raised by 2°C and the sample is left undisturbed for 30 minutes. The process is repeated until a temperature of 42°C is reached, which is the highest temperature we could get inside the sample with our heating system. The results are given in figure 5.5(a).

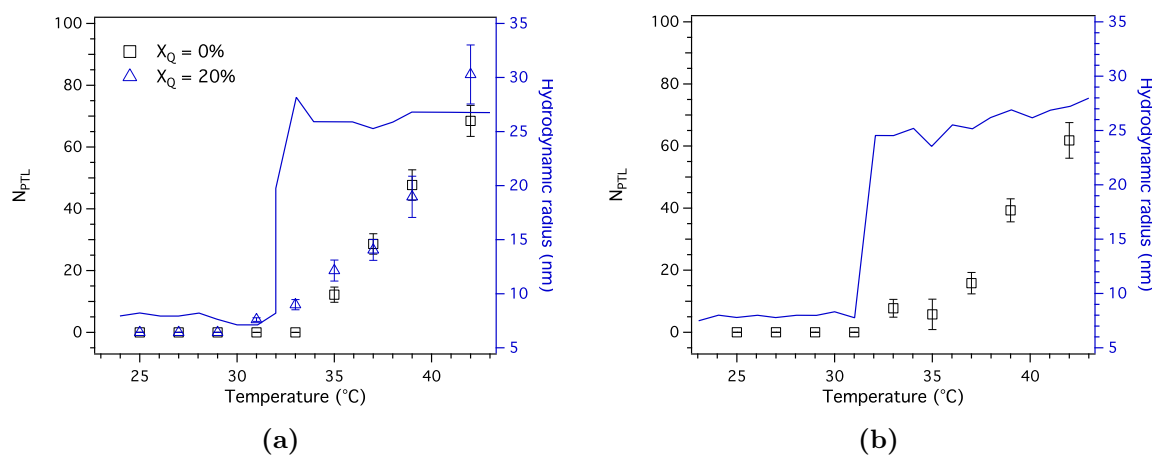


Figure 5.5: (a) Adsorption of TAT-ELP_{BC} on a zwitterionic membrane (□) and on a negatively charged one (△) (20% of negatively charged lipids) and (b) adsorption of Arg8-ELP_{BC} on a zwitterionic membrane. The measurement of the N_{PTL} was performed above and below the CMT, at a concentration of CPP-ELP_{BC} in the solution equal to 20 μ M. The measurement of the hydrodynamic radius as a function of temperature is given for both CPP-ELP_{BC} to highlight their CMTs (plain lines). For both types of CPPs the adsorption increases with the temperature, with a linear increase of N_{PTL} of about 8 °C⁻¹ in all cases.

We have found that the adsorption of TAT-ELP_{BC} increases with the temperature of the sample for both the charged and non-charged membrane. The experiment was also performed with Arg8-, Arg5-ELP_{BC}, and with the two corresponding control ELP_{BC}s (without the CPP function), on GUVs made of zwitterionic lipids for comparison. The adsorption of Arg8-ELP_{BC} increases with the temperature (*cf.* figure 5.5(b)), in a similar way as the TAT-ELP_{BC}. For TAT-ELP_{BC}, a linear increase of 8.6 ± 0.9 N_{PTL} per Celsius degree (ELP.°C⁻¹) was found, while a linear fit of the increases of Arg8-ELP_{BC} returns 8.2 ± 0.7 ELP.°C⁻¹. This last fit is only given as comparison, as the evolution of Arg8-ELP_{BC} is more comparable to an exponential increase, as shown in figure 5.5(b). Meanwhile, neither Arg5-ELP_{BC} nor the control ELP_{BC}s interact with the zwitterionic membrane of the GUVs, even at temperatures as high as 42°C.

A-2.c Calculation of the enthalpy and entropy of adsorption

Experimental results obtained with the adsorption of the TAT-ELP_{BC} as a function of the temperature for membrane charges of 0 and 20% of negatively charged lipids were converted using equation 5.7 into constant of equilibrium K in order to determine the enthalpy and entropy of adsorption. The dependance of $R \ln(K)$ as function of $1/T$ is shown on figure 5.6.

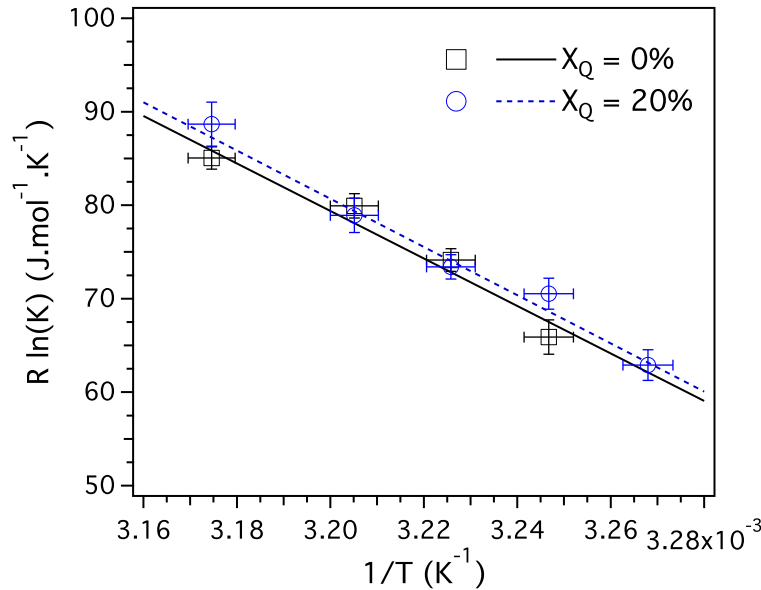


Figure 5.6: $R \ln(K)$ as a function of $1/T$ obtained applying equation 5.7 for the adsorption of micelles of TAT-ELP_{BC} on a zwitterionic membrane and a membrane with a low proportions of charge (20% of negatively charged lipids). Measurements were performed at a polypeptide concentration of 20 μ M. The data are adjusted with straight lines, for which the slope corresponds to minus the enthalpy of adsorption, and the intercept to the entropy of adsorption, following equation 5.8.

The data were then fitted using equation 5.8. Considering the precision of the fit on the data, ΔH was found equal to 254 ± 39 and 258 ± 2020 kJ.mol^{-1} respectively for the zwitterionic and charged membrane, and ΔS was equal to 897 ± 124 and 910 ± 63 $\text{J.mol}^{-1}.K^{-1}$. The adsorption of the micelles on GUVs is therefore an endothermic process, and the entropy of adsorption is mainly due to the changes of entropy of water [241]. Indeed, no counterions can leave the lipid membrane toward the bulk water in the case of a zwitterionic membrane. However, this phenomenon can explain the slight difference between the entropy of adsorption on zwitterionic and charged membranes. In the previous hypothesis, where only 8% of the polypeptides in the micelles interact with the membrane, ΔH is equal to 35.1 ± 5.4 kJ.mol^{-1} for the neutral

membrane and $35.7 \pm 2.8 \text{ kJ.mol}^{-1}$ for the negatively charged one, and ΔS is found equal to $123 \pm 17 \text{ J.mol}^{-1}.\text{K}^{-1}$ for the neutral membrane and $126 \pm 9 \text{ J.mol}^{-1}.\text{K}^{-1}$ for the charged one. We can compare these values to the ones found by Ziegler *et al.* [239] for the adsorption of bare TAT sequence on a membrane with 25% of charged lipid, which are equal to $-8.20 \text{ kJ.mol}^{-1}$ for ΔH and $-11.4 \text{ J.mol}^{-1}.\text{K}^{-1}$ for ΔS . As comparison, for the adsorption of poly(L-lysine) (15-30 kDa) on glass spheres, ΔH was found equal to $-21.3 \text{ kJ.mol}^{-1}$ and ΔS to $209.2 \text{ J.mol}^{-1}.\text{K}^{-1}$ [240], so respectively $-1.26 \text{ kJ.mol}^{-1}$ and $12.40 \text{ J.mol}^{-1}.\text{K}^{-1}$ for a similar amount of nominal charges per polymer. It is interesting to note that the adsorption of bare sequences of TAT and poly(L-lysine) were both found exothermic, unlike the adsorption of the TAT-ELP_{BC}.

B High charge density regime

B-1 Charge effects at a high charge densities: a qualitative description

We also investigated the effect of high membrane charges in the range of 30% to 50%. We measured the N_{PTL} for a sample of TAT-ELP_{BC} brought in contact with GUVs made of different proportions of charged lipids. The measurements were performed at 29°C and 35°C, to compare the behaviour of the CPP-ELP_{BC} in their unimer and micellar states. Experiments were performed by first incubating the sample at 29°C under the microscope prior to the observation, and then by increasing the temperature up to 35°C to measure the adsorption of the micelles.

In the low charge density regime, we had observed for micelles a jump in N_{PTL} at 7.5%. Above this value, the N_{PTL} seemed to be constant. Here we see that if we further increase the membrane charge density, it gets more complex. Above 30%, the CPP-ELP_{BC} adsorb in their unimer state on the membrane of the GUVs, and at 50% we observe a demixing of the fluorescence on the GUV surface, with two domains of low and high fluorescence (*cf.* figure 5.8). Adsorption is measured on the large domain of low fluorescence, as it always covers at least 60% of the whole surface.

Therefore we decided to consider separately this high charge density regime and the physiological one. We first discuss the adsorption of the ELP_{BC} in their unimer state, and then perform the thermodynamical analysis we had done for the physiological charge regime.

B-1.a Unimers adsorption as a function of membrane charge

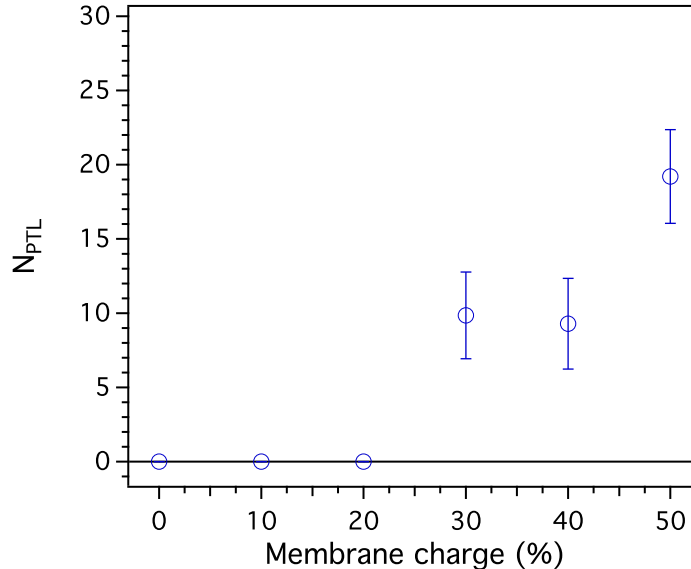


Figure 5.7: Effect of the membrane charge on the adsorption of unimers of TAT-ELP_{BC} on lipid membranes with low and high proportions of negatively charged lipids (> 30%). The measurements have been performed at 29°C and at a polypeptide concentration of 20 μ M. For 30% of negative lipids and more, the unimers of TAT-ELP_{BC} adsorb on the lipid membrane.

The adsorption of the CPP-ELP_{BC} unimers is remarkably strong on highly charged membrane. As a comparison the N_{PTL} for a CPP-ELP_{BC} as unimers on a membrane charge of 30% at room temperature is equal to the one obtained on a zwitterionic membrane in its micellar state, at 35°C (respectively 10 ± 3 and 12 ± 2). The adsorption is even stronger at 50% of charges, with a N_{PTL} of 19 ± 3 . We see that the electrostatic interactions between the negatively charged membrane and the positively charged CPP-ELP_{BC} are strong enough above 30% of charges to directly trigger the adsorption of the unimers. Moreover, it is interesting to note that, if one considers an unimer of CPP-ELP_{BC} as a gaussian coil with a radius of 7.8 μ m and 8 positive charges, the corresponding lipid membrane charge would be equal to 29%, which appears to be the threshold at which the unimer adsorb on the surface of the vesicle.

We have witnessed the same behaviour with Arg8-ELP_{BC}, which was able to adsorb on the lipid membrane in its unimer state as well ($T < CMT$) for 50% of charged lipids. Moreover, the adsorption on the GUV of both TAT-ELP_{BC} and Arg8-ELP_{BC} in their unimer state had a strong impact on the arrangement of the surface of the vesicle. Indeed, as one can see on figure 5.8, the adsorption induces a phase separation, with

two domains which appear with different intensities on the coronae of the GUVs. Above the CMT, the fluorescence of the coronae of the GUVs becomes homogeneous, but the phase separation would occur again if the sample was cooled back down to 29°C. This heterogeneous adsorption is thus reversible.

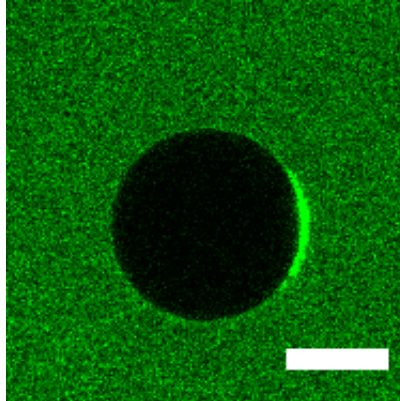


Figure 5.8: Confocal picture of a GUV made of DOPC/DOPG at molar fraction of 1/1 brought in contact with a solution of TAT-ELP_{BC} in its unimer state. Due to the high amount of negatively charged lipids in the membrane, the TAT-ELP_{BC} adsorbs heterogeneously on the surface of the GUV.

A similar phenomenon has been observed by Patarraia *et al.* [242], with the adsorption of Cytochrome C on lipid membranes containing different proportions of DOPG. They have indeed shown that the Cytochrome C was able as well to induce changes in the phase separations diagram of a lipid mixture of DOPG/eSM/Chol (50/40/10), so with a similar amount of charges than in our samples.

B-1.b Micelles adsorption as a function of membrane charge

For the adsorption of CPP-ELP_{BC} under their micellar form, the N_{PTL} seems to be increasing above 30% of charges. This behaviour is in contradiction with the initial observation we have made, on the fact that two steady states of adsorption exist depending on the membrane charge below and above a threshold of 7.5% of charges. Nonetheless, this result may come from an experimental bias: in the protocol used for all the measurements, we brought the GUVs and CPP-ELP_{BC} in their unimer state together before the sample was heated up to bring the CPP-ELP_{BC} in their micellar state. The temperature-concentration relation given by the CMT suggest that a small fraction of unimers can still exist in the solution, meaning that unimers could still be decorating the surface of the GUVs as the micelles form, thus disturbing the micelles adsorption. However, this would be in contradiction with the observations made by

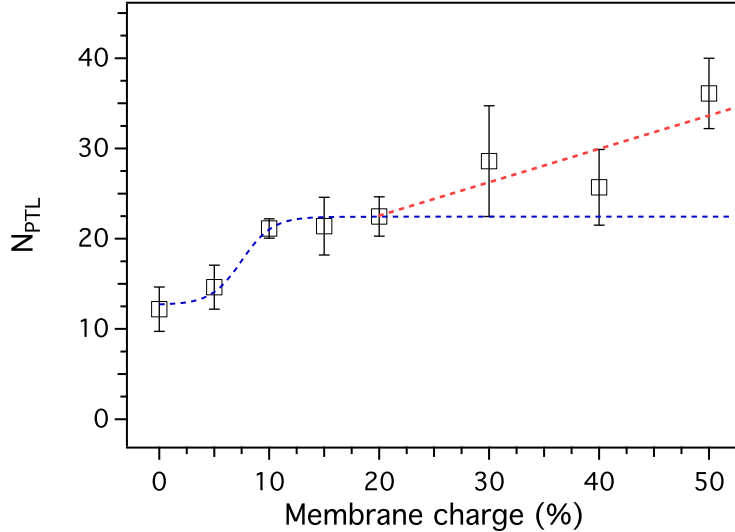


Figure 5.9: Effect of the membrane charge on the adsorption of micelles of TAT-ELP_{BC} on lipid membranes with low and high proportions of negatively charged lipids (> 30%). N_{PTL} previously measured for low membrane charges are given here for comparison. The measurements have been performed at 35°C and at a polypeptide concentration of 20 μ M. Blue dashed line corresponds to the sigmoid fitted on the physiologicla range of membrane charge in figure 5.2, and red dashed line is a guide line given to visualize the evolution of the N_{PTL} above 30%.

Kurzbaach *et al.* [243], who suggested that above the CMT no detectable amount of unimers remain in the solution.

B-2 Langmuir adsorption model: structure of the adsorbed layer

We investigate here in details the adsorption of unimers and micelles of CPP-ELP_{BC} on a membrane with 50% of negatively charged lipids, but as a function of the concentration to understand how strong is the electrostatic interaction between the CPP-ELP_{BC} and the negatively charged lipid, and also in which configuration the unimers decorate the surface. Furthermore, we investigate how the pre-adsorption of unimers of CPP-ELP_{BC} could prevent the adsorption of micelles of the same polypeptides.

B-2.a Construction of an unimers monolayer

We measured the N_{PTL} as a function of the polypeptides concentration in solution, in order to obtain Langmuir's isotherms (*cf.* figure 5.10). The data were fitted with

the Langmuir model to obtain N_{PTL}^{Max} and K .

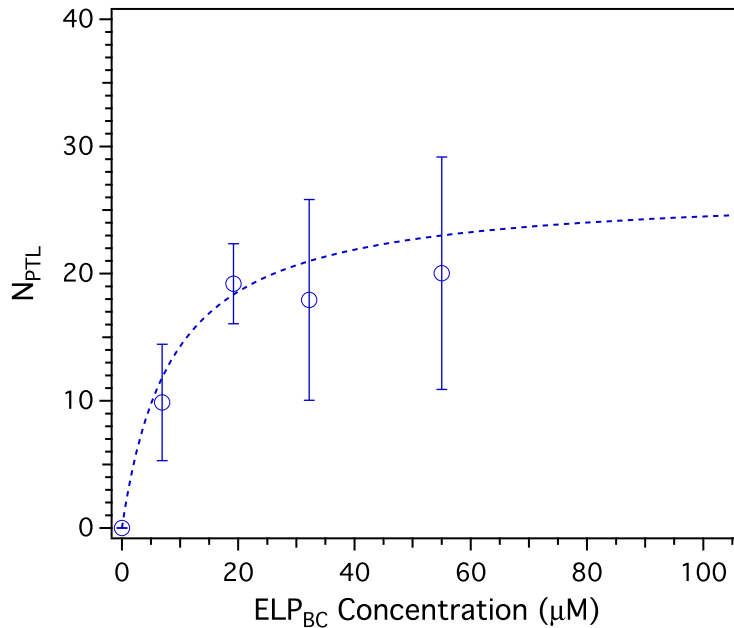


Figure 5.10: Adsorption isotherms obtained from the experimental measurement of the N_{PTL} for the adsorption of unimers of TAT-ELP_{BC} on GUVs with a membrane composition of 50% of negatively charged lipids at different polypeptides concentrations in solution. The measurements were performed at 29°C. The adsorption shows a clear plateau, meaning that the maximal surface coverage has been reached at a polypeptide concentration of 10 μM. The dashed line is the fit obtained using the Langmuir isotherm adsorption model.

For the polypeptides in their unimer state the plateau expected by the adsorption model for a single adsorbed monolayer is quickly reached. The precision on K is therefore impacted, but we have found an order of magnitude of 10^6 M^{-1} ($100000 \pm 200000 \text{ M}^{-1}$). This value is close to the $130000 \pm 30000 \text{ M}^{-1}$ for bare TAT sequences on pure DOPG membranes found by Rao *et al.* [237].

The fitted value of N_{PTL}^{Max} is 30 ± 10 , which corresponds to a mass coverage of $4 \pm 1 \text{ mg.m}^{-1}$. If we consider the peptide as a spherical coil which adsorbs and remains spherical after binding, this N_{PTL}^{Max} corresponds to a surface coverage of $500\% \pm 200\%$. Of course, this implies that this assumption is not valid, and we suggest that the peptides should reorganise on the vesicle surface as a polymer brush, as illustrated in figure 5.11.

With a surface per peptide of $23 \pm 8 \text{ nm}^2$, we can calculate the length of the polymer brush on the surface. Since the CPP-ELP_{BC} is in theta solvent in water [244],

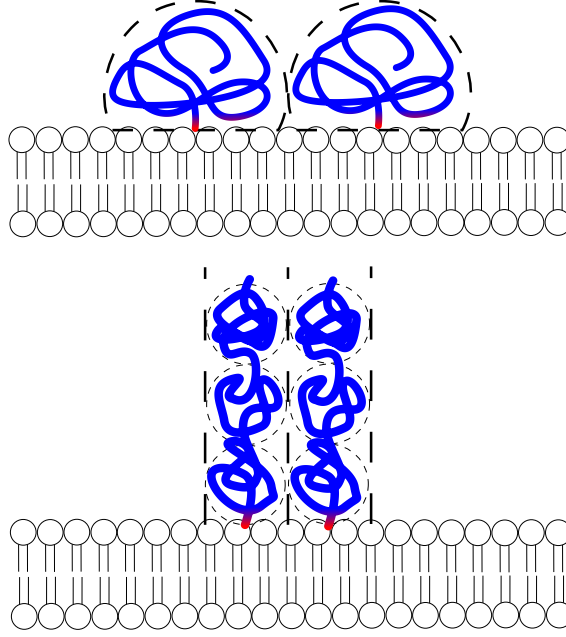


Figure 5.11: Illustration of the two hypotheses used to describe the adsorption of unimers on the surface. (Top) Mushroom-like surface decoration. The maximum surface coverage one can expect is calculated from the hydrodynamic radius of the spheres. (Bottom) Brush-like surface coverage of the unimers of polypeptides on the lipid membrane.

this length is given by Alexander-De Gennes as

$$\begin{aligned}
 l_{brush} &= R_g \left(\frac{\sigma}{\sigma^*} \right)^{-\frac{1}{2}} \\
 &= R_g \left(\frac{R_g}{D} \right)
 \end{aligned} \tag{5.9}$$

with R_g the radius of gyration of the polymer, σ the measured surface occupied by the polymer on the membrane, σ^* the surface at which two polymers on a membrane interact with each other, and D the measured distance between brushes [245]. In θ solvent, the value of R_g can be estimated by

$$R_g = aN^{\frac{1}{2}}. \tag{5.10}$$

With a monomer length of 0.37 nm found by Hassouneh *et al.* [244], the R_g of the TAT-ELP_{BC} is found equal to 8.9 nm, a slightly higher value than the one experimentally measured for the hydrodynamic radius R_h (6.0 ± 0.7 nm). With this value of R_g and the measured surface per peptide, equation 5.9 returns a length for the 600 amino acids long polypeptide brush of 17 ± 3 nm.

As the plateau is reached for concentration as low as 10 μM , this proves that the surface of the GUV was already saturated in the experiments in which we have measured the adsorption of micelles on negatively charged membranes. In this geometry, the threshold of membrane charge, above which all the charges of the unimers are compensated by the surface density of charges in the lipid membrane, corresponds a membrane charge of 24%.

B-2.b Construction of a micelles monolayer

The same experiments were performed also at 35°C to measure Langmuir isotherm for the adsorption of micelles of TAT-ELP_{BC} on a 50% charged membrane. Results are given in figure 5.12.

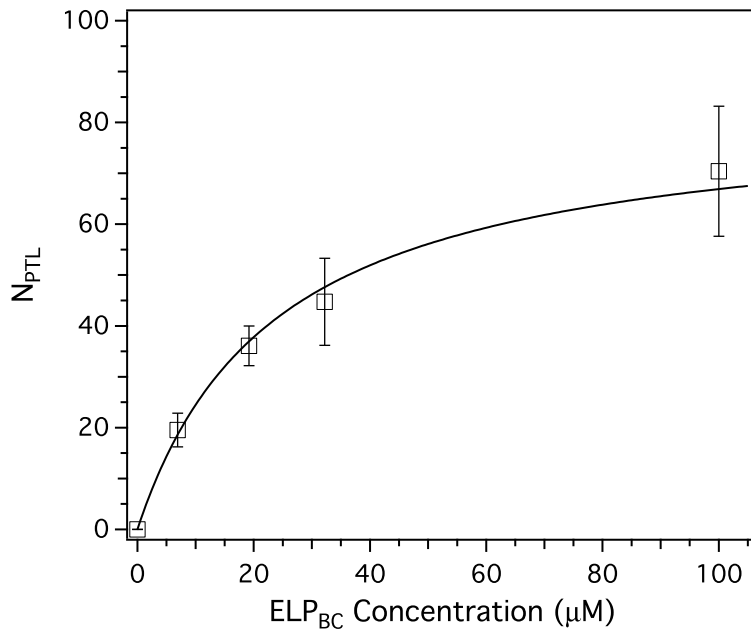


Figure 5.12: Adsorption isotherms obtained for the adsorption of micelles of TAT-ELP_{BC} on GUVs with a membrane composition of 50% of negatively charged lipids. The N_{PTL} measurements were performed at 35°C as a function of the concentration. The plain line is the fit obtained using the equation of a Langmuir isotherm.

N_{PTL}^{Max} is found equal to 80 ± 20 and K equal to $4000000 \pm 2000000 \text{ M}^{-1}$ for the polypeptides micelles. If we consider the hypothesis raised before, that N_{PTL}^{Max} for micelles should be constant and equal to 140 ± 30 , because N_{PTL}^{Max} is constrained by steric hindrance, and compare this result of K with the value obtained for 10 and 20% of charges ($800000 \pm 300000 \text{ M}^{-1}$), we see contradictions.

We can argue that the GUV was already saturated with CPP-ELP_{BC} unimers at 29°C. At 35°C, a temperature close to the CMT, we suggest that a non-negligible population of CPP-ELP_{BC} unimers is still suspended in solution, and the CPP-ELP_{BC} micelles are therefore in competition with the unimers to adsorb on the surface of the GUVs. Indeed, K for the unimers is found 10 times higher than the one for micelles on membrane with 20% charges. Another possible explanation is that the behaviour of the CPP-ELP_{BC} as a function of the membrane charge above 20% of membrane charges becomes dependant of the charge in a third regime.

B-3 Thermodynamic analysis

B-3.a Effect of the temperature

Similarly to what we have done in the previous section, we determined experimentally the enthalpy and entropy of adsorption for the TAT-ELP_{BC} on high membrane charge, by investigating first the effect of the temperature on the adsorption on a membrane with 50% of negatively charged lipids. The results are shown in figure 5.13(a).

At 42°C, the N_{PTL} measured for the adsorption of TAT-ELP_{BC} on a membrane with 50% of charged lipid is as high as 140 which corresponds to the N_{PTL}^{Max} found for micelles in the physiological regime of membrane charges. If we consider that the value of N_{PTL}^{Max} is not affected by the temperature, this confirms that this measured value is indeed affected by the presence of the unimers already decorating the GUVs before the sample is heated up. Nevertheless, this value also confirms that the affinity of the TAT-ELP_{BC} for the membrane is not the same for a membrane charge of 50% than at 20%. Indeed, even if we consider a perturbation induced by the presence of the unimers, the N_{PTL} would have been inferior or equal to the N_{PTL} value at 42°C for a membrane charge of 20%. Moreover, this observation is confirmed by the fact that the increase of adsorption as a function of the temperature is stronger at 50% than at 20 or 0%, with a linear increase of $14 \pm 3 \text{ ELP} \cdot \text{C}^{-1}$, as compared to $8.2 \pm 0.7 \text{ ELP} \cdot \text{C}^{-1}$ for 0%.

From the results obtained for TAT-ELP_{BC} (*cf.* figure 5.13(a)), we can also investigate the evolution of the N_{PTL} for the adsorption of the unimers on the GUVs as a function of the temperature. In fact, the N_{PTL} do not seem to depend of it, while the value of K is expected to increase with the temperature. This observation can be explained by the fact that the value of N_{PTL}^{Max} is almost reached for a temperature as low as 25°C (N_{PTL} value of 16 ± 5). In this case, a variation of the value of K would have a very little effect on the adsorption.

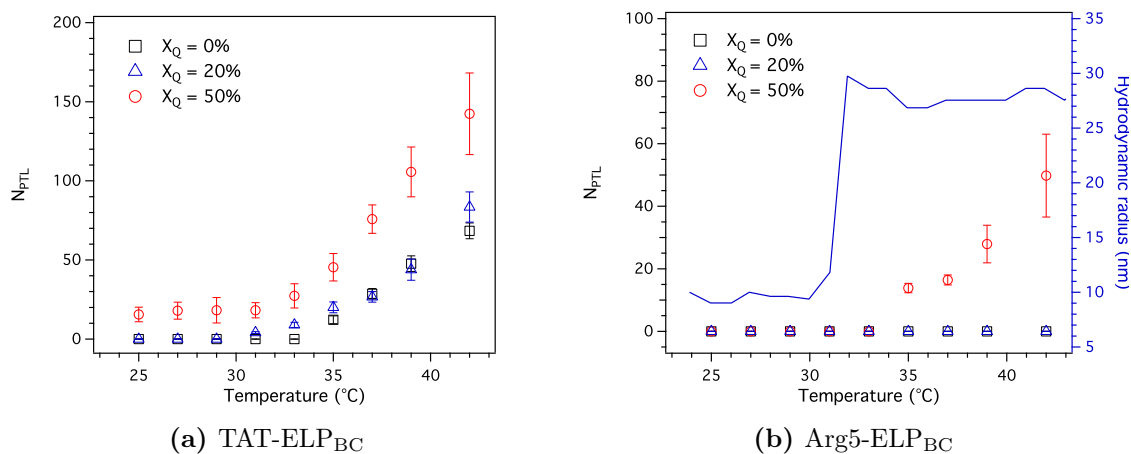


Figure 5.13: Effect of the temperature on the adsorption of CPP-ELP_{BC} on a negatively charged membrane. (a) Adsorption of TAT-ELP_{BC} as a function of the temperature or different membrane charges (0, 20 and 50% of negative lipids in the membrane). The presence of negative charges enhance the adsorption on the membrane, with a linear increase of 14 ELP. $^{\circ}\text{C}^{-1}$ at 50% of negative lipids. The presence of a high amount of negative lipids in the membrane is able to trigger the adsorption of the unimers of TAT-ELP_{BC}. (b) Adsorption of Arg5-ELP_{BC} as a function of the temperature for different membrane charges (0, 20 and 50% of negative lipids in the membrane), evaluated by the measurement of the N_{PTL} for different temperatures above and below the CMT. The measurement of the hydrodynamic radius as a function of temperature is given for both CPP-ELP_{BC} to highlight the CMT of the polypeptide. Adsorption of Arg5-ELP_{BC} only occurs for a membrane charge of 50%, and the adsorption of the micelles is enhanced by the temperature, with a linear increase of about 6 ELP. $^{\circ}\text{C}^{-1}$.

We also performed adsorption experiments as a function of the temperature for Arg5-ELP_{BC} (*cf.* figure 5.13(b)) and for the two control ELP_{BC}s without any CPP function. Interestingly, the high amount of negative charges in the membrane is able to trigger the adsorption of Arg5-ELP_{BC}. Its behaviour with the temperature is similar to the one of TAT-ELP_{BC} and Arg8-ELP_{BC} at low membrane charges, but with a slightly smaller linear increase of adsorption of 6 ± 2 ELP. $^{\circ}\text{C}^{-1}$. It is interesting to note that this effect was not observed with a membrane charge of 20%. If we consider the micelles of Arg5-ELP_{BC} as hard spheres with a hydrodynamic radius of 28.1 nm and an aggregation number of 89, the surface charges density correspond to a membrane of 31% of charged lipids. This may explain the differences of behaviour between Arg5-ELP_{BC} at 20 and 50%.

As expected, none of the control ELP_{BCS} adsorbed, even at 50%. This confirms that only the CPP function of the CPP-ELP_{BC} is able to interact with the membrane, even with a high amount of charges in the membrane.

B-3.b Estimation of the enthalpy and entropy of adsorption

Measurements of thermodynamic quantities were also performed on the adsorption of TAT-ELP_{BC} on membranes with 50% of negatively charged lipids, both as unimers and micelles. For this purpose, data gathered for the figure 5.13(a) were used and computed using the protocol described in section A-2, as shown in figure 5.14. However, despite the presence of unimers on the surface of the GUVs prior to the formation of micelles, we used for the micelles a N_{PTL}^{Max} equal to the one of the TAT-ELP_{BC} for the low membrane charges, *i.e.* 140 ± 30 . For the unimers, the value found at 30 ± 10 is used.

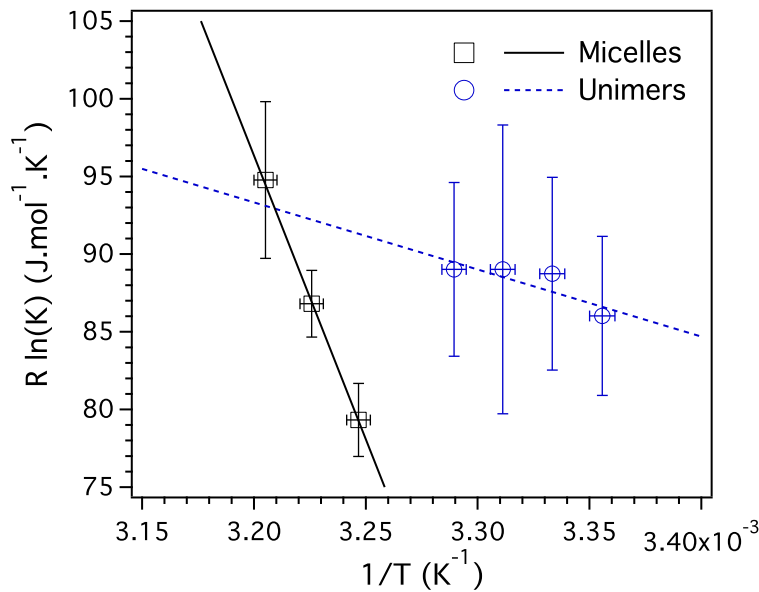


Figure 5.14: Adsorption of unimers and micelles of TAT-ELP_{BC} on a membrane with a high proportion of charge (50% of negatively charged lipids) as a function of temperature. $R \ln(K)$ as a function of $1/T$ are computed from the N_{PTL} measured using equation 5.7. Measurements were performed at a polypeptide concentration of $20 \mu\text{M}$.

Adsorption of unimers is found endothermic too, with a ΔH of $40 \pm 20 \text{ kJ.mol}^{-1}$, which corresponds to $16 \pm 8 k_B T$, about 6 times lower than the one of the micelles adsorbing on low membrane charges. The entropy of adsorption is also found lower,

with a ΔS equals to $240 \pm 60 \text{ J.mol}^{-1}.\text{K}^{-1}$. These values are however close to the ones found by Latour *et al.* for the adsorption of poly(L-lysine) on glass sphere [240].

Enthalpy and entropy of adsorption of the micelle adsorbing on a 50% charged membrane is higher than the rest of the values measured, with respectively $367 \pm 9 \text{ kJ.mol}^{-1}$ ($143 \pm 4 k_B T$) and $1280 \pm 30 \text{ J.mol}^{-1}.\text{K}^{-1}$. If we consider that only 8% of the peptides in the micelle interact with the membrane, the values of entropy and enthalpy are respectively found equal to $50.7 \pm 1.2 \text{ kJ.mol}^{-1}$ ($19.8 \pm 0.5 k_B T$) and $177 \pm 4 \text{ J.mol}^{-1}.\text{K}^{-1}$. One can note that by calculating so the order of magnitude of the enthalpy of adsorption is the same for the micelles than for the unimers at low temperature on a negatively charged membrane. The overall results for high and low membrane charges are given in table 5.3.

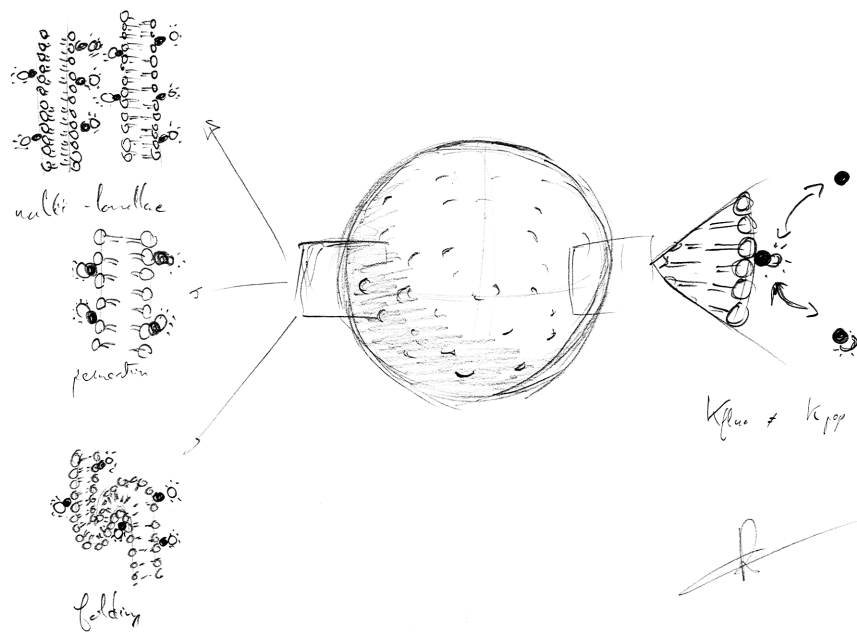
	X_Q (%)	ΔG (kJ.mol ⁻¹)	ΔH (kJ.mol ⁻¹)	ΔS (J.mol ⁻¹ .K ⁻¹)
Micelles	0	-4.60 ± 0.07	35.1 ± 5.4	123 ± 17
	10-20	-4.8 ± 0.1	35.7 ± 2.8	126 ± 9
	50	-5.4 ± 5.1^a	50.7 ± 1.2	177 ± 4
Unimers	0	-	-	-
	10-20	-	-	-
	50	-4.1 ± 4.3	40 ± 20	240 ± 60

Table 5.3: List of all the values of constant of adsorption at equilibrium (K), enthalpy (ΔH) and entropy (ΔS) of adsorption of TAT-ELP_{BC} on GUVs, measured by fitting the data with equation 5.7. All the values are given per unimers of CPP-ELP_{BC}, in the hypothesis where only 8% of the polypeptides of the micelles interact with the membrane.

^aThe value of K for the adsorption of micelles of polypeptides on the surface with a 50% membrane charge is biased experimentally due to the presence of unimers on the surface of the GUVs prior to the formation of the micelle.

KEY-POINTS OF THE CHAPTER

- Results are consistent with the adsorption of CPP-ELP_{BC} on the lipid membrane as a single monolayer (Langmuir model for adsorption).
- The presence of negatively charged lipids in the membrane modify the adsorption of the CPP-ELP_{BC}.
 - ▶ The adsorption of the CPP-ELP_{BC} micelles is enhanced by the membrane charge. A membrane charge threshold of around 9% between a low and a medium surface coverage regimes correspond to the charge density of the CPP-ELP_{BC}.
 - ▶ CPP-ELP_{BC} unimers adsorb on the GUV for membrane charge densities above 30%. Micelles adsorb on top of a membrane already covered by an unimer monolayer.



CHAPTER 6 Adsorption and penetration of short cell-penetrating peptides

IN this last chapter, we investigate the interaction between short sequences of TAT 47-57 and the lipid membrane of GUVs. Although TAT-lipid interactions have been studied in the literature, our goal is to reach a level of quantitative understanding of these systems that is only now possible by applying the methods that we developed and explained in Chapter 4.

As we see below, despite the smaller mass of the TAT peptides compared to the TAT-ELP conjugates, we will see below that the interaction behaviour is here of a more complex nature. We describe the different issues which may arise, how they would impact the N_{PTL} measurement and how to solve them.

A Adsorption, penetration and folding

A-1 Adsorption of the short CPP

In the previous chapter we showed that we can get the affinity of adsorption of a molecule on a GUV from N_{PTL} measurements. We tried here to reproduce the experiments performed on the CPP-ELP_{BC} but for short TAT sequences (sTAT).

We mixed sTAT with 1% of HL488-labelled sTAT at different concentrations, from 1 to 20 μM and incubated them with GUVs made either of pure DOPC, or from a mixture of DOPC/DOPG at a molar ratio of 4/1. To compare the results with CPP-ELP_{BC}, the sample is heated at 35°C.

At concentrations above 12 μM , the incubation of GUVs with sTAT lead to the destruction of all vesicles in the sample, possibly by bursting, which reduced the observation in the range of concentrations from 1 to 12 μM . For concentrations as low as 2 μM , we observed that sTAT was able to penetrate inside the GUVs, even those made of pure DOPC. This is in contradiction with the results described by Ciobanasi *et al.* [231] who stated that penetration can only occur in the presence of DOPE or of negatively charged lipids in the membrane. However, as shown in figure 6.1, only a fraction of the GUVs in the sample were filled with CPPs.

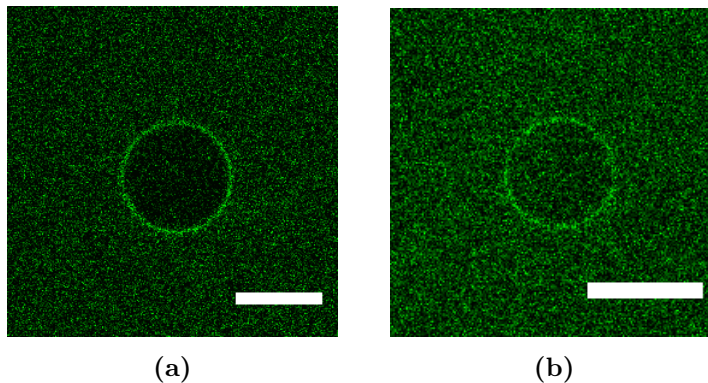


Figure 6.1: Confocal pictures of two GUVs taken from the same sample of GUVs of DOPC immersed in a solution of sTAT at 2 μM with 1% of HL488-labelled sTAT, observed at the temperature of 35°C. Some of the vesicles observed appeared empty (a), while others appeared filled with fluorescent molecules (b). We can conclude that, in our experimental set-up, penetration of labelled sTAT is possible, but does not occur systematically. Scale bar correspond to 30 μm .

The N_{PTL} measurement for the different samples of the same batch revealed that

multiple populations of N_{PTL} seemed to be mixed together, as shown in figure 6.2.

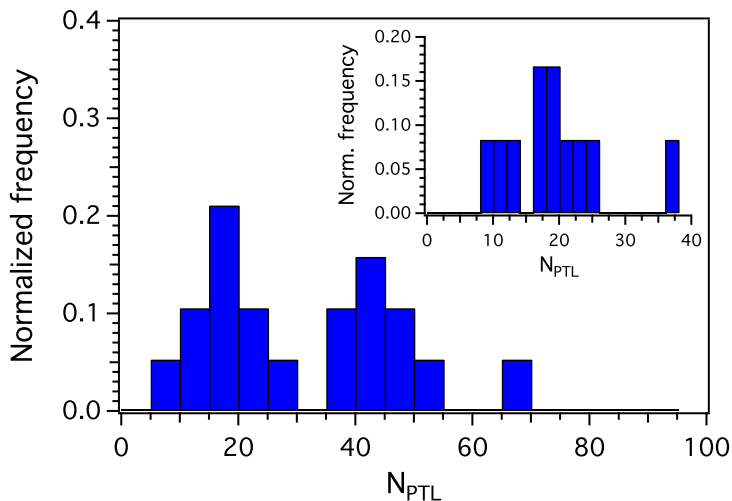


Figure 6.2: Histogram of the distribution of N_{PTL} values measured for a sample of GUVs of DOPC/DOPG at a molar ratio of 4/1 immersed in a solution of sTAT at 2 μ M. The histogram shows that the distribution is made of at least two distinct populations, one with a mean N_{PTL} value around 20 and another one around 40. The histogram in inset corresponds to the distribution of N_{PTL} values from the same sample, taken between 0 and 40 with a thinner binning (2 instead of 5) which suggest that the distribution of the population around 20 is the concatenation of two populations: one with a mean N_{PTL} value around 10 and the other one around 20.

Moreover, it appeared that the mean values of these distributions were multiples of a common lower value. While a simple factor 2 between the mean values of two populations can be explained by the penetration of sTAT inside a fraction of the GUVs, we reported other factors greater than 2. To investigate further the adsorption of the sTAT, it appears to us critical to understand the mechanism at the origin of this multiplicity, and how to analyse the data in order to extract the true N_{PTL} .

A-2 Membrane folding

We may assume that these various N_{PTL} distributions would have different origins. All the hypothesis that we now state rely on the fact that the thickness of the lipid bilayer (about 5 nm) is negligible as compared to the maximal resolution of the optical microscope (about 200 nm). If this condition applies, then it is not possible to distinguish whether one or both leaflets of the bilayers are decorated, nor whether several lipid bilayers are located in the same voxel. We can therefore predict that penetration

- which will decorate both sides of the bilayer - and multilamellar vesicles might return different N_{PTL} than for a single decorated leaflet. The presence of MLVs in our sample has been optically confirmed, as shown in figure 6.3.

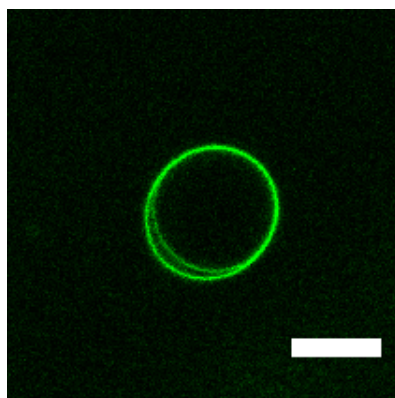


Figure 6.3: Confocal picture of a MLV of DOPC immersed in a solution of sTAT at a concentration of $2 \mu\text{M}$. While MLVs can not be easily distinguished from GUVs under an optical microscope, a partial detachment of the several bilayers proved here the nature of the vesicle. Scale bar corresponds to $20 \mu\text{m}$.

Another possibility is to consider the folding of the membrane of the GUV. If a lipid membrane undergoes folding while being decorated by fluorescent molecules, the amount of fluorescent dyes per voxel will increase, along with N_{PTL} . As a matter of fact, peptide-induced membrane foldings have been reported for several types of peptides, and it seems to be a rather universal behaviour induced by cationic membrane-active biomolecules [246][247][248].

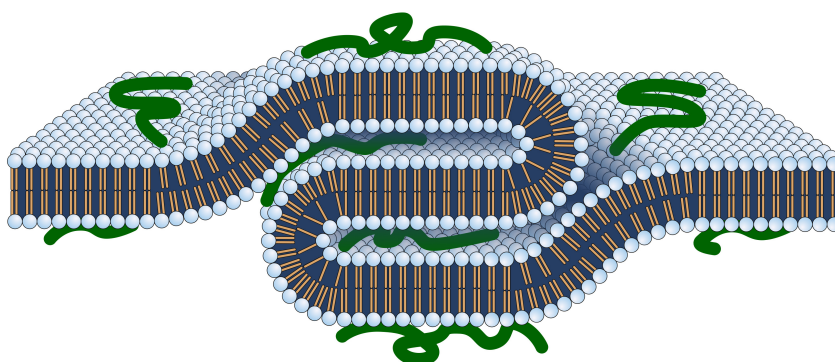


Figure 6.4: Illustration of the peptide-induced membrane folding which can occur on a GUV.

Peptides that induce formation of dense regions on the GUV surface, a visual hint

for the presence of membrane folding, were also found responsible for the aggregation of LUVs containing negatively charged lipids [249]. We can therefore expect that the cationic peptides here would bridge and bind the lipid bilayers as well.

Indeed, in our systems we investigate the interaction of cationic cell-penetrating peptides with GUVs made of zwitterionic and negatively charged lipids, membrane foldings are therefore likely to occur. However, the surface of our vesicles is homogeneously decorated, which does not correspond to the punctual dense regions of fluorescence usually reported for membrane folding. We assumed that this could be due to the fact that bridging was strong enough to pull the folds all over the surface of the GUV. To prove our hypothesis, we incorporated ultra-pure water to the sTAT solution to make them swell by osmotic shock after the initial sample. Right after the dilution, an important proportion of the GUVs in the sample displayed the presence of small bright regions on their surface, as shown in figure 6.5. This suggested that the bridging effect from the sTAT was indeed strong enough to scatter the membrane folding on the entire surface of the vesicle.

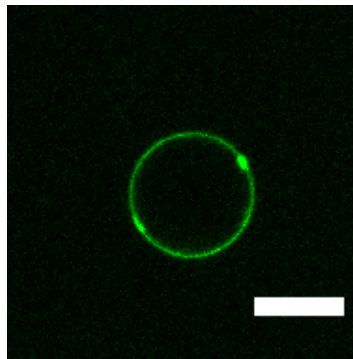


Figure 6.5: Confocal picture of a GUV of DOPC initially immersed in a solution of sTAT at $2 \mu\text{M}$, and diluted in ultra-pure water to stretch its surface. The GUV displays two dense regions of fluorescence on its membrane, an indicator of the presence of membrane folding. Scale bar corresponds to $20 \mu\text{m}$.

A-3 Dealing with multiplicity

We have seen above that three phenomenon at least could occur which could explain the presence of multiple distributions of N_{PTL} in a same sample. As the extraction of the true N_{PTL} , corresponding to the adsorption of only one side of a single bilayer, is not straightforward, we developed here an analytical method to easily evaluate and extract this value.

A-3.a Theoretical background

Cell-penetrating peptides are known to be able to translocate through model membranes, using therefore only passive methods of internalisation. In this configuration, both sides of the membrane are decorated with fluorescently-labeled molecules, as shown in figure 6.6. So far, we were measuring the number of molecules adsorbed on the lipid membrane per membrane surface unit. If penetration occurs, then the number of molecules adsorbed is twice the number we were previously measuring.

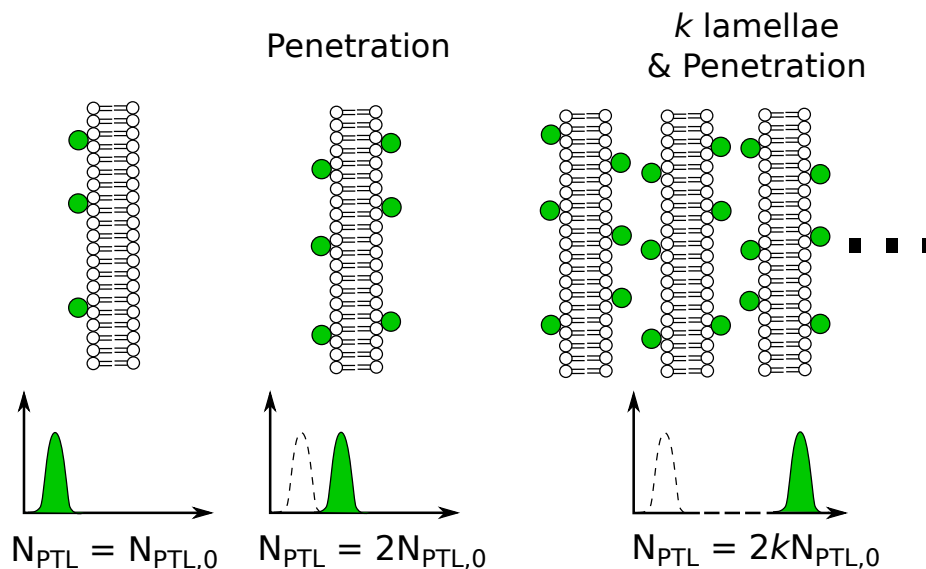


Figure 6.6: Illustration of the effect of the penetration on the measurement of the N_{PTL} value for the adsorption of molecules on a (middle) *GUV*, and (right) on a multilamellar vesicle. The case of the adsorption of molecules on a *GUV* without penetration (left) is given as reference. Due to the maximal resolution of the optical microscope, it is not possible to distinguish the two leaflets of a bilayer, or even the different bilayers making a multilamellar vesicle membrane. Therefore, for a *GUV*, the N_{PTL} measured will correspond to two times the true N_{PTL} , and for a *MLV* of k lamellae, the N_{PTL} will correspond to $2k$ times the N_{PTL} .

Moreover, if the membrane folds n times, one can expect the number of molecules decorating the membrane to undergo a $(2n + 1)$ -fold increase, as shown in figure 6.7.

One can also estimate that a small fraction of vesicles in the sample will neither fold nor be penetrated by the CPP. For these *GUVs*, the number of molecules decorating the membrane will correspond to the value measured by the N_{PTL} , as described previously. As a consequence, an experiment on a single sample of *GUVs* might lead to the following observations:

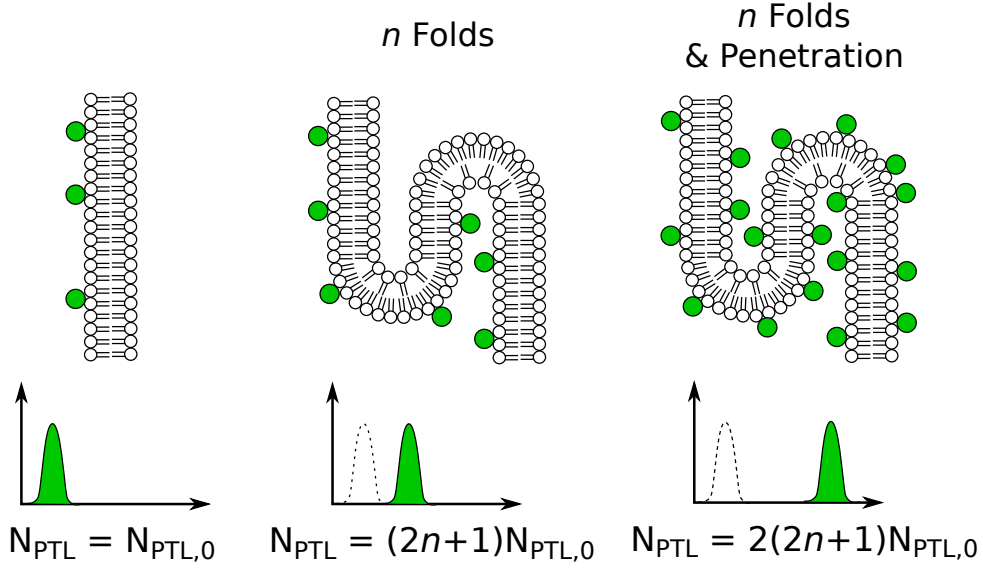


Figure 6.7: Illustration of the effect of the membrane folding on the measurement of the N_{PTL} value for the adsorption of molecules on a GUV (middle) without or (right) with penetration of the molecule inside the GUV. The case of the adsorption of molecules on a GUV without penetration or membrane folding (left) is given as reference. Due to the maximal resolution of the optical microscope, it is not possible to detect a membrane folding covering the whole surface of the GUV. Therefore, for a GUV folded n times, the N_{PTL} value measured will correspond to $(2n + 1)$ times the N_{PTL} value without penetration, and $2(2n + 1)$ times with penetration.

- GUVs with neither membrane folding nor CPP penetration (N_{PTL})
- GUVs without penetrating but with n foldings ($(2n + 1) \times N_{PTL}$)
- GUVs with penetration but without membrane folding ($2 N_{PTL}$)
- GUVs with penetration and membrane folding ($(2n + 1) \times 2 N_{PTL}$)
- MLVs made of k lamellae, with neither membrane folding nor CPP penetration ($k N_{PTL}$)
- MLVs made of k lamellae, with penetration but without membrane folding ($2k N_{PTL}$)
- MLVs made of k lamellae, with or without penetrating, and with n foldings

For all these reasons, it is unlikely that a single measurement of the N_{PTL} of a sample will return a value comparable directly to the values measured with the CPP-ELP_{BC}. Indeed, as many distinct populations of GUV might be present in the sample,

the resulting N_{PTL} distribution might not correspond to a simple Gaussian distribution, but to a concatenation of several Gaussian distributions. Nonetheless, as shown in the list above, all the N_{PTL} distributions one will extract will be multiple of the same value. It is therefore possible to calculate the "true" N_{PTL} , *i.e.* the one defined with the CPP-ELP_{BC}, from these distribution, by extracting the mean of each distribution.

A-3.b Extraction of the means of concatenated distributions

The main problem when it comes to extracting the mean values of the several distributions in a concatenated list of values is the precision of the binning of the representation, as illustrated in figure 6.8. If the binning is too large, the different distributions might be hidden in a global distribution, whose mean value will not correspond to the true mean values of the distributions hidden inside (*cf.* figure 6.8(a)). If the binning is small enough, the true distributions will start to appear (*cf.* figure 6.8(b)). However, it is not possible to evaluate objectively below which binning we should analyse each set of values.

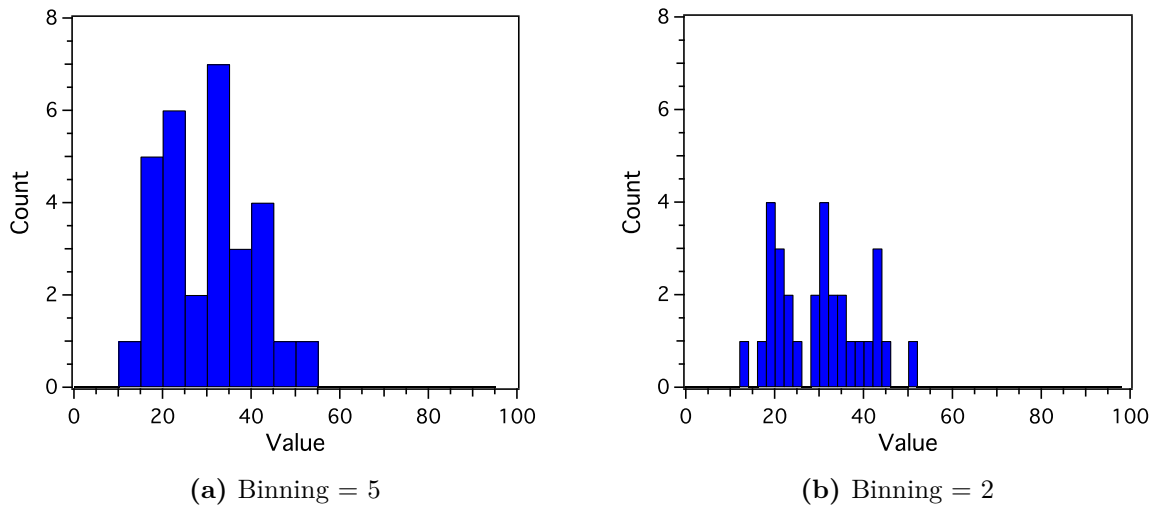


Figure 6.8: Representation of the effect of the binning of experimental data on the apparent shape of the distribution. The same 30 random values, generated using 3 Gaussian distributions with given mean values and standard deviations ($\langle x_i \rangle = 20, 30$ and 40 , and respective $\sigma_i = 3, 4$ and 5), were used to create both histograms. (a) With a large binning, the shape of the whole distribution is close to the one of a distribution generated by a single Gaussian distribution, with a mean value of about 30, while (b) a thinner binning gives some hints about the presence of three Gaussian distributions. However, it is not possible to say below which binning the data should be represented.

The integration of the histogram of a distribution returns a sigmoid function whose inflection point corresponds to the x coordinate of the maximal value of the corresponding Gaussian, *i.e.* the mean of the distribution. In a similar way, the integration of a sum of distributions will return a sum of sigmoid functions, for which each inflection point will correspond to the mean of the corresponding distribution (*cf.* figure 6.9(a)). With a normalized distribution, this sum of sigmoid functions correspond to the density of probability of the distribution.

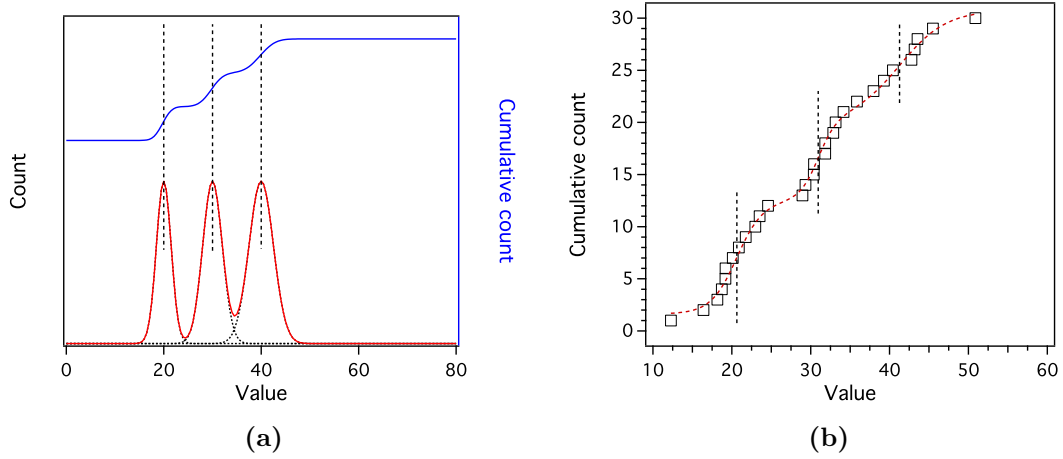


Figure 6.9: (a) Representation of the three Gaussian distribution used to generate the random values given in figure 6.8, with a superimposition of the cumulative count of the same Gaussian functions. The dashed lines highlight the fact that the inflection points of the cumulative count correspond exactly to the central values of the different Gaussian distributions. (b) Representation of the random values given in figure 6.8 in the form of the cumulative count of the values. Without the need of any binning, the three sigmoid functions appear clearly, and were fitted using equation 6.1 to calculate the different mean values. For a better accuracy, the mean values are expressed as $2\langle x_0 \rangle$, $3\langle x_0 \rangle$ and $3\langle x_0 \rangle$. The fit returned a value of $\langle x_0 \rangle$ equals to 10.318.

By sorting the data by ascending values and plotting the cumulative count for each of these values, one will obtain the density of probability of the distribution, and will therefore highlight the eventual various distributions concatenated in the global one, as shown in figure 6.9(b). The data can be then fitted by a simple sum of N sigmoids, one per expected distribution, such as the one given in equation 6.1.

$$CS(x) = A_{N+1} + \sum_i^N \frac{A_i - A_{i+1}}{1 + \exp\left(\frac{x - k_i \langle x_0 \rangle}{dx_i}\right)} \quad (6.1)$$

In the case of mean values $\langle x_1 \rangle$, $\langle x_2 \rangle$, $\langle x_3 \rangle$, etc. being multiples of the same mean value $\langle x_0 \rangle$, one can replace $\langle x_1 \rangle$, $\langle x_2 \rangle$, $\langle x_3 \rangle$, etc. by the corresponding $k_1 \langle x_0 \rangle$, $k_2 \langle x_0 \rangle$, $k_3 \langle x_0 \rangle$, etc. Therefore, the fit of the cumulative count of the data will return the value of $\langle x_0 \rangle$, which in our case corresponds to the value of the N_{PTL} value for the decoration of one side of the lipid bilayer, hence removing all multiplicity from penetration, membrane folding or of several layers of lipid bilayers.

A-4 Determination of N_{PTL}

The analytical method described above was used on the different set of data gathered using the measurement of the N_{PTL} values for the adsorption of sTAT on GUVs made of DOPC and of mixtures of DOPC/DOPG at a molar fraction of 4/1. The representation of the collected data as their cumulative count confirmed that there were indeed several distributions of decorated GUVs concatenated in our measurements, which allowed us to extract the effective N_{PTL} for every sample studied under the microscope. An example of such an extraction is given in figure 6.10.

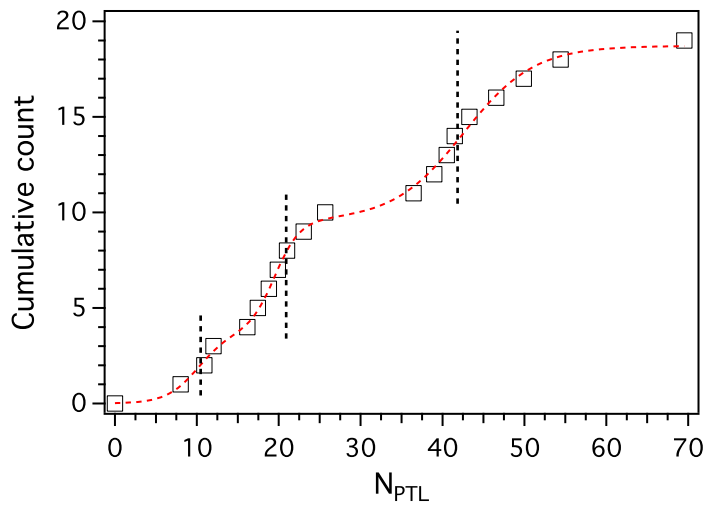


Figure 6.10: Representation of the N_{PTL} values obtained in figure 6.2 as the cumulative count of the values. Under this representation, three different inflexion points can be seen, which correspond to three distinct distributions of N_{PTL} values. Data were fitted using equation 6.1 and three sigmoid functions. The returned mean N_{PTL} value $\langle x_0 \rangle$ was found to be equal to 10.6, with k_1 , k_2 and k_3 respectively equal to 1, 2 and 4.

We repeated the measurements for ten samples of GUVs of DOPC/DOPG at a molar ratio of 4/1 immersed in a solution of sTAT at a concentration of 2 μM , but for different proportions of HL488-labelled sTAT. All the extractions returned an av-

verage mean N_{PTL} value $\langle x_0 \rangle$ of 5.4 ± 0.7 , but with different multiplicities. All these multiplicities are given in figure 6.11.

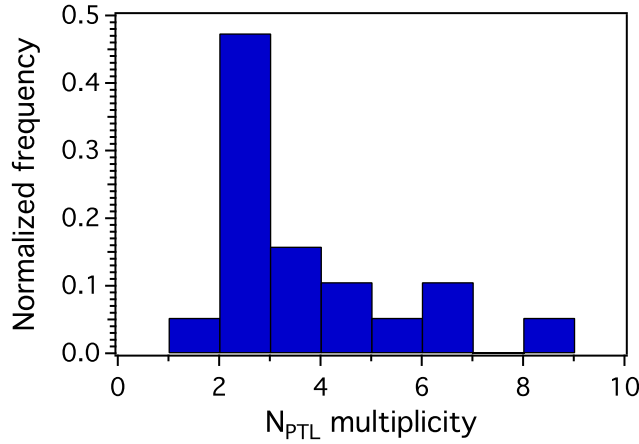


Figure 6.11: Distribution of all the N_{PTL} values multiplicity obtained for the extraction of the mean N_{PTL} value in a sample of GUVs of DOPC/DOPG at a molar fraction of 4/1 immersed in sTAT at a concentration of $2 \mu\text{M}$, for different proportions of HL488-labelled sTAT. While the most important multiplicity measured was 2, corresponding to the effect of the penetration of sTAT inside the GUVs, we also observed multiplicities of 4, 6 and 8, which can be explained by the presence of MLVs in the solution, and multiplicities of 3, 5 which can only be explained by the presence of membrane foldings, respectively folded one and two times.

These results show that we clearly have an effect of penetration (multiplicity of 2), but they also enhance the presence of MLVs (multiplicity of 4, 6 and 8) or membrane foldings, with membrane folding up to two times (multiplicity of 3 and 5).

While this analytical method allowed us to extract a correct mean N_{PTL} for all samples, it requires a large number of data points. For example, the measurement of the N_{PTL} for sTAT at $2 \mu\text{M}$ on GUVs made of mixture of DOPC/DOPG (4/1), around 200 radial profiles of different GUVs were required. We did not collect enough data to obtain Langmuir isotherms for membrane made of DOPC or DOPC/DOPG (4/1). As shown in figure 6.12, even with about 30 vesicles per sample, we are not able to extract a precise N_{PTL} .

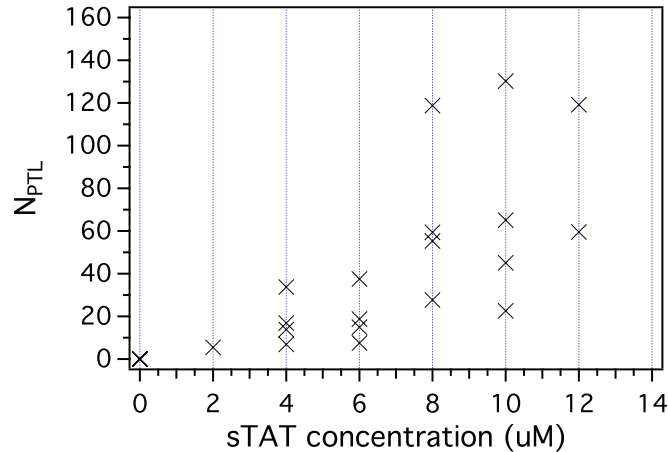


Figure 6.12: Plot of all the data points collected for measuring the Langmuir isotherm of the adsorption of sTAT on the surface of GUVs made of DOPC/DOPG at a molar ratio of 4/1. With an average of 20 intensity profiles collected per concentration, our analytical method was not able to discriminate more than 2 up to 4 potential values for the true N_{PTL} value.

B Influence of the fluorophore on the adsorption

The CPP-ELP_{BCS} used in the previous chapters have molecular weights of about 50 kDa. The AF488 used to label the CPP-ELP_{BC} has a molecular weight of 643 g/mol, which represents 1% of the total molecular weight of the polypeptide. Moreover, when the CPP-ELP_{BC} self-assemble, the fluorescent probes are brought inside the micelles, far from their shells. We can thus consider that the presence of the fluorescent dye does not perturb the adsorption of the CPPs.

In opposition, the sTAT has a molecular weight of 1560 g/mol, while HL488 used for labelling weights 584 g/mol. Therefore, HL488 represents about 37% of the total weight of the peptide. Also, the dye is not protected, which means that the adsorption of the HL488-labelled sTAT can be strongly influenced by the presence of the fluorophores, the affinity of the labelled CPP K_{fluor} being probably different from the non-labelled one K_{pep} .

We verified experimentally this assumption by plotting the N_{PTL} obtained for the adsorption of sTAT on GUVs made of a mixture of DOPC/DOPG for different proportions of HL488-labelled sTAT. The values correspond to the $\langle N_{PTL,0} \rangle$ obtained by extracting the sigmoids from the cumulative counts. We can see that N_{PTL} seems to increase with the proportion of fluorescent peptides, as shown in figure 6.14.

To be able to quantify the effect of the fluorescent dye on the affinity of the CPP

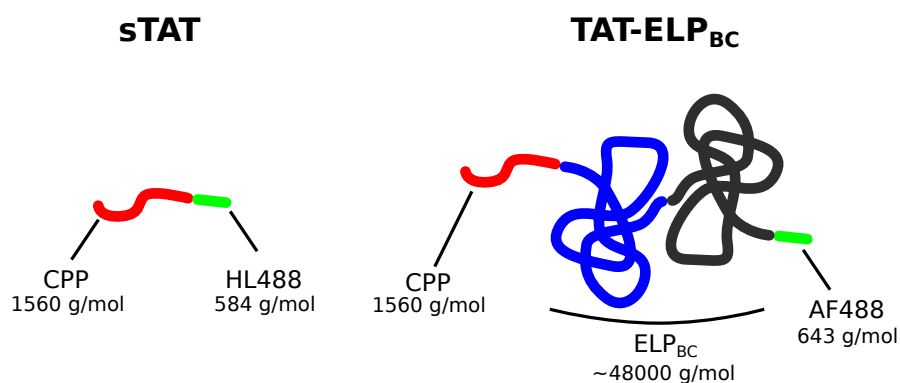


Figure 6.13: Representation of the difference of proportions between the molecular weight of the fluorescent dye and the molecular weight of the labelled molecule, in the case of a sCPP (left) and a CPP-ELP_{BC}. In the case of the polypeptide, the dye represent 1% of the total molecular weight, while it corresponds to 37% in the case of the sCPP.

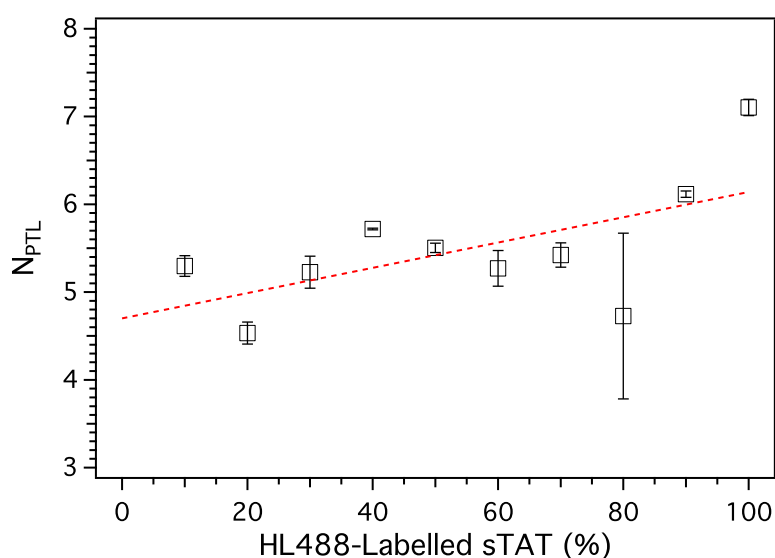


Figure 6.14: Evolution of the N_{PTL} value as a function of the proportion of HL488-labelled sTAT. The N_{PTL} value are measured in the case of adsorption of sTAT on GUVs made of a mixture of DOPC/DOPG at a molar ratio of 4/1. The N_{PTL} values are found slightly increasing with the proportion of labelled peptides, which indicates that the dye has an effect on the adsorption of the molecule.

for the membrane, we describe here a procedure based on the measurement of the N_{PTL} . This investigation have been made easier thanks to the precious advices from Dr. Alexandra Barbelivien, Assistant Professor at the department of Psychology at the University of Strasbourg.

B-1 Theoretical background

The effect of labelling a molecule of interest by ligand-receptor binding has been widely studied in pharmacology. Many books describe the different methods of evaluation of this effect such as the measurement of the IC_{50} (half maximal inhibitory concentration), which consists in measuring the concentration of a substance needed to inhibit a given biological process like the adsorption of a ligand by half [250]. However, the methods developed in pharmacology are mostly relative to radioactively labelled molecules *in vivo*, with concentration of non-labelled species being regulated by the organism.

In our case, we investigate the effect of a fluorescent dye grafted on a ligand, where the concentrations of both labelled and non-labelled ligands are controlled. We therefore suggest here a reinterpretation of the methods used in pharmacology adapted to our system. The adsorption of a molecule A on a surface while being in competition with several adsorptions of species B , C , *etc.* is expressed in the Langmuir isotherm model by the relation

$$N_{PTL,A} = N_{PTL,A}^{Max} \frac{K_A C_A}{1 + \sum_{i=A,B,\dots} K_i C_i}. \quad (6.2)$$

Since we only have two species, labelled and non-labelled sCPPs, we know that the number of labelled peptides adsorbed $N_{PTL,fluo}$ and the number of non-labelled peptides adsorbed $N_{PTL,pep}$ add up to define the total number of peptides adsorbed $N_{PTL,tot}$. Using equation 6.2, we can define

$$\begin{aligned} N_{PTL,fluo} &= N_{PTL,fluo}^{Max} \frac{K_{fluo} C_{fluo}}{1 + K_{fluo} C_{fluo} + K_{pep} C_{pep}} \\ N_{PTL,pep} &= N_{PTL,pep}^{Max} \frac{K_{pep} C_{pep}}{1 + K_{fluo} C_{fluo} + K_{pep} C_{pep}} \\ N_{PTL,tot} &= N_{PTL,fluo} + N_{PTL,pep} \\ &= \frac{N_{PTL,fluo}^{Max} K_{fluo} C_{fluo} + N_{PTL,pep}^{Max} K_{pep} C_{pep}}{1 + K_{fluo} C_{fluo} + K_{pep} C_{pep}}. \end{aligned} \quad (6.3)$$

We assume that in equation 6.3 the maximal number of peptides adsorbed on the membrane is not modified by the presence of a fluorescent probe, so $N_{PTL,fluo}^{Max} = N_{PTL,pep}^{Max}$. We also define $K_{fluo} = f K_{pep}$, so

$$N_{PTL,tot} = N_{PTL,tot}^{Max} \frac{K_{pep} (f C_{fluo} + C_{pep})}{1 + K_{pep} (f C_{fluo} + C_{pep})}. \quad (6.4)$$

The total concentration C_{tot} is simply defined as the sum of the concentration of the two peptides $C_{fluo} + C_{pep}$. If we perform experiments with a constant C_{tot} by making variations of x , the ratio of C_{fluo} . Thus equation 6.4 can be rewritten as

$$N_{PTL,tot} = N_{PTL,tot}^{Max} \frac{K_{pep} C_{tot} (1 + x(f - 1))}{1 + K_{pep} C_{tot} (1 + x(f - 1))}. \quad (6.5)$$

In equation 6.5 we see that, if the fluorophore does not modify the adsorption of the peptide, $K_{fluo} = K_{pep}$ and therefore $f = 1$. Hence equation 6.5 becomes 5.2, and the N_{PTL} can be directly obtained by measuring the adsorption of the fluorescent peptides, without any correction. If $K_{fluo} \neq K_{pep}$, then it is crucial to determine the value of f to measure the value of K_{pep} using equation 6.5 for fitting the Langmuir isotherms.

The value of f can be determined experimentally by measuring the value of the $N_{PTL,fluo}$ at a constant C_{tot} for different values of x . The resulting data can be then fitted with the following equation

$$N_{PTL,fluo} = N_{PTL,fluo}^{Max} \frac{K_{pep} C_{tot} f}{1 + K_{pep} C_{tot} (1 + x(f - 1))}. \quad (6.6)$$

Typical results one could obtain with this method are illustrated in figure 6.15.

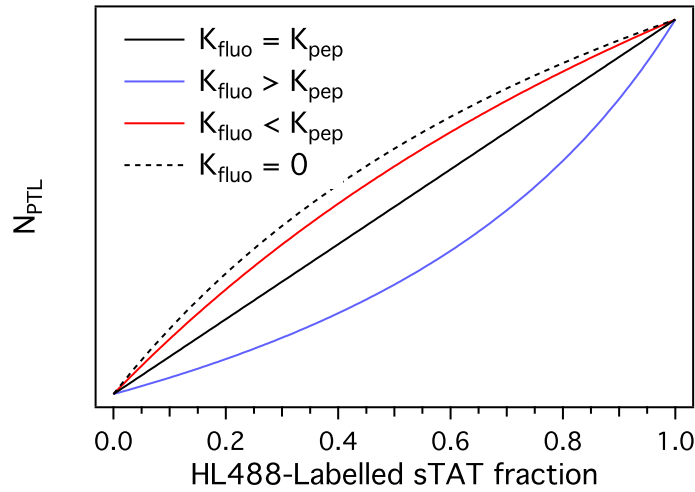


Figure 6.15: Typical curves one could obtain with equation 6.6 for different ratio between K_{fluo} and K_{pep} . The inflexion of the curve depends on f , the ratio between K_{fluo} and K_{pep} , but also on K_{pep} , $N_{PTL,tot}^{Max}$ and C_{tot} .

B-2 Evaluation of the affinity of the short TAT

Following the method described above, we rearrange the data shown in figure 6.14 into values of N_{PTL}^{Max} as a function of the proportion of HL488-labelled sTAT at a sTAT total concentration of $2 \mu\text{M}$. The resulting data, shown in figure 6.16, confirms that the presence of the fluorescent dye has an effect on the adsorption, and K_{fluo} is larger than K_{pep} .

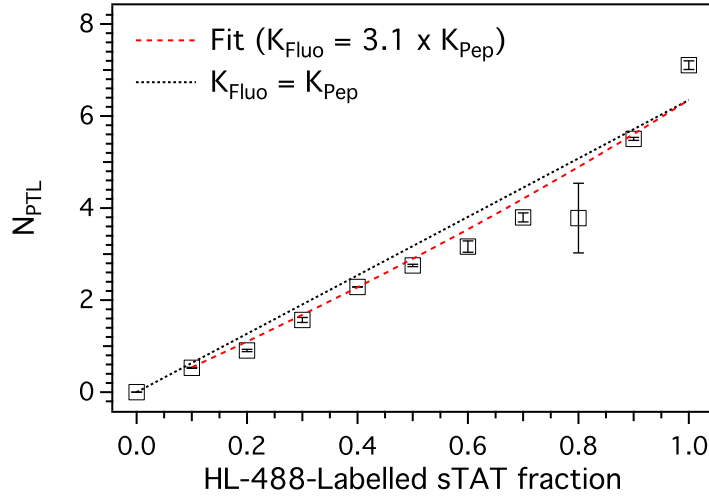


Figure 6.16: Evolution of the N_{PTL} as a function of the proportion of HL488-labelled sTAT, for a total concentration of labelled and non-labelled sTAT equals to $2 \mu\text{M}$. The dashed line is the fit obtained with equation 6.6. It confirms that the affinity of the labelled molecule is higher than the unlabelled one.

However, we could not fit the data using equation 6.6 to evaluate f , the ratio between K_{fluo} and K_{pep} . Indeed, equation 6.6 shows that K_{pep} is dependant of f and of N_{PTL}^{Max} , one could get a good precision on K_{pep} only if one knows N_{PTL}^{Max} or f . We evaluate K_{pep} using an assumed N_{PTL}^{Max} from the work of Rao *et al.* on adsorption of the same peptide on LUVs made of POPC and POPG [237]. They have reported that the maximal number of sTAT adsorbed on POPC and POPG were strictly different, with corresponding N_{PTL}^{Max} respectively of 2 and 70. While we could not prove experimentally that even CPP-ELP_{BC} does or does not have the same N_{PTL}^{Max} with GUVs made of 100% of DOPG, our measurements of the adsorption of sTAT on GUVs of DOPC with concentration as low as $2 \mu\text{M}$ resulted in N_{PTL} values higher than 2. We therefore decided to test our method with their N_{PTL}^{Max} value for POPG, by assuming that the value should be equal to the one of DOPC and DOPC/DOPG at a molar ratio of 4/1. A N_{PTL}^{Max} of 70 corresponds to a mass coverage of $0.26 \text{ mg}\cdot\text{m}^{-2}$. If we assume that the

sTAT adsorbs as a rigid chain on the membrane, this N_{PTL}^{Max} corresponds to a surface coverage of 60%.

The new fit, with a fixed N_{PTL}^{Max} value of 70, returned a value of f equals to 3.1 ± 0.1 , and the corresponding value of K is of $49900 \pm 300 \text{ M}^{-1}$. The latter is in the range of constant of adsorption at equilibrium found by Rao *et al.*, with 34500 M^{-1} for POPC and $133,000 \text{ M}^{-1}$ for POPG, and also in the range found by Ziegler *et al.* for liposomes of POPC/POPG (3/1) with 8000 M^{-1} and $110,000 \text{ M}^{-1}$ for POPC/POPG (1/1) [239]. This means that the affinity of the labelled sTAT for the membrane is three time greater than the affinity of the non-labelled sTAT, with a K_{fluo} of 150000 M^{-1} .

KEY-POINTS OF THE CHAPTER

- bare short sequences of TAT are able to adsorb and penetrate zwitterionic and negatively charged GUVs.
- We confirm that TAT interactions with lipid bilayers in GUVs can result in the formation of membrane folds. If the GUV is not stretched enough, the folds can spread over the entire GUV surface.
- Due to penetration, membrane folding, and presence of MLVs, the N_{PTL} measurement requires good enough statistic and an appropriate analytical method.
- The presence of a fluorescent probe on the TAT increases the affinity of the peptide for the membrane, by roughly a factor three.

CONCLUSIONS

SUMMARISING the most important findings of three years of intense scrutiny of the behaviour of systems composed of lipids and peptides is not an easy task. I would like however to highlight three different facets of the outcome of my PhD project: the scientific discoveries that were made, the new methods developed to make those discoveries possible and the “side-products” that brought me into exploring and learning in the field of Soft Matter and Biophysics at large.

Central to the conclusion of my studies is the mechanism of interaction with membranes of the self-assembling elastin-like polypeptides (ELP_{BC}) functionalised with cell penetrating peptide (CPP) functions. We found, similarly to many other cargo bearing CPPs, that the attachment of the large ELP_{BC} polymer to the CPP reduces its affinity to lipid membranes. For instance, TAT molecules adsorb strongly onto the zwitterionic DOPC bilayers from a micromolar solution, while the cargo bearing TAT- ELP_{BC} does not display any sign of adsorption even at 100 mM. There is thus at least two orders of magnitude difference in the affinity constants of the two molecules. Most significantly, the assembly of TAT- ELP_{BC} as micelles above 30°C allows recovering the affinity to DOPC. The micelles of TAT- ELP_{BC} adsorb on the membrane surface, as micelles, while the unimers do not adsorb! This confirmed and quantified (we measured an affinity constant of order of $5 \times 10^3 M^{-1}$) the intuition of our collaborators from Duke University that developed this class of molecules. Moreover, by studying ELP_{BC} with oligo-arginine functions of different arginine numbers we found that a minimum amount of these cationic groups, say between six and eight, is necessary for recovering affinity in the micellar state. We also found that the micelles do not translocate across

the DOPC membrane, bringing an important clarification into this field, where the behaviour of the pristine bilayers gauges the behaviour of more complex compositions.

Trying to better approach the lipid complexity of the biological membranes, we studied systematically the effect of added charges to the membranes, by working with mixtures of uncharged (DOPC) and charged (DOPG) lipids. We found that at physiologically relevant charge fractions, say below 30%, the TAT-ELP_{BC} unimers do not adsorb on the membrane, charge fractions equal or larger than 30% are necessary for unimer attachment. As expected, micelles display larger surface coverage rates on charged membranes as compared to the zwitterionic ones, and we provided a measure of the influence of the charges on the affinity constants of the micelles to the membrane; roughly, the presence of about ten or twenty percent of charges doubles the value of the affinity constant. Importantly, at these physiologically relevant charge densities (and perhaps surprisingly even well above) no micelle translocation was detected. This strongly points to an influence of self-assembly in cell uptake, as observed by our collaborators, directed at the adsorption to the cell membrane, final uptake requiring active cellular processes.

Understanding the molecularly complex CPP-ELP_{BC} required also, to benchmark the interaction strength and interaction behaviour, to study the bare CPP molecules. We studied thus what we thought would be the simpler behaviour of TAT molecules in the presence of zwitterionic and charged membranes. To our surprise, the membrane behaviour is in this case more evolved and the quantitative analysis more challenging due to the presence of membrane folds. We developed the first quantitative analysis of folding effects and we were able to quantify the influence of the fluorophore on the affinity of the TAT to the bilayers, finding a threefold increase.

None of these scientific findings would have been possible without the methodological developments that took an important part of my attention during the PhD. Arguably the most far-reaching progress concerns the possibility of quantifying surface coverage of fluorescently labelled molecules from a simple analysis of confocal pictures. This method has the potential of becoming widely used in the Soft Matter and in the Biology communities. I defined carefully the conditions required for a proper functioning of these measurements and used them extensively throughout my PhD work. The number of fluorophores adsorbed per thousand lipids or NPTL has become a common designation that one finds in my manuscript and in our papers.

I prepared thousands of Giant Vesicles samples during these three years. This task would have been impossible without the facility provided by the new GUV forming caps that I developed, or the PTFE well plated adapted for gel-assisted formation. And

obviously, the statistical treatment of the results would not have been possible without all the lines of code that I wrote to automatize measurement and fitting procedures.

Working in an exciting environment where many scientific projects are under way, drags one inevitably into activity zones peripheral to our central project, but also very interesting and a source of learning. I engaged into several projects, some of them that are not described in this manuscript and some others that bared fruits that I am proud of. For instance, inspired by nanoparticle-membrane studies carried in the group by RICM means, an optical microscopy interference technique, I developed an ImageJ plug-in that computes time and space correlations, a plug-in that will become shortly publically available for universal use.

The results and the methodological developments of this PhD open a large number of perspectives, some as quite obvious extensions of the work described in this manuscript. Here I discuss three core challenges that emerged during my project, important enough in my opinion to pursue as independent projects.

We concluded, based on our fluorescent studies that the micelles adsorb on the membranes as micelles and that a reasonable picture for the decorated GUV is that of a bilayer covered with a full carpet of small micellar spheres. This is certainly worth investigating further, by other techniques, certainly by AFM if temperature control is possible, possibly also by scattering techniques. In particular, the high coverage numbers observed for the charged membranes, that we interpreted as packing micelles more tightly, could correspond to conformational changes say from micelles to ELP_{BC} bilayers or other geometries.

The formation of folds is an interesting phenomenon that is not understood. Now that we can have a quantitative handling of the surface coverage of the peptides, it would be interesting to explore the physical parameters controlling fold formation, perhaps by coupling fluorescent measurements to tension control, for instance by micropipette. One could then for instance prepare GUVs with a finite amount of surface covered by folds, allowing exploring for instance the partition of CPP adsorption between the fold and the pristine regions.

Methodologically, we have shown that the gel-assisted method of vesicle growth can be adapted to easily encapsulate DNA molecules. This opens a whole new area of exploration, where GUV systems can be prepared to explore membrane permeation to DNA in specific conditions as for instance under oxidation, to measure pore crossing under the conditions where controlled pores can be formed, perhaps to explore DNA hybridization or other biologically relevant functions involving confined or encapsulated DNA molecules.

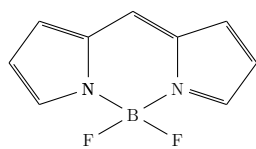
APPENDICES

THE appendices of this work include descriptions, schematics, and results on different parts of the subjects investigated here. The following items can be found in the appendices:

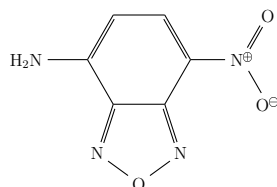
1. Skeletal formulae of the different fluorescent probes
2. Excitation and emission spectra of the fluorescent probes
3. Graphic experimental protocols created for the interns
4. Blueprints of the electroformation caps
5. Detailed results on the interaction between GUVs made of electrically charged lipids and DNA
6. Blueprints of the heating stage for the confocal microscope
7. Algorithm for the computation of the N_{PTL}

Apx-1 Fluorescent probes

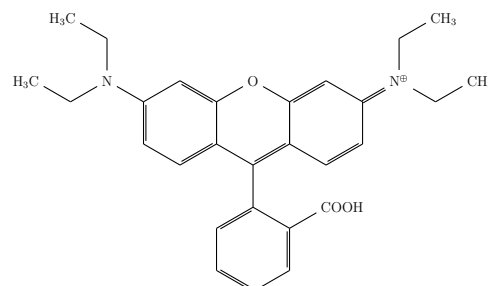
Skeletal formula of the different fluorescent probes listed in *table 2.2* and used in this work: (a) BODIPY, (b) NBD, (c) Rhodamin B, and (d) YOYO-1.



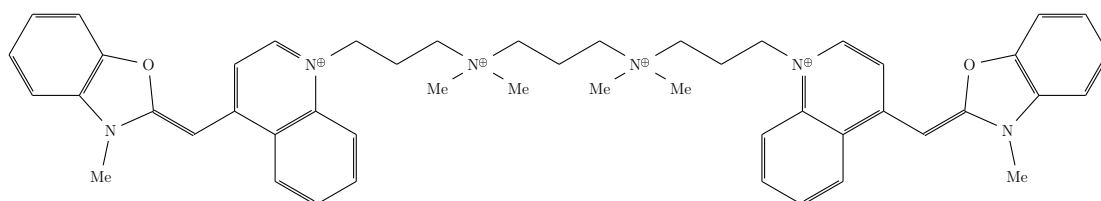
(a) BODIPY



(b) NBD



(c) RhoB

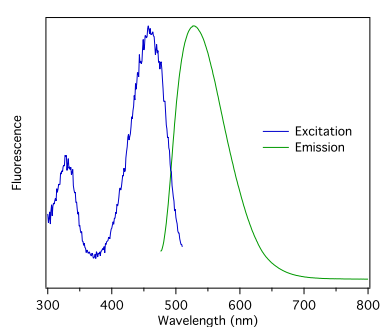


(d) YOYO-1

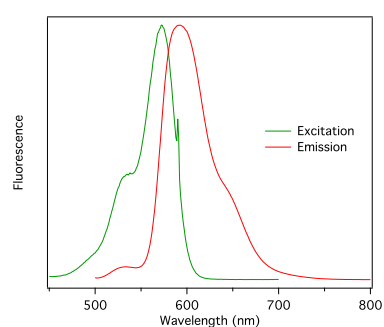
As described by the provider, AlexaFluor 488 (AF488) is a fluorescein-based dye developed by Molecular Probes (Invitrogen, Carlsbad, CA, USA). HyLite 488 (HL488) is a fluorescent probe developed by AnaSpec (Eurogentec, Fremont, CA, USA). While no information could be found on HL488 structure, its molecular weight and fluorescence spectrum seem to indicate that HL488 is also derivating from fluorescein.

Apx-2 Fluorescence spectra

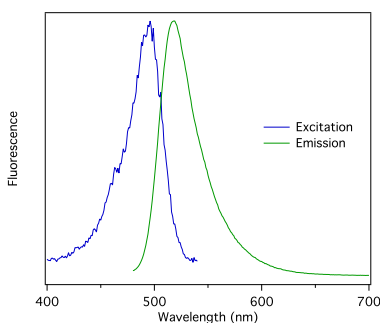
Fluorescence spectra of the different dyes used in this work: (a) NBD, (b) RhoB, (c) AF488, (d) HL488, and (e) BODIPY. NBD and RhoB were attached to DOPE, and the spectra of the labeled lipid were recorded with a large unilamellar vesicle/small unilamella vesicle mixture. AF488, HL488 and BODIPY attached to polypeptides were dissolved in PBS and measured at room temperature. Emission and excitation spectra are taken at their respective maximum value for the excitation and emission.



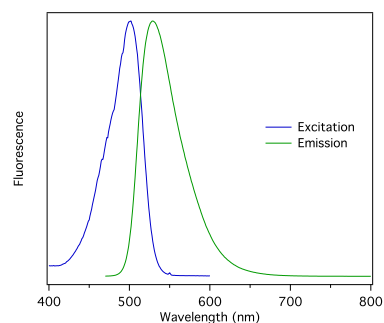
(a) NBD



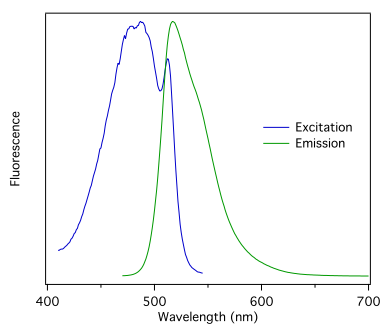
(b) RhoB



(c) AF488



(d) HL488

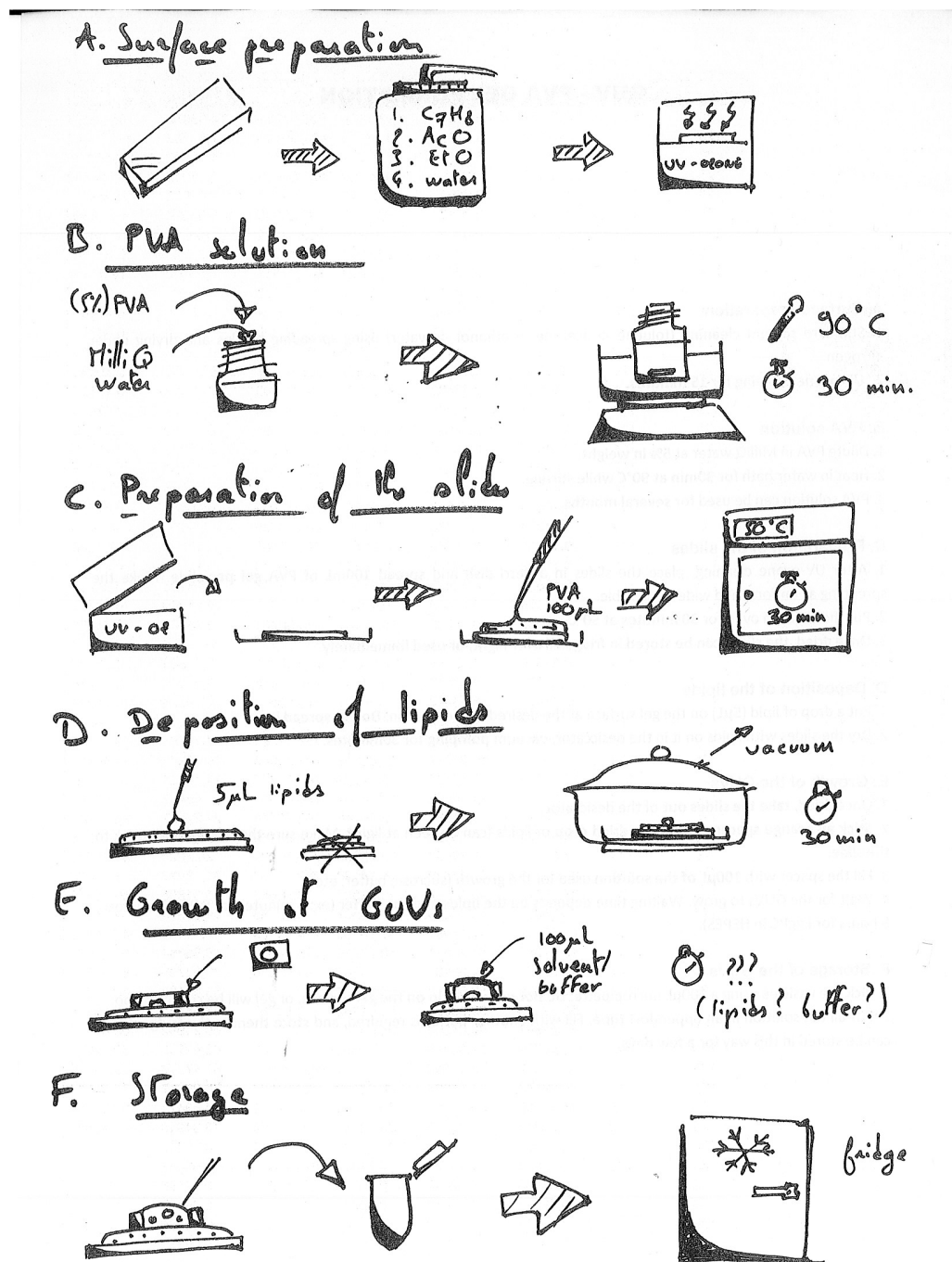


(e) BODIPY

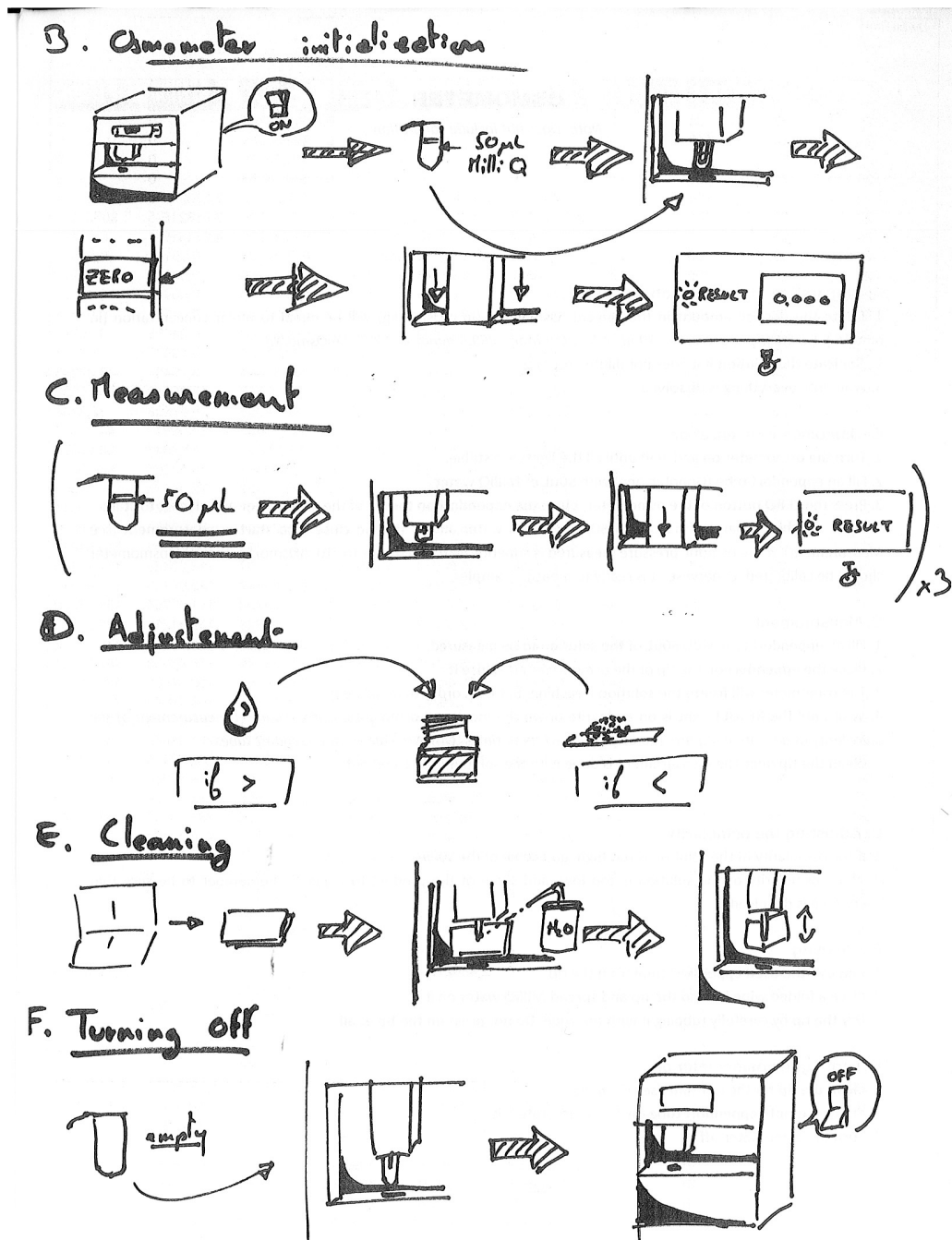
Apx-3 Graphic experimental protocols

Serie of cartoons describing different protocols used in the team to prepare samples. These illustrations have been created for the interns of the team.

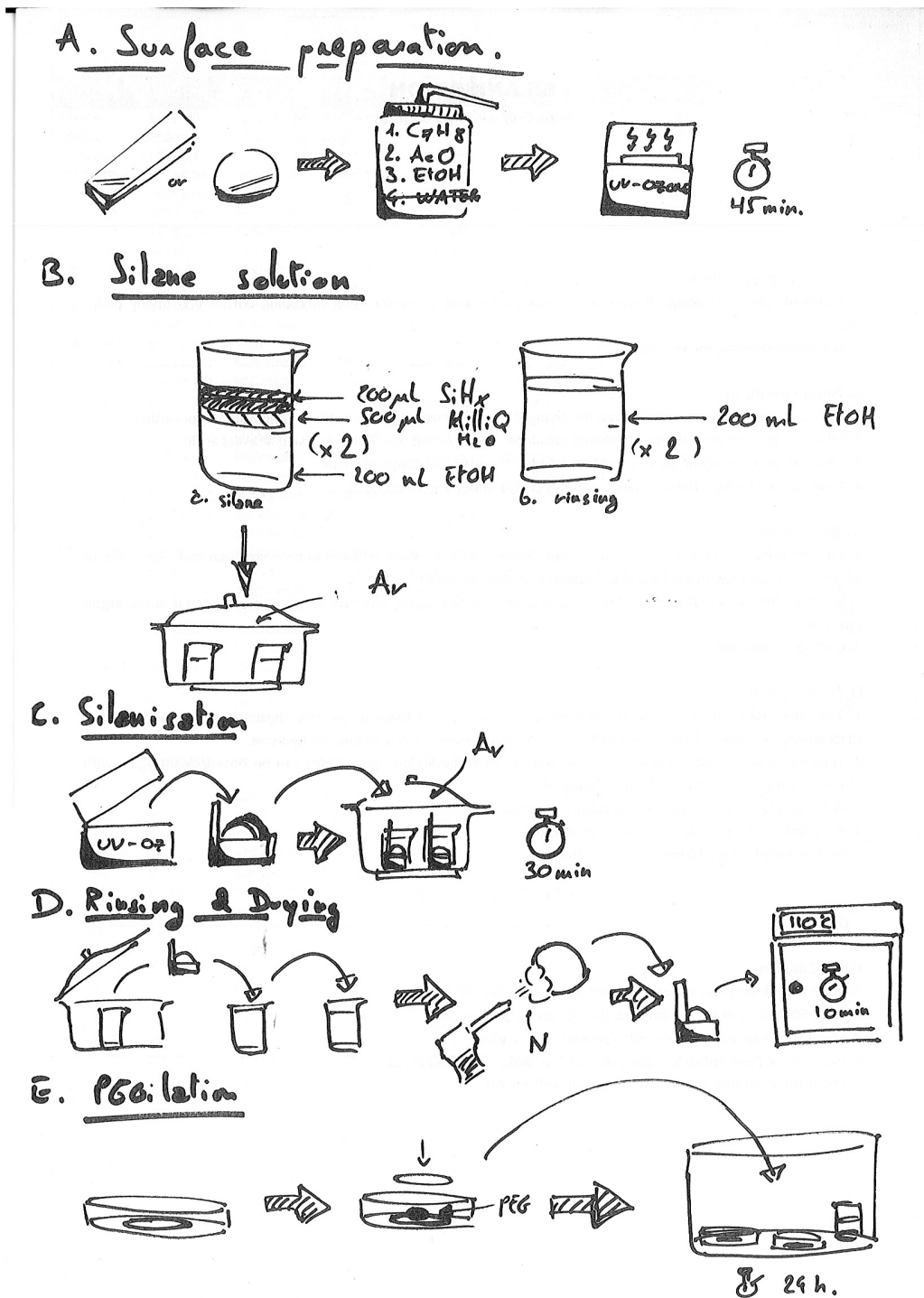
Protocol for the preparation of GUVs using the PVA-gel assisted method.



Protocol for measuring the osmolarity of a solution using the cryoscopic osmometer.

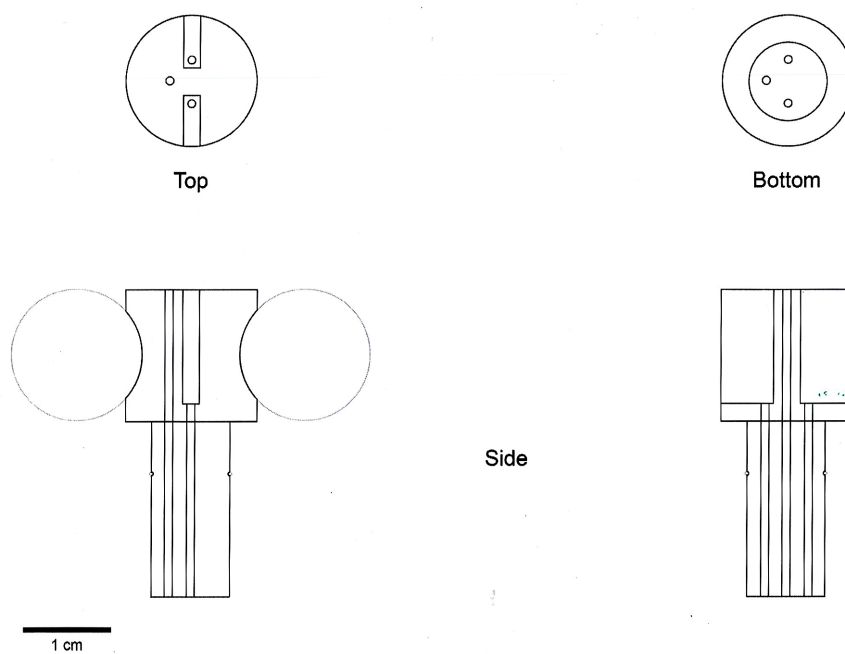


Protocol for the silanization and PEGylation of glass surfaces.



Apx-4 PTFE electroformation cap

Blueprints of the PTFE electroformation cap designed during my PhD.



Apx-5 Interactions between charged lipids and DNA

To extend the applications of the PVA-gel formation of GUVs in saline solution described in section B of chapter 3, experiments were conducted with negatively and positively charged lipids, namely DOPG and DOTAP. The GUVs formed thereof were mixed with DNA and their interaction are described below. This part of the work was performed with Nicolas Schalek during his third year of bachelor degree's internship under my supervision.

Apx-5-1 Growth of electrically charged GUVs

Nice GUVs are known to grow easily from spread DOPC. While we have shown in chapter 3 of this work that even neutral mixture such as EggPC could grow in a saline solution with saline PVA gel, we were also interested by the growth of electrically charged lipids in salt. For this purpose, we reproduced the experiments with DOPG and DOTAP, respectively negatively and positively charged lipids. The DOPG is often used for building bilayers that mimic membranes of real cells, while DOTAP is of wide importance for drug delivery applications, in which it is expected to be an efficient carrier for DNA [251].

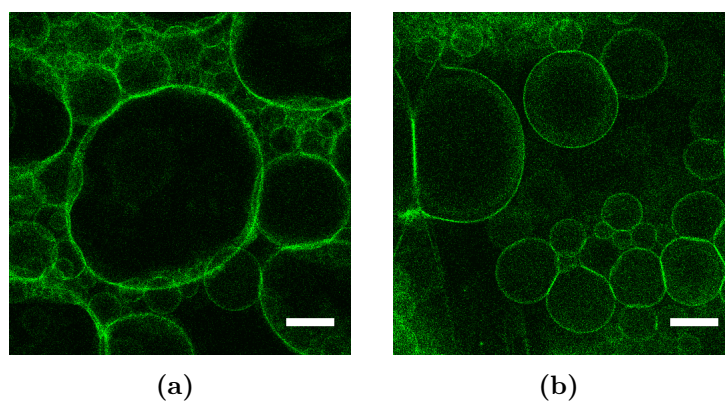


Figure Apx-5.1: Confocal pictures of NBD-labelled vesicles of DOPG (a) and DOTAP (b), growing on a PVA gel. Both growth solution and PVA gel have a salt concentration of 150 mM. Despite the saline medium, both types of vesicles are able to grow, with diameters as large as 200 μm . Scale bar represents 45 μm .

Similarly to zwitterionic lipids, both DOPG and DOTAP were able to reach sizes as big as 200 μm in diameter in a saline growth solution on a saline PVA gel (*cf.* figure Apx-5.1). Control experiments showed that addition of salt to the PVA was

required to obtain GUVs. Furthermore, the vesicles could be easily collected from the growth chamber, diluted into the isotonic saline glucose solution and observed under microscope.

However, DOTAP vesicles were found to be unstable once they reached the glass surface, exploding systematically. To overcome this problem, 5 % of polyethylene glycol (PEG) functionalized lipids (DOPE-PEG₅₀₀₀, 5000 referring to the molecular weight of the polymer) were added to the DOTAP, reducing significantly the GUV bursting.

Apx-5-2 Interaction with DNA

Charged GUVs grown in saline solution were mixed with a solution of salmon sperm DNA fragments (≤ 2000 bp, Invitrogen) labelled with YOYO-1.

YOYO-1 labelled DNA is prepared by adding 1.5 μL of YOYO-1 at 20 μM to 100 ng of DNA. This solution is then diluted in 200 μL of the solution of GUV, after collection from the growth chamber and dilution in the isotonic glucose solution. The whole system is then observed under the confocal microscope to investigate the interactions between DNA and GUV made of different lipid compositions. The experiments were performed with vesicles made of pure DOPC, DOPG and DOTAP, all in a solution with 150 mM of NaCl. The results are portrayed in figure Apx-5.2.

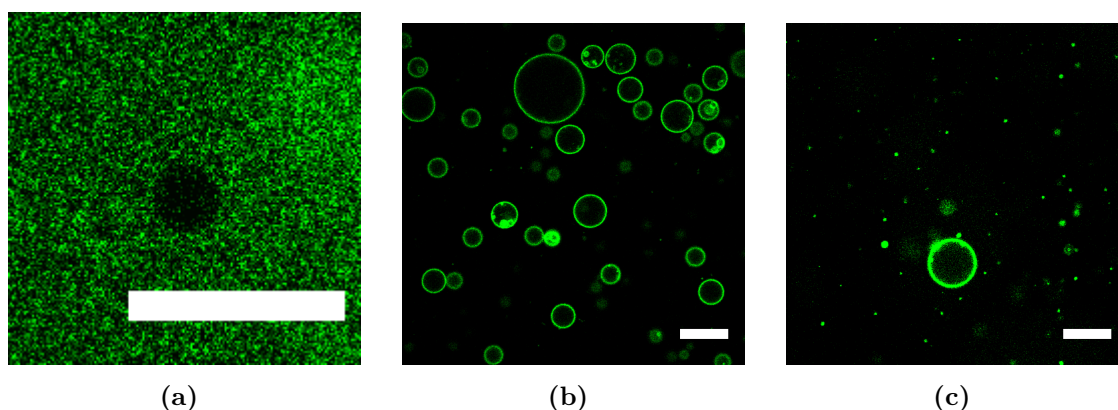


Figure Apx-5.2: Confocal pictures of GUVs formed in saline solution, brought in contact with YOYO-1-labelled salmon sperm DNA. (a) Pure DOPC GUVs: DNA does not cross nor adsorb on GUV. (b) Pure DOPG GUVs: DNA adsorbs on the lipid membrane. (c) Pure DOTAP GUVs: DNA adsorbs on the lipid membrane. For (b) and (c), the intensities inside and outside the GUVs are equal. The microscopes settings are set to avoid saturation due to presence of the coronae on the GUVs. Scale bar represents 45 μm .

Vesicles made of DOPC show no interaction with the YOYO-1 labelled DNA. In the case of DOTAP (*cf.* figure Apx-5.2(b)), the DNA adsorbs onto the membranes. Both phenomena can be explained by simple electrostatic considerations: DNA is a negatively charged molecule. While it shows no interaction to zwitterionic membranes (DOPC), it is attracted and binds strongly to cationic membranes made of DOTAP.

Nonetheless, while DOPG is a negatively charged lipid, all vesicles made of pure DOPG display a corona in fluorescence microscopy, like for DOTAP, suggesting that the DNA binds on these negative membranes as well (*cf.* figure Apx-5.2(d)). This observation was not consistent with the fact that DNA is a highly negatively charged biomolecule supposed to be repelled by the negatively charged membrane of a DOPG GUV.

As the attraction between two highly negatively charged entities seems unlikely, we searched for other plausible explanations. We suggested that the YOYO-1 used to probe the DNA could be attracted by the membrane of DOPG, YOYO-1 bearing 4 nominal positive charges. This hypothesis had to be carefully checked, as the quantum yield of the unbound YOYO-1 is negligible as compared to the one of the YOYO-1 on DNA. To test our idea, we added 50 μL of YOYO-1 at 0.2 μM without DNA in a 100 μL solution of DOPG GUVs under the confocal. As predicted, the GUVs all displayed a green corona, proving that the membrane of DOPG is able to attract the YOYO-1 and activate its fluorescence capacity (*cf.* figure Apx-5.3(a)). The same experiments were conducted with GUVs made of pure DOPS, another negatively charged lipid, which also displayed a green corona. This leads to the conclusion that the negative charges of the membrane are sufficient to attract the YOYO-1. We also repeated the experiments with membrane charges in the biological range of negative membrane charges, namely a mixture of DOPC/DOPG with 20% of DOPG. Here again, the GUVs appeared fluorescent, meaning they were able to interact with the YOYO-1, as shown in figure Apx-5.3(b).

Knowing that the lipid membranes could attract YOYO-1, we had to be assured that the YOYO-1 binding to the membrane was not the one in excess during the preparation of the labelled DNA. This hypothesis was motivated by the strong constant of association of YOYO-1 with DNA, with K equals to $8 \times 10^8 \text{ M}^{-1}$ [252]. To test the hypothesis, we added only one third of the amount of YOYO-1 required to label the sample of DNA (0.5 μL of YOYO-1 at 20 μM in a for 100 ng of Salmon sperm DNA) and repeated the experiments with GUVs made of pure DOPG and DOPS. In both cases, the GUVs turned fluorescent with the typical green corona. However, the same experiments conducted with GUVs made of DOPC/DOPG and DOPC/DOPS, with

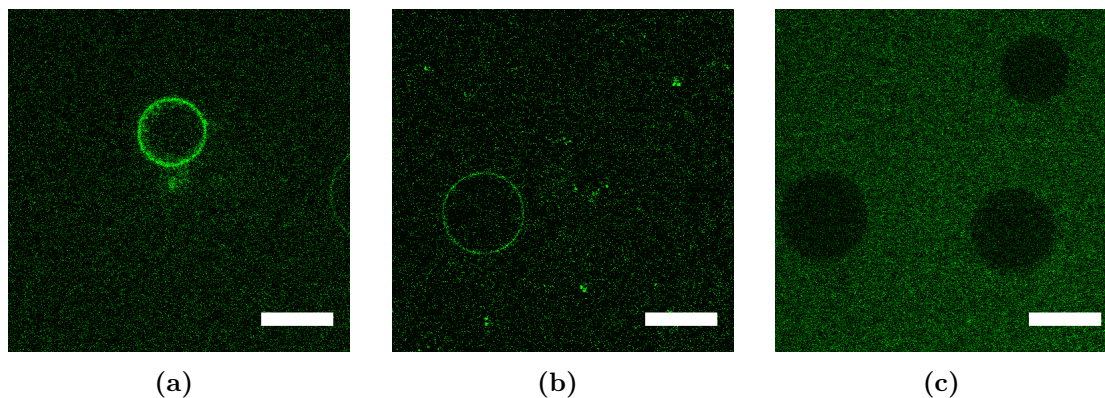


Figure Apx-5.3: Confocal pictures of negatively charged GUVs formed in saline conditions, brought in contact with a solution of YOYO-1 ((a) and (b)), and with a solution of YOYO-1-labelled DNA (c). Vesicles made of negatively charged lipids, from 100% of DOPG (a) or DOPS to 20% of DOPG or DOPS (b) mixed with DOPC, are all able to interact with the YOYO-1 and activate its fluorescence properties. While GUVs of pure negatively charged lipids are able to extract the YOYO-1 from the DNA (figure Apx-5.2(c)), the GUVs of low negative charges does not interact with the DNA and cannot extract the YOYO-1 from it (c). Scale bar represents 45 μm .

20% of negatively charged lipids in both cases, did not lead to any interaction between the GUVs and the YOYO-1, which remained in the bulk with the DNA (*cf.* figure Apx-5.3(c)). We therefore proved that the negatively charged membranes were able to extract the YOYO-1 from the DNA, but only above a certain threshold of negative charge in the membrane, which is above the biological range of membrane charge.

The experiments were also performed with a longer DNA molecule, namely DNA extracted from lambda-phage (48502 bp, Fermentas). The results were identical to the ones with salmon sperm DNA, both with DOPC and DOTAP membranes.

Apx-5-3 DNA encapsulation

The experimental setup was used to test encapsulation. The purpose here was to encapsulate DNA inside the vesicles during the formation process. The encapsulation of DNA in vesicles is of huge interest in the gene therapy, where the liposomes are known to be excellent carrier for the DNA [253].

Each well of the PTFE plate was filled with 70 μL of PVA gel mixed with 10 μL of the 100 ng salmon sperm DNA solution labelled with YOYO-1. Because of the presence of DNA inside the PVA, the gel solution was only heated to 50°C for 30 minutes. Identically to the protocol described above, the lipid solution was then spread on the annealed gel, dried for 30 minutes, and then hydration with the sucrose saline solution for the growth. After one hour of formation, the vesicles were collected, diluted in an isotonic glucose saline solution, and left undisturbed for 15 minutes before observation in the confocal microscope.

In these conditions, in the case of DOPC, all the vesicles in the sample appeared filled with DNA, as pictured in figure Apx-5.4(a). Using a calibration of the fluorescence intensity of YOYO-1 labelled DNA as function of the concentration of the biomolecule, the fluorescence of the encapsulated DNA was quantified for three different concentrations of DNA mixed in the PVA gel. The resulting measurement have shown that the average concentration per vesicle was strictly proportional to the concentration of DNA in the PVA gel before annealing at a $13 \pm 5\%$ ratio (*cf.* figure Apx-5.4(b)).

Similar experiments performed with DOTAP have shown similar results to the experiments where the DNA was brought in contact with the GUVs after the formation, where DNA adsorbed on the surface but did not penetrate inside the GUVs. We also tried to encapsulate the long lambda-phage DNA inside DOPC vesicles, but absolutely no vesicles in the sample appeared to contain measurable DNA traces. We can conclude that the lambda-phage DNA is too long for being encapsulated within DOPC vesicles in these conditions. A possible explanation is the entanglement of polymer chains in the PVA-gel which can prevent the long DNA chains to move inside freely.

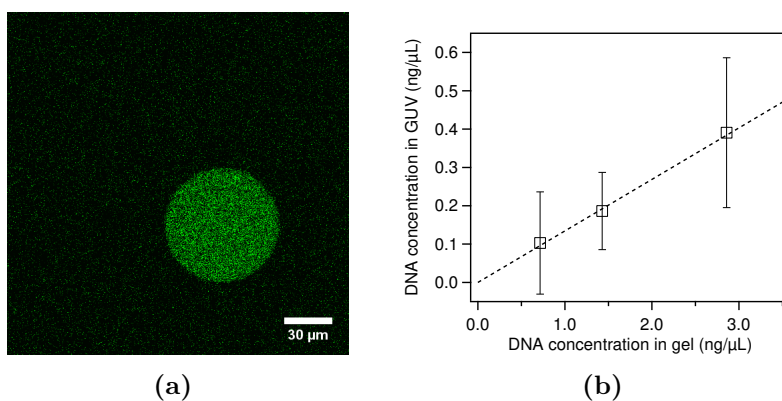


Figure Apx-5.4: Results on the yield of DNA encapsulation in DOPC GUVs. (a) Confocal picture of YOYO-1-labelled DNA encapsulated inside a DOPC vesicle. (b) Measurement of the concentration of DNA encapsulated inside the GUVs as a function of the initial concentration of DNA added to the gel prior to the annealing process. The graph proves that there is a strong correlation between the concentration added in the gel and the concentration found inside the GUVs, with a ratio of $13 \pm 5\%$ between the concentration added in the gel and the concentration found in the GUVs. Scale bar represents $30 \mu\text{m}$.

Apx-7 Computation procedure for the measurement of the N_{PTL}

We give here the algorithm used for the computation of the N_{PTL} . The algorithm has been used on several data analysis software and with different languages, such as Python.

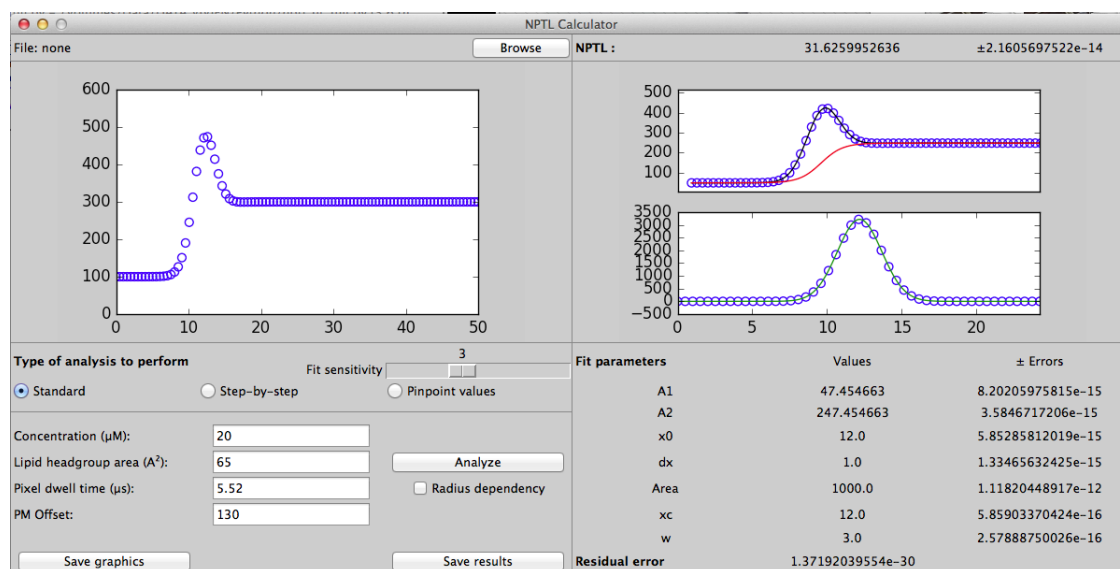


Figure Apx-7.5: Graphical interface to measure the adsorbed amount from the microscope intensity profile.

User-defined parameters:

- $B(O_{PM}, DT)$: Intensity calibration for the given PM offset (O_{PM}) and pixel dwell time (DT).
- A_H : Area per lipid (\AA^2).
- C_b : Polypeptide bulk concentration (μM).

```

## Math functions
gaussian(x, areaGauss, xCtrGauss, widthGauss) = (areaGauss / (widthGauss *
sqrt(pi/2)) ) * exp(-2*sqrt(x-xCtrGauss)/sqrt(widthGauss))
sigmGauss(x, a1, a2, xCtrSig, slopeSig, areaGauss, xCtrGauss, widthGauss) = a1
+ (a2-a1) / (1+ exp((xCtrSig - x)/slopeSig)) + gaussian(x, areaGauss, xCtrGauss,
widthGauss)

## Correction of the recorded intensity
Signal = Signal - B(OPM, DT);

## Initialize the fit parameters
xCenter = x position at intensity max;
a1 = average of the 10 points close to R = 0;
errA1 = standard deviation of the 10 points close to R = 0;
a2 = average of the 10 points close to R = R_Max;
errA2 = standard deviation of the 10 points close to R = R_Max;
i = R_Max;
While intensity[i] < a2 + 2*errA2 # Search the right limit of the Gaussian
do
i = i - 1;
done
widthGauss = (x[i] - xCenter) * 2/3;
slopeSig = widthGauss / 2; # Arbitratry value for the slope of the Sigmoid
areaGauss = (intensity[xCenter] - a2) * widthGauss / 0.8;

## Run the fit
a1, a2, xCtrSig, slopeSig, areaGauss, xCtrGauss, widthGauss =
Fit[sigmGauss(Signal, a1, a2, xCenter, slopeSig, areaGauss, xCenter, width-
Gauss)]

## Integrate the Gaussian function
integGauss = Integrate[gaussian(x, areaGauss, xCtrGauss, widthGauss)]

## Calculate the Nptl value
Nptl = integGauss / a2 / ((xCtrGauss + xCtrSig)/2)*6.02*C_b*A_H/1000

```

REFERENCES

- [1] Center for Innate Immunity and Immune Disease. Artist's rendering of a eukaryotic cell. <https://ciiid.washington.edu/content/signaling-human-cell-transgenics>.
- [2] Theodore Nicolas Gobley. Recherches chimiques sur le jaune d'oeuf - examen comparatif du jaune d'oeuf et de la matière cérébrale. *Journal de Pharmacie et de Chimie*, 11:409–12, 1847.
- [3] E Gorter and F Grendel. On bimolecular layers of lipoids on the chromocytes of the blood. *J Exp Med*, 41(4):439–43, March 1925.
- [4] Encyclopædia Britannica. Membrane. <https://www.britannica.com/science/membrane-biology>.
- [5] I Langmuir. The shapes of group molecules forming the surfaces of liquids. *Proc Natl Acad Sci USA*, 3(4):251–7, April 1917.
- [6] R Lipowsky and E Sackmann, editors. *Handbook of biological physics: Structure and dynamics of membranes*, chapter 3, pages 97–160. Elsevier Science, Amsterdam, 1995.
- [7] J J Myher, A Kuksis, and S Pind. Molecular species of glycerophospholipids and sphingomyelins of human erythrocytes: improved method of analysis. *Lipids*, 24(5):396–407, May 1989.

-
- [8] Eoin Fahy, Shankar Subramaniam, Robert C Murphy, Masahiro Nishijima, Christian R H Raetz, Takao Shimizu, Friedrich Spener, Gerrit van Meer, Michael J O Wakelam, and Edward A Dennis. Update of the lipid maps comprehensive classification system for lipids. *J Lipid Res*, 50 Suppl:S9–14, Apr 2009.
- [9] E Fahy, S Subramaniam, R Murphy, M Nishijima, C Raetz, T Shimizu, F Spener, G van Meer, M Wakelam, and E Dennis. Lipid maps classification system. <http://www.lipidmaps.org/data/structure/index.html>, 2017-12-05.
- [10] Gerrit van Meer. Cellular lipidomics. *EMBO J*, 24(18):3159–65, Sep 2005.
- [11] Thomas E. Andreoli. *Membrane physiology*. Plenum Medical Book Co., New York, 2nd ed edition, 1987.
- [12] Tuscany Diet: Biochemistry and Nutrition. List of fatty acids: Iupac and common names, shorthands. <http://www.tuscany-diet.net/lipids/list-of-fatty-acids/>, June 2017.
- [13] S J Singer and G L Nicolson. The fluid mosaic model of the structure of cell membranes. *Science*, 175(4023):720–31, Feb 1972.
- [14] R D Kornberg and H M McConnell. Inside-outside transitions of phospholipids in vesicle membranes. *Biochemistry*, 10(7):1111–20, Mar 1971.
- [15] Minoru Nakano, Masakazu Fukuda, Takayuki Kudo, Naoya Matsuzaki, Takuto Azuma, Kazuhisa Sekine, Hitoshi Endo, and Tetsuro Handa. Flip-flop of phospholipids in vesicles: kinetic analysis with time-resolved small-angle neutron scattering. *J Phys Chem B*, 113(19):6745–8, May 2009.
- [16] L K Tamm and H M McConnell. Supported phospholipid bilayers. *Biophys J*, 47(1):105–13, Jan 1985.
- [17] Gregor Cevc and Derek Marsh. *Phospholipid bilayers: physical principles and models*, volume v. 5 of *Cell biology : a series of monographs*. Wiley, New York, 1987.
- [18] Louic S Vermeer, Bert L de Groot, Valérie Réat, Alain Milon, and Jerzy Czaplicki. Acyl chain order parameter profiles in phospholipid bilayers: computation from molecular dynamics simulations and comparison with 2h nmr experiments. *Eur Biophys J*, 36(8):919–31, Nov 2007.

- [19] R Montecinos and S Neira-Jimenez. Effect of low concentration of dhpc on the dppc/sm bilayer. *J Chil Chem Soc*, 59(2):2512–2515, 2014.
- [20] T Heimburg. A model for the lipid pretransition: coupling of ripple formation with the chain-melting transition. *Biophys J*, 78(3):1154–65, Mar 2000.
- [21] Thomas Kaasgaard, Chad Leidy, John H Crowe, Ole G Mouritsen, and Kent Jørgensen. Temperature-controlled structure and kinetics of ripple phases in one- and two-component supported lipid bilayers. *Biophys J*, 85(1):350–60, Jul 2003.
- [22] Derek Marsh. *Handbook of lipid bilayers*. CRC Press, Taylor and Francis Group, Boca Raton, FL., 2nd ed edition, 2013.
- [23] Avanti Polar Lipids. Phase transition temperatures for glycerophospholipids. <https://avantilipids.com/tech-support/physical-properties/phase-transition-temps/>, Jun 2017.
- [24] R Koynova and B Tenchov. Transitions between lamellar and non-lamellar phases in membrane lipids and their physiological roles. *OA Biochemistry*, 1(1):1–9, 2013.
- [25] Miranda L Schmidt, Latifa Ziani, Michelle Boudreau, and James H Davis. Phase equilibria in dopc/dppc: Conversion from gel to subgel in two component mixtures. *J Chem Phys*, 131(17):175103, Nov 2009.
- [26] D J Recktenwald and H M McConnell. Phase equilibria in binary mixtures of phosphatidylcholine and cholesterol. *Biochemistry*, 20(15):4505–10, Jul 1981.
- [27] J H Ipsen, G Karlström, O G Mouritsen, H Wennerström, and M J Zuckermann. Phase equilibria in the phosphatidylcholine-cholesterol system. *Biochim Biophys Acta*, 905(1):162–72, Nov 1987.
- [28] Derek Marsh. Liquid-ordered phases induced by cholesterol: a compendium of binary phase diagrams. *Biochim Biophys Acta*, 1798(3):688–99, Mar 2010.
- [29] J Wolff, C M Marques, and F Thalmann. Thermodynamic approach to phase coexistence in ternary phospholipid-cholesterol mixtures. *Phys Rev Lett*, 106(12):128104, Mar 2011.

-
- [30] Jiang Zhao, Jing Wu, Frederick A Heberle, Thalia T Mills, Paul Klawitter, Grace Huang, Greg Costanza, and Gerald W Feigenson. Phase studies of model biomembranes: complex behavior of dspc/dopc/cholesterol. *Biochim Biophys Acta*, 1768(11):2764–76, Nov 2007.
- [31] L Bagatolli and P B Sunil Kumar. Phase behavior of multicomponent membranes: experimental and computational techniques. *Soft Matter*, 5:3234–3248, July 2009.
- [32] D Needham and R M Hochmuth. Electro-mechanical permeabilization of lipid vesicles. role of membrane tension and compressibility. *Biophys J*, 55(5):1001–9, May 1989.
- [33] J Daillant, E Bellet-Amalric, A Braslau, T Charitat, G Fragneto, F Graner, S Mora, F Rieutord, and B Stidder. Structure and fluctuations of a single floating lipid bilayer. *Proc Natl Acad Sci U S A*, 102(33):11639–44, Aug 2005.
- [34] W Helfrich. Elastic properties of lipid bilayers: theory and possible experiments. *Z Naturforsch C*, 28(11):693–703, 1973.
- [35] Zhong-can and Helfrich. Bending energy of vesicle membranes: General expressions for the first, second, and third variation of the shape energy and applications to spheres and cylinders. *Phys Rev A Gen Phys*, 39(10):5280–5288, May 1989.
- [36] R Dimova and R Lipowsky. Lipid membranes in contact with aqueous phases of polymer solutions. *Soft Matter*, 8:6409–6415, 2012.
- [37] Andreas Rørvig-Lund, Azra Bahadori, Szabolcs Semsey, Poul Martin Bendix, and Lene B Oddershede. Vesicle fusion triggered by optically heated gold nanoparticles. *Nano Lett*, 15(6):4183–8, Jun 2015.
- [38] R Lipowsky. Spontaneous tubulation of membranes and vesicles reveals membrane tension generated by spontaneous curvature. *Faraday Discuss.*, 161:305–331, 2013.
- [39] P H Barry and J M Diamond. Effects of unstirred layers on membrane phenomena. *Physiol Rev*, 64(3):763–872, Jul 1984.
- [40] D Papahadjopoulos, S Nir, and S Oki. Permeability properties of phospholipid membranes: effect of cholesterol and temperature. *Biochim Biophys Acta*, 266(3):561–83, Jun 1972.

- [41] W K Subczynski, J S Hyde, and A Kusumi. Oxygen permeability of phosphatidylcholine–cholesterol membranes. *Proc Natl Acad Sci U S A*, 86(12):4474–8, Jun 1989.
- [42] J Gutknecht, M A Bisson, and F C Tosteson. Diffusion of carbon dioxide through lipid bilayer membranes: effects of carbonic anhydrase, bicarbonate, and unstirred layers. *J Gen Physiol*, 69(6):779–94, Jun 1977.
- [43] E P Giorgi and W D Stein. The transport of steroids into animal cells in culture. *Endocrinology*, 108(2):688–97, Feb 1981.
- [44] A Walter and J Gutknecht. Permeability of small nonelectrolytes through lipid bilayer membranes. *J Membr Biol*, 90(3):207–17, 1986.
- [45] E Orbach and A Finkelstein. The nonelectrolyte permeability of planar lipid bilayer membranes. *J Gen Physiol*, 75(4):427–36, Apr 1980.
- [46] R E Wood, F P Wirth, Jr, and H E Morgan. Glucose permeability of lipid bilayer membranes. *Biochim Biophys Acta*, 163(2):171–8, Sep 1968.
- [47] Nicole J Yang and Marlon J Hinner. Getting across the cell membrane: an overview for small molecules, peptides, and proteins. *Methods Mol Biol*, 1266:29–53, 2015.
- [48] T Graham. The bakerian lecture: On osmotic force. *Phil. Trans. R. Soc. Lond.*, 144:177–228, January 1854.
- [49] J H van’t Hoff. The role of osmotic pressure in the analogy between solutions and gases. *Zeitschrift fur physikalische Chemie*, 1:481–508, 1887.
- [50] H N Morse and J C W Frazer. The osmotic pressure and freezing points of solution of cane sugar. *American Chemical Journal*, 34:1, 1905.
- [51] E Sackmann. Membrane bending energy concept of vesicle- and cell-shapes and shape-transitions. *FEBS Letters*, 346:3–16, 1994.
- [52] Y Levin and M A Idiart. Pore dynamics of osmotically stressed vesicles. *Physica A*, 331:571–578, 2004.
- [53] E Neumann and K Rosenheck. Permeability changes induced by electric impulses in vesicular membranes. *J Membr Biol*, 10(3):279–90, Dec 1972.

-
- [54] E Neumann, M Schaefer-Ridder, Y Wang, and P H Hofschneider. Gene transfer into mouse lyoma cells by electroporation in high electric fields. *EMBO J*, 1(7):841–5, 1982.
- [55] A-L Bernard, M-A Guedeau-Boudeville, O Sandre, S Palacin, J-M di Meglio, and L Jullien. Permeation through lipid bilayers by adhesion of giant vesicles on decorated surfaces. *Langmuir*, 16(17):6801–6808, 2000.
- [56] C Tribet and F Vial. Flexible macromolecules attached to lipid bilayers: impact on fluidity, curvature, permeability and stability of the membranes. *Soft Matter*, 4:68–81, 2008.
- [57] A Polozova and F M Winnik. Mechanism of the interaction of hydrophobically-modified poly-(n-isopropylacrylamides) with liposomes. *Biochim Biophys Acta*, 1326(2):213–24, Jun 1997.
- [58] D Huster, G Paasche, U Dietrich, O Zschörnig, T Gutberlet, K Gawrisch, and K Arnold. Investigation of phospholipid area compression induced by calcium-mediated dextran sulfate interaction. *Biophys J*, 77(2):879–87, Aug 1999.
- [59] M Schulz, A Olubummo, and W H Binder. Beyond the lipid-bilayer: interaction of polymers and nanoparticles with membranes. *Soft Matter*, 8:4849–4864, 2012.
- [60] J M Sanderson and E J Whelan. Characterisation of the interactions of aromatic amino acids with diacetyl phosphatidylcholine. *Phys. Chem. Chem. Phys.*, 6(5):1012–1017, 2004.
- [61] C Ladaviere, C Tribet, and S Cribier. Lateral organization of lipid membranes induced by amphiphilic polymer inclusions. *Langmuir*, 18:7320–7327, 2002.
- [62] M A Deverall, E Gindl, E-K Sinner, H Besir, J Ruehe, M J Saxton, and C A Naumann. Membrane lateral mobility obstructed by polymer-tethered lipids studied at the single molecule level. *Biophys J*, 88(3):1875–86, Mar 2005.
- [63] Alexander A Yaroslavov, Nikolay S Melik-Nubarov, and Fredric M Menger. Polymer-induced flip-flop in biomembranes. *Acc Chem Res*, 39(10):702–10, Oct 2006.
- [64] I Langmuir. The adsorption of gases on plane surfaces of glass, mica and platinum. *J Am Chem Soc*, 40(9):1361–1403, 1918.

- [65] P W Atkins. *Physical Chemistry*. Oxford University Press, 6 edition, 1998.
- [66] Burkhard Bechinger, Jarbas M Resende, and Christopher Aisenbrey. The structural and topological analysis of membrane-associated polypeptides by oriented solid-state nmr spectroscopy: established concepts and novel developments. *Biophys Chem*, 153(2-3):115–25, Jan 2011.
- [67] Christopher Aisenbrey and Burkhard Bechinger. Molecular packing of amphipathic peptides on the surface of lipid membranes. *Langmuir*, 30(34):10374–83, Sep 2014.
- [68] G McKay, H S Blair, and J R Gardner. Adsorption of dyes on chitin 1. equilibrium studies. *Journal of Applied Polymer Science*, 27:3043–3057, 1982.
- [69] S Brunauer, P H Emmett, and E Teller. Adsorption of gases in multimolecular layers. *J Am Chem Soc*, 60(2):309–319, 1938.
- [70] A Ebadi, J S Soltan Mohammadzadeh, and A Khudiev. What is the correct form of bet isotherm for modeling liquid phase adsorption. *Adsorption*, 15:65–73, 2009.
- [71] A D Bangham, M M Standish, and J C Watkins. Diffusion of univalent ions across the lamellae of swollen phospholipids. *J Mol Biol*, 13(1):238–52, Aug 1965.
- [72] F Szoka, Jr and D Papahadjopoulos. Comparative properties and methods of preparation of lipid vesicles (liposomes). *Annu Rev Biophys Bioeng*, 9:467–508, 1980.
- [73] Peter Walde, Katia Cosentino, Helen Engel, and Pasquale Stano. Giant vesicles: preparations and applications. *Chembiochem*, 11(7):848–65, May 2010.
- [74] Susanne F Fenz and Kheya Sengupta. Giant vesicles as cell models. *Integr Biol (Camb)*, 4(9):982–95, Sep 2012.
- [75] J P Reeves and R M Dowben. Formation and properties of thin-walled phospholipid vesicles. *J Cell Physiol*, 73(1):49–60, Feb 1969.
- [76] M I Angelova and D S Dimitrov. Liposome electroformation. *Faraday Discuss. Chem. Soc.*, 81:303–311, 1986.

-
- [77] Kim S Horger, Daniel J Estes, Ricardo Capone, and Michael Mayer. Films of agarose enable rapid formation of giant liposomes in solutions of physiologic ionic strength. *J Am Chem Soc*, 131(5):1810–9, Feb 2009.
- [78] Andreas Weinberger, Feng-Ching Tsai, Gijsje H Koenderink, Thais F Schmidt, Rosângela Itri, Wolfgang Meier, Tatiana Schmatko, André Schröder, and Carlos Marques. Gel-assisted formation of giant unilamellar vesicles. *Biophys J*, 105(1):154–64, Jul 2013.
- [79] S Pautot, B J Frisken, and D A Weitz. Production of unilamellar vesicles using an inverted emulsion. *Langmuir*, 19:2870–2879, 2003.
- [80] Ho Cheung Shum, Daeyeon Lee, Insun Yoon, Tom Kodger, and David A Weitz. Double emulsion templated monodisperse phospholipid vesicles. *Langmuir*, 24(15):7651–3, Aug 2008.
- [81] A L Bailey and P R Cullis. Membrane fusion with cationic liposomes: effects of target membrane lipid composition. *Biochemistry*, 36(7):1628–34, Feb 1997.
- [82] K Morigaki and P Walde. Giant vesicle formation from oleic acid/sodium oleate on glass surfaces induced by adsorbed hydrocarbon molecules. *Langmuir*, 18:10509–10511, 2002.
- [83] Kei Funakoshi, Hiroaki Suzuki, and Shoji Takeuchi. Formation of giant lipid vesiclelike compartments from a planar lipid membrane by a pulsed jet flow. *J Am Chem Soc*, 129(42):12608–9, Oct 2007.
- [84] D D Lasic. The mechanism of vesicle formation. *Biochem J*, 256(1):1–11, Nov 1988.
- [85] M Hishida, H Seto, N Yamada, and K Yoshikawa. Hydration process of multi-stacked phospholipid bilayers to form giant vesicles. *Chemical Physics Letters*, 455:297–302, 2008.
- [86] M I Angelova and D S Dimitrov. A mechanism of liposome electroformation. *Progress in Colloid and Polymer Science*, 76:59–67, 1988.
- [87] Toshinori Shimanouchi, Hiroshi Umakoshi, and Ryoichi Kuboi. Kinetic study on giant vesicle formation with electroformation method. *Langmuir*, 25(9):4835–40, May 2009.

- [88] Nicolas Rodriguez, Frédéric Pincet, and Sophie Cribier. Giant vesicles formed by gentle hydration and electroformation: a comparison by fluorescence microscopy. *Colloids Surf B Biointerfaces*, 42(2):125–30, May 2005.
- [89] Tanja Pott, Hélène Bouvrais, and Philippe Méléard. Giant unilamellar vesicle formation under physiologically relevant conditions. *Chem Phys Lipids*, 154(2):115–9, Aug 2008.
- [90] L-Ruth Montes, Alicia Alonso, Felix M Goñi, and Luis A Bagatolli. Giant unilamellar vesicles electroformed from native membranes and organic lipid mixtures under physiological conditions. *Biophys J*, 93(10):3548–54, Nov 2007.
- [91] B J Battersby, R Grimm, S Huebner, and G Cevc. Evidence for three-dimensional interlayer correlations in cationic lipid-dna complexes as observed by cryo-electron microscopy. *Biochim Biophys Acta*, 1372(2):379–83, Jul 1998.
- [92] L Saunders, J Perrin, and D Gammack. Ultrasonic irradiation of some phospholipid sols. *J Pharm Pharmacol*, 14:567–72, Sep 1962.
- [93] Y Kagawa and E Racker. Partial resolution of the enzymes catalyzing oxidative phosphorylation. *The Journal of Biological Chemistry*, 246(17):5477–5487, 1971.
- [94] L D Mayer, M J Hope, and P R Cullis. Vesicles of variable sizes produced by a rapid extrusion procedure. *Biochim Biophys Acta*, 858(1):161–8, Jun 1986.
- [95] F Szoka, Jr and D Papahadjopoulos. Procedure for preparation of liposomes with large internal aqueous space and high capture by reverse-phase evaporation. *Proc Natl Acad Sci U S A*, 75(9):4194–8, Sep 1978.
- [96] M J Hope, M B Bally, G Webb, and P R Cullis. Production of large unilamellar vesicles by a rapid extrusion procedure: characterization of size distribution, trapped volume and ability to maintain a membrane potential. *Biochim Biophys Acta*, 812(1):55–65, Jan 1985.
- [97] M B Abramson, R Katzman, and H P Gregor. Aqueous dispersions of phosphatidylserine: Ionic properties. *J Biol Chem*, 239:70–6, Jan 1964.
- [98] S M Johnson, A D Bangham, M W Hill, and E D Korn. Single bilayer liposomes. *Biochim Biophys Acta*, 233(3):820–6, Jun 1971.
- [99] H Hauser. Methods of preparation of lipid vesicles: assessment of their suitability for drug encapsulation. *Trends in Pharmacological Sciences*, 3:274–277, 1982.

-
- [100] T Heimburg. Lipid ion channels. *Biophys Chem*, 150(1-3):2–22, Aug 2010.
- [101] Karim El Kirat, Sandrine Morandat, and Yves F Dufrene. Nanoscale analysis of supported lipid bilayers using atomic force microscopy. *Biochim Biophys Acta*, 1798(4):750–65, Apr 2010.
- [102] C L Armstrong, M D Kaye, M Zamponi, E Mamontov, M Tyagi, T Jenkins, and M C Rheinstader. Diffusion in single supported lipid bilayers studied by quasi-elastic neutron scattering. *Soft Matter*, 6:5864–5867, 2010.
- [103] A Pockels. Surface tension. *Nature*, 43:437–439, 1891.
- [104] K B Blodgett. Films built by depositing successive monomolecular layers on a solid surface. *J Am Chem Soc*, 57(6):1007–1022, 1935.
- [105] I Langmuir and V J Schaefer. Activities of urease and pepsin monolayers. *J Am Chem Soc*, 60(6):1351–1360, 1938.
- [106] P Mueller, D O Rudin, H T Tien, and W C Wescott. Reconstitution of cell membrane structure in vitro and its transformation into an excitable system. *Nature*, 194:979–80, Jun 1962.
- [107] Eleonora Zakharian. Recording of ion channel activity in planar lipid bilayer experiments. *Methods Mol Biol*, 998:109–18, 2013.
- [108] Gaurav Tiwari, Ruchi Tiwari, Birendra Sriwastawa, L Bhati, S Pandey, P Pandey, and Saurabh K Bannerjee. Drug delivery systems: An updated review. *Int J Pharm Investig*, 2(1):2–11, Jan 2012.
- [109] Sönke Svenson. *Carrier-based drug delivery*, volume 879. American Chemical Society, Washington, D.C., 2004.
- [110] Ernest Moles, Patricia Urbán, María Belén Jiménez-Díaz, Sara Viera-Morilla, Iñigo Angulo-Barturen, Maria Antònia Busquets, and Xavier Fernández-Busquets. Immunoliposome-mediated drug delivery to plasmodium-infected and non-infected red blood cells as a dual therapeutic/prophylactic antimalarial strategy. *J Control Release*, 210:217–29, Jul 2015.
- [111] Tao Yang, Min-Koo Choi, Fu-De Cui, Jung Sun Kim, Suk-Jae Chung, Chang-Koo Shim, and Dae-Duk Kim. Preparation and evaluation of paclitaxel-loaded pegylated immunoliposome. *J Control Release*, 120(3):169–77, Jul 2007.

- [112] Barbara Kneidl, Michael Peller, Gerhard Winter, Lars H Lindner, and Martin Hossann. Thermosensitive liposomal drug delivery systems: state of the art review. *Int J Nanomedicine*, 9:4387–98, 2014.
- [113] Diego Dos Santos Ferreira, Sávia Caldeira de Araújo Lopes, Marina Santiago Franco, and Mônica Cristina Oliveira. pH-sensitive liposomes for drug delivery in cancer treatment. *Ther Deliv*, 4(9):1099–123, Sep 2013.
- [114] Amichai Yavlovich, Brandon Smith, Kshitij Gupta, Robert Blumenthal, and Anu Puri. Light-sensitive lipid-based nanoparticles for drug delivery: design principles and future considerations for biological applications. *Mol Membr Biol*, 27(7):364–81, Oct 2010.
- [115] V S Trubetsky and V P Torchilin. Use of polyoxyethylene-lipid conjugates as long-circulating carriers for delivery of therapeutic and diagnostic agents. *Advanced Drug Delivery Reviews*, 16(2-3):311–320, 1995.
- [116] M A Hammad and B W Müller. Increasing drug solubility by means of bile salt-phosphatidylcholine-based mixed micelles. *Eur J Pharm Biopharm*, 46(3):361–7, Nov 1998.
- [117] P K Narain, E J DeMaria, and D M Heuman. Lecithin protects against plasma membrane disruption by bile salts. *J Surg Res*, 78(2):131–6, Aug 1998.
- [118] K Müller. Structural dimorphism of bile salt/lecithin mixed micelles. a possible regulatory mechanism for cholesterol solubility in bile? x-ray structure analysis. *Biochemistry*, 20(2):404–14, Jan 1981.
- [119] Anatoly N Lukyanov and Vladimir P Torchilin. Micelles from lipid derivatives of water-soluble polymers as delivery systems for poorly soluble drugs. *Adv Drug Deliv Rev*, 56(9):1273–89, May 2004.
- [120] Aparna Krishnadas, Israel Rubinstein, and Hayat Onyüksel. Sterically stabilized phospholipid mixed micelles: in vitro evaluation as a novel carrier for water-insoluble drugs. *Pharm Res*, 20(2):297–302, Feb 2003.
- [121] J Courraud, C Charnay, J P Cristol, J Berger, and S Avallone. In vitro lipid peroxidation of intestinal bile salt-based nanoemulsions: potential role of antioxidants. *Free Radic Res*, 47(12):1076–87, Dec 2013.

-
- [122] Uttam Kedar, Prasanna Phutane, Supriya Shidhaye, and Vilasrao Kadam. Advances in polymeric micelles for drug delivery and tumor targeting. *Nanomedicine*, 6(6):714–29, Dec 2010.
- [123] K Yasugi, T Nakamura, Y Nagasaki, M Kato, and K Kataoka. Sugar-installed polymer micelles: synthesis and micellization of poly(ethylene glycol)-poly(D,L-lactide) block copolymers having sugar groups at the peg chain end. *Macromolecules*, 32:8024–8032, 1999.
- [124] Yogesh B Patil, Udaya S Toti, Ayman Khedair, Linan Ma, and Jayanth Panyam. Single-step surface functionalization of polymeric nanoparticles for targeted drug delivery. *Biomaterials*, 30(5):859–66, Feb 2009.
- [125] K B Thurmond, 2nd, T Kowalewski, and K L Wooley. Water-soluble knedel-like structures: the preparation of shell-cross-linked small particles. *J Am Chem Soc*, 118:7239–7240, 1996.
- [126] Won, Davis, and Bates. Giant wormlike rubber micelles. *Science*, 283(5404):960–3, Feb 1999.
- [127] K S Murthy, Q Ma, C G Clark Jr, E E Remsen, and K L Wooley. Fundamental design aspects of amphiphilic shell-crosslinked nanoparticles for controlled release applications. *Chem Commun*, pages 773–774, 2001.
- [128] Kevin Letchford and Helen Burt. A review of the formation and classification of amphiphilic block copolymer nanoparticulate structures: micelles, nanospheres, nanocapsules and polymersomes. *Eur J Pharm Biopharm*, 65(3):259–69, Mar 2007.
- [129] D Quintanar-Guerrero, E Allémann, H Fessi, and E Doelker. Preparation techniques and mechanisms of formation of biodegradable nanoparticles from preformed polymers. *Drug Dev Ind Pharm*, 24(12):1113–28, Dec 1998.
- [130] A Lamprecht, N Ubrich, H Yamamoto, U Schäfer, H Takeuchi, C M Lehr, P Maincent, and Y Kawashima. Design of rolipram-loaded nanoparticles: comparison of two preparation methods. *J Control Release*, 71(3):297–306, Apr 2001.
- [131] P Calvo, J L Vila-Jato, and M J Alonso. Evaluation of cationic polymer-coated nanocapsules as ocular drug carriers. *International Journal of Pharmaceutics*, 153:41–50, 1997.

- [132] F Dalençon, Y Amjaud, C Lafforgue, F Derouin, and H Fessi. Atovaquone and rifabutine-loaded nanocapsules: formulation studies. *International Journal of Pharmaceutics*, 153:127–130, 1997.
- [133] Noemia Pereira da Silva Santos, Silene Carneiro Nascimento, Marcela Silvestre Outtes Wanderley, Nicodemos Teles Pontes-Filho, José Figueiredo da Silva, Célia Maria Machado Barbosa de Castro, Eugênia Cristina Pereira, Nicácio Henrique da Silva, Neli Kika Honda, and Nereide Stela Santos-Magalhães. Nanoencapsulation of usnic acid: An attempt to improve antitumour activity and reduce hepatotoxicity. *Eur J Pharm Biopharm*, 64(2):154–60, Oct 2006.
- [134] G Luo, X Yu, C Jin, F Yang, D Fu, J Long, J Xu, C Zhan, and W Lu. Lyp-1-conjugated nanoparticles for targeting drug delivery to lymphatic metastatic tumors. *International Journal of Pharmaceutics*, 385:150–156, 2010.
- [135] Erem Bilensoy, Can Sarisozen, Gunes Esendagli, A Lale Dogan, Yesim Aktas, Murat Sen, and N Aydin Mungan. Intravesical cationic nanoparticles of chitosan and polycaprolactone for the delivery of mitomycin c to bladder tumors. *Int J Pharm*, 371(1-2):170–6, Apr 2009.
- [136] J Bai, Y Li, J Du, S Wang, J Zheng, Q Yang, and X Chen. One-pot synthesis of polyacrylamide-gold nanocomposite. *Materials Chemistry and Physics*, 106:412–415, 2007.
- [137] G Amato. Silica-encapsulated efficient and stable si quantum dots with high biocompatibility. *Nanoscale Res Lett*, 5(7):1156–60, May 2010.
- [138] L Wei, N Hu, and Y Zhang. Synthesis of polymer—mesoporous silica nanocomposites. *Materials*, 3(7):4066–4079, 2010.
- [139] Anthony J Di Pasqua, Silvia Wallner, Deborah J Kerwood, and James C Dabrowiak. Adsorption of the pt(ii) anticancer drug carboplatin by mesoporous silica. *Chem Biodivers*, 6(9):1343–9, Sep 2009.
- [140] Zhenhuan Li, Kunmei Su, Bowen Cheng, and Yanchao Deng. Organically modified mcm-type material preparation and its usage in controlled amoxicillin delivery. *J Colloid Interface Sci*, 342(2):607–13, Feb 2010.
- [141] Eric D Smolensky, Hee-Yun E Park, Thelma S Berquó, and Valérie C Pierre. Surface functionalization of magnetic iron oxide nanoparticles for mri applications

- effect of anchoring group and ligand exchange protocol. *Contrast Media Mol Imaging*, 6(4):189–99, 2011.
- [142] Albert Figuerola, Riccardo Di Corato, Liberato Manna, and Teresa Pellegrino. From iron oxide nanoparticles towards advanced iron-based inorganic materials designed for biomedical applications. *Pharmacol Res*, 62(2):126–43, Aug 2010.
- [143] T Neuberger, B Schopf, H Hofmann, M Hofmann, and B von Rechenberg. Superparamagnetic nanoparticles for biomedical applications: Possibilities and limitations of a new drug delivery system. *Journal of Magnetism and Magnetic Materials*, 293:483–496, 2005.
- [144] Yachong Guo, Emmanuel Terazzi, Ralf Seemann, Jean Baptiste Fleury, and Vladimir A Baulin. Direct proof of spontaneous translocation of lipid-covered hydrophobic nanoparticles through a phospholipid bilayer. *Sci Adv*, 2(11):e1600261, Nov 2016.
- [145] Astrid Walrant, Lucrèce Matheron, Sophie Cribier, Stéphane Chaignepain, Marie-Lise Jobin, Sandrine Sagan, and Isabel D Alves. Direct translocation of cell-penetrating peptides in liposomes: a combined mass spectrometry quantification and fluorescence detection study. *Anal Biochem*, 438(1):1–10, Jul 2013.
- [146] Akiko Eguchi and Steven F Dowdy. sirna delivery using peptide transduction domains. *Trends Pharmacol Sci*, 30(7):341–5, Jul 2009.
- [147] Maarja Mae and Ulo Langel. Cell-penetrating peptides as vectors for peptide, protein and oligonucleotide delivery. *Curr Opin Pharmacol*, 6(5):509–14, Oct 2006.
- [148] Rishi R Lulla, Stewart Goldman, Tohru Yamada, Craig W Beattie, Linda Bressler, Michael Pacini, Ian F Pollack, Paul Graham Fisher, Roger J Packer, Ira J Dunkel, Girish Dhall, Shengjie Wu, Arzu Onar, James M Boyett, and Maryam Fouladi. Phase i trial of p28 (nsc745104), a non-hdm2-mediated peptide inhibitor of p53 ubiquitination in pediatric patients with recurrent or progressive central nervous system tumors: A pediatric brain tumor consortium study. *Neuro Oncol*, 18(9):1319–25, Sep 2016.
- [149] A D Frankel and C O Pabo. Cellular uptake of the tat protein from human immunodeficiency virus. *Cell*, 55(6):1189–93, Dec 1988.

- [150] M Green and P M Loewenstein. Autonomous functional domains of chemically synthesized human immunodeficiency virus tat trans-activator protein. *Cell*, 55(6):1179–88, Dec 1988.
- [151] A Joliot, C Pernelle, H Deagostini-Bazin, and A Prochiantz. Antennapedia homeobox peptide regulates neural morphogenesis. *Proc Natl Acad Sci U S A*, 88(5):1864–8, Mar 1991.
- [152] Angela D Ragin, Rashida A Morgan, and Jean Chmielewski. Cellular import mediated by nuclear localization signal peptide sequences. *Chem Biol*, 9(8):943–8, Aug 2002.
- [153] J Oehlke, A Scheller, B Wiesner, E Krause, M Beyermann, E Klauschenz, M Melzig, and M Bienert. Cellular uptake of an alpha-helical amphipathic model peptide with the potential to deliver polar compounds into the cell interior non-endocytically. *Biochim Biophys Acta*, 1414(1-2):127–39, Nov 1998.
- [154] Sébastien Deshayes, Thomas Plénat, Gudrun Aldrian-Herrada, Gilles Divita, Christian Le Grimellec, and Frédéric Heitz. Primary amphipathic cell-penetrating peptides: structural requirements and interactions with model membranes. *Biochemistry*, 43(24):7698–706, Jun 2004.
- [155] G Elliott and P O’Hare. Intercellular trafficking and protein delivery by a herpesvirus structural protein. *Cell*, 88(2):223–33, Jan 1997.
- [156] Sílvia Pujals and Ernest Giralt. Proline-rich, amphipathic cell-penetrating peptides. *Adv Drug Deliv Rev*, 60(4-5):473–84, Mar 2008.
- [157] Shan Gao, Melissa J Simon, Christopher D Hue, Barclay Morrison, 3rd, and Scott Banta. An unusual cell penetrating peptide identified using a plasmid display-based functional selection platform. *ACS Chem Biol*, 6(5):484–91, May 2011.
- [158] Fumiaki Nakayama, Takeshi Yasuda, Sachiko Umeda, Masahiro Asada, Toru Imamura, Viktor Meineke, and Makoto Akashi. Fibroblast growth factor-12 (fgf12) translocation into intestinal epithelial cells is dependent on a novel cell-penetrating peptide domain: involvement of internalization in the in vivo role of exogenous fgf12. *J Biol Chem*, 286(29):25823–34, Jul 2011.
- [159] Stephen M Fuchs and Ronald T Raines. Pathway for polyarginine entry into mammalian cells. *Biochemistry*, 43(9):2438–44, Mar 2004.

-
- [160] Mazin Magzoub, Staffan Sandgren, Pontus Lundberg, Kamila Oglecka, Johanna Lilja, Anders Wittrup, L E Goran Eriksson, Ulo Langel, Mattias Belting, and Astrid Graslund. N-terminal peptides from unprocessed prion proteins enter cells by macropinocytosis. *Biochem Biophys Res Commun*, 348(2):379–85, Sep 2006.
- [161] A Scheller, J Oehlke, B Wiesner, M Dathe, E Krause, M Beyermann, M Melzig, and M Bienert. Structural requirements for cellular uptake of alpha-helical amphipathic peptides. *J Pept Sci*, 5(4):185–94, Apr 1999.
- [162] Jose A Gomez, Joseph Chen, Justine Ngo, Dagmar Hajkova, I-Ju Yeh, Vivian Gama, Masaru Miyagi, and Shigemi Matsuyama. Cell-penetrating penta-peptides (cpp5s): Measurement of cell entry and protein-transduction activity. *Pharmaceuticals (Basel)*, 3(12):3594–3613, Dec 2010.
- [163] C E Schafmeister, J Po, and G L Verdine. An all-hydrocarbon cross-linking system for enhancing the helicity and metabolic stability of peptides. *J Am Chem Soc*, 122:5891–5892, 2000.
- [164] S B Fonseca, M P Pereira, and S O Kelley. Recent advances in the use of cell-penetrating peptides for medical and biological applications. *Advanced Drug Delivery Reviews*, 69:953–964, 2009.
- [165] Fatemeh Madani, Staffan Lindberg, Ulo Langel, Shiroh Futaki, and Astrid Gräslund. Mechanisms of cellular uptake of cell-penetrating peptides. *J Biophys*, 2011:414729, 2011.
- [166] Young S Choi and Allan E David. Cell penetrating peptides and the mechanisms for intracellular entry. *Curr Pharm Biotechnol*, 15(3):192–9, 2014.
- [167] E Vives, P Brodin, and B Lebleu. A truncated hiv-1 tat protein basic domain rapidly translocates through the plasma membrane and accumulates in the cell nucleus. *J Biol Chem*, 272(25):16010–7, Jun 1997.
- [168] Jean Philippe Richard, Kamran Melikov, Eric Vives, Corinne Ramos, Birgit Verbeure, Mike J Gait, Leonid V Chernomordik, and Bernard Lebleu. Cell-penetrating peptides. a reevaluation of the mechanism of cellular uptake. *J Biol Chem*, 278(1):585–90, Jan 2003.
- [169] Samira Jafari, Solmaz Maleki Dizaj, and Khosro Adibkia. Cell-penetrating peptides and their analogues as novel nanocarriers for drug delivery. *Bioimpacts*, 5(2):103–11, 2015.

- [170] Erez Koren and Vladimir P Torchilin. Cell-penetrating peptides: breaking through to the other side. *Trends Mol Med*, 18(7):385–93, Jul 2012.
- [171] Judith Mueller, Ines Kretzschmar, Rudolf Volkmer, and Prisca Boisguerin. Comparison of cellular uptake using 22 cpps in 4 different cell lines. *Bioconjug Chem*, 19(12):2363–74, Dec 2008.
- [172] Arwyn T Jones and Edward J Sayers. Cell entry of cell penetrating peptides: tales of tails wagging dogs. *J Control Release*, 161(2):582–91, Jul 2012.
- [173] S Futaki, T Suzuki, W Ohashi, T Yagami, S Tanaka, K Ueda, and Y Sug-iura. Arginine-rich peptides. an abundant source of membrane-permeable peptides having potential as carriers for intracellular protein delivery. *J Biol Chem*, 276(8):5836–40, Feb 2001.
- [174] Gisela Tunnemann, Gohar Ter-Avetisyan, Robert M Martin, Martin Stöckl, Andreas Herrmann, and M Cristina Cardoso. Live-cell analysis of cell penetration ability and toxicity of oligo-arginines. *J Pept Sci*, 14(4):469–76, Apr 2008.
- [175] Todd A Aguilera, Emilia S Olson, Margaret M Timmers, Tao Jiang, and Roger Y Tsien. Systemic in vivo distribution of activatable cell penetrating peptides is superior to that of cell penetrating peptides. *Integr Biol (Camb)*, 1(5-6):371–81, Jun 2009.
- [176] James R Maiolo, Marc Ferrer, and Elizabeth A Ottinger. Effects of cargo molecules on the cellular uptake of arginine-rich cell-penetrating peptides. *Biochim Biophys Acta*, 1712(2):161–72, Jun 2005.
- [177] D J Mitchell, D T Kim, L Steinman, C G Fathman, and J B Rothbard. Poly-arginine enters cells more efficiently than other polycationic homopolymers. *J Pept Res*, 56(5):318–25, Nov 2000.
- [178] Sarah R Macewan and Ashutosh Chilkoti. Digital switching of local arginine density in a genetically encoded self-assembled polypeptide nanoparticle controls cellular uptake. *Nano Lett*, 12(6):3322–8, Jun 2012.
- [179] D E Thrall. Clinical requirements for localized hyperthermia in the patient. *Radiat Environ Biophys*, 17(3):229–32, 1980.
- [180] S K Alpard, R A Vertrees, W Tao, D J Deyo, R L Brunston, Jr, and J B Zwischenberger. Therapeutic hyperthermia. *Perfusion*, 11(6):425–35, Nov 1996.

-
- [181] D W Urry, W D Cunningham, and T Ohnishi. Studies on the conformation and interactions of elastin. proton magnetic resonance of the repeating pentapeptide. *Biochemistry*, 13(3):609–16, Jan 1974.
- [182] T A T Lee, A Cooper, R P Apkarian, and Conticello V P. Thermo-reversible self-assembly of nanoparticles derived from elastin-mimetic polypeptides. *Advanced Materials*, 12(15):1105–1110, Aug 2000.
- [183] W R Gray, L B Sandberg, and J A Foster. Molecular model for elastin structure and function. *Nature*, 246(5434):461–6, 1973.
- [184] J A Foster, E Bruenger, W R Gray, and L B Sandberg. Isolation and amino acid sequences of tropoelastin peptides. *J Biol Chem*, 248(8):2876–9, Apr 1973.
- [185] D W Urry. Entropic elastic processes in protein mechanisms. i. elastic structure due to an inverse temperature transition and elasticity due to internal chain dynamics. *J Protein Chem*, 7(1):1–34, Feb 1988.
- [186] J-E Park and J-I Won. Thermal behaviors of elastin-like polypeptides (elps) according to their physical properties and environmental conditions. *Biotechnology and Bioprocess Engineering*, 14:662–667, 2009.
- [187] Trine Christensen, Wafa Hassouneh, Kimberley Trabbic-Carlson, and Ashutosh Chilkoti. Predicting transition temperatures of elastin-like polypeptide fusion proteins. *Biomacromolecules*, 14(5):1514–9, May 2013.
- [188] K Gast. Dynamic and static light scattering. In V N Uversky and S Longhi, editors, *Instrumental Analysis of Intrinsically disordered proteins: assessing structure and conformation*. John Wiley & Sons, 2010.
- [189] E Garanger, S R Macewan, O Sandre, A Brulet, L Bataille, A Chilkoti, and S Lecommandoux. Structural evolution of a stimulus-responsive diblock polypeptide micelle by temperature tunable compaction of its core. *Macromolecules*, 48:6617–6627, Sep 2015.
- [190] M I Angelova, S Soleau, P Meleard, J F Faucon, and P Bothorel. Preparation of giant vesicles by external ac electric fields. kinetics and applications. *Progress in Colloid and Polymer Science*, 89:127–131, 1992.
- [191] Avanti Polar Lipids. Equipment - avanti mini extruder. <https://avantilipids.com/divisions/equipment/>, 2017.

REFERENCES

- [192] Nikon. Lateral resolution of a microscope. <https://www.microscopyu.com/microscopy-basics/resolution>, 2017-29-05.
- [193] Nikon. Depth of field of a microscope. <https://www.microscopyu.com/microscopy-basics/depth-of-field-and-depth-of-focus>, 2017-29-05.
- [194] G B David and B S Williamson. Amplitude-contrast microscopy in histochemistry. *Histochemie*, 27(1):1–20, 1971.
- [195] F Zernike. Phase contrast, a new method for the microscopic observation of transparent objects. *Physica*, 9(7):686–698, 1942.
- [196] G Nomarski. Interféromètre à polarisation. Patent FR1059123 A, 1952.
- [197] A S Curtis. The mechanism of adhesion of cells to glass. a study by interference reflection microscopy. *J Cell Biol*, 20:199–215, Feb 1964.
- [198] A Zilker, H Engelhard, and E Sackmann. Dynamic reflection interference contrast (ric-) microscopy : a new method to study surface excitations of cells and to measure membrane bending elastic moduli. *J Phys France*, 48(12):2139–2151, Feb 1957.
- [199] Jörg Schilling, Kheya Sengupta, Stefanie Goennenwein, Andreas R Bausch, and Erich Sackmann. Absolute interfacial distance measurements by dual-wavelength reflection interference contrast microscopy. *Phys Rev E Stat Nonlin Soft Matter Phys*, 69(2 Pt 1):021901, Feb 2004.
- [200] K Lindfors, T Kalkbrenner, P Stoller, and V Sandoghdar. Detection and spectroscopy of gold nanoparticles using supercontinuum white light confocal microscopy. *Phys Rev Lett*, 93(3):037401, Jul 2004.
- [201] A Baeyer. Ueber eine neue klasse von farbstoffen. *Berichte der Deutschen chemischen Gesellschaft*, 4(2):555–558, 1871.
- [202] ThermoFisher Scientific. Probes online newsletter from january 2014. <https://www.thermofisher.com/fr/fr/home/references/newsletters-and-journals/probesonline/probesonline-issues-2014/probesonline-jan-2014.html>, 2014.
- [203] A Moldavan. Photo-electric technique for the counting of microscopical cells. *Science*, 80(2069):188–189, Aug 1934.

-
- [204] M H Julius, T Masuda, and L A Herzenberg. Demonstration that antigen-binding cells are precursors of antibody-producing cells after purification with a fluorescence-activated cell sorter. *Proc Natl Acad Sci U S A*, 69(7):1934–8, Jul 1972.
- [205] T Mayr. Catalog of fluorophores. <http://www.fluorophores.tugraz.at/substance/>, 2017-06-06.
- [206] P R Selvin. The renaissance of fluorescence resonance energy transfer. *Nat Struct Biol*, 7(9):730–4, Sep 2000.
- [207] D Axelrod, D E Koppel, J Schlessinger, E Elson, and W W Webb. Mobility measurement by analysis of fluorescence photobleaching recovery kinetics. *Biophys J*, 16(9):1055–69, Sep 1976.
- [208] H S Rye, S Yue, D E Wemmer, M A Quesada, R P Haugland, R A Mathies, and A N Glazer. Stable fluorescent complexes of double-stranded dna with bis-intercalating asymmetric cyanine dyes: properties and applications. *Nucleic Acids Res*, 20(11):2803–12, Jun 1992.
- [209] N Hamilton. Quantification and its applications in fluorescent microscopy imaging. *Traffic*, 10:951–961, 2009.
- [210] H Christensen, M Hansen, and J Sorensen. Counting and size classification of active soil bacteria by fluorescence in situ hybridization with an rrna oligonucleotide probe. *Appl Environ Microbiol*, 65(4):1753–61, Apr 1999.
- [211] M J Saxton and K Jacobson. Single-particle tracking: applications to membrane dynamics. *Annu Rev Biophys Biomol Struct*, 26:373–99, 1997.
- [212] C Fink, F Morgan, and L M Loew. Intracellular fluorescent probe concentrations by confocal microscopy. *Biophys J*, 75(4):1648–58, Oct 1998.
- [213] S Hamann, J F Kiilgaard, T Litman, F J Alvarez-Leefmans, B R Winther, and Zeuthen T. Measurement of cell volume changes by fluorescence self-quenching. *Journal of Fluorescence*, 12(2):139–145, 2002.
- [214] S Arai, S-C Lee, D Zhai, M Suzuki, and Y T Chang. A molecular fluorescent probe for targeted visualization of temperature at the endoplasmic reticulum. *Scientific Reports*, 4(6701):1–6, 2014.

- [215] M Minsky. Microscopy apparatus. Patent US3013467 A, 1961.
- [216] Leica. Pinhole controls optical slicing. <http://www.leica-microsystems.com/science-lab/pinhole-controls-optical-slicing/>, 2017-29-05.
- [217] W Rasband. Imagej. <https://imagej.nih.gov/ij/>, 2017-29-05.
- [218] J Swedlow, R Baldock, R Carazo Salas, A Brazma, I Davis, P French, S Shorte, E Bertrand, G Zanetti, I Goldberg, R Murphy, K Elcieri, and G Danuser. Bio-format plugin for imagej. <http://www.openmicroscopy.org/site/products/bio-formats>, 2017-29-05.
- [219] Yong Zhou, Christina K Berry, Patrick A Storer, and Robert M Raphael. Peroxidation of polyunsaturated phosphatidyl-choline lipids during electroformation. *Biomaterials*, 28(6):1298–306, Feb 2007.
- [220] Morris Kates. *Techniques of lipidology - Isolation, analysis and identification of lipids*. North-Holland Pub. Co., Amsterdam, 1972.
- [221] E G Bligh and W J Dyer. A rapid method of total lipid extraction and purification. *Can J Biochem Physiol*, 37(8):911–7, Aug 1959.
- [222] Emilie Perret, Andrew Leung, Anne Morel, Helene Feracci, and Pierre Nassoy. Versatile decoration of glass surfaces to probe individual proteinprotein interactions and cellular adhesion. *Langmuir*, 18(3):846–854, January 2002.
- [223] Pierre Gilles de Gennes. *Scaling concepts in polymer physics*. Cornell University Press, Ithaca, N.Y., 1979.
- [224] Laurent Limozin and Kheya Sengupta. Quantitative reflection interference contrast microscopy (ricm) in soft matter and cell adhesion. *Chemphyschem*, 10(16):2752–68, Nov 2009.
- [225] Laurent Limozin and Kheya Sengupta. Modulation of vesicle adhesion and spreading kinetics by hyaluronan cushions. *Biophys J*, 93(9):3300–13, Nov 2007.
- [226] William H Press, Saul A Teukolsky, William T Vetterling, and Brian P Flannery. *Numerical recipes in C: the art of scientific computing*. Cambridge University Press, Cambridge, 2nd ed edition, 1992.
- [227] C H Paik and M D Fox. Fast hartley transforms for image processing. *IEEE Trans Med Imaging*, 7(2):149–53, 1988.

-
- [228] P Carl. Radial profile extended plugin for imagej. <https://imagej.nih.gov/ij/plugins/radial-profile-ext.html>, 2017-29-05.
- [229] Andreas Weinberger, Vivien Walter, Sarah R MacEwan, Tatiana Schmatko, Pierre Muller, André P Schroder, Ashutosh Chilkoti, and Carlos M Marques. Cargo self-assembly rescues affinity of cell-penetrating peptides to lipid membranes. *Sci Rep*, 7:43963, Mar 2017.
- [230] A Mishra, G Hwee Lai, N W Schmidt, V Z Sun, A R Rodriguez, R Tong, L Tang, J Cheng, T J Deming, D T Kamei, and G C L Wong. Translocation of hiv tat peptide and analogues induced by multiplexed membrane and cytoskeletal interactions. *Proc Natl Acad Sci U S A*, 108(41):16883–8, Oct 2011.
- [231] Corina Ciobanasu, Jan Peter Siebrasse, and Ulrich Kubitscheck. Cell-penetrating hiv1 tat peptides can generate pores in model membranes. *Biophys J*, 99(1):153–62, Jul 2010.
- [232] G J Fleer, M A Cohen Stuart, J M H M Scheutjens, T Cosgrove, and B Vincent. *Polymers at interfaces*. Springer, 1993.
- [233] A Johner and J F Joanny. Adsorption of polymeric brushes: Bridging. *The Journal of Chemical Physics*, 96:6257–6273, 1992.
- [234] Bart D van Rooijen, Mireille M A E Claessens, and Vinod Subramaniam. Membrane binding of oligomeric alpha-synuclein depends on bilayer charge and packing. *FEBS Lett*, 582(27):3788–92, Nov 2008.
- [235] Benoît Sorre, Andrew Callan-Jones, John Manzi, Bruno Goud, Jacques Prost, Patricia Bassereau, and Aurélien Roux. Nature of curvature coupling of amphiphysin with membranes depends on its bound density. *Proc Natl Acad Sci U S A*, 109(1):173–8, Jan 2012.
- [236] G Decher and J-D Hong. Buildup of ultrathin multilayer films by a self-assembly process, consecutive adsorption of anionic and cationic bipolar amphiphiles on charged surfaces. *Macromol. Symp.*, 46:321–327, 1991.
- [237] Yi Rao, Sheldon J J Kwok, Julien Lombardi, Nicholas J Turro, and Kenneth B Eisenthal. Label-free probe of hiv-1 tat peptide binding to mimetic membranes. *Proc Natl Acad Sci U S A*, 111(35):12684–8, Sep 2014.

- [238] J-H Choi, S-O Kim, E Linaryd, E C Dreaden, V P Zhdanov, P T Hammond, and N-J Cho. Influence of pH and surface chemistry on poly(L-lysine) adsorption onto solid supports investigated by quartz crystal microbalance with dissipation monitoring. *J Phys Chem B*, 119(33):10554–10565, 2015.
- [239] André Ziegler, Xiaochun Li Blatter, Anna Seelig, and Joachim Seelig. Protein transduction domains of hiv-1 and siv tat interact with charged lipid vesicles. binding mechanism and thermodynamic analysis. *Biochemistry*, 42(30):9185–94, Aug 2003.
- [240] R A Latour, Jr, S D Trembley, Y Tian, G C Lickfield, and A P Wheeler. Determination of apparent thermodynamic parameters for adsorption of a midchain peptidyl residue onto a glass surface. *J Biomed Mater Res*, 49(1):58–65, Jan 2000.
- [241] B Cabane and S Hénon. *Liquides : Solutions, dispersions, émulsions, gels*. Collection Echelle. Belin, 2003.
- [242] Salome Patarraia, Yonggang Liu, Reinhard Lipowsky, and Rumiana Dimova. Effect of cytochrome c on the phase behavior of charged multicomponent lipid membranes. *Biochim Biophys Acta*, 1838(8):2036–45, Aug 2014.
- [243] D Kurzbach, W Hassouneh, J R McDaniel, E A Jaumann, A Chilkoti, and D Hinderberger. Hydration layer coupling and cooperativity in phase behavior of stimulus responsive peptide polymers. *Journal of the American Chemical Society*, 135(30):11299–11308, 2013.
- [244] W Hassouneh, E B Zhulina, A Chilkoti, and M Rubinstein. Elastin-like polypeptide diblock copolymers self-assemble into weak micelles. *Macromolecules*, 48(12):4183–4195, 2015.
- [245] S Alexander. Adsorption of chain molecules with a polar head a scaling description. *Journal de Physique*, 38(8):983–987, 1977.
- [246] Yukihiro Tamba, Shinya Ohba, Masayo Kubota, Hiroe Yoshioka, Hisashi Yoshioka, and Masahito Yamazaki. Single guv method reveals interaction of tea catechin (-)-epigallocatechin gallate with lipid membranes. *Biophys J*, 92(9):3178–94, May 2007.

-
- [247] Marcia P dos Santos Cabrera, Dayane S Alvares, Natalia B Leite, Bibiana Monson de Souza, Mario S Palma, Karin A Riske, and João Ruggiero Neto. New insight into the mechanism of action of wasp mastoparan peptides: lytic activity and clustering observed with giant vesicles. *Langmuir*, 27(17):10805–13, Sep 2011.
- [248] Yen-Fei Chen, Tzu-Lin Sun, Yen Sun, and Huey W Huang. Interaction of daptomycin with lipid bilayers: a lipid extracting effect. *Biochemistry*, 53(33):5384–92, Aug 2014.
- [249] Tatiana M Domingues, Bruno Mattei, Joachim Seelig, Katia R Perez, Antonio Miranda, and Karin A Riske. Interaction of the antimicrobial peptide gomesin with model membranes: a calorimetric study. *Langmuir*, 29(27):8609–18, Jul 2013.
- [250] Yves Landry and Jean-Pierre Gies. *Pharmacologie - Des cibles vers l'indication thérapeutique*. Dunod, Paris (FR), 2003.
- [251] Kai K Ewert, Ayesha Ahmad, Nathan F Boussein, Heather M Evans, and Cyrus R Safinya. Non-viral gene delivery with cationic liposome-dna complexes. *Methods Mol Biol*, 433:159–75, 2008.
- [252] M Maaloum, P Muller, and S Harlepp. Dna-intercalator interactions: structural and physical analysis using atomic force microscopy in solution. *Soft Matter*, 9:11233–11240, 2013.
- [253] Shunsuke F Shimobayashi and Masatoshi Ichikawa. Emergence of dna-encapsulating liposomes from a dna-lipid blend film. *J Phys Chem B*, 118(36):10688–94, Sep 2014.

**INTERACTIONS DES MEMBRANES LIPIDIQUES AVEC DES
PEPTIDES PENETRATEURS DE CELLULES AUTO-ASSEMBLANTS**

Résumé

Les peptides à pouvoir pénétrateur de cellule (CPP) sont des oligopeptides cationiques faisant partie des vecteurs les plus étudiés dans le cadre du développement du transport ciblé de médicaments à l'intérieur de l'organisme. Les applications principales sont par exemple le traitement des cancers ou la thérapie génique. Néanmoins, certaines caractéristiques des CPPs rendent leur utilisation médicale compliquée, tels que leur manque de spécificité à l'égard de cellules cibles ou la perte de leurs propriétés pénétrantes lorsqu'un cargo moléculaire leur est greffé. L'une des solutions envisagées pour résoudre ces problèmes présentés est leur greffage sur des polypeptides di-blocs auto-assemblés basés sur de l'élastine (ELP_{BC}), des systèmes développés par l'équipe d'Ashutosh Chilkoti à l'Université de Duke (USA). Des travaux précédents ont montré que ces macromolécules, que l'on appelle CPP-ELP_{BC}, retrouvaient les propriétés pénétrantes du CPP même en présence d'un cargo et permettaient également d'induire une spécificité à l'encontre des cellules cancéreuses. En revanche, le mécanisme de pénétration de ces systèmes restait inconnu.

Dans cette thèse, je me suis concentré sur l'étude du mécanisme de pénétration des CPPs et CPP-ELP_{BC} au travers de membranes lipidiques modèles, et en particulier sur l'adsorption de ces molécules à la surface de vésicules unilamellaires géantes (GUV). Le développement d'une nouvelle méthode de quantification de la fluorescence en microscopie confocale m'a permis de réaliser des mesures simples de comptage de peptides à la surface des vésicules, ce qui m'a permis par la suite de procéder à des mesures thermodynamiques de l'adsorption des peptides.

Mots-clés : lipides, peptides à pouvoir pénétrateur de cellules, membranes modèles, adsorption, fluorescence, microscopie confocale, polypeptides similaires à l'élastine

Résumé en anglais

Cell-penetrating peptides (CPP) are cationic oligopeptides currently investigated as potential vectors for targeted drug delivery design, for applications in cancer treatment and/or gene therapy. Nevertheless, some drawbacks make the CPPs complex to for medical applications, such as their lack of specificity toward target cells or the loss of their penetrating properties once they have been grafted with a molecular cargo. One of the solutions studied to overcome these issues is the binding of the CPP unit on a self-assembling elastin-like diblock polypeptide (ELP_{BC}), a macromolecular system designed by the team of Ashutosh Chilkoti from Duke University (USA). While it has already been proven that these molecules, named CPP-ELP_{BC}, recover the penetrating properties of the CPP despite the presence of a cargo and also induce a selectivity toward tumorous cells, the exact mechanism of translocation is still under debate.

In this PhD thesis, I focused on the investigation of the translocation mechanism of the CPPs and CPP-ELP_{BC} using model lipid membranes, and specifically the adsorption of these molecules at the surface of giant unilamellar vesicles (GUV). The development of a new quantification method of fluorescence in confocal microscopy allowed me to directly count the peptides adsorbed on the surface of the GUVs, which I used to perform thermodynamic measurements on the peptide adsorption.

Key-words : lipids, cell-penetrating peptides, model membranes, adsorption, fluorescence, confocal microscopy, elastin-like polypeptides